

**Isolation of Wear Debris from Periarticular  
Tissue and In Vivo Biocompatibility of  
Silicon Nitride Particles**

Jayna Patel

Submitted in accordance with the requirements for the  
degree of Doctor of Philosophy

The University of Leeds  
School of Mechanical Engineering

August 2018

The candidate confirms that the work submitted is her own, except where work which has formed part of jointly authored publications has been included. The contribution of the candidate and the other authors to this work has been explicitly indicated below. The candidate confirms that appropriate credit has been given within the thesis where reference has been made to the work of others.

Chapter 3 is based on three joint authorship publications:

- Patel, J., Lal, S., Wilshaw, S.P., Hall, R.M. and Tipper, J.L., 2018. Validation of a novel particle isolation procedure using particle doped tissue samples. *Data in brief*, 18, pp.1802-1807.
- Patel, J., Lal, S., Wilshaw, S.P., Hall, R.M. and Tipper, J.L., 2018. Recovery rate data for silicon nitride nanoparticle isolation using sodium polytungstate density gradients. *Data in Brief*, 19, pp.1474-1476.
- Patel, J., Lal, S., Wilshaw, S.P., Hall, R.M. and Tipper, J.L., 2018. Development and optimisation data of a tissue digestion method for the isolation of orthopaedic wear particles. *Data in Brief*, 20, pp. 173-177.

Chapter 4 is based on a joint authorship publication:

- Patel, J., Lal, S., Nuss, K., Wilshaw, S.P., von Rechenberg, B., Hall, R.M. and Tipper, J.L., 2018. Recovery of low volumes of wear debris from rat stifle joint tissues using a novel particle isolation method. *Acta biomaterialia*, 71, pp.339-350.

As the lead author the candidate was responsible for laboratory work, analysis and writing of the papers. Contributions by Nuss, K and von Rechenberg, B included the design and implementation of the in-life phase of the rat study. Contributions by other authors included discussions on experimental design and analysis, critique and proof-reading of the manuscripts, and obtaining funding for the study.

This copy has been supplied on the understanding that it is copyright material and that no quotation from the thesis may be published without proper acknowledgement.

## Acknowledgements

I would firstly like to express my sincere gratitude to my primary supervisor, Professor Joanne Tipper, who has invested so much time over the years in supporting my research. Joanne's patience, reassurance and continued advice has helped me with my research immeasurably. I would also like to thank my co-supervisor, Professor Richard Hall, who has been really encouraging and has shown me different ways to view and critique my work. I would like to thank my co-supervisor, Dr Stacy-Paul Wilshaw, who has leant his time and expertise to help me with my histological analysis.

I would like to thank the whole technical team at IMBE and those at LEMAS, who have helped me to capture countless images of particles. I am also grateful to the team at the Musculoskeletal Research Unit, University of Zurich, without whom much of this research would not be possible.

I would like to thank Dr Saurabh Lal, who has been an invaluable friend and mentor throughout my PhD. I would also like to thank Jo, Judy, Kritika, Mateusz, Mek and Xiaojie, with whom I share lots of happy memories during the past few years. I am also lucky enough to have two amazing brothers, Anish and Milan, and a wonderful aunt, Deena.

I am eternally grateful to my parents, whom I love and admire. Your encouragement has made me feel like I can achieve anything.

Finally, I would like to thank my boyfriend, Michał, who heroically made the journey from Portsmouth to Leeds on countless occasions to visit me during my PhD. I love you for your kindness and generosity and look forward to spending much more time with you.

I dedicate this work to my parents and to Michał.

## Abstract

Adverse biological reactions to orthopaedic wear particles have led to the investigation of silicon nitride (SiN) coatings for implants, which may improve the biocompatibility of hip replacements. However, the analysis of wear particles is impeded by suboptimal methods to isolate wear particles from tissue. The aim of this research was to develop an improved method to isolate wear particles from tissue samples and to evaluate the *in vivo* biocompatibility of SiN particles. The method involved digestion of tissue samples with papain (1.56 mg.ml<sup>-1</sup>) and proteinase K (1 mg.ml<sup>-1</sup>). Samples were then subjected to density gradient ultracentrifugation using sodium polytungstate (SPT) and washing through further rounds of ultracentrifugation.

The isolation method was validated by subjecting tissue samples doped with 0.0025 mm<sup>3</sup> of silicon nitride (SiN), or 0.025 mm<sup>3</sup> of cobalt chromium (CoCr) or titanium particles to the isolation procedure. Particles were filtered and analysed using scanning electron microscopy (SEM), elemental analysis and image analysis software before and after isolation. The method had no significant effect on SiN, CoCr or titanium particle geometries.

Volumes of 0.018 mm<sup>3</sup> of SiN, CoCr or titanium particles were injected into rat stifle joints. After seven days animals were euthanised, and the stifle joints were formalin-fixed. Stifle joint tissues were harvested and subjected to particle isolation using the validated protocol. No significant changes to SiN or CoCr particle geometries occurred. Titanium particles were similar in size, aspect ratio and circularity before and after isolation, though particle numbers were insufficient for statistical analysis. Histology of stifle joint tissues demonstrated that all three particle types caused a degree of inflammation; in the SiN group, numbers of macrophages but not lymphocytes were significantly elevated. Necrosis and increases in synovial thickness were observed in the CoCr group, but were absent in the SiN and titanium groups.

Rabbits were implanted with CoCr stifle joint prostheses, which were either uncoated or coated with SiN. After 12 weeks the rabbits were euthanised. Tissue samples from the joints were formalin-fixed and subjected to the



particle isolation process. SiN coating particles, CoCr substrate particles, and zirconium dioxide particles from bone cement were isolated from the samples. Due to apparent coating failure, the coating particles were 1 – 100  $\mu\text{m}$  in size and were columnar or shard-like in morphology. Histological analysis of rabbit samples from the coated group demonstrated a moderate macrophage infiltrate including giant cells, with few lymphocytes and no necrosis. Overall, SiN particles were relatively biocompatible, particularly in comparison to CoCr particles. However, analysis of a functional SiN coating must be carried out over a longer timeframe to enable chronic reactions to SiN coating particles to be fully evaluated.

# Table of Contents

<b>Acknowledgements</b> .....	<b>ii</b>
<b>Abstract</b> .....	<b>iii</b>
<b>Table of Contents</b> .....	<b>v</b>
<b>List of Abbreviations</b> .....	<b>x</b>
<b>List of Figures</b> .....	<b>xiii</b>
<b>List of Tables</b> .....	<b>xxii</b>
<b>Chapter 1 Introduction</b> .....	<b>- 1 -</b>
1.1 Introduction to total hip replacement .....	- 1 -
1.2 Total hip replacement materials .....	- 2 -
1.3 Wear mechanisms at the bearing surfaces of hip replacements.....	- 6 -
1.4 Mechanical testing of hip replacements .....	- 8 -
1.5 Isolation of wear particles from serum.....	- 11 -
1.6 In vitro biocompatibility testing of wear particles .....	- 16 -
1.7 Animal models for biocompatibility testing.....	- 16 -
1.7.1 An overview of different species used as animal models-	16 -
1.7.2 Anatomy of the stifle joint .....	- 18 -
1.8 Analysis of tissue samples .....	- 19 -
1.9 Isolation of wear particles from tissue .....	- 21 -
1.10 Size and shape of wear particles .....	- 24 -
1.11 Biological responses to wear debris.....	- 26 -
1.11.1 Biological responses to polyethylene wear debris...-	27 -
1.11.2 Biological responses to CoCr wear debris .....	- 29 -
1.11.3 Biological responses to silicon nitride wear debris ..-	33 -
1.11.4 Biological responses to other ceramic wear debris .-	34 -
1.11.5 Biological responses to titanium particles .....	- 35 -
1.12 The need for improved hip replacements.....	- 35 -
1.13 Coatings for hip replacements.....	- 38 -
1.14 Silicon nitride as a coating for hip replacements .....	- 40 -
1.15 Project aims and rationale.....	- 42 -
<b>Chapter 2 Materials and Methods</b> .....	<b>- 44 -</b>
2.1 Materials.....	- 44 -
2.2 Methods .....	- 44 -
2.2.1 Cleaning of glassware and tubes .....	- 44 -

2.2.2	Filtration of stock solutions and particle suspensions .....	- 44 -
2.2.3	Measuring and adjusting pH of solutions .....	- 44 -
2.2.4	Stock solutions .....	- 45 -
2.2.5	Generation of clinically relevant cobalt chromium particles using a pin-on-plate wear simulator .....	- 46 -
2.2.6	Particle characterisation .....	- 54 -
2.2.7	Statistical analysis of particle parameters .....	- 55 -
2.2.8	Particle isolation from tissue.....	- 55 -
2.2.9	General histological techniques .....	- 58 -
<b>Chapter 3 Development of a novel method to isolate wear particles from tissue .....</b>		<b>- 61 -</b>
3.1	Background.....	- 61 -
3.2	Aims.....	- 61 -
3.3	Overview of experiments.....	- 62 -
3.4	Materials and Methods.....	- 64 -
3.3.1	Creating a silicon nitride particle suspension .....	- 64 -
3.4.1	Creating cobalt chromium and titanium particle suspensions .....	- 64 -
3.4.2	Isolating particles from serum to quantify particle recovery .....	- 64 -
3.4.3	Preparation of tissue samples for tissue digestion and particle isolation experiments .....	- 66 -
3.4.4	Developing a method for effective digestion of tissue.....	- 68 -
3.4.5	Testing the final particle isolation technique.....	- 69 -
3.5	Results.....	- 70 -
3.5.1	Characterisation of particles prior to isolation experiments.....	- 70 -
3.5.2	Isolating particles from serum to quantify particle recovery .....	- 83 -
3.3.2	Imaging of silicon nitride particles isolated from serum .....	- 85 -
3.3.3	Developing a method for effective digestion of tissue and initial particle isolation experiments from tissue.....	- 86 -
3.5.3	Testing the final isolation protocol .....	- 89 -
3.5.4	Testing the final particle isolation technique in cobalt chromium and titanium particles .....	- 93 -

3.6 Discussion.....	- 101 -
<b>Chapter 4 In vivo investigation of silicon nitride nanoparticles using a rat model .....</b>	<b>- 106 -</b>
4.1 Background.....	- 106 -
4.2 Aims.....	- 107 -
4.3 Overview of experiments.....	- 107 -
4.4 Materials and Methods.....	- 109 -
4.4.1 Generation of particle suspensions for injection into rat stifle joints .....	- 109 -
4.4.2 Characterisation of particle suspensions.....	- 110 -
4.4.3 Animal model .....	- 110 -
4.4.4 Particle isolation from injected rat stifle joints.....	- 112 -
4.4.5 Statistical analysis comparing non-injected particles with particles post-isolation from tissues .....	- 114 -
4.4.6 Histology of rat stifle joints .....	- 114 -
4.5 Results.....	- 122 -
4.5.1 Characterisation of particle suspensions prior to injection into rat stifle joints .....	- 122 -
4.5.2 Observations of rats and rat stifle joints prior to and after sacrifice.....	- 138 -
4.5.3 Particle isolation from injected rat stifle joints.....	- 139 -
4.5.4 Visual observation of isolated particles using SEM .....	- 142 -
4.5.5 Comparison of SEM images of isolated particles with non-injected particles.....	- 142 -
4.5.6 Elemental analysis of isolated particles.....	- 146 -
4.5.7 Characterisation of isolated particles with image analysis and comparisons with non-injected particles.....	- 155 -
4.5.8 Analysis of decalcified stifle joint sections.....	- 157 -
4.6 Discussion.....	- 193 -
4.6.1 Isolation of particles from injected stifle joints .....	- 193 -
4.6.2 Histological analysis of stifle joint sections.....	- 196 -
<b>Chapter 5 Investigation of the biocompatibility of silicon nitride coatings using an in vivo rabbit model .....</b>	<b>- 201 -</b>
5.1 Background.....	- 201 -
5.2 Aims.....	- 202 -
5.3 Overview of experiments.....	- 202 -

5.4	Materials and methods .....	204 -
5.4.1	In vivo model .....	204 -
5.4.2	Prosthesis design.....	205 -
5.4.3	Coating details .....	206 -
5.4.4	Surgical implantation of the stifle joint prostheses. -	206 -
5.4.5	In-life phase of the rabbit study .....	210 -
5.4.6	Euthanasia and dissection.....	210 -
5.4.7	Particle isolation from periprosthetic tissue of rabbit stifle joints.....	213 -
5.4.8	Histological analysis of periprosthetic tissues .....	214 -
5.5	Results .....	216 -
5.5.1	In-life observations and surgical complications .....	216 -
5.5.2	Macroscopic observation of stifle joints and periprosthetic tissue .....	217 -
5.5.3	Particle isolation from periprosthetic tissue samples.....	219 -
5.5.4	Histological analysis of periprosthetic tissue .....	233 -
5.5.5	Summary of results .....	238 -
5.6	Discussion.....	241 -
	<b>Chapter 6 Discussion.....</b>	<b>246 -</b>
6.1	General discussion.....	246 -
6.2	Development and application of a particle isolation method..	247 -
6.3	Comparison of the animal models .....	249 -
6.4	Biocompatibility of SiN, CoCr and titanium particles .....	252 -
6.5	Limitations of the studies.....	256 -
6.6	Future work .....	257 -
6.7	Conclusions.....	261 -
	<b>References.....</b>	<b>264 -</b>
	<b>Appendix A Lists of all equipment, reagents and consumables.....</b>	<b>288 -</b>
	<b>Appendix B Food, housing and environmental parameters of the animal studies .....</b>	<b>293 -</b>
	<b>Appendix C Testing the particle isolation method on particle-injected rat cadavers prior to application to an in vivo study .-</b>	<b>295 -</b>
	Materials and Methods.....	295 -
	Results .....	296 -

<b>Appendix D Immunohistochemical labelling of macrophages in particle-injected rat stifle joint tissues .....</b>	<b>- 297 -</b>
Methods .....	- 297 -
Stock solutions for antibody labelling .....	- 297 -
Antibody labelling protocol .....	- 298 -
Results .....	- 299 -

## List of Abbreviations

ASTM	American Standard for Testing and Materials
ALVAL	Aseptic, lymphocyte-dominated vasculitis-associated lesion
BSA	Bovine serum albumin
CD4	Cluster of differentiation 4
COC	Ceramic-on-ceramic
CoCr	Cobalt chromium
COP	Ceramic-on-polyethylene
CrCN	Chromium carbon nitride
CrN	Chromium nitride
DLC	Diamond-like carbon
EDTA	Ethylenediaminetetraacetic acid
EDX	Energy dispersive X-ray analysis
ELISA	Enzyme-linked immunosorbency assay
FBS	Foetal bovine serum
Fc	Fragment crystallisable
FDA	Food and Drug Administration
FEG-SEM	Field emission gun scanning electron microscopy
g	Grams
GSH	Glutathionine
h	Hour
HCl	Hydrochloric acid
HEPES	N-(2-hydroxyethyl) piperazine-N'-(2-ethanulfonic acid)
HRP	Horseradish peroxidise
IFN	Interferon
IL-1 $\beta$	Interleukin-1 $\beta$
IL-6	Interleukin-6
IL-8	Interleukin-8

ISO	International Standards Organisation
M	Mol per litre
mg	Milligram
MHC	Major histocompatibility complex
min	Minute
ml	Millilitre
mm	Millimetre
mm <sup>3</sup>	Millimetre cubed
MMA	Methylmethacrylate
MOM	Metal-on-metal
MPa	Mega pascals
MPC	2--methacryloyloxethyl phosphorylcholine
MTT	3-(4,5-Dimethylthiazol-2-yl)-2,5-Diphenyltetrazolium Bromide
N	Newton
NJR	National Joint Registry
OPG	Osteoprotegerin
PBMNCs	Peripheral blood mononuclear cells
(D)PBS	Phosphate buffered saline
	PEEK Polyether ether ketone
PGE <sub>2</sub>	Prostaglandin E <sub>2</sub>
Ra	Roughness
RANKL	Receptor activator of nuclear factor kappa-B ligand
SEM	Scanning electron microscopy
SiN	Silicon nitride
SSB	Single strand breaks
SWD	Silicon wafer display
TiN	Titanium nitride
TNF- $\alpha$	Tumour necrosis factor-alpha
THR	Total hip replacement



UHMWPE	Ultra high molecular weight polyethylene
UK	United Kingdom
UV	Ultraviolet
US(A)	United States (of America)
v/v	Volume/volume
w/v	Weight/volume

## List of Figures

Figure 1.1. The major components of a hip replacement. ....	- 2 -
Figure 1.2. Schematic representations of wear mechanisms. ....	- 8 -
Figure 1.3. Key research processes involved in development and testing of novel orthopaedic devices. ....	- 9 -
Figure 1.4. A reciprocating six-station pin-on-plate machine. ....	- 10 -
Figure 1.5. An overview for isolation of ceramic, metal or polymer wear particles from tissue. ....	- 12 -
Figure 1.6. Dissected view of a left rabbit stifle joint, with the patellar ligament displaced medially to the joint. ....	- 19 -
Figure 1.7. An overview for isolation of ceramic, metal or polymer wear particles from tissue.. ....	- 21 -
Figure 1.8. RANK/RANKL/OPG modulation of osteoclastogenesis.....	- 28 -
Figure 2.1. Engineering drawing of pins and plates used.....	- 47 -
Figure 2.2 A. The components of a reciprocating six-station pin-on-plate wear simulator excluding the cantilever arms. ....	- 48 -
Figure 2.3. Load calibration of the pin-on-plate machine.....	- 49 -
Figure 2.4. Screws required for assembly of the linear bearing trays.....	- 50 -
Figure 2.5. Assembly of the linear bearing trays.. ....	- 51 -
Figure 2.6. Assembly of the pin holders.. ....	- 52 -
Figure 2.7. Assembled pin-on-plate station. ....	- 53 -
Figure 2.8 Schematic representation of particle isolation method.. ....	- 56 -
Figure 3.1. Overview of experiments detailed in this chapter. ....	- 63 -
Figure 3.2. Dissection and harvesting of synovial tissue from a porcine cadaver. ....	- 67 -
Figure 3.3. Scanning electron micrograph of commercial SiN particles at (A) a magnification of 2,000x and (B) a higher magnification of 100,000x. ....	- 71 -

Figure 3.4. Elemental analysis of commercial silicon nitride particles.. ...	- 72 -
Figure 3.5. Elemental mapping of commercial SiN particles, with the chemical symbol of the element above.. .....	- 73 -
Figure 3.6. (A) The size distribution of commercial silicon nitride particles and (B) the average particle parameters.....	- 74 -
Figure 3.7. Scanning electron micrograph of CoCr particles generated by pin-on-plate at (A) a magnification of 2,000x and (B) a higher magnification of 100,000x. ....	- 75 -
Figure 3.8. Elemental analysis of CoCr particles generated by pin-on-plate. ....	- 77 -
Figure 3.9. Elemental mapping of CoCr particles generated by pin-on-plate, with the chemical symbol of the element above.. .....	- 78 -
Figure 3.10. (A) Size distribution of CoCr particles and (B) average particle parameters.. .....	- 79 -
Figure 3.11. Scanning electron micrograph of titanium particles generated by pin-on-plate, at a magnification of 500x.....	- 80 -
Figure 3.12. Elemental analysis of titanium particles generated by pin-on-plate.. .....	- 81 -
Figure 3.13. Elemental mapping of titanium particles generated by pin-on-plate. ....	- 82 -
Figure 3.14. (A) Size distributions and (B) mean particle characteristics for titanium particles.. .....	- 83 -
Figure 3.15. Filter membrane with isolated silicon nitride particles deposited on the surface, which have formed a cracked layer.....	- 84 -
Figure 3.16. Adherence of silicon nitride particles to filtration equipment. ....	- 85 -
Figure 3.17. Commercial SiN particles at (A and B) a magnification of 2,000x and (C and D) a high magnification of 10,000x, before (A and C) and after (B and D) isolation.....	- 86 -
Figure 3.18. Appearance of tissues during initial digestion experiments. ....	- 87 -

Figure 3.19. (A) Tissue sample prior to digestion, and (B) after 48 h of a digestion protocol involving frequent proteinase K replenishment in the presence of glycine.....	88 -
Figure 3.20. Appearance of tissue samples during a tissue digestion experiment using papain and proteinase K..	89 -
Figure 3.21. Commercial silicon nitride particles (A and C) before isolation, and (B and D) following isolation from tissue using the final method, at (A and B) a magnification of 2,000x and (C and D) a higher magnification of 100,000x. ....	90 -
Figure 3.22. Elemental analysis of commercial silicon nitride particles..	91 -
Figure 3.23. Elemental mapping of isolated SiN particles, with the chemical symbol of the element above..	92 -
Figure 3.24. (A) Size distributions of commercial silicon nitride particles prior to and after isolation from tissue and (B) average particle parameters. ....	93 -
Figure 3.25. Scanning electron micrographs of CoCr particles (A-D), at magnifications of 2,000x (A and B) and 100,000x (C and D), and titanium particles at a magnification of 500x (E and F), not subject to isolation (left) and after isolation (right). ....	94 -
Figure 3.26. Elemental analysis of isolated CoCr particles. ....	95 -
Figure 3.27. Elemental mapping of isolated cobalt chromium particles...-	96 -
Figure 3.28. Elemental analysis of isolated titanium particles. ....	97 -
Figure 3.29. Elemental mapping of isolated titanium particles. ....	98 -
Figure 3.30. (A) Particle size distributions and (B) mean particle characteristics for CoCr, for both isolated and non-isolated particles.....	99 -
Figure 3.31. (A) Particle size distributions and (B) mean particle characteristics for titanium, for both isolated and non-isolated particles.....	100 -
Figure 4.1. Overview of experiments outlined in this chapter.....	108 -

Figure 4.2. Dissection and harvesting of rat stifle joint tissue for particle isolation.....	- 113 -
Figure 4.3. Schematic representation of embedding and cutting orientation of the intact stifle joints. ....	- 116 -
Figure 4.4. Scanning electron micrographs of non-injected commercial SiN particles.....	- 123 -
Figure 4.5. Elemental mapping of non-injected commercial SiN particles.....	- 125 -
Figure 4.6. Elemental spectra of non-injected commercial SiN particles.....	- 126 -
Figure 4.7. (A) Size distribution of non-injected commercial silicon nitride particles and (B) average particle parameters. ....	- 127 -
Figure 4.8. Scanning electron micrographs of non-injected CoCr particles.....	- 129 -
Figure 4.9. Elemental analysis of non-injected CoCr particles generated by pin-on-plate. ....	- 130 -
Figure 4.10. Elemental analysis of non-injected CoCr particles generated by pin-on-plate. ....	- 131 -
Figure 4.11. (A) Size distribution of non-injected CoCr particles generated by pin-on-plate wear testing and (B) average particle parameters. ....	- 132 -
Figure 4.12. Scanning electron micrograph of non-injected titanium particles.....	- 134 -
Figure 4.13. Elemental analysis of non-injected titanium particles generated by pin-on-plate wear testing.. ....	- 135 -
Figure 4.14. Elemental analysis of non-injected CoCr particles generated by pin-on-plate. ....	- 136 -
Figure 4.15. (A) Size distribution of non-injected titanium particles generate by pin-on-plate wear testing and (B) average particle parameters.....	- 137 -

Figure 4.16. Appearance of intact stifle joints following formalin fixation and storage in 70% (v/v) ethanol.....	- 139 -
Figure 4.17. Appearance of SiN injected rat tissue samples, and an untreated control rat tissue sample from a contralateral stifle joint (last tube on right), post-digestion. ....	- 141 -
Figure 4.18. Pellet of CoCr particles isolated from a CoCr injected rat stifle joint (33.76) during the washing stages of the particle isolation protocol, following each ultracentrifugation step. ....	- 142 -
Figure 4.19. Commercial silicon nitride particles (<50nm, Sigma) imaged by high resolution scanning electron microscopy. ....	- 143 -
Figure 4.20. Clinically relevant CoCr particles generated using a pin-on-plate wear tester, filtered onto polycarbonate filter membranes at a volume of 0.018 mm <sup>3</sup> , and imaged by high resolution scanning electron microscopy. ....	- 144 -
Figure 4.21. Clinically relevant titanium particles generated using a pin-on-plate wear tester, filtered onto polycarbonate filter membranes at a volume of 0.018 mm <sup>3</sup> , and image by high resolution scanning electron microscopy. ....	- 145 -
Figure 4.22. Elemental analysis of SiN particles isolated from an injected rat stifle (33.90R).. ....	- 147 -
Figure 4.23. Elemental spectra of SiN particles isolated from an injected rat stifle joint (33.85R). ....	- 148 -
Figure 4.24. Elemental analysis of CoCr particles isolated from an injected rat stifle (33.76R).. ....	- 150 -
Figure 4.25. Elemental spectra of CoCr particles isolated from an injected rat stifle joint (33.76R). ....	- 152 -
Figure 4.26. Elemental analysis of titanium particles isolated from an injected rat stifle joint (33.81R).....	- 153 -
Figure 4.27. Elemental spectra of titanium particles isolated from an injected rat stifle joint (33.81R).....	- 154 -

Figure 4.28. Size distributions for non-injected particles, and particles isolated from injected rat stifle joints, for (A) Si <sub>3</sub> N <sub>4</sub> (B) CoCrMo and (C) Ti-6Al-4V material groups.....	156 -
Figure 4.29. Whole joint section taken from a depth of up to 1500 µm into the joint capsule, from a non-treated contralateral rat stifle joint (animal 33.86; control joint), stained with H&E. ....	159 -
Figure 4.30. Images of histological sections taken from a depth of up to 1500 µm into the joint capsule of a non-treated contralateral rat stifle joint (33.86L), stained with H&E.....	160
Figure 4.31. Whole joint sections taken from depths of up to 1500 µm into the joint capsule, from SiN-injected rat stifle joints, stained with H&E.. ....	163 -
Figure 4.32. Whole joint sections taken from depths of up to 1500 µm into the joint capsule, from CoCr-injected rat stifle joints, stained with H&E.. ....	164 -
Figure 4.33. Whole joint sections taken from depths of up to 1500 µm into the joint capsule, from titanium-injected rat stifle joints, stained with H&E.....	165 -
Figure 4.34 Images of particles within H&E stained sections. SiN-injected rat 33.86 (A), CoCr-injected rats 33.73 (B), 33.74 (C and D) and 33.75 (E), and titanium-injected rats 33.82-33.84 (F-H). ...	167 -
Figure 4.35. Images captured from a whole joint section from (A) a SiN injected rat stifle joint, (B) and (C) a CoCr injected joint and (D) a titanium injected joint.....	169 -
Figure 4.36. Elemental analysis of tissue sections from rat stifle joints injected with (A) SiN, (B) CoCr and (C) titanium.. ....	170 -
Figure 4.37. Images of synovium taken from H&E stained sections from depths of up to 1500 µm into rat stifle joint capsules.....	173 -
Figure 4.38. Images of inflammatory cell infiltrates within the fat pad taken from H&E stained sections from depths of up to 1500 µm into a SiN-injected rat stifle joint capsule (33.87). ....	174 -

Figure 4.39. Images of inflammatory cell infiltrates and engulfed particles taken from H&E stained sections of CoCr-injected rat stifle joints (A and B; 33.74 and 33.75 respectively) and a titanium-injected rat stifle joint (C; 33.84)..	- 176 -
Figure 4.40. Histological scoring of rat stifle joint sections, showing differences between material groups and controls.	- 180 -
Figure 4.41. Histological scoring of synovial thickness in terms of average cell number in rat stifle joint sections, showing variations between individual animals.	- 181 -
Figure 4.42. Histological scoring of vascularisation in rat stifle joint sections, showing variations between individual animals. (A). SiN, (B) CoCr and (C) titanium group.	- 182 -
Figure 4.43. Histological scoring of the average total number of cells within a 400x field of view of the fat pad, showing variations between individual animals.	- 184 -
Figure 4.44. Histological scoring of the average number of macrophages and lymphocytes within a 400x field of view of the fat pad, showing variations between individual animals.	- 185 -
Figure 4.45. Histological scoring of injected stifle joints, including the average number of macrophages and lymphocytes and the average total number of cells within a 400x field of view of the fat pad, showing variations between different scorers.	- 187 -
Figure 5.1. Overview of experiments outlined in this chapter.	- 203 -
Figure 5.2. Design of rabbit stifle joint prostheses.	- 206 -
Figure 5.3. Surgical procedure to open the joint compartment for prosthesis implantation.	- 208 -
Figure 5.4. Surgical fitting of the rabbit stifle joint prosthesis parts.	- 209 -
Figure 5.5. Surgical procedure to repair stifle joint function and close the joint compartment.	- 210 -
Figure 5.6. Dissection of rabbit stifle joints for histology.	- 212 -



Figure 5.7. Embedding and cutting orientation of rabbit histological samples.....	- 215 -
Figure 5.8. (A) Appearance of an untreated rabbit stifle joint, immediately following sacrifice and removal of the skin and subcutis (rabbit 34.01). (B) Appearance of the contralateral treated rabbit stifle joint. ....	- 217 -
Figure 5.9. Appearance of an untreated rabbit stifle joint (A; 34.01L) and the contralateral treated joint (B; 34.01R; uncoated group) immediately following sacrifice and during dissection. ....	- 218 -
Figure 5.10. Appearance of the patella, patellar ligament and fat pad from an untreated rabbit stifle joint (A; 34.01L), or from treated joints from the uncoated group (B; 34.01R) and coated group (C; 34.17R). ....	- 219 -
Figure 5.11. A. Appearance of periprosthetic tissue digests from the SiN-coated group (From left: 34.17R, 34.22R, 34.24R) and a control tissue digest from an untreated stifle joint (34.24L). B. The corresponding particle pellet formed after density gradient ultracentrifugation.....	- 220 -
Figure 5.12. Scanning electron micrographs of particles isolated from rabbit periprosthetic tissue from rabbit 34.03. ....	- 221 -
Figure 5.13. Particles isolated from periprosthetic tissue from around coated implants from rabbit 34.17. ....	- 222 -
Figure 5.14. A. High magnification (100,000x) electron micrograph of isolated polyhedral particles (sample from rabbit 34.17). B. View of large, flake-like particles (sample from rabbit 34.24) at 10,000x magnification. ....	- 223 -
Figure 5.15. Elemental analysis of particles isolated from rabbit periprosthetic tissue from the uncoated group (34.03).. ....	- 224 -
Figure 5.16. Elemental spectra of CoCr aggregates isolated from rabbit periprosthetic tissue from the uncoated group (34.03). ....	- 225 -

Figure 5.17. Elemental analysis of particles isolated from rabbit periprosthetic tissue from the coated group (34.17).....	- 227 -
Figure 5.18. Elemental spectra of particles isolated from rabbit periprosthetic tissue from the coated group (34.17).....	- 228 -
Figure 5.19. Elemental analysis of particles isolated from rabbit periprosthetic tissue from the coated group (34.24).....	- 230 -
Figure 5.20. Elemental spectra of particles isolated from rabbit periprosthetic tissue from the coated group (34.24).....	- 231 -
Figure 5.21. Elemental analysis of flake-like CoCr particles isolated from rabbit periprosthetic tissue from the coated group (34.24)....	- 232 -
Figure 5.22. Images of H&E-stained fat pad sections (uncoated group)-	234 -
Figure 5.23. Images of H&E-stained fat pad sections (Coated group). .	- 236 -
Figure 5.24. Appearance of uncoated and coated retrieved rabbit prostheses.....	- 237 -

## List of Tables

Table 1.1. Comparison of properties for major hip prostheses materials. . - 4 -	
Table 1.2. Isolation methodologies for metal or ceramic particles from tissue or serum and associated advantages and disadvantages. .. - 13 -	
Table 1.3. A comparison of electron microscopy techniques. .... - 15 -	
Table 1.4. Isolation methodologies for metal or ceramic particles from tissue and associated advantages and disadvantages. .... - 23 -	
Table 2.1. Cell identification within H&E stained tissue sections. .... - 60 -	
Table 4.1. Particles used for injection into rat stifle joints and overall in vivo study design including groups, time points and animal numbers. .... - 109 -	
Table 4.2. Dissected wistar rat, in which the left intact stifle joint has been removed. .... - 111 -	
Table 4.3. Programme used for intact rat stifle joints. .... - 115 -	
Table 4.4. Semiquantitative scoring of inflammatory cell infiltrates, adapted from ISO 10993-6 (2016). .... - 119 -	
Table 4.5. Semiquantitative scoring of vascularisation, fibrosis and fatty infiltration, adapted from ISO 10993-6 (2016). .... - 120 -	
Table 4.6. Semiquantitative scoring of overall tissue reaction to a material, adapted from ISO 10993-6 (2016). .... - 121 -	
Table 4.7. Identification numbers used for each animal sample for particle isolation. .... - 140 -	
Table 4.8. Average parameters for non-injected particles, and particles isolated from injected rat stifle joints, for SiN, CoCr and Titanium material groups. .... - 157 -	
Table 4.9. Identification numbers used for each animal sample for histological analysis. .... - 157 -	
Table 4.10. Elemental components of particles detected by energy dispersive X-ray spectroscopy within tissue sections and post-isolation from tissue. .... - 171 -	

Table 4.11. Semi-quantitative score of the overall reaction to SiN particles, based on methods adapted from ISO 10993-6 (2016)...	189 -
Table 4.12. Semi-quantitative score of the overall reaction to CoCr particles, based on methods adapted from ISO 10993-6 (2016)...	190 -
Table 4.13. Semi-quantitative score of the overall reaction to titanium particles, based on methods adapted from ISO 10993-6 (2016)...	191 -
Table 5.1. Details of samples from animal study. ....	204 -
Table 5.2. Programmes used for rabbit tissue samples. ....	214 -
Table 5.3. Summary of rabbit study results (uncoated group).....	238 -
Table 5.4. Summary of rabbit study results (coated group).....	239 -
Table 6.1. Advantages and disadvantages of the rat and rabbit model. -	251 -

# Chapter 1

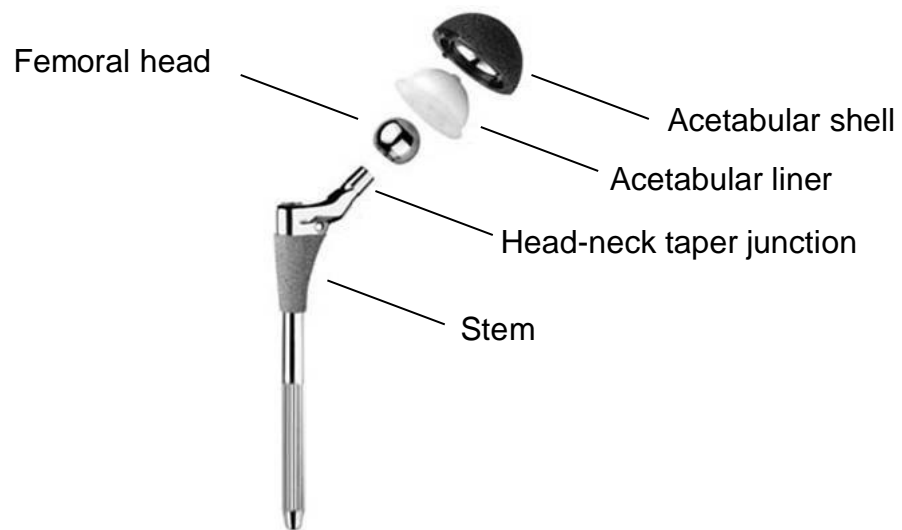
## Introduction

The research described in this thesis was part of a collaborative project to produce and test a novel hip replacement device employing a silicon nitride (SiN) coating. The scope of this PhD within the wider project was to develop novel methodology to isolate wear debris from tissue samples and to test the *in vivo* biocompatibility of a SiN coating. This chapter broadly details the preclinical testing of hip replacements and the biological response to hip replacement materials, specifically regarding wear particles, before describing the need for an improved hip replacement device.

### 1.1 Introduction to total hip replacement

Hip replacements are an extremely common surgical intervention; 101,651 hip replacements were performed in England and Wales in 2016 (NJR, 2017). The vast majority (90%) of hip replacements are performed to treat osteoarthritis (NJR 2017). Osteoarthritis leads to inflammation of the joint and associated pain and joint stiffness. Other morbidities which may be treated with hip replacement surgery include rheumatoid arthritis, hip fractures, dislocation, trauma, septic arthritis, bone tumours, hip dysplasia, bone diseases, and avascular necrosis (Lu-Yao *et al.*, 1994; Crabtree *et al.*, 2001; Blomfeldt *et al.*, 2005; Sadowski and Gabay, 2006; Darowski, 2007; Menzies *et al.*, 2012; Gruener and Camacho, 2014; Amara *et al.*, 2014). Total hip replacement (THR) provides an effective and long-lasting solution to nearly all types of hip injury and disease. Alternatives to THR exist, such as anti-inflammatory or pain-relieving injections or drugs, but these are often only effective in the short-term (Wienecke and Gotzsche, 2004). Partial hip replacement may be performed to treat fractures of the hip, but long-term clinical outcomes are poorer compared to total hip replacement (Keating *et al.*, 2006). Other alternatives, such as hip resurfacing, are unsuitable for patients with weakened bones, and have become less popular due to concerns about the long-term safety of the procedures (Walsh *et al.*, 2005).

Total hip replacement involves replacement of the acetabulum, the femoral head, and a large portion of bone from the femur. Hip replacements thus consist of several components – these include the femoral stem, the femoral head, the acetabular cup, which may consist of an insert and backing, and depending on the model, one or more taper junctions, coatings or fixatives (Figure 1.1).



**Figure 1.1. The major components of a hip replacement.** Note that designs vary considerably.

Adapted from <http://www.healthbase.com/resources/orthopedics/total-hip-replacement-surgery-implants>.

## 1.2 Total hip replacement materials

Hip prosthesis components are manufactured from a variety of materials, including metals, ceramics and polymers. Metals used are mainly cobalt chromium (CoCr) and titanium alloys, while types of polymers include ultra-high molecular weight polyethylene (UHMWPE) and polyether ether ketone (PEEK). Ceramics include alumina, zirconia-toughened alumina (ZTA). Silicon nitride (SiN) is another ceramic which is currently under investigation as a material for hip replacements. Choice of component material must consider several mechanical properties. For example, the Young's modulus, which is a measure of elasticity or stiffness, is an important consideration for the stem. Implants manufactured from materials with a particularly high

Young's Modulus, which are much stiffer than bone, will cause the implant to shield the surrounding bone from stress (Weinans *et al.*, 1992). When osteocytes are unable to detect stress, osteoblasts do not form new bone, leading to bone loss (Weinans *et al.*, 1992). Furthermore, the femoral head and acetabular cup liner, which provide the bearing surfaces of a hip replacement, must be low-wearing to prevent failure of the device. Femoral-acetabular bearing couples may consist of a hard femoral head articulated against a hard acetabular cup (hard-on-hard bearings) or a hard femoral head articulated against a relatively soft acetabular cup to reduce friction (hard-on-soft bearings). Properties of selected orthopaedic materials currently used in hip replacements, or under investigation for use in hip replacements, are given in Table 1.1.

Titanium, alloyed with 6% (w/w) aluminium and 4% (w/w) vanadium to increase toughness, is often used for the stem and taper. The alloy is relatively lightweight, has a lower Young's modulus (105 – 115 GPa) than other orthopaedic metals, and a higher fracture toughness (75 MPa m<sup>1/2</sup>) than ceramics (Bal and Rahaman, 2012). The porosity of titanium can be controlled to match that of bone, allowing osteoblasts to migrate in and form bone around it, thus fixing it in place (termed osseointegration). Titanium stems are often coupled with a CoCr or ceramic head. Titanium is not used as a femoral bearing material since it is relatively soft and has poor tribological performance, which would lead to high wear and mechanical failure of the device. Titanium shells are also widely used.

CoCr alloy, consisting of cobalt with 26-30% chromium, 5-7% molybdenum, and up to 0.35% carbon (ISO 5832 – 12:2007) is also commonly used to produce femoral stems despite the higher Young's Modulus (210 – 250 GPa) and thus greater impact on bone loss compared to titanium stems (Kim, 2004). Molybdenum is added to make the alloy highly resistant to corrosion. CoCr alloy is often used to produce femoral bearings due to the low wear rate of the material (Ridzwan *et al.*, 2007). Acetabular cups are often made from a cobalt chromium shell with a polymer or ceramic insert. In the past, CoCr femoral heads were used in combination with an acetabular cup produced entirely of CoCr – these were termed 'metal-on-metal' (MOM) bearings. Due to safety concerns, their usage has dramatically declined and is now rare (NJR, 2017).

**Table 1.1. Comparison of properties for major hip prostheses materials.** Note that properties for bone vary greatly with factors including age and lifestyle; additionally, properties for materials may differ depending on the manufacturing process. Adapted from Bal and Rahaman, 2012.

Property	Cortical bone	SiN	Alumina	ZTA	CoCr	PEEK	Titanium	UHMWPE
Density (g cm <sup>-3</sup> )	1.85	3.44	3.99	4.37	8.50	1.29	4.43	0.945****
Young's Modulus (GPa)	8-12	300-320	400-450	350	210-250	4.2	105-115	0.69
Compressive strength (MPa)	130-190	2500-3000	2000-3000	4300	600-1800	130-140	950-990	20.7
Fracture toughness (MPa m <sup>1/2</sup> )	2-12* 5.1-6.4**	8-11	4-5	5.7	50-100	2.7-4.3	75	2.8-3.0
Vickers hardness (GPa)	0.27- 0.57***	13-16	14-16	19.1	3-4	0.26-0.28	3.4	0.06-0.08
Surface composition	Lipid layer on cartilage	SiNH <sub>2</sub> , SiOH, SiO <sub>2</sub>	Al <sub>2</sub> O <sub>3</sub>	Al <sub>2</sub> O <sub>3</sub> , ZrO <sub>2</sub>	CoO, Cr <sub>2</sub> O <sub>3</sub>	OH groups	TiO <sub>2</sub> , Al <sub>2</sub> O <sub>2</sub>	Ethylene chains (C <sub>2</sub> H <sub>4</sub> ) <sub>n</sub>

\*longitudinal (Wang *et al.*, 2002) and transverse (Zioupou and Currey, 1998) values for human femur. \*\*Hench, 1991. \*\*\*Zwierzak *et al.*, 2009.

\*\*\*\*Walsh *et al.*, 2000



Ceramics are used to manufacture femoral bearings and acetabular cup liners, and function as bearing surfaces. A THR employing all-ceramic bearing surfaces is referred to as a 'ceramic-on-ceramic' (COC), while a THR employing a ceramic head articulated against a polyethylene cup is termed a 'ceramic on polyethylene' (COP). Orthopaedic ceramics were first developed in the 1970s from alumina ( $\text{Al}_2\text{O}_3$ ) and have since undergone changes through the decades to reduce micro-grain size and improve mechanical strength, leading to the current fourth-generation 'BIOLOX DELTA,' a mixed oxide ceramic consisting of zirconia ( $\text{ZrO}_2$ ; 17% weight) toughened alumina (82% weight; ZTA), with small additions of chromium oxide (0.5% weight) and strontium aluminate (0.5%), which increase toughness (Wang *et al.*, 2011). Calcium phosphates and zirconia-based ceramics, as well as plastic-ceramic composites, have also been investigated (Jaffe *et al.*, 2009). Ceramics may be polished to create a very low surface roughness; they also have good wettability, which may create a fluid film that reduces friction and wear in ceramic bearings. However, ceramics have a poor fracture resistance, with an incidence of fracture which ranges from 0.004% to 2% (Hamilton *et al.*, 2010). Bearings that employ ceramics are also prone to squeaking in approximately 0.7% to 20.9% of cases (Mai *et al.*, 2009). Due to their high stiffness and brittleness, ceramics are not used as a stem material in total hip replacement devices.

SiN is a ceramic which is currently used in cervical spacers and spinal fusion implants, with good clinical results (Taylor *et al.*, 2010); it also has the orthopaedic benefit of being visible on radiographs (Bal and Rahaman, 2012). Whilst not currently in clinical use in hip replacements, bearings manufactured from silicon nitride (SiN) have been developed for THR (Bal *et al.*, 2008); the resulting bearings, when tested using hip joint simulators, had a low wear rate, similar to alumina-alumina, when articulating against a SiN cup against a CoCr or SiN femoral head. Bulk silicon nitride femoral head bearings (Amedica Corps) have recently been implanted into patients (Chang, 2014), but as yet there is no clinical data available. SiN also has a higher fracture toughness and higher flexural strength than alumina, which reduces the risk of device fracture (Bal and Rahaman, 2012).

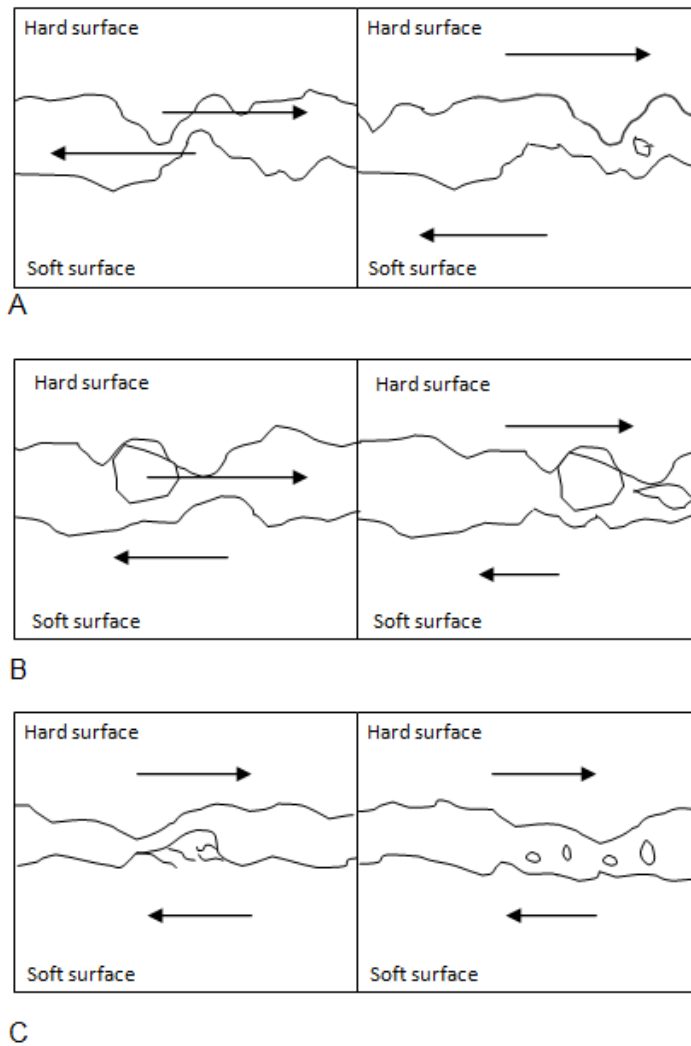
Polyethylene was among the first successfully implanted orthopaedic materials, and hence much of the literature focuses on this material, providing a wide knowledge base. Polyethylene is used to produce acetabular cups, which are used in combination with a CoCr femoral head – these are termed metal-on-polyethylene (MOP) bearings. The use of highly crosslinked ultra-high molecular weight polyethylene (UHMWPE) reduces the high wear associated with older MOP bearings (Kurtz, 2009). Other polymers and polymer composites, most successfully polyetheretherketone (PEEK), have also been investigated. PEEK, a thermoplastic, is a relatively new bearing material that has been used widely in spinal implants. Carbon-fibre reinforced PEEK has high mechanical strength and a lower wear rate than UHMWPE (Scholes and Unsworth, 2000). A systematic review greatly favours the use of carbon fibre reinforced PEEK, citing favourable material properties (Li *et al.*, 2015). Another benefit is that PEEK is detectable with X-ray imagery. A PEEK acetabular cup performs best when articulating against a ceramic femoral head (Brockett *et al.*, 2012). However, PEEK bearings are somewhat niche due to high production costs (Sonntag *et al.*, 2012).

Stems and acetabular cups are often cemented in place. Hybrid fixation, in which the stem is cemented, and the cup is uncemented, is increasing in popularity (NJR, 2017). In cemented stems, polymer bone cement which is comprised of polymethylmethacrylate (PMMA) is used to fix the implant into the femur and distribute load. Bone cement often contains additives such as a radiopacifier, most commonly barium sulphate, to facilitate medical imaging. In uncemented hip replacements, stems are often coated with hydroxyapatite, which aids osseointegration (Theis and Ball, 2003).

### **1.3 Wear mechanisms at the bearing surfaces of hip replacements**

Several different mechanisms for wear at the bearing surfaces of hip replacements exist. In a hard-on-soft scenario, adhesive wear may occur when small segments of a bearing surface adhere to the opposing surface, and this adherence is stronger than bonds within the softer material, so that a piece of the softer material is removed as the surfaces continue to move (Goodman and Wright, 2001). Abrasive wear occurs when the micro-

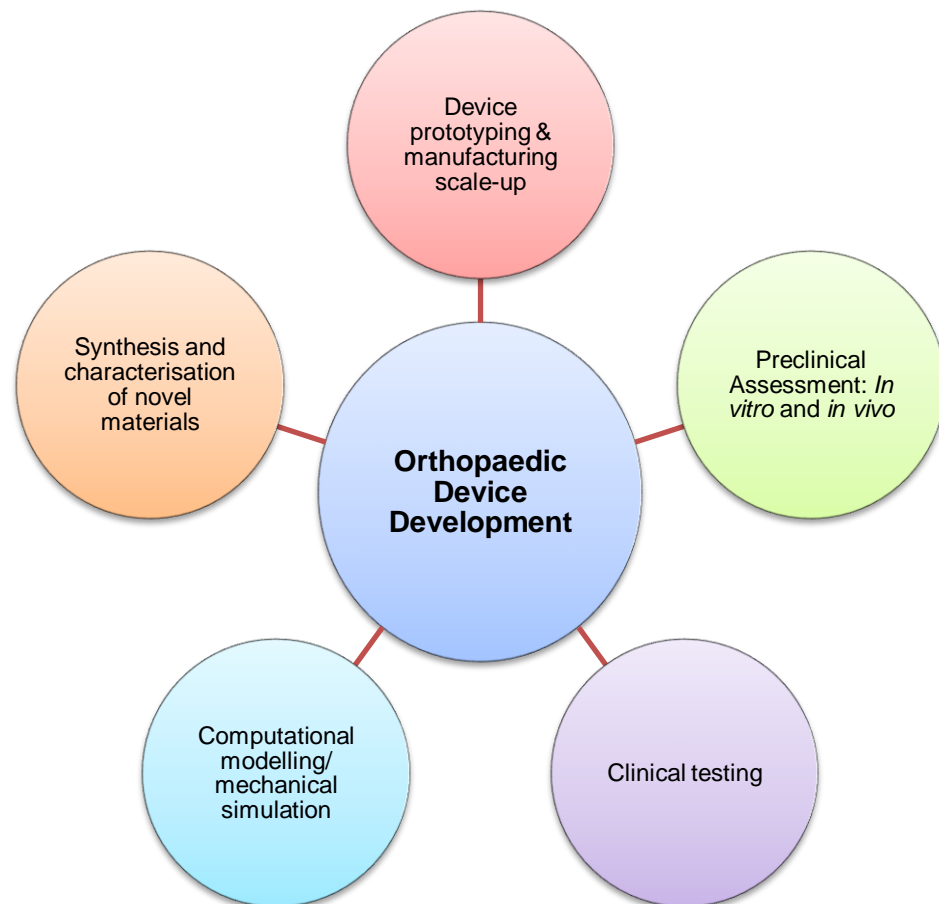
roughness of the harder surface abrades against the softer surface, removing a fragment (Figure 1.2A). Another type of abrasive wear occurs when a fragment of hard material becomes embedded in the softer material, such that when motion occurs the fragment abrades the soft material, removing the softer material. This is termed 3rd body wear (Figure 1.2B); (Goodman and Wright, 2001). Fatigue wear occurs when the softer material reaches the limit of its tolerance to subsurface shear stresses, resulting in subsurface cracks and pitting that releases wear particles (Figure 1.2C); (Goodman and Wright, 2001). Wear occurs not only at the articulating surfaces; fretting wear and fatigue occurs at the taper junctions. Fretting wear is characterised by repeated motion, such as vibration or cyclic motion, which leads to wear and corrosion. Such wear mechanisms may affect the mechanical performance of implants and result in the significant build-up of wear debris, otherwise referred to as wear particles.



**Figure 1.2. Schematic representations of wear mechanisms.** (A) Abrasive wear, in which a hard surface with asperities moving relative to a soft surface with asperities removes part of the softer surface, (B) third body wear, in which a third body scrapes off some material from a softer surface, and (C) fatigue wear, in which microfractures culminate in the release of debris.

#### **1.4 Mechanical testing of hip replacements**

Development of a novel hip replacement device may involve several research processes (Figure 1.3). If novel materials are to be employed, fabrication and assessment of the materials, including mechanical testing, may involve quick, low-labour wear screening tests.

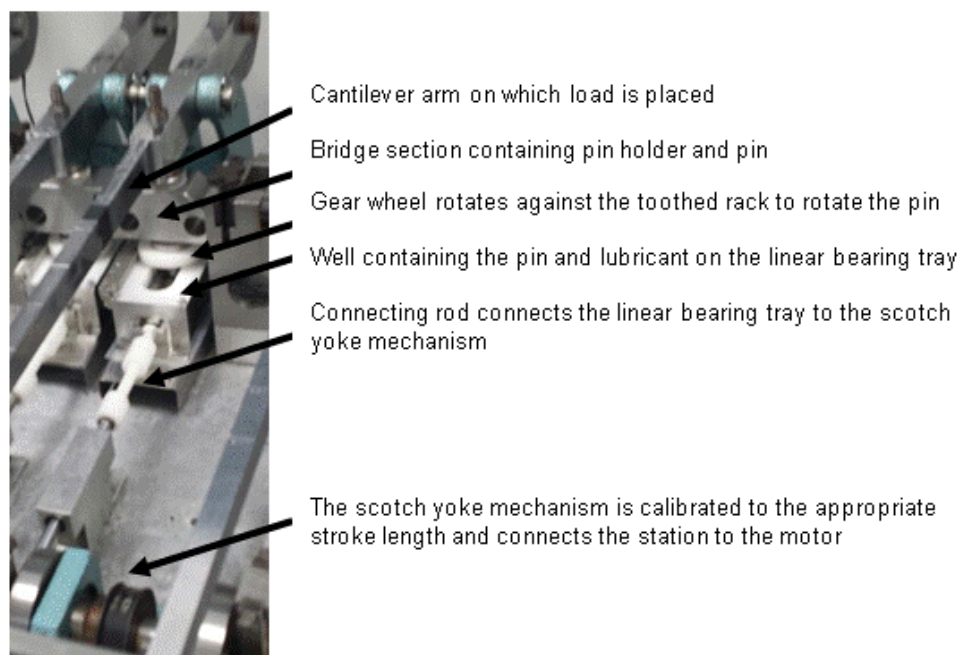


**Figure 1.3. Key research processes involved in development and testing of novel orthopaedic devices.**

These allow the wear properties of materials to be tested free from the confounding effects of implant design. During a wear test, the test material is articulated against a moving or stationary abrasive surface, and the test material itself is either stationary, or it rotates or traces a track with respect to the surface. One of the main types of wear test is performed using a pin-on-plate machine, where the pin and plate are produced from the test materials. The method is cheap and high through-put to perform, and variations, such as pin-on-drum, pin-on-disc or pin-on-flat, exist. Furthermore, a circulating ring on a flat surface, or crossed cylinders that rotate against each other, may be employed.

Pin-on-plate machines can be used to generate clinically relevant wear (Figure 1.4); in this regard, realistic *in vivo* contact stresses, appropriate surface roughness, lubrication, pin geometry and multidirectional sliding

contact is required (Wang *et al.*, 1996). Standards, including those from the American Society for Testing and Materials (ASTM), exist for the use of pin-on-plate machines and similar devices; these specify the weight-loss method of wear determination, for hard-on-soft bearings employing bovine serum (or similar) lubrication, allowing material combinations to be ranked by their associated wear factors (ASTM F1714-96, 2013). The materials employed must also be manufactured according to ASTM standards to produce the typical mechanical qualities, geometries and surface finishes encountered in clinical use.



**Figure 1.4. A reciprocating six-station pin-on-plate machine.** The plates and lubricant are placed inside baths and each pin is articulated against a plate inside the well; the plate moves in a linear fashion while the pin rotates. The cantilever arms transfer load onto the pins.

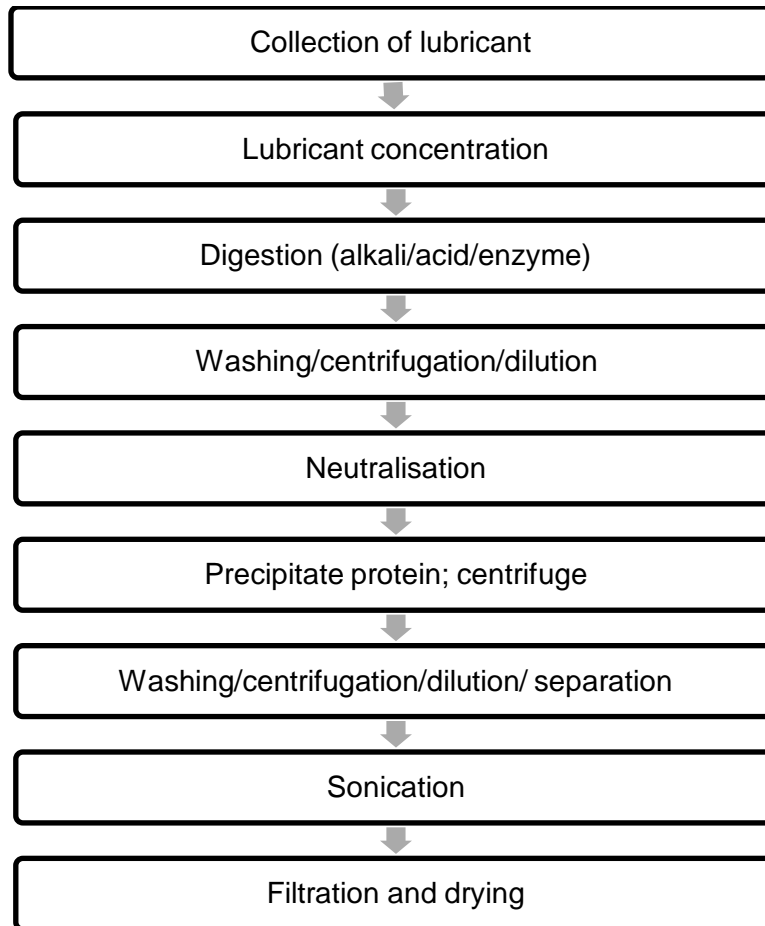
At a more advanced stage of testing, hip joint wear simulators test the actual prostheses in conditions that resemble the environment of the human hip more closely. The lubricant is typically foetal bovine serum, or less frequently synovial fluid, and the joint undergoes motions to simulate the natural human gait cycle. The cycles closely replicate human hip joint biomechanics. It is estimated that an average person undergoes 1-2 million gait cycles a year;

thus, 1 million cycles in a hip simulator corresponds to six months to a year of usage, while young and active people may undergo many more gait cycles (Silva *et al.*, 2002). Standards are also in place for hip simulator testing, including ASTM F3047M (2015). The international standards organization (ISO) also produces documents to indicate details such as the required surface finishes and sphericity of metal and ceramic femoral prostheses and polymer acetabular cups (ISO 7206-2, 2011). Methods to simulate wear under adverse conditions, such as mal-positioning of the components, have also been developed (Nevelos *et al.*, 1999; Nevelos *et al.*, 2000; Stewart *et al.*, 2001; Leslie *et al.*, 2009; Al-Hajjar *et al.*, 2010; Al-Hajjar *et al.*, 2013; Partridge *et al.*, 2018).

## **1.5 Isolation of wear particles from serum**

It is useful to isolate the wear particles produced by pin-on-plate wear testing or from hip joint simulators for downstream analysis, since wear particle characteristics have important consequences for the biocompatibility of a prospective orthopaedic material. Particles generated in water under sterile conditions do not generally require an isolation process prior to analysis. However, as described in the previous section (section 1.4), the generation of clinically relevant wear particles often requires use of a lubricant containing protein. Thus, particles develop a protein corona, which requires removal prior to particle characterisation. An overview containing the typical stages common to most particle isolation methods from simulator lubricant serum is given in Figure 1.5. Firstly, lubricant is collected after running the pin-on-plate or hip simulator. The volumes are often hundreds of millilitres, and thus, volumes are often reduced by sample concentration using ultracentrifugation to facilitate sample processing during the later stages of the isolation protocol. Proteins within the samples are then digested, either enzymatically or with acids/bases, or a combination of both, to enable separation of the protein from particles (Niedzwiecki *et al.*, 2001). Digestion protocols vary as although acid/base digestion is efficient (Baxter *et al.*, 2009), such methods are undesirable due to the potential to damage particles these chemicals create; such particle changes include a reduction in particle size and changes to particle shape and composition (Catelas *et al.*, 2001). Many protocols employ

density gradient ultracentrifugation to facilitate removal of proteins. Particles are then sonicated to minimise agglomeration, washed and may be filtered prior to characterisation. An overview of isolation protocols for metal and ceramic particles is given in Table 1.2.



**Figure 1.5. An overview for isolation of ceramic, metal or polymer wear particles from tissue.** Particle isolation from simulator serum is similar to isolation from tissue but requires a less intensive digestion stage. Note that this chart represents a generalization, and that there are various protocols adapted for the type of material; for example, neutralization is unnecessary if the digestion method is enzymatic. Adapted from Nine *et al.* (2014).



**Table 1.2. Isolation methodologies for metal or ceramic particles from tissue or serum and associated advantages and disadvantages.** Note that not all simulators were hip simulators, hence particle sizes may differ from those expected for hip replacement wear debris.

Paper	Type of isolation	Brief description of isolation method	Advantages/ disadvantages
Schmiedberg <i>et al.</i> , 1994	CoCr and Titanium alloy in bovine serum from intervertebral disc simulations	Centrifugation, enzymatic digestion, washing with NaOH, sonication	Use of NaOH may affect particles due to their reactive nature (Catelas <i>et al.</i> , 2001); size range 0.137- 30 µm
Brown <i>et al.</i> , 2007	CoCr from simulator serum	Use of MOPs buffer, boiling with SDS, Enzymatic digestion with Papain, Proteinase K, yeast lytic enzyme and zymolyase; heated to 180°C for 4 hours; filtered onto 5, 1 and 0.1 µm pore-size filters	Avoided use of acids or bases; particles aggregated; 0.007-0.156 µm size range; lots of steps; not sensitive enough to isolate low volumes of particles
Billi <i>et al.</i> , 2012	CoCr and Alumina wear particles from bovine serum (produced in simulators)	Enzymatic digestion, ultracentrifugation using layers of denaturants and a metal-selective high-density layer	A wide range of particle sizes recovered (0.004-1 µm), particles well separated; Aggressive digestion avoided; Numerous steps make this protocol lengthy and expensive
Lal <i>et al.</i> , 2016	SiN and CoCr from particle-doped serum	Enzymatic digestion using proteinase K, ultracentrifugation using sodium polytungstate density gradients, washing	Validated in terms of particle recovery on very low particle volumes of $6.66 \times 10^{-6} \text{ mm}^3.\text{ml}^{-1}$ and shown not to affect particle size or morphology

Similar methods have been used to isolate polyethylene particles. However, polyethylene cannot be subjected to high temperatures, and different density gradient constituents must be used to account for the low density of polyethylene. Billi *et al.* (2012) created a method for isolation of UHMWPE referred to as silicon wafer display (SWD). This involved complex enzymatic digestion with several stages including the use of proteinase K, three-step ultracentrifugation, followed by deposition onto a silicon wafer by centrifugation. However, the process developed by Billi *et al.* (2012) is relatively lengthy, expensive and doesn't allow recovery of particles for subsequent cell studies.

Following particle isolation, particles are generally characterised by scanning electron microscopy (SEM). This enables particles to be imaged and may be used in combination with energy dispersive x-ray spectroscopy (EDX), a technique to analyse the elemental composition of particles. Software is available to measure particles, providing particle size distributions and shape parameters such as the circularity and aspect ratio of particles. Transmission electron microscopy can also be a useful technique to study wear particles. The relative advantages of both techniques are given in Table 1.3.

**Table 1.3. A comparison of electron microscopy techniques.** Adapted from Crawford and Burke, 2004.

	SEM	TEM
Method	Scans the surface with a focussed beam of electrons, resulting in electrons being back-scattered and emitted from the sample	Transmitting electrons through a sample; differences in tone of areas on a micrograph indicate density
Advantages	Can view relatively large areas Enables viewing of fine topological detail Can be combined with elemental analysis SEM images can be used to produce 3D reconstructions	Very high resolution below 0.5Å Higher possible magnifications of 1,000,000x (possible to image individual molecules) Enables internal structures to be viewed Can be combined with elemental analysis Can determine fine crystalline structure
Disadvantages	Cannot elucidate internal structure Maximum magnification is lower than TEM (500,000x) Maximum image resolution is lower than TEM (0.5 nm; the resolution is limited by the width of the exciting electron beam and the interaction volume of electrons in a solid) Sputter coating process may alter sample surface Samples may oxidize during sample preparation process	Only small areas can be viewed Samples must be extremely thin (50-100 nm); particles may be bisected leading to inaccurate particle sizing Produces 2D images Sample preparation could lead to changes to particle geometry and composition

## **1.6 In vitro biocompatibility testing of wear particles**

Wear debris isolated from the lubricant of pin-on-plate machines or hip simulators can be incubated with cells *in vitro* to determine biocompatibility of the materials. Cellular assays might assess cytotoxicity, genotoxicity or modifications in cell behaviour, particularly regarding inflammation, and they offer a relatively fast way to test the biological response to wear debris. Cells used are often human or mouse and may be either primary cells such as peripheral blood mononuclear cells (PBMNCs) or cell lines such as U937 macrophages. The advantage of primary blood cells is their high clinical relevance; however, PBMNCs may vary substantially depending on the genetics of the hosts, as some individuals are more 'aggressive responders' to wear debris than others (Matthews *et al.*, 2000). Morrison *et al.* (1995) tested the biocompatibility of hip prosthesis materials including PEEK in fibroblasts and osteoblasts using a number of indicators for cytotoxicity, including the MTT assay, leakage of lactate dehydrogenase, intracellular levels of glutathione (GSH) and total cell protein. In addition, the production of pro-inflammatory cytokines (IL-1 $\beta$  and TNF- $\alpha$ ) and other proteins can be measured using an enzyme-linked immunosorbency assay (ELISA) (Anderson *et al.*, 2008). Such experiments offer a direct way of (often quantitatively) assessing the impact of biomaterials on cells in a controlled environment. It is important to ensure that the wear debris used in these studies are sterile, since the presence of bacteria and endotoxins could lower cell viability and induce inflammatory responses, making it difficult to interpret results.

## **1.7 Animal models for biocompatibility testing**

### **1.7.1 An overview of different species used as animal models**

Alongside *in vitro* testing of wear debris, animal testing is an indispensable tool for assessing the biocompatibility of materials. Dissemination of the material, osseointegration, local tissue damage, systemic changes, organ toxicity and inflammatory processes, and (where applicable) dissolution of a material may be analysed. Different animal species are associated with various advantages and disadvantages. At the very least, to be useful the

animal must have significant physiological similarities to humans, ruling out the use of non-mammals in orthopaedic studies. Other factors such as costs to acquire and care for animals, animal housing requirements and public perception of that animal in research must be considered. An existing knowledge base of the physiology of that animal is also a necessity, especially because the attributes of bone remodelling can vary between species (Pearce *et al.*, 2007).

Mice and rats are key animals used in medical research as very detailed biological databases exist for these animals. While cheap and easy to keep, they have too small a stature and lack the necessary bone density to test most orthopaedic prostheses. They are also too short-lived for long term studies; however, these animals could be a useful starting point for assessing the biocompatibility of small quantities of biomaterial, especially since many institutions lack the facilities for keeping larger animals, or large animals in significant numbers. An early rat model for the evaluation of implant materials involved the injection of polyethylene particles in the femur of rats (Howie *et al.*, 1988). Furthermore, a rat model was successfully used to demonstrate the effects of particle size and morphology on the inflammatory response to PMMA particles (Gelb *et al.*, 1994). PMMA particles were introduced by injection into a subcutaneous air pouch. Another rat model employing intra-articular injections of particles has also successfully replicated clinically relevant responses to polyethylene particles (Millet *et al.*, 2002).

Rabbits are another popular choice for testing of prostheses. Though bone turnover occurs faster in rabbits compared to humans (Newman *et al.*, 1995), rabbit models have several advantages. Rabbits are easy to keep and handle and quickly reach skeletal maturity (Pearce *et al.*, 2007). Rabbits are also the smallest animals to have a Haversian system – the structure of bone also found in human cortical bone. Rabbit bone mineral density is also similar to that of human bone ( $2.51 \text{ g.cm}^{-3}$  versus  $2.49 \text{ g.cm}^{-3}$  in humans; Wang *et al.*, 1998). Rabbits are therefore useful for initial screening of implants prior to testing in larger animals. A variety of methods have been used to create chambers in the bone of rabbits, enabling exposure of rabbit tissues to particles (Goodman, 1994; Trindade *et al.*, 1999; Goodman *et al.*, 2003). Plugs made from PMMA, containing a groove for particle placement, have

also been inserted into rabbit femora to study biological reactions to particles (Kubo *et al.*, 1999). Tibial hemiarthroplasties have been developed (Goodman *et al.*, 1992), and used to study the effect of particles surrounding an implant (Sacomen *et al.*, 1998). A patellofemoral hemiarthroplasty replacing part of the femur has been used to study the effect of particles on osseointegration of an implant (Sundfelt *et al.*, 2002).

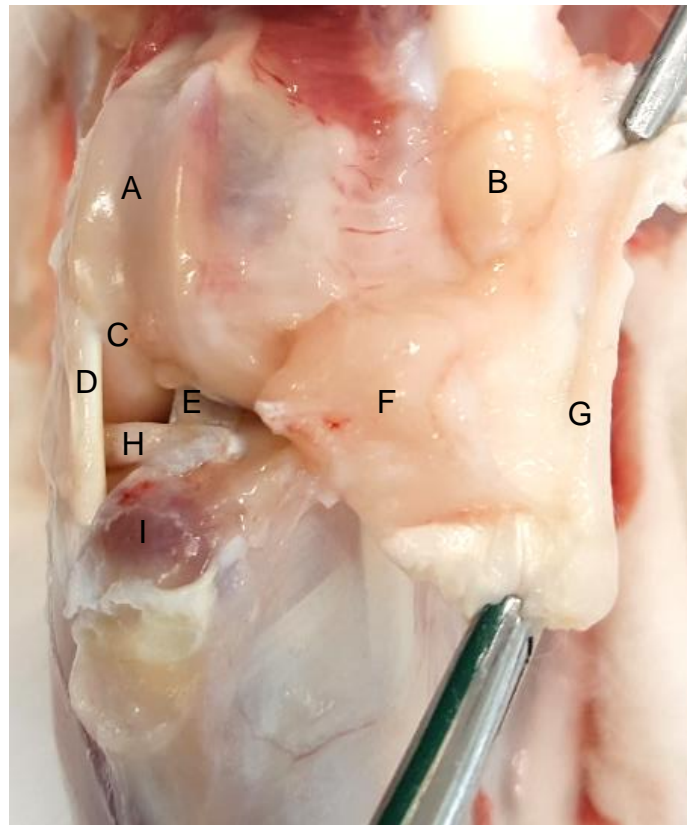
Larger animal models for long term studies include dogs, pigs, goats and sheep. Between 1970 and 2001, 9% of animal studies in orthopaedics utilised dogs (Martini *et al.*, 2001). This is due to the trainable nature of dogs, which makes them easier to work with, as well as the availability of surgical expertise in dog hip replacement and the existing designs for dog prostheses, since hip replacements are already an established veterinary intervention in the canine. For example, Skurla *et al.* (2005) used the canine to assess implant stability in a MOP system. However, the use of sheep in orthopaedic research has increased and now rivals the use of dogs (Langlois and Hamadouche, 2011), perhaps due to the negative public perception of the use of dogs. Bone volumes are similar in aged sheep and aged humans (Turner and Villanueva, 1993). In addition, their weight is more similar to that of humans, and their larger stature make the use of larger implants possible (Newman *et al.*, 1995). Additionally, it is suggested that bone remodelling and bone growth onto porous surfaces is similar in sheep and humans (Willie *et al.*, 2004).

A major limitation of animal models are differences in anatomy, physiology, loading and gait cycle. No species is an ideal model, and therefore the best approach would be to use more than one type of animal for testing and combine data from each of these.

### **1.7.2 Anatomy of the stifle joint**

With regard to the hip joint, it is often difficult to standardise surgical procedures, and since the stifle joint is the largest synovial joint in quadrupeds, this is often assessed instead. The stifle joint is the equivalent of the knee in humans. It tends to contain fatty tissue, which is useful for gauging immunological responses (Muir *et al.*, 2007). The main anatomical structures of the stifle joint are given in Figure 1.6.

The synovial membrane lines the joint capsule and consists of type A synoviocytes, which are macrophage-like cells that engulf any debris in the synovial fluid, and more abundant type B synoviocytes, which are fibroblast-like cells involved in protein production (Iwanaga *et al.*, 2000).



**Figure 1.6. Dissected view of a left rabbit stifle joint, with the patellar ligament displaced medially to the joint. A. Patella groove. B. Patella. C. Femoral condyles. D. Origin of the long digital extensor tendon. E. Cruciate ligament. F. Fat pad. G. Patellar ligament. H. Lateral meniscus. I. Tibial plateau.**

## **1.8 Analysis of tissue samples**

Physiological and behavioural changes, radiographic findings and blood tests may be used during the in-life phase of an animal study to evaluate biological reactions to a material. In particular, concentrations of ions in the blood may be tested. Such tests can also be applied to synovial fluid and tissue samples following sacrifice of the animal. More commonly, histological analysis is used to analyse tissue reactions to materials. Histology is a reliable technique that involves staining fixed tissue sections, usually with haematoxylin and eosin

(H&E), and viewing the sections using light microscopy. It can be used to study morphological changes to the joint, wear particle dissemination, soft tissue reactions including inflammatory cell infiltration and bone tissue responses such as osseointegration or bone resorption, in thin sections of tissue (Hatton *et al.*, 2002). H&E staining can be used in combination with polarized light microscopy which allows particles to be imaged more clearly. Such techniques are also commonly applied to explants of human periprosthetic tissue. Histological studies have played a major role in developing the current understanding of the biological response to wear debris.

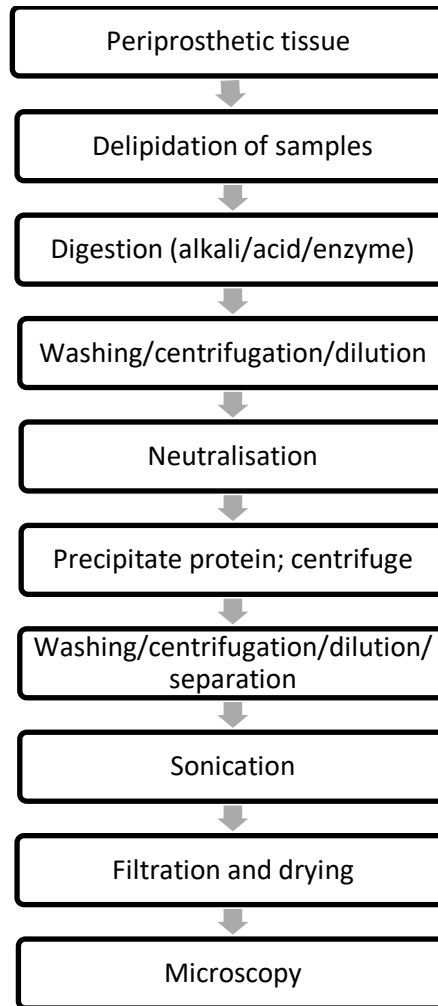
For example, Hatton *et al.* (2002) used histology to determine the distribution of alumina wear particles from tissue retrieved at revision and to determine the biological response, using a semi-quantitative grading measurement for necrosis, necrobiosis, macrophages, giant cells, neutrophils, lymphocytes and wear debris, using scales from 1-5 or 1-7. The different cell types were identified by cell size, nuclear morphology and cytoplasmic colour. Methods for semi-quantitative scoring are described in ISO 10993-6, though the exact methodologies supplied are vague; for example, there are no criteria for which specific anatomical sites should be analysed, or for how to identify particular cell types. Alternatively, cells can be labelled using antibodies for cell-specific markers, in combination with a secondary antibody and staining kit (Ren *et al.*, 2008). Inflammatory mediators and proinflammatory cytokines can also be stained in this way. Protocols for antibody labelling of tissue sections are not supplied in any detail in the ISO standards for biological testing.

Transmission electron microscopy (TEM) can be used directly on prepared cells or tissues and is a useful tool for viewing nanoscale particles in endosomal compartments (Cobelli *et al.*, 2011). However, electron microscopy is more labour intensive and expensive than light microscopy and cannot be combined with the multitude of stains that can be used to analyse histological tissue sections (Gartner and Hyatt, 2006). Additionally, particles must be isolated from tissue before they can be effectively characterised.



## 1.9 Isolation of wear particles from tissue

Wear particles can be isolated from tissue samples using similar techniques to those described for serum samples in section 1.5 (Figure 1.7). However, sample concentration may not be required, sample de-lipidation may be required, and the digestion techniques used may differ.



**Figure 1.7. An overview for isolation of ceramic, metal or polymer wear particles from tissue.** Particle isolation from tissue is similar to isolation from simulator serum but requires a more intensive digestion stage. Note that this chart represents a generalization, and that there are various protocols adapted for the type of material; for example, de-lipidation may not be necessary if only metal or ceramic particles are being retrieved. Neutralization is unnecessary if the digestion method is enzymatic. Adapted from Nine *et al.* (2014).

Particle isolation has been frequently applied alongside histological studies to human periprosthetic explant samples; however, to the author's knowledge, particle isolation techniques have not been applied to animal tissue. This may be due to the relatively short time frame used in animal studies, which limits the production of wear debris. Moreover, particle isolation techniques are not sensitive enough to isolate the very low particle volumes from tissues. In fact, new techniques to improve particle isolation from tissue have not been developed for metal or ceramic particles in the last decade. A summary of various methods for isolation of metal and ceramic wear particles from tissue is detailed in Table 1.4.

Though it has been suggested that nitric acid does not alter alumina particles (Bohler *et al.*, 2000 and Mochida *et al.*, 2001), it is most likely that nitric acid would damage ceramic particles as it is well known that nitric acid can dissolve bone and metals. As such, enzymatic methods are greatly preferred for tissue digestion to retrieve metal and ceramic particles. Since tissue contains collagen and elastin, additional enzymes including collagenases, as well as broad specify enzymes known to break down tissue proteins, such as papain (Zhao *et al.*, 2012), are often employed. Later stages of the protocol are similar to those for serum, and usually involve centrifugation.

**Table 1.4. Isolation methodologies for metal or ceramic particles from tissue and associated results and limitations.**

Paper	Type of isolation	Brief description of isolation/digestion method	Brief description of results and limitations
Margevicius <i>et al.</i> , 1994	CoCr alloy and Titanium (and polyethylene) from periprosthetic tissue from knee and hip replacements	Various acid digestion protocols; segments of tissue were harvested from paraffin blocks, deparaffinized in toluene; tissue was digested with alternative acids, sonicated; then filtered at various sizes	Nitric acid (and not HCl or Sodium hypophosphate) was effective for tissue digestion and authors suggest that it did not alter particles; size range 0.58-0.79 $\mu\text{m}$ ; a few more than 100 $\mu\text{m}$ (no distinction was made between metal and polyethylene particles)
Lerouge <i>et al.</i> , 1998	Alumina, zirconia and titanium alloy wear particles from periprosthetic tissue	Tissue cut into small fragments, digested using collagenase and dilute formic acid, centrifuged in sucrose gradient, washed, sonicated and filtered	The use of a 0.2 $\mu\text{m}$ filter eliminated all particles smaller than 0.2 $\mu\text{m}$ in size; possible damage from formic acid (since it was used to disintegrate bone); size distribution 0.2-2 $\mu\text{m}$ ; particles well separated
Doorn <i>et al.</i> , 1998	CoCr from periprosthetic tissues	Tissues defatted by washing with chloroform and methanol, use of MOPS, boiling with SDS, proteins removed with centrifugation, use of papain and proteinase K, sonication, spraying onto a surface	Size range of particles from 0.02-0.834 $\mu\text{m}$ Poor topological detail - use of TEM rather than SEM; possible loss of particles
Bohler <i>et al.</i> , 2000; Mochida <i>et al.</i> , 2001	Alumina and TiAlV from periprosthetic tissue; Alumina from periprosthetic tissue	Adapted from Margevicius <i>et al.</i> , 1994 using concentrated nitric acid, sonication, particle dispersant filtration (10, 0.4 and 0.1 microns); Bohler <i>et al.</i> also had a centrifugation step and applied gentle pressure during filtration	0.13-78.38 $\mu\text{m}$ size range of particles in Bohler <i>et al.</i> ; similar in Mochida <i>et al.</i> Pressure shown not to damage filter. Nitric acid shown not to damage alumina particles; removes hemosiderin particles (which appear similar to wear debris)
Hatton <i>et al.</i> , 2002	Alumina from periprosthetic tissues	Laser capture microdissection of paraffin embedded tissue sections	Particles were not totally isolated, limiting morphological analysis; no digestion/damage to particles; good size range 0.005-3.2 $\mu\text{m}$
Schmiedberg <i>et al.</i> , 2006	CoCr alloy from periprosthetic tissue	Tissue was minced and heated in SDS, then incubated with papain and pepsin	1-100 $\mu\text{m}$ particle size range identified; however metal particles tend to be in a nanoscale size range
Milosev and Remskar, 2009	CoCr from periprosthetic tissues	Based on Catelas <i>et al.</i> , 2001 enzymatic digestion and Doorn <i>et al.</i> , 1998; boiling with SDS, washing, sonicating, centrifuging, papain, proteinase K	Did not achieve high resolution images; 0.04-0.12 $\mu\text{m}$ size range

Campbell *et al.* (1995) developed a method for isolating UHMWPE particles from periprosthetic tissues that became widely adopted. Briefly, the method involved delipidating tissues by immersion in a 2:1 methanol to chloroform mixture for 24 h, prior to dicing and digestion with 5 M (Molar) NaOH. The digest was layered on top of sucrose gradients and ultracentrifuged, and then the top layer containing the particles was rinsed of sucrose. This was followed by isopropanol density gradient ultracentrifugation and filtration of the particle-containing layer with a 0.2 µm filter. However, extracting the material from top layers could lead to particle loss. To prevent loss of nano-sized particles which would occur due to use of a 0.2 µm filter, 0.01 and 0.015 µm filters are preferable. Visentin *et al.* (2004) proposed an alternative method whereby tissue slices were digested with sodium hypochlorite directly onto polycarbonate filters. However, since the slices were only 20 µm thick, large particles may have been dissected, leading to an underestimation in size. Billi *et al.* (2012) compared their method for isolation of particles from serum to that of Campbell *et al.* (1995), and found greater reproducibility, accuracy and sensitivity, and found that the size distribution was not shifted toward larger particle sizes, which occurred in the previous method due to loss of small particles. This suggests that methods for isolation of particles from tissue require improvement to be as effective as methods from serum, perhaps by preventing the use of large numbers of steps and by ensuring that no particle loss occurs during centrifugation.

### **1.10 Size and shape of wear particles**

Polyethylene produces the largest wear particles, which also exhibit the greatest range in morphology. Based on observations from failed prostheses, polymers, in particular UHMWPE, tend to float and may be flakes, splinters, filamentous (sometimes hundreds of micrometers in length), round or granular. The larger and flat, block shaped particles tend to result from adhesive wear, while flakes are usually due to fatigue wear (Nine *et al.*, 2014). Cross-linked UHMWPE produces smaller wear debris than non-cross-linked polyethylene, with some in the nanometer size range. In 2001, Howling *et al.* demonstrated that most UHMWPE particles are in the size range of 0.1-0.5

µm, although large particles approaching millimeters in size constituted a large volume of the debris.

CoCr particles are generally several orders of magnitude smaller and more numerous than UHMWPE debris. Tipper *et al.* (2001) found that MOM wear debris generated in a physiological anatomical hip joint simulator were mostly  $30 \pm 2.25$  nm in size; these were oval or round and very uniform in shape. The majority of CoCr particles are round, with a few shard or needle-like particles (Brown *et al.*, 2007). Savio *et al.* (1994) also reported metal wear debris as needle shaped and granular. CoCr particles were also reported as clustered and may be aggregates of smaller particles (Dorr *et al.*, 1990). Doorn *et al.* (1998) characterised metal wear particles isolated from the periprosthetic tissues from first and second-generation MOM hip prostheses. The particles were in the size range 20 – 834 nm, with most approximately 50-100 nm, and were mainly round in shape.

Generally, the smallest wear particles are generated by ceramics, although metals may release single ions. Ceramic particles are mainly nanoscale, with a granular or circular structure (Dorr *et al.*, 1990). Tipper *et al.* (2001) found that the majority of the wear debris produced by COC hip replacements *in vitro* were  $9 \pm 0.5$  nm, and like metal wear debris, were very uniform in size and oval or round in shape. However, large particles up to 1 µm in size have also been found (Hatton *et al.*, 2002), and Yoon *et al.*, 2008 found abundant ceramic wear debris with a mean size of 0.71 µm (range 0.13–7.2 µm) in periprosthetic tissue.

Bone cement (PMMA) particles may also be present in the joint cavity, primarily generated from implant loosening; these can be submicron but tend to be very large; size ranges of 1-110 µm (Zhang *et al.*, 2015) and up to 1 mm have been reported. The particles may be shards, spherical, granular or irregular pieces (Savio *et al.*, 1994).

Titanium particles display a very wide size range, from less than 1 µm up to 1 mm (Savio *et al.*, 1994); many report a size range of 1-5 or 5-25 µm. Another study reports a size range 10-400 µm (Shanbhag *et al.*, 1994). Thus, titanium particles are relatively large in comparison to orthopaedic metals or ceramics. Titanium alloy wear debris also exhibit a variety of morphologies, and may be

irregular, flake-like, or spherical, depending on the wear mechanism which produced them (Zhang *et al.*, 2015).

The size and shape of wear debris is linked to the biological response toward various implant materials.

### **1.11 Biological responses to wear debris**

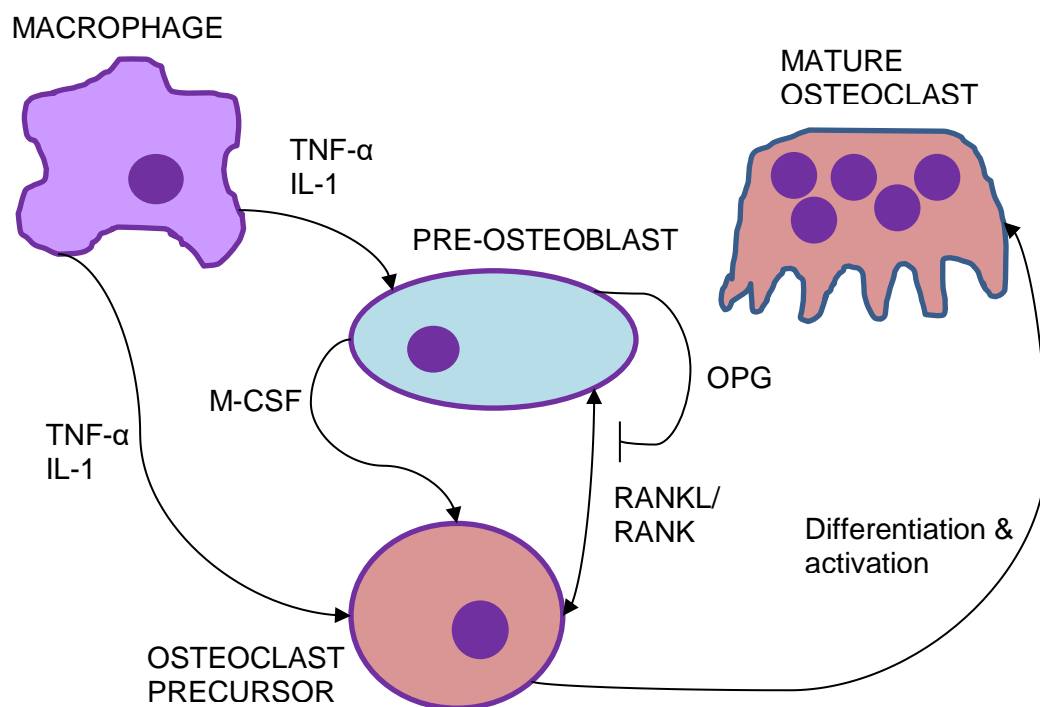
It has become apparent that the survivorship of prostheses is limited to approximately 25 years, with few exceptions (NJR, 2017). The most common reasons for hip replacement failures are aseptic loosening, pain and adverse reactions to particulate wear debris, which are responsible for 24%, 18%, and 17% of failures respectively (NJR, 2017). Several reasons for revision were often given and categories were not mutually exclusive. Further, the extent of adverse reactions to wear debris is likely to be underestimated, as this was not an option on the revision report forms during the early phase of the National Joint Registry. Aseptic loosening of the implant is often the result of osteolysis, which may be caused by the biological consequences of wear debris (Rajpura *et al.*, 2014). Materials which may be relatively inert in bulk form yet elicit chronic inflammatory reactions in particulate form. During the initial stages of an inflammatory response, mast cells that gather near blood vessels release neuropeptides and histamine; this is followed by cellular invasion of neutrophils and monocytes (Murphy, 2012). These leukocytes stick to the blood vessel endothelium, slowing the blood stream and causing erythrocytes to agglomerate; they are able to migrate into tissue, and recruit macrophages through the release of prostaglandins and leukotrienes (Murphy, 2012). Further biological responses vary by material, as the mechanical properties and use of the material affects the size and shape of the particles released, with important effects on the biological responses to the particles (Ingham and Fisher, 2000). For example, size affects the *in vivo* dissemination of particles and the ability of cells to phagocytose particles, and aspect ratio may also affect cellular uptake of particles (Chithrani *et al.*, 2006). Further, different materials have different corrosion characteristics and release different ions, which may vary in toxicity.

### **1.11.1 Biological responses to polyethylene wear debris**

Evidence suggests that UHMWPE wear debris generated at articulating surfaces which have entered the periprosthetic tissue, and are less than 5-10  $\mu\text{m}$  in diameter, are endocytosed by recruited macrophages. This triggers a nonspecific foreign body reaction. The macrophages release proinflammatory cytokines, some of which are chemokines such as IL-8 that attract greater cell infiltration; macrophages also fuse to create giant, multi-nucleated cells that surround or engulf larger particles (Ingham and Fisher, 2000). Granulomatous tissue containing macrophages and giant cells forms around the wear debris, walling the site off; this encapsulation becomes thicker over time. It is characterized by the activation of certain cellular mechanisms including release of tumor necrosis factor  $\alpha$  (TNF- $\alpha$ ), other interleukins (IL-1 $\beta$  and IL-6), local inflammatory mediators such as prostaglandin E<sub>2</sub> (PGE<sub>2</sub>) and nitric oxide (NO), matrix metalloproteinases, such as collagenase (MMP1 and 13), and stromelysin (MMP3) (El Warrak *et al.*, 2004). The macrophages are thought to cause bone resorption through the release of the above cytokines and inflammatory mediators, which stimulate the production of increased numbers of pre-osteoclasts and increase the activity of osteoclasts, leading to osteolysis around the implant and subsequent loosening (Ingham and Fisher, 2000). Macrophages also release PGE<sub>2</sub> and can stimulate the production of PGE<sub>2</sub> from fibroblasts as well; the release of PGE<sub>2</sub> has been suggested to stimulate osteoblasts to release an osteoclast activating factor (Tashjian and Levine, 1978). In addition to cytokines and degradative enzymes, some leukocytes release free radicals, which aid further cell migration by loosening cell junctions and also contribute to periprosthetic fibrosis (Kinov *et al.*, 2005). This type of fibrosis is thought to play a role in aseptic loosening.

The cytokines TNF- $\alpha$  and IL-1 released by activated macrophages stimulate the production of macrophage colony stimulating factor (M-CSF) and increase receptor activator of nuclear factor kappa-B ligand (RANKL) expression in pre-osteoblasts (Hofbauer *et al.*, 1999). In the presence of M-CSF, RANKL binds to RANK receptors expressed by osteoclast precursors (Figure 1.8). This stimulates a NF- $\kappa\beta$  pathway that causes the osteoclast precursors to differentiate into osteoclasts (Khosla, 2001). A molecule secreted by pre-osteoblasts, osteoprotegerin (OPG), modulates the RANK/RANKL pathway

by binding to RANKL and preventing RANKL from binding to RANK, and therefore inhibiting osteoclast differentiation and activity (Khosla, 2001). The RANK/RANKL/OPG system is modulated not only by the pro-resorptive cytokines TNF- $\alpha$  and IL-1, but also TGF- $\beta$ , which increases OPG production and therefore inhibits osteoclast differentiation, and various other cytokines and hormones, including oestrogen, glucocorticoids, and parathyroid hormone (PTH) (Khosla, 2001). It has been found that polyethylene particles induce human monocytes to release elevated levels of TNF- $\alpha$  and upregulate levels of RANK mRNA (Baumann *et al.*, 2004). Baumann *et al.* (2004) suggested this may play an important role in periprosthetic osteoclastogenesis.



**Figure 1.8. RANK/RANKL/OPG modulation of osteoclastogenesis.** Pro-resorptive cytokines stimulate pre-osteoblasts to release macrophage colony stimulating factor (M-CSF) and receptor activator nuclear factor kappa-B ligand (RANKL), causing osteoclasts to differentiate and activate. This is inhibited by osteoprotegerin (OPG) expression, which binds to RANKL and prevents receptor activator nuclear factor kappa-B (RANK) from binding. Adapted from Khosla, 2001.



Elongated UHMWPE wear particles are thought to elicit a stronger cellular reaction than globular particles, in terms of increased pro-inflammatory gene expression (Ren *et al.*, 2003). The most significant factor in terms of the biological response is the concentration of the wear volume that is in the 'critical size range', which is the range in which macrophages become activated to produce an inflammatory response. The critical size range includes the approximate size range of bacterial pathogens which the macrophages have evolved to ingest, which is 0.2-0.8  $\mu\text{m}$  in size (Ingham and Fisher, 2000). A study which evaluated the *in vitro* response of murine macrophages to polyethylene particles of defined size distributions at defined volume doses determined cell response through the measure of secreted cytokines, and was therefore able to indicate a critical size range (Green *et al.*, 1998). This study found that particles of mean sizes of 0.49, 4.3 and 7.2  $\mu\text{m}$  significantly elevated the levels of TNF- $\alpha$  and IL-1 $\beta$  in the macrophages, as determined by an ELISA, when dosed in a 10:1 ratio of the volume of particles ( $\mu\text{m}^3$ ) to cell number. At a 100:1 ratio, IL-6 production was significantly elevated for mean particle sizes of 0.49 and 4.3  $\mu\text{m}$ . Particles outside the 0.49-7.2  $\mu\text{m}$  range produced considerably lower levels of cytokine activity. This study therefore indicated that the size and volume of polyethylene particles are critical factors in macrophage activation. The authors suggested that particles in the phagocytosable size range of 0.3-10  $\mu\text{m}$  were the most biologically active. Though smaller particles of a critical size range are produced in cross-linked polyethylene, the much lower wear volume increases the biocompatibility of cross-linked polyethylene over non-crosslinked polyethylene. UHMWPE particles in the 0.1-1 $\mu\text{m}$  size range have been found to be more biologically active than the larger particles, and it was found that particles of a size below approximately 50 nm failed to elicit a proinflammatory response in PBMNCs (Liu *et al.*, 2015).

Similar reactions, involving giant cells, increased proinflammatory cytokine release and bone resorption, have been reported for bone cement particles of PMMA (Maloney *et al.*, 1990; Willert *et al.*, 1990; Gibon *et al.*, 2017).

### **1.11.2 Biological responses to CoCr wear debris**

Interest in MOM designs increased in the 1980's, due to the lower wear rate afforded by MOM implants. After it became clear that immunological reactions

associated with UHMWPE debris limited the lifetime of MOP prostheses in the 1990s, usage of MOM THRs increased. However, metal debris and ions released from THRs and surface replacements employing MOM bearings, have been found to exhibit a whole range of biological consequences in the last decade; thus, the usage of MOM has sharply declined since 2010 (NJR, 2017). For example, adverse reactions to metal debris for MOM THRs have a reported incidence of 18% at 41 months for the ASR system, which was withdrawn (Haddad *et al.*, 2011). This section relates specifically to cobalt chromium (CoCr) wear particles, the bearing material used in MOM devices.

During investigation into the cellular reactions to wear particles from first and second-generation MOM prostheses, Doorn *et al.* (1996) found that a common reaction was necrobiosis; cell necrosis without the release of collagenases or subsequent loss of the extracellular matrix. The researchers found cell necrosis to be the second most common reaction, and 'tumoural calcinosis-like' necrosis to be the third. The latter consisted of discrete patches of necrosis that radiated outward, each of which was surrounded by multiple layers of histiocytes. These types of cell death are consistent with a report which investigated tissue responses to metal wear particles produced from a CoCr stem of a failed THR (Milosev *et al.*, 2000). Aroukatos *et al.*, 2010, also identified severe necrosis surrounding MOM THRs. Various studies have also demonstrated cytotoxic effects of CoCr particles *in vitro*; for example, Germain *et al.* (2003) used 30 nm CoCr particles generated by pin-on-plate wear tests in a study of the viability of murine fibroblasts (L929) and a human histiocyte cell line (U937); the authors found that particle volumes of 50  $\mu\text{m}^3$  and 5  $\mu\text{m}^3$  per cell caused a significant reduction in cell viability for both cell types. Metal wear particles are thought to cause necrosis through their engulfment into macrophages; once inside corrosion of metal particles inside acidic lysosomes leads to the release of toxic levels of metal ions that result in cell death.

The cytotoxic effect of metal wear debris has also been postulated to be a cause of osteolysis and aseptic loosening (Haddad *et al.*, 2011). Osteolysis associated with a second generation uncemented MOM implant has been reported (Beaule *et al.*, 2001), though the cause of the osteolysis was not deduced. Brown *et al.* (2006) suggested that osteolysis would be unlikely under normal wear conditions, since the low wear rate of MOM implants and

the dissemination of wear particles would reduce the local particle concentration, and thus cytotoxicity, of metal wear debris. In fact a study of 96 Metasul MOM THR implants found no evidence of osteolysis at 5-11 years post implantation (Dorr *et al.*, 2004). Multi-nucleated giant cells have not been associated with nanoscale debris produced by MOM implants, and the cytokine most often associated with osteolysis, TNF- $\alpha$ , is present only at low levels (Brown *et al.*, 2006). Though *in vitro* studies have demonstrated the production of osteolytic cytokines, this may be due to engulfment of micron-sized particle aggregates, rather than nanoscale wear particles. Brown *et al.* (2013) found evidence that nano-sized and micron-sized metal particles exert different effects in a mouse model; metal nanoparticles, and not micron-sized particles, caused significant DNA damage to cells when assessed at 40 weeks post injection of the particles into mice.

DNA damage, indicating genotoxicity, has also been demonstrated for metal wear debris *in vitro* (Papageorgiou *et al.*, 2007); though the DNA damage may be fixed in the long term (Hafez *et al.*, 2011). Chromium (VI) and not lower valence states of chromium is a known carcinogen due to the ability of the ion to enter cells; once inside cells it is reduced to Cr(V), Cr(IV) and Cr(III). However, Cr (VI) has not been detected as a result of MOM wear, and it has not yet been firmly established whether cobalt or molybdenum are carcinogenic. Tsaousi *et al.* (2010) identified chromosomal aberrations in response to CoCr particles at doses of 1 mg, which corresponds to a relatively high volume of 0.12 mm<sup>3</sup>. Overall, the committee for the Mutagenicity of Chemicals in Food, Consumer Products and the Environment has stated that exposure to orthopaedic metals, particularly CoCr, is associated with increased genotoxicity. Chromium (V), (IV) and (III) are known to cause single strand breaks (SSBs), inversions, deletions and other types of DNA damage through the formation of DNA adducts and free radicals. Increased levels of aneuploidy and chromosomal translocations have been found in bone marrow cells adjacent to metal prostheses in MOP implants, and also in peripheral lymphocytes (Doherty *et al.*, 2001). Metal particles are suspected to be associated with the increased occurrence of certain cancers in joint replacement patients; prostate and melanoma cancers were elevated in patients following THR, however some cancers including bone cancers were

lowered, and the effects may not be causal (Onega, 2006). Rats have been used as an animal model to investigate the carcinogenicity of CoCr particles, suggesting a slight increased risk of tumours (Swanson *et al.*, 1973). However, in humans, factors such as medication must be considered and a possible link between cancer and prostheses has not yet been confirmed, with long follow-up times required due to the latency of tumours.

MOM implants can create metallosis, large scale staining of tissues due to metal deposition, which is caused by abnormally high wear of the bearing surface or taper junction (Hart *et al.*, 2010). The metal ions and debris can lead to cell necrosis and the formation of masses of inflammatory cells known as pseudotumours (Haddad *et al.*, 2011). Soft tissue aseptic lymphocyte-dominated vasculitis-associated lesions (ALVAL) may also be present; these are lesions characterised by dense perivascular lymphocytic infiltrates, which usually cause pain (Watters *et al.*, 2010). One study reported the occurrence of ALVAL to be 5% at ten years for the Metasul MOM implant (Eswaramoorthy *et al.*, 2008). Soft tissue reactions were present in 0.3% - 3.4% of patients in response to CoCr particles at a maximum follow up of seven years (Haddad *et al.*, 2011).

In the presence of low wear, it has been suggested that cell mediated hypersensitivity, resembling type IV delayed hypersensitivity, leads to ALVAL and is involved in tissue damage (Milosev *et al.*, 2006). Metal ions, including cobalt and chromium, are capable of complexing with proteins to produce allergens, thus creating hypersensitivity; Brown *et al.* (2013) suggest that micron size metal particles also created a type IV response. This type of hypersensitivity is an established clinical condition in 10-15% of the population (Brown *et al.*, 2006). Reactions to metal ions involve activation and clonal expansion of MHC class II CD4 T-lymphocytes that are metal ion specific. This leads to production of cytokines including IFN - $\gamma$  and a chronic inflammatory response that could lead to osteolysis (Hallab *et al.*, 2001). Patients with MOM prostheses have raised metal ion sensitivities compared to the general population (Hallab *et al.*, 2001).

Systemic dissemination of metal nanoparticles and ions, primarily through the lymphatic system to distant organs can occur (Bitar and Parvizi, 2015).

Dissemination may cause severe symptoms that may include heart problems, visual impairment, cognitive impairment, nerve impairment, thyroid problems, auditory impairment and skin rash (Keegan et al., 2007). Clinical studies have also shown that implant and wear debris corrosion lead to elevated blood serum levels of metal ions in patients with MOM and MOP implants (Bitar and Parvizi, 2015; Savarino *et al.*, 1999). Serum levels of cobalt and chromium have been raised 6-7 times above normal levels in MOM patients (Ladon *et al.*, 2004). Similarly, Macdonald *et al.* (2003) carried out a clinical trial in which patients who received a MOM hip replacement had a 7.9- and 2.3-fold increase in erythrocyte cobalt and chromium respectively, while patients who received MOP implants had 1.5- and 2.2-fold increases. There is also concern that, with implants being introduced into younger patients, metal ions could impact on foetal development. In a cross-sectional study of pregnant women, it was found that the placental cord blood contained about twice the concentration of metal ions in women with MOM implants versus women without (Ziaee *et al.*, 2007). Discrepancies in the measured metal ion concentrations may have arisen between the two studies due to the different devices used, and due to measurements being performed either on whole blood samples, or on erythrocytes only. Studies have shown that MOM implants may result in a lower blood concentration of T and B lymphocytes, myeloid cells and natural killer cells, and that this may be due to the cytotoxic effects of metal ions (Savarino *et al.*, 1999). However, a high concentration of T and B lymphocytes are found in various tissues as a result of MOM prostheses, due to inflammatory effects of the particles (Haddad *et al.*, 2011).

### **1.11.3 Biological response to silicon nitride wear debris**

In comparison to studies on biological reactions to CoCr and UHMWPE particles, information on the biocompatibility of SiN is limited. Studies in rabbits *in vivo* and *in vitro* studies in rabbit marrow stromal cells and mouse fibroblasts have indicated that SiN in the form of ceramic discs and femoral implants has a favourable biocompatibility profile; as well as not eliciting any cytotoxicity, the material encourages osteoblast attachment and bone formation (Howlett *et al.*, 1989), (Neumann *et al.*, 2004). An *in vitro* study involving human PBMNCs showed that both nanoscale and micron-scale SiN particles do not cause cytotoxicity, oxidative stress, genotoxicity or release of

TNF- $\alpha$  (Lal *et al.*, 2018). Globular silicon nitride particles with a narrow size distribution averaging 0.19  $\mu\text{m}$  have been used *in vitro* in cell studies to determine levels of cytotoxicity (Mazzochi and Belosi, 2008). These authors found no difference between negative controls and cells cultured with SiN; however, dosage of particles was unclear. Another study found that SiN nanoparticles were endocytosed and did not affect cell viability but interfered with the function of human osteoblast cell lines and stimulated high levels of TNF- $\alpha$  secretion in a murine macrophage cell line (Zhang *et al.*, 2011). The results suggested that SiN nanoparticles may be bioactive, but only at very high doses (500 ppm) which may not be achieved in relation to implant wear *in vivo* due to the dissolution characteristics of SiN.

#### **1.11.4 Biological responses to other ceramic wear debris**

Similar to SiN, ceramic wear particles have been found to be relatively biocompatible compared to other orthopaedic particles. Hatton *et al.* (2002) reported that alumina particles with a mean size of  $0.5 \pm 0.19 \mu\text{m}$  induced the production of TNF- $\alpha$  from peripheral blood mononuclear cells *in vitro*. However, the volume of particles required to produce significant adverse reactions are unlikely to ever be reached *in vivo* (Hatton *et al.*, 2003), even under severe wear conditions. *In vivo* studies in mice, comparing zirconia and alumina ceramics to control mice, found that neither ceramic produced any significant difference in cytokine levels, and there were no resultant osteolytic lesions (Warashina *et al.*, 2003). Germain *et al.* (2003) found that when U937 cells were dosed at  $50 \mu\text{m}^3$  per cell of clinically relevant alumina wear particles produced in a hip simulator, cell viability was reduced by 18%. However, the same amount of cobalt chrome particles generated by pin-on-plate wear testing reduced U937 cell viability by 97%. In a clinical trial assessing 800 patients with an alumina COC hip replacement, there were no reports of implant failure as a result of aseptic loosening (Garino, 2000). However, one animal study found that subcutaneous aluminium oxide disc implants produce local sarcomas in rats (Kirkpatrick *et al.*, 2000). Small increases in the expression of RANK, OPG and TNF- $\alpha$  have been found in response to alumina particles (Bylski *et al.*, 2009), and a study exposing rat stifle joints to nanoscale alumina and zirconia particles produced a nonspecific granulomatous response (Roualdes *et al.*, 2010). These studies suggest that

where a response to ceramic particles is elicited, the pathway appears to be a foreign-body response similar to that caused by polyethylene particles.

#### **1.11.5 Biological responses to titanium particles**

Titanium wear debris are often suggested to be relatively biologically inert, partly since the wear debris are usually outside of the critical size range of approximately 0.1 -1  $\mu\text{m}$  known to elicit inflammatory responses (Ingham and Fisher, 2000). Long term studies in mice have also indicated a favourable biocompatibility profile for titanium particles (Rae, 1986). However, other studies have indicated that titanium particles are immunologically active (Shanbhag *et al.*, 1995; Wang *et al.*, 1997; Vermes *et al.*, 2001). Thus, the biocompatibility of titanium particles is somewhat contentious. Titanium particles below a certain size are known to be phagocytosed by macrophages (Lalor *et al.*, 1991) and are occasionally reported to cause type IV sensitivity reactions (Lalor *et al.*, 1991; Vijayaraghavan *et al.*, 2012). Titanium debris have produced elevated levels of proinflammatory cytokines and osteolytic lesions in mice *in vivo* (Warashina *et al.*, 2003). Giant cells were also observed surrounding titanium particles. This would suggest that titanium particles elicit responses similar to those seen with UHMWPE particles. This is supported by *in vitro* studies which show that titanium particles cause significant release of TNF- $\alpha$  (Zhang *et al.*, 2011; Lal *et al.*, 2018).

#### **1.12 The need for improved hip replacements**

The cumulative probability of revision for hip replacements in England and Wales is currently 6.8% at 13 years (NJR, 2017). The Swedish Hip Arthroplasty Register (2010) recorded a 3-10% failure rate across all prostheses at 10 years. Revision surgeries tend to be less successful than primary interventions, as shown by the cumulative probability of hip re-revision at 13 years, which is approximately 17% (NJR, 2017). Further, the total number of hip replacement procedures continues to rise with an increase of 3.5% in 2016 compared to the previous year (NJR, 2017).

Although hip replacements are considered a relatively successful intervention, increased growth in the revision market and the presence of defective, recalled hip prostheses, such as the 2012 Stryker Rejuvenate Modular and

ABG II Modular-Neck Hip Stems, as well as the Depuy ASR, are problems that must be overcome. The biological reactions to wear particles, which limit the lifetime of current prostheses, represent a real problem in the current market. Hip replacement failures affect the quality of life of thousands of individuals and are a heavy burden on health care systems; the cost of total hip replacement surgery in Europe may range from 1290 euros (Hungary) to 8739 euros (Netherlands) for full treatment, with the implant making up on average 34% of the cost (Stargardt, 2008).

Moreover, there is a changing age demographic of the populations of most developed countries. Globally, the world population is expected to reach 10 billion by 2050, and the percentage of people aged over 65 years is predicted to increase from 7% (in 2000) to 16% (UN, 2012). In America the proportion of over 65s has increased from 8.1% in 1950 to 12.8% in 2009, and this is predicted to increase to 20.2% in 2050 (Shrestha, 2006). As hip replacements are more commonly performed in over 65s, it is predicted that demand for hip replacements will grow; indeed, the demand for primary THR per 100,000 people has increased by 50% in the US, and revision THR by 3.7 procedures per 100,000 per decade between 1990 and 2002 (Kurtz *et al.*, 2005). In England, Wales and Northern Ireland, the number of primary THRs has risen year on year, with 87,733 cases in 2016 compared to 86,496 the previous year (NJR 2017). Patients are expected to live longer and be more active to a later age, thus they require more reliable, longer-lasting implants. Furthermore, the Asian market may in future dwarf the European and American markets; two thirds of the world's middle class is predicted to be Asian by 2050.

Kurtz *et al.* (2005) showed that rates of THR have increased not only in the over 65s, but in the under 65s as well. Currently, a greater number of young patients than ever are undergoing THR (NJR, 2017). Failure rates are higher in younger patients, possibly due to higher activity levels (Kilgus *et al.*, 1991; NJR, 2017). The prospect of multiple revision surgeries in a young patient's lifetime likely leads many surgeons and patients to reject or postpone THR as an intervention. Further evidence that younger patients have a greater need for revision comes from statistics published by an early NJR report, which show that overall ten-year revision rates in the UK between 2003 and 2013



were 9.12% in males under 55 years, compared to 3.45% in patients greater than 75 years. This trend occurs despite the highest-performing implants being chosen for younger patients. Kurtz *et al.* (2009) predicted demand to grow by a factor of 5.9 in people aged between 45 and 54 from 2006 to 2030, suggesting that patients under 65 may contribute greatly to the future demand for hip replacements.

All of the above has led to interest in the development of alternative biomaterials (Sonntag *et al.*, 2012), and also in the development of more realistic test methods of these materials, since current failures were not predicted using existing methods (Sedrakyan, 2012).

One approach to improve THR has been the development of novel systems that more closely replicate the natural joint, known as cushion bearings. These use a hard bearing that articulates against a relatively soft bearing, allowing high conformity and full fluid film lubrication. The 'cushion' cup component may be made from polycarbonate urethane. In combination with a CoCr head, polycarbonate urethane exhibits lower wear than UHMWPE in hip simulations (Elsner *et al.*, 2010). Long term *in vivo* studies using a soft polyurethane lining in a hard outer cup were also encouraging (Carbone *et al.*, 2006). However clinical trials employing such a system in 394 patients which commenced in 2010 required several revisions at the 12-month follow up (Moroni *et al.*, 2012).

Hydrogels such as polyvinyl alcohols, polyvinylpyrrolidone and poly-2-hydroxyethylmethacrylate are also used in cushion bearings; they consist of a framework of hydrophilic polymer chains that may absorb large amounts of water without dissolving and possess a viscoelastic property comparable to that of cartilage (Sonntag *et al.*, 2012). Hydrogels form a fluid film that reduces frictional torque; 2--methacryloyloxethyl phosphorylcholine (MPC) polymer grafted onto a CoCr alloy for simulation as an artificial hip bearing demonstrated an extremely low coefficient of friction of 0.01 (Kyomoto *et al.*, 2009), comparable to that of normal cartilage, which has a coefficient of friction of 0.001 (Unsworth *et al.*, 1975). However, the mechanical instability of hydrogel systems limits their clinical suitability (Ushio *et al.*, 2004; Kobayashi and Oka, 2004); further hydrogel models are under development.

However, given that the primary cause for hip replacement failure is adverse responses to wear debris, most research has focussed on the development of relatively low-wearing, highly biocompatible materials. This has led to the investigation of ceramic-like coatings to enhance the function of hip replacements.

### **1.13 Coatings for hip replacements**

Coatings for THR may be applied to the stem, taper or bearing surfaces. Hydroxyapatite coatings applied to stems have been in widespread clinical use for years to enhance fixation of uncemented systems by osseointegration; however, coatings for the taper and bearing surfaces are still in the developmental stages. Coatings may allow relatively expensive materials with desirable characteristics to be used in commercially viable ways. Such coatings are typically either a few  $\mu\text{m}$  thick or between 10 and 100  $\mu\text{m}$  thick (Holmberg and Matthews, 1994).

The deposition protocol of a coating may greatly affect the quality of adhesion, chemical properties, homogeneity, overall morphology and stress resistance of that coating (Holmberg and Matthews, 1994). There are two main deposition methodologies; chemical vapour deposition (CVD) and physical vapour deposition (PVD). In typical CVD, the substrate is exposed to one or more volatile precursors, which react and/or decompose on the substrate surface to produce the desired deposit. Frequently, volatile by-products are also produced, which are removed by gas flow through the reaction chamber. There are many different variations of CVD, with the main distinction being the level of pressure at which the method is performed; CVD can operate at atmospheric pressure, low pressure and in vacuum (McEntire, and Lakshminarayanan, 2012).

Physical vapour deposition (PVD) involves purely physical processes such as high-temperature vacuum evaporation of the coating material with subsequent condensation onto the substrate, or plasma sputter bombardment rather than involving a chemical reaction as in chemical vapour deposition. PVD coatings can have excellent abrasion resistance and PVD has the flexibility to utilise virtually any type of inorganic and some organic coating materials on an

equally diverse group of substrates and surfaces using a wide variety of finishes (McEntire, and Lakshminarayanan, 2012).

There are many variants of PVD, one of which is high-power impulse magnetron sputtering (HIPIMS). This can be used both as a direct deposition method and as a pre-deposition method to prime the substrate material for adhesion (McEntire, and Lakshminarayanan, 2012). HIPIMS utilises extremely high-power densities in short pulses, resulting in a high degree of ionisation of the sputtered metal and a high rate of molecular gas dissociation which result in high density deposited films.

Rockwell indentation and scratch tests can be used to assess the level of adhesion, on a scale where class 0 represents no adhesive delamination or cracking and class 3 represents complete delamination. A good coating should have a surface roughness of less than 20 nm, scratch adhesion of greater than 30N and a coating hardness of at least 20 GPa (Holmberg and Matthews, 1994).

A coating which shows promise as a bearing surface is diamond-like carbon (DLC). It is biologically inert and adheres strongly to UHMWPE, titanium and CoCr, among other biomaterials (Holmberg and Matthews, 1994). In addition, it is highly wear resistant and exhibits low-friction; friction is lower on a DLC coated surface sliding against another DLC coated surface when compared to alumina on alumina articulation, and in hip simulators DLC has been found to reduce wear of DLC coated CoCr prostheses (Holmberg and Matthews, 1994).

A similar new coating is nanocrystalline diamond (NCD). It has favourable hardness, smoothness and corrosion resistance, and in wear tests against itself, outperformed conventional MOM, COC and COP bearings (Amaral *et al.*, 2008). However, adhesion of the coating to metal substrates was an issue (Vila *et al.*, 2006), and there are few other studies regarding this material.

Pyrolytic carbon is a surface coating with a structure consisting of graphene-like layers; it reportedly has good fatigue resistance, wettability and wear resistance (Ma and Sines, 2000; Ratner *et al.*, 2004; Revell, 2008). Although it has been used very successfully in various joints of the upper limb, with

reportedly excellent biocompatibility, it has not been thoroughly evaluated in a load-bearing scenario (Sonntag *et al.*, 2012).

Another variety of surface coatings are nitrated or carbonated chromium, titanium or silicon. Advantages include increased hardness and decreased metal ion release (Stone *et al.*, 1991; Heide and Schultze, 1993).

Williams *et al.* (2003) reported on the effectiveness of diamond-like carbon (DLC) coatings, as well as titanium nitride (TiN), chromium nitride (CrN) and chromium carbon nitride (CrCN) coatings, on CoCr implants, finding that thin (1-2 micron) TiN and DLC coatings quickly wore through, while better results were achieved with CrN and CrCN coatings of 8-12µm. The thick (8-12 µm) CrN and CrCN coatings had decreased wear compared to MOM bearings. Particles generated from surface engineered coatings (TiN, CrCN and CrN) did not significantly affect the cell viability of L929 fibroblasts; CrCN was particularly biocompatible.

TiN-coated femoral heads have been used clinically (Harman *et al.*, 1997; Raimondi and Pietrabissa, 2000). Although in the latter study, the implant was well-functioning, both studies identified wear debris resulting from adhesive failure of the coating. Harman *et al.* (1997) also found evidence of TiN coating fretting, coating breakthrough, and third-body wear.

#### **1.14 Silicon nitride as a coating for hip replacements**

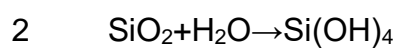
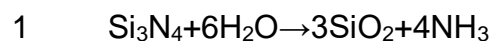
Silicon nitride is perhaps the most promising new coating material for implants. SiN can be formulated into a porous substrate on one part of an implant and can be polished to create a hard bearing surface on another part of the same implant; so that it can perform as a bearing whilst allowing osseointegration (Bal and Rahaman, 2012). A SiN coating could potentially be applied to the bearing surfaces, stem, and even the taper junction, to enhance the performance of the implant.

Low-pressure CVD is unsuitable for silicon nitride coatings thicker than 200 nm due to susceptibility of the coating to tensile stress (Sze, 2001). However, thicker SiN coatings may be produced by PVD. SiN coatings 1-1.7µm thick produced by PVD demonstrated an amorphous or nanocrystalline structure (Olofsson *et al.*, 2012). Most of the coatings exhibited a fine surface

microstructure and columnar cross-sectional appearance, a hardness of approximately 20 GPa and a coefficient of friction against itself of between 0.12 and 0.22, similar to that of bulk silicon nitride (Olofsson *et al.*, 2012).

The mechanical wear of SiN occurs primarily through surface microfractures (Olofsson *et al.*, 2012). Pin-on-disc tests undertaken at Uppsala University (UU) in which bulk silicon nitride pins were articulated against SiN-coated CoCr discs, show that the wear rates of the coatings produced by Olofsson *et al.* (2012) were approximately three times higher than the wear rate of bulk SiN and twenty times lower than that of uncoated CoCr. The findings suggest that such coatings could be suitable for hip replacements. (Olofsson *et al.*, 2012).

Silicon nitride has complex wear properties, since it experiences primarily mechanical abrasion, but also tribochemical wear, through dissolution via two major consecutive reactions:



SiN reacts with water to produce silicon dioxide and ammonia. The silicon dioxide then reacts with water to form silicon hydroxide (Rahaman and Bal, 2012). This mechanism creates a lubricating, hydrated silicon oxide film, that contributes to the subsequent low wear of the bearing surfaces. The dissolution rate for SiN coatings was 0.2-1.4 nm a day, or on average about 0.5 nm a day, equivalent to a rate of 0.18  $\mu\text{m}$  per annum (Pettersson *et al.*, 2016). This would provide a lifetime of approximately 40 years for a 7  $\mu\text{m}$  thick coating. It was also found that increasing the atomic ratio of nitrogen to silicon lowered dissolution, indicating the potential for adapting the dissolution of the coating for hip replacement. Furthermore, particles from SiN coatings are soluble *in vivo*, dissolving at a rate of approximately 0.33 - 2 nm per day, depending on the characteristics of the particles (Maloney, 2005). The slow release of silicon from the wear particles into the surrounding tissue might enhance implant fixation, since silicon has been shown to increase the speed and quality of natural bone formation, which could lead to more rapid osseointegration (Lopez-Alvarez *et al.*, 2009).

## 1.15 Project aims and rationale

The need for a longer-lasting, biocompatible hip replacement has been outlined in section 1.12 of this chapter. Since all articulating surfaces and some non-articulating surfaces are prone to some degree of wear and corrosion, there is a need to produce not only a low-wearing material, but a highly biocompatible material. Evidence presented in section 1.11 suggests that the best materials to satisfy these requirements are ceramics.

Silicon nitride is unique as a material in that it demonstrates three properties which no other orthopaedic material demonstrates in combination:

- high wear resistance
- biocompatibility (based on the limited data which is currently available for SiN wear debris)
- particles with dissolution characteristics.

However, due to the relatively high cost of the material, a SiN device may consist of a metal device with a SiN coating, rather than the material in bulk form. The fabrication of such a prosthesis, consisting of a SiN-coated CoCr femoral bearing and acetabular cup, and a titanium stem, was the intention of the LifeLong Joints Project - a consortium of 15 institutions funded by the European Union to deliver a next generation hip prosthesis, as well as deliver novel testing methodologies.

The LifeLong Joints project objectives included:

- development, characterisation and tribological testing of novel silicon nitride coatings for articulating and non-articulating surfaces
- development of advanced computational and *in vitro* simulations to test the devices
- production and preclinical testing of prototype devices
- finalisation of the manufacturing process
- delivery of *in vivo* data to evaluate biocompatibility and functionality

This PhD project was concerned with the delivery of *in vivo* data, in collaboration with the University of Zurich (Musculoskeletal Research Unit).

Though the literature indicates a favourable biocompatibility profile for SiN, there is currently no data on the *in vivo* response to SiN coating particles. Therefore an *in vivo* investigation into the biological consequences of SiN as a coating for hip replacements is warranted, which was a major aim of this PhD research. These studies aim to elucidate possible inflammatory pathways elicited by the particles, in addition to further biological reactions. As part of this investigation, a major objective was to retrieve SiN particles from the tissue samples from the *in vivo* studies in order to analyse the particles. It was therefore necessary firstly to develop the methodology required, since as detailed in section 1.9, the current methods are inadequate and have not been tested on SiN.

The PhD project objectives were thus as follows:

- To develop and validate a sensitive method to isolate SiN wear debris from tissues
- To use animal models to evaluate biological responses to particles
- To isolate and analyse wear particles from animal tissues
- To determine the biocompatibility of silicon nitride coating particles

This will enable greater understanding of the suitability of a SiN coating for total joint replacement prostheses. If successful, such a device would lead to improved therapeutic outcomes by providing an option for a longer-lasting THR.

## **Chapter 2**

### **Materials and Methods**

#### **2.1 Materials**

The equipment, reagents and consumables used throughout this research are given in Tables 1-3 of Appendix A.

#### **2.2 Methods**

##### **2.2.1 Cleaning of glassware and tubes**

Unless otherwise stated, all reusable glassware, tubes and filter units that were used during particle experiments were cleaned with household detergent, rinsed in tap water, rinsed three times with distilled water and rinsed once with sterile filtered water. New disposable tubes and pipette tips were rinsed once with sterile filtered water prior to use.

##### **2.2.2 Filtration of stock solutions and particle suspensions**

Filter units were cleaned as described in 2.2.1 and set up inside a class II cabinet. Stock solutions were filtered using a duran filter unit connected to a vacuum pump, with a 0.02  $\mu\text{m}$  anapore filter membrane, and collected directly into a clean tube. Particle suspensions were filtered onto 25 mm or 47 mm polycarbonate filters using corresponding filter unit sizes.

##### **2.2.3 Measuring and adjusting pH of solutions**

The pH and temperature probes of a HANNA pH 212 pH meter were rinsed in distilled water and used in conjunction by immersion to a depth of approximately 4 cm below the surface of the solution to be tested. Firstly, buffer solutions of pH 4, pH 7 and pH 10 were tested to check the accuracy of the pH meter and used to calibrate the pH meter if necessary. The pH of a sample was tested and adjusted by adding pre-made sodium hydroxide or hydrochloric acid solutions of 6 M or 12 M initially and then 1 M or 0.1 M, dropwise with a Pasteur pipette and with the use of a magnetic stirrer.



## **2.2.4 Stock solutions**

### **2.2.4.1 Calcium chloride stock solution (0.5 M)**

A solution of 0.5 M CaCl<sub>2</sub> was produced by dissolving the powder in sterile filtered water, and the solution was filtered as described in section 2.2.2. The CaCl<sub>2</sub> solution was stored at room temperature in a sterile plastic screw cap tube for up to three months.

### **2.2.4.2 Glycine stock (1 M)**

A solution of 1 M glycine stock was prepared by dissolving glycine powder in sterile water. The solution was filtered as described in section 2.2.2 and stored at room temperature in a sterile plastic screw cap tube for up to three months.

### **2.2.4.3 HEPES buffer stock solution (1 M)**

A solution of 1 M HEPES buffer was prepared by dissolving HEPES powder in sterile water and adjusting the pH to 7.5 as described in 2.2.3. CaCl<sub>2</sub> stock was added to an end concentration of 30 mM. The HEPES buffer was filtered as described in section 2.2.2 and stored at 4°C in a sterile plastic screw cap tube for up to three months.

### **2.2.4.4 Preparation of proteinase K stock solution (20 mg.ml<sup>-1</sup>)**

A dry weight of 100 mg of proteinase K powder was added to a sterile plastic bijou on ice. A volume of 2 ml of sterile water and 500 µl of 1 M HEPES stock containing 30 mM CaCl<sub>2</sub> (made as described in section 2.2.4.3) was added to the tube and the volume was made up to 5 ml using sterile water to give final concentrations of 0.1 M HEPES and 3 mM CaCl<sub>2</sub>. The stock was vortexed to mix and stored at -20 °C for up to three months.

### **2.2.4.5 SDS stock solution**

A solution of 10% (v/v) sodium dodecyl sulphate (SDS) was prepared by diluting ultrapure 100% SDS in sterile filter water. The solution was stored at room temperature in a sterile plastic screw cap tube for up to one year.

### **2.2.4.6 Sodium polytungstate solutions**

To produce a sodium polytungstate (SPT) solution of 2 g·cm<sup>-3</sup> in density, commercial SPT stock solution (85% v/v) was diluted 50% (v/v) in sterile filtered water. The solution was filtered as described in section 2.2.2.

To produce a sodium polytungstate (SPT) solution of  $1.6 \text{ g}\cdot\text{cm}^{-3}$  in density, filtered  $2 \text{ g}\cdot\text{cm}^{-3}$  SPT solution was diluted 50% (v/v) in sterile filtered water.

To produce a sodium polytungstate (SPT) solution of  $1.2 \text{ g}\cdot\text{cm}^{-3}$  in density,  $1.6 \text{ g}\cdot\text{cm}^{-3}$  SPT solution was diluted 50% (v/v) in sterile filtered water.

All SPT solutions were stored in sterile 50 ml plastic screw cap tubes for up to six months at room temperature out of direct sunlight.

## **2.2.5 Generation of clinically relevant cobalt chromium particles using a pin-on-plate wear simulator**

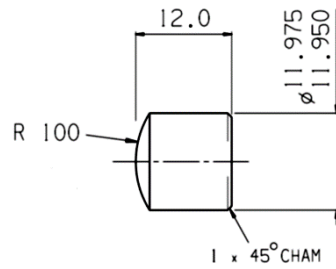
### **2.2.5.1 Introduction**

While commercially available silicon nitride (SiN) particles were used in experiments, due to the unavailability of relevant SiN-coated components, clinically relevant cobalt chromium (CoCr) particles could be produced from the relevant alloy using a pin-on-plate wear tester. These particles were generated to dope tissue samples with during initial particle isolation experiments.

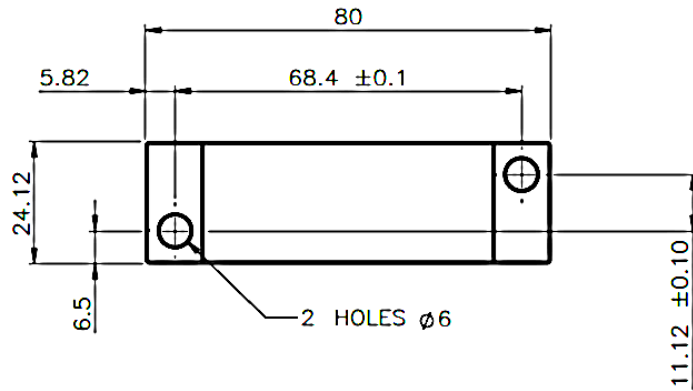
### **2.2.5.2 Preparation of pins and plates**

Cobalt chromium alloy (ASTM F1537) pins and plates ( $n=6$ ) with high carbon content ( $>0.2\%$  weight) were prepared and the contact surfaces polished to a smooth surface roughness ( $R_a$   $0.01\text{--}0.02 \mu\text{m}$ ) by technical staff in the School of Mechanical Engineering. Dimensions of the pins and plates are given in Figure 2.1. The pins and plates were cleaned in household detergent solution in an ultrasonic bath for 10 minutes, then in 1% (v/v) Distel disinfecting solution in an ultrasonic bath for 10 minutes; subsequently, cleaning in 70% (v/v) isopropanol in an ultrasonic bath for 10 minutes was performed. The pins and plates were dried using paper tissue.

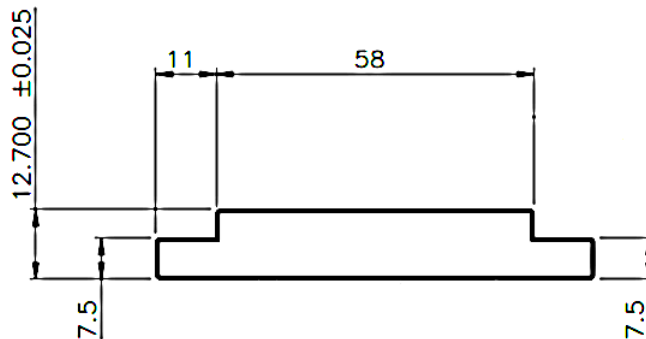
A



B



C

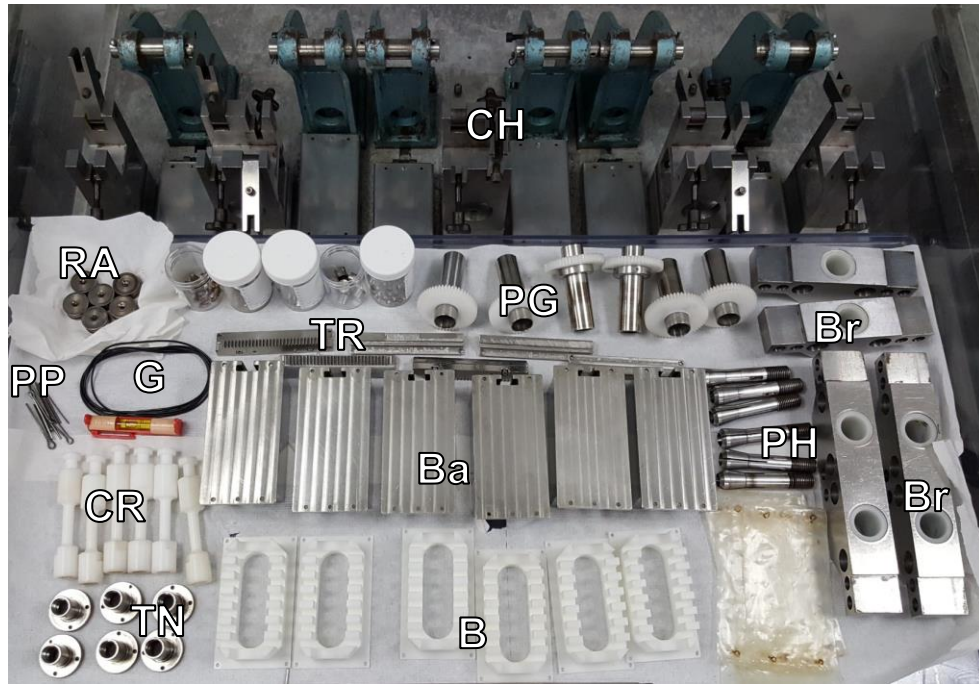


**Figure 2.1. Engineering drawing of pins and plates used.** All length measurements are given in millimetres. (A) Pins had a curved articulating surface and chamfered edges. (B) Plate dimensions from a top-down perspective. (C) Plate dimensions from a lateral view.

CHAM = chamfer,  $\phi$  = diameter, R = radius.

### 2.2.5.3 Overview of wear simulator components and set-up

Components of the pin-on-plate wear simulator are given in **Figure 2.2**. Prior to assembly, the stroke length and load for each station was calibrated.



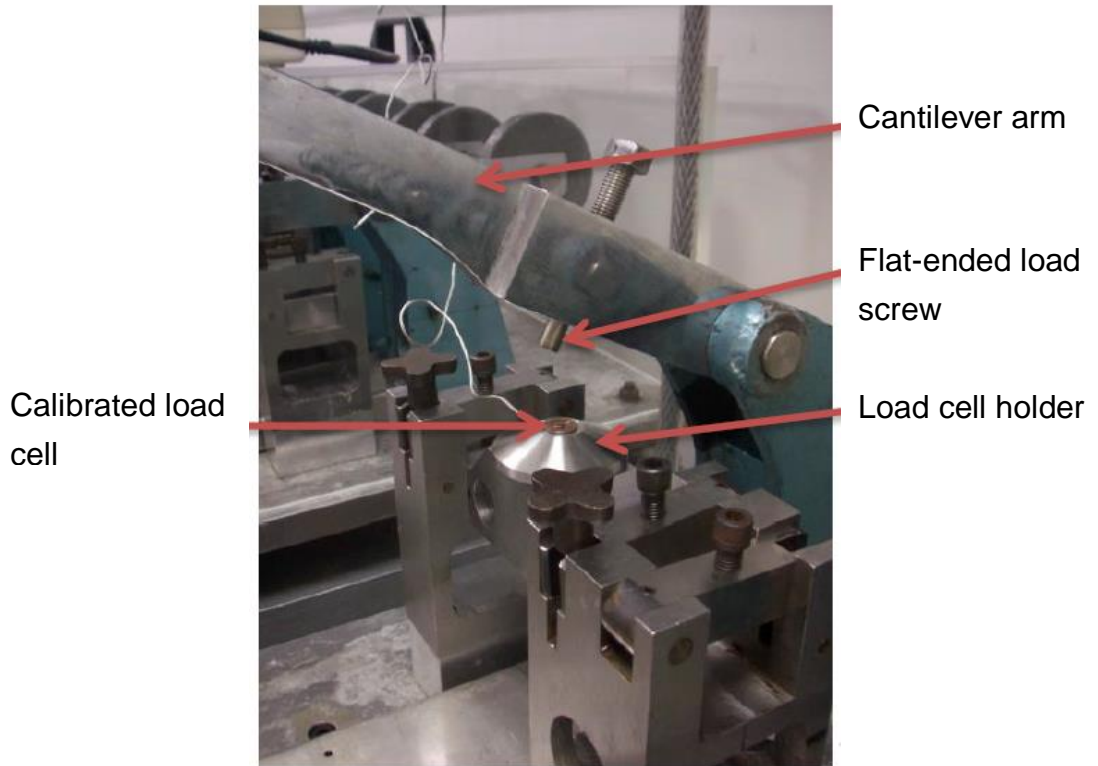
**Figure 2.2 A. The components of a reciprocating six-station pin-on-plate wear simulator excluding the cantilever arms. B = baffles,**

**Ba = baths, Br = bridges, CH = cantilever arm holders, CR = connecting rods, G = gaskets, PG = polymer gear wheels, PH = pin holders, PP = pivot pins, RA = racer assemblies, TR = toothed racks, TN = threaded nut.**

#### **2.2.5.4 Load calibration and stroke length of the pin-on-plate wear simulator**

Stroke length of the simulator was set to 28 mm by a member of the IMBE technical staff. The bridge sections and cantilever arms were inserted into the stations ensuring correct orientation and positioning and secured with pivot pins. For each station the spherical ended load screw was replaced with a flat ended load screw. A calibrated 444 N load cell (in its holder) was placed in the bridge under the loading point (Figure 2.3A). The cantilever arm was gently lowered to contact the load cell, and a spirit level was placed on the cantilever arm to adjust the load screw until the cantilever arm was horizontal (Figure 2.3B). The load cell was set to zero. The appropriate weight for that station was placed on the cantilever arm, and then moved until the load cell indicator reached approximately 80 N. The position of the weight on the cantilever arm was marked for reference with tape. This process was repeated for each station.

A



B

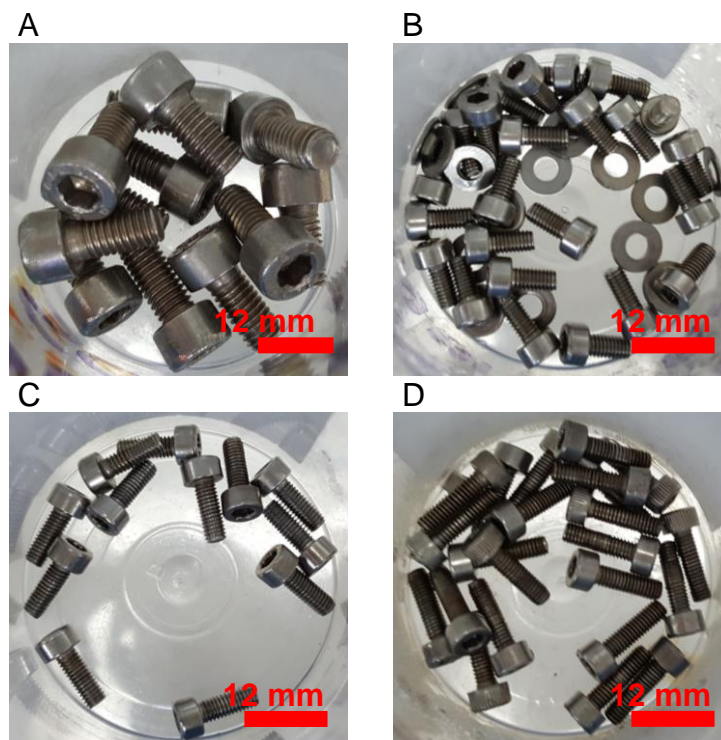


**Figure 2.3. Load calibration of the pin-on-plate machine.** A. Setting up the load cell and flat ended load screw. B. Use of a spirit level to ensure horizontal positioning of the cantilever arm.

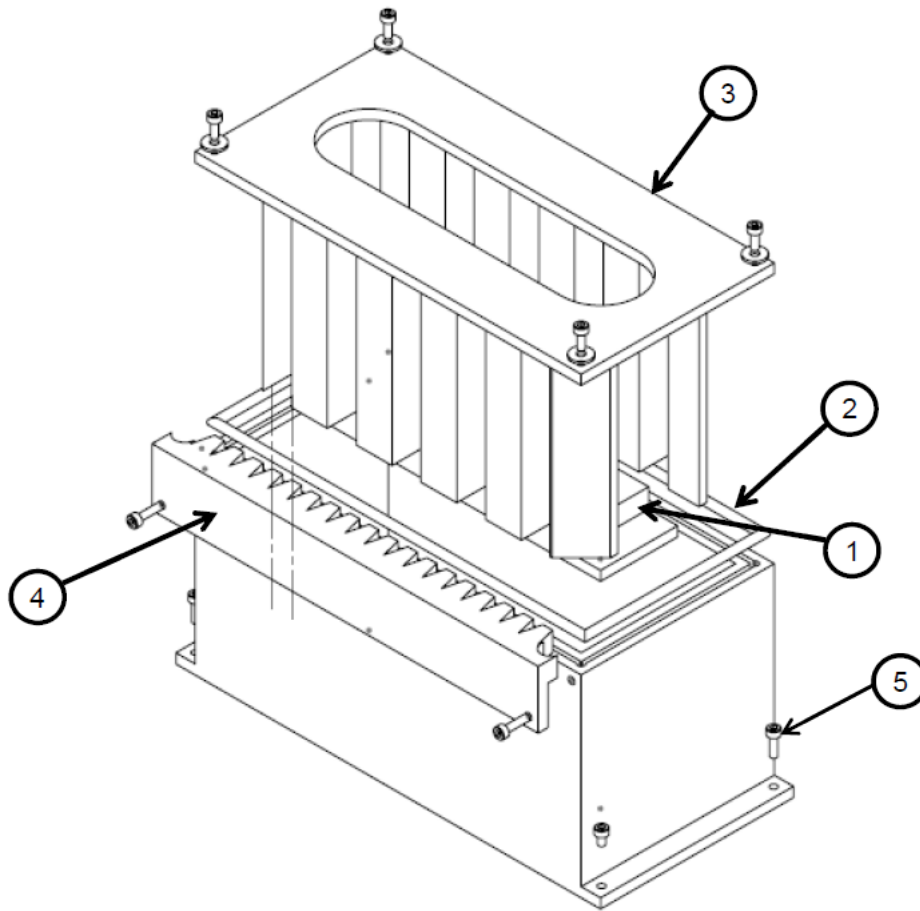
#### 2.2.5.5 Assembly of the linear bearing trays

A variety of screws were required for assembly of the linear bearing trays (Figure 2.4). Metal plates were fixed into baths using M5 cap head screws,

ensuring the screw head did not protrude above the wear surface of the plate. A gasket was placed in the recess at the top of each bath and clamped with the corresponding baffle (Figure 2.5). Each baffle was secured using 4 × 6 mm M3 cap head screws and washers per bath. A toothed rack was secured to the left-hand side of each bath using 2 × 8 mm M3 screws per bath. Each bath was placed onto the linear bearing on top of a plastic linear bearing cover and fastened with 4 × 10 mm M3 screws per bath. The scotch yoke mechanism was connected using a connecting rod. Each bath was filled with 60ml of sterile water for lubrication.



**Figure 2.4. Screws required for assembly of the linear bearing trays.** A. M5 cap head screws to secure the plate into the bath. B-D. M3 cap head screws of 6, 8 and 10 mm respectively, to secure the other parts of the linear bearing trays.

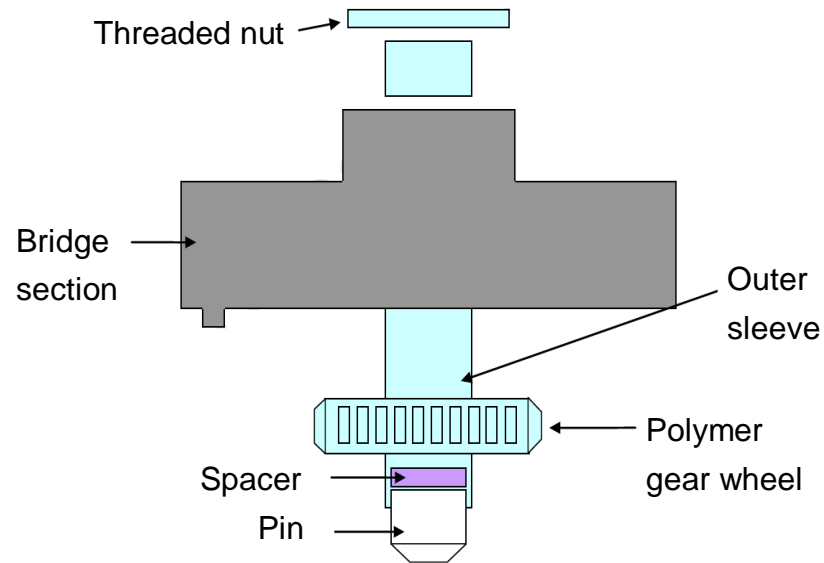


**Figure 2.5. Assembly of the linear bearing trays.** 1. Plate. 2. Gasket. 3. Baffle. 4. Toothed rack. 5. M3 screw.

#### **2.2.5.6 Assembly of the pin holders**

A gear wheel was attached to each pin holder outer sleeve and the grub screw inside tightened. Each collet was placed into an outer sleeve ensuring correct alignment of keys and tapers and a threaded nut was loosely screwed onto the end of each collet/outer sleeve assembly (Figure 2.6). A spacer was placed into each collet, of a size large enough to ensure that there was no contact between the threaded nut and the bridge section, but small enough to ensure that the gear wheel contacted the toothed rack and not the baffle and the pin made contact with the plate, once the test pins were in place. The test pins were placed into each collet and the threaded nut tightened to secure the pin in place. Pins were replaced into the same station after each measurement interval.



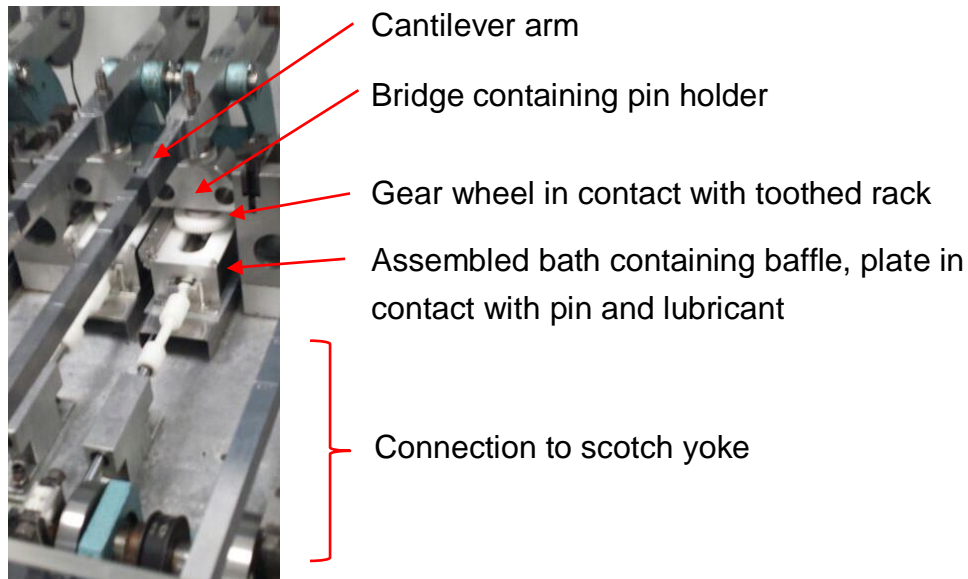


**Figure 2.6. Assembly of the pin holders.** Each pin holder consisted of a pin and spacer placed within a collet and an outer sleeve screwed to a threaded nut; the pin holders were then threaded through the bridge section.

#### **2.2.5.7 Final assembly of the pin-on-plate wear simulator**

Each pin holder assembly was threaded through the required bridge section such that the threaded nut was uppermost. The clamps for the bridge sections were tightened, adjusting the screw in the clamp to apply pressure to the bridge, and ensuring correct positioning of each bridge section. The thrust bearing was assembled for each station by placing a raceway in the recess at the top of each threaded nut, then the bearings were lightly greased with Vaseline and placed in the raceway, and the second raceway was placed on top. A round-ended screw was added to each cantilever arm and adjusted until contacting the depression in the top of the second raceway, using a spirit level such that the cantilever arms were horizontal. The locknuts were tightened. The counter was reset, and the motor was started on a low speed, increasing the speed slowly to the required setting using a calibrated stopwatch. The correctly numbered weights were placed on the cantilever arms at the positions marked during calibration of the load. The components were inspected to ensure correct functioning and adjusted if necessary and the machine was covered with the lid.





**Figure 2.7. Assembled pin-on-plate station.** The plates and lubricant were placed inside baths and each pin was articulated against each plate inside each bath; the plates moved in a linear fashion while the pins rotated. The cantilever arms transferred load onto the pins.

#### **2.2.5.8 Maintenance of the pin-on-plate wear simulator**

During operation the general functioning of the simulator was checked and corrected if necessary. Lubricant levels were also checked and replenished as necessary each day. Fluid level was kept at least 2 mm above the plate wear surface. The simulator was run for at least four days before being dismantled for collection of the debris and cleaning.

#### **2.2.5.9 Dismantling the wear test simulator and collection of wear debris**

The speed controller was lowered until the machine stopped and the motor was switched off, noting the number of cycles. The counter-weights, cantilever arms, ball bearing assemblies, bridge sections (including the assembled pin holders) and connecting rods were removed. Each bath was unscrewed from the linear trays and the baffles carefully unscrewed and removed. A sterile syringe was used to remove the debris from each bath by flushing the liquid in and out of the syringe several times to ensure all of the particles were in suspension, then extracting all of the liquid and storing it in separate, clean, appropriately labelled bottles. A volume of 60ml of sterile water was used to

flush out any adherent debris, and this was also added to the corresponding bottle. The bottles were stored at -20°C. The plates and pins were removed and cleaned as in section 2.2.5.2. All simulator components were disconnected and cleaned in detergent solution until no visible contamination remained, rinsed in distilled water and dried with tissue paper.

## **2.2.6 Particle characterisation**

### **2.2.6.1 Introduction**

This section describes the methods used to characterise commercially available particles, particles produced by pin-on-plate wear, and particles isolated from samples, of any material, which were all characterised in terms of size, morphology, aggregation and chemical composition in the same way. This required creating suspensions of particles, which were collected onto filters and sputter coated prior to analysis using a scanning electron microscope couple with energy dispersive X-ray spectroscopy (EDX). Scanning electron micrographs were then used to measure specific particle parameters using image analysis software.

### **2.2.6.2 Re-suspending particles**

Particles were sonicated in sterile filtered water in an ice-cold water bath for 20 minutes, using a clean pipette tip to disaggregate the particles every 5 minutes by flushing the suspension several times during sonication.

### **2.2.6.3 Sample preparation**

Suspensions of particles were filtered as described in section 2.2.2. The filters were dried for a minimum of 12 h at room temperature and the filters were mounted directly onto aluminium stubs using copper tape or carbon stub adhesives. The edges of each filter were trimmed to fit the stub and carbon paint was applied to the edges of each stub. The stubs were left to dry for 5 minutes at room temperature before being coated with platinum or iridium to a thickness of 4 nm.

### **2.2.6.4 Scanning electron microscopy**

The filter membranes were imaged using a Hitachi SU8230 Cold FEG SEM. A voltage of 2 kV and working distance of 3 mm was used. For each stub, at least three random fields of view were captured at a magnification of 100,000x

for particle characterisation; however, for micron-scale particles, lower magnifications of 100x, 500x and 1,000x were used.

#### **2.2.6.5 Elemental analysis**

Elemental characterisation of the particles was performed by energy dispersive x-ray analysis to confirm the composition of the particles. A voltage of 15 kV and working distance of 15 mm was used during scanning electron microscopy. A spectrum of elements was produced by selecting areas within a field of view using Aztec 3.3 software. Elemental peaks were verified using reference spectra. Elemental maps were also produced using Aztec 3.3 software.

#### **2.2.6.6 ImageJ measurement of particle parameters**

The CFE-SEM micrographs of the SiN particles were subsequently analysed using computer software, ImageJ version 1.49, to measure the Feret's diameter ( $D_{max}$ , defined as the greatest distance between any two points on the particle boundary), aspect ratio (major particle axis / minor particle axis) and circularity (as given by  $4\pi \times \text{area} / [\text{perimeter}^2]$ ). A minimum of 150 particles from each sample (or a minimum of 100 in the case of titanium particles) were characterised in accordance with the standard practice for characterisation of particles (ASTM F1877-05 (2010)).

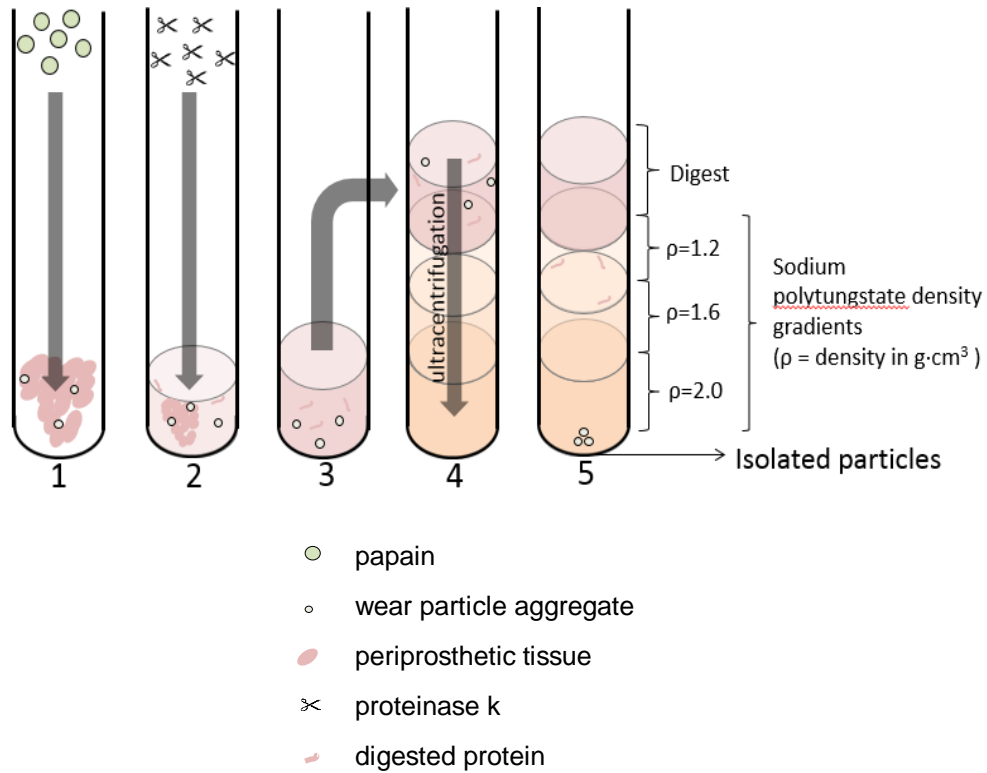
#### **2.2.7 Statistical analysis of particle parameters**

An assessment of normality using a Shapiro-Wilkes test (IBM SPSS statistics version 20) was initially performed to evaluate the distribution of the particles. The particle size distributions, aspect ratio and circularity before and after isolation were compared using Kolmogorov-Smirnov tests (IBM SPSS statistics version 20) to determine whether there were any statistically significant differences ( $p < 0.05$ ). All statistical tests were performed on raw (unbinned) data.

#### **2.2.8 Particle isolation from tissue**

The particle isolation procedure consists of a tissue digestion stage, using papain and proteinase K enzymes, followed by density gradient ultracentrifugation using sodium polytungstate gradients (Figure 2.8); further

rounds of ultracentrifugation were then used to remove residual sodium polytungstate.



**Figure 2.8 Schematic representation of particle isolation method.** Briefly, tissue is digested with papain (1) and then proteinase K (2), producing a homogeneous digest (3), which is layered on top of density gradients and ultracentrifuged (4), leaving pelleted particles and supernatant containing a protein band (5), which was removed by aspiration from the particles.

### 2.2.8.1 Digestion of tissue proteins

Tissue samples were washed three times in sterile filtered water and minced to 1 mm<sup>3</sup> in a sterile culture dish using a scalpel. The samples were sonicated in an ice cooled water bath for 20 min prior to digestion. To each sample, 300 µl of 1 M HEPES buffer (pH 7.5) was added. A volume of 1 ml of 1 M glycine solution was added. A volume of 520 µl of sterile water was then added and each sample was vortexed gently to mix. A volume of 180 µl of buffered papain suspension (26 mg.ml<sup>-1</sup>) was then pipetted into each tube, and the samples were vortexed again. The final volume in each tube was therefore 3 ml and the end concentrations of HEPES, glycine and papain were 0.1 M, 0.33 M and

1.56 mg.ml<sup>-1</sup> respectively. The samples were incubated at 50 °C on an orbital shaker with moderate agitation.

After 6 h, 10% (v/v) SDS was added to each sample to create a final concentration of 0.5% (v/v) and samples were gently vortexed. Proteinase K stock solution (prepared as described in section 2.2.4.4) was added to each sample to create a concentration of 1 mg.ml<sup>-1</sup> and the tubes were vortexed again. Samples were incubated at 50 °C overnight with moderate agitation, after which the proteinase K was replenished by the addition of 150 µl of proteinase K, vortexing before and after the addition of proteinase K. Proteinase K replenishment was repeated after 6 h. Digestion was complete after a total of 48 h.

### **2.2.8.2 Density gradient ultracentrifugation**

A volume of 2 ml of 2 g·cm<sup>-3</sup> sodium polytungstate solution was added to ultracentrifuge tubes. A further 2 ml of 1.6 g·cm<sup>-3</sup> sodium polytungstate solution was carefully layered on top by pipetting dropwise at a 45° angle against the side of the tube. A volume of 2 ml of 1.2 g·cm<sup>-3</sup> sodium polytungstate solution was carefully layered on top of the previous layer using the same technique. The digest sample was resuspended as described in 2.2.6.2. Each sample was layered on top of the density gradients by again pipetting against the side of the tube to prevent disturbing the density gradients. To the empty tubes, 1 ml of sterile water was added and a pipette was used to rinse the sides of each digest tube, before adding the sterile water to each sample tube. This was repeated twice more to ensure all particles were removed. The tubes were placed into SW40 buckets and balanced with the addition of sterile water to just below the rim of each tube. The samples were then ultracentrifuged at 40,000 RPM (average RCF 202,048g) for 4 hours. The supernatant was slowly removed from each sample using serological pipettes, leaving approximately 1 ml at the bottom of each tube.

### **2.2.8.3 Removal of sodium polytungstate**

The particles pelleted at the bottom of the tubes were re-suspended in the remaining supernatant and transferred to clean tubes. To the empty tubes, 1ml of sterile water was added and a pipette was used to flush the water several times during sonication, before adding the sterile water to each

sample tube. This was repeated twice more to ensure all particles were removed and added to the new sample tubes. The tubes were placed into SW40 buckets and filled and balanced with sterile water and ultracentrifuged at 35,000 rpm (average RCF 154,693g). The supernatant was then slowly removed from each sample using serological pipettes, leaving approximately 1ml at the bottom of each tube. A volume of 3ml of sterile water was added to each tube and the particles were re-suspended. The tubes were added to SW40 buckets and filled and balanced with sterile water and ultracentrifuged again (Beckman Optima L-90K ultra-centrifuge and SW-40 rotor) at 35,000 rpm. The supernatant was then slowly removed from each sample using serological pipettes, leaving approximately 1 ml at the bottom of each tube. A volume of 3ml of sterile water was added to each tube and the particles were resuspended. The tubes were placed into SW40 buckets and filled and balanced with sterile water and ultracentrifuged once more at 35,000 rpm. The supernatant was slowly removed from each sample using serological pipettes, leaving approximately 1ml at the bottom of each tube. Isolated particle samples were sealed with parafilm and stored at -20°C. Isolated particles were characterised in the same way as non-isolated particles, as detailed in 2.2.6.

## **2.2.9 General histological techniques**

### **2.2.9.1 Wax embedding of tissues**

Samples were placed in embedding moulds and covered in molten wax. The plastic cassette base was placed on top of the corresponding mould and the moulds were topped up with molten wax. The wax was cooled overnight at room temperature, after which the moulds were removed, and the excess wax trimmed away. Wax blocks were stored at room temperature.

### **2.2.9.2 Dewaxing and hydration of tissue sections**

Slides were placed in slide holders and dewaxed by immersion in a pot of xylene for 10 min, then in a pot of fresh xylene for a further 10 min. Sections were then immersed into successive pots of 100% (v/v) ethanol for 3 min, 2 min and 2 min followed by immersion into a pot of 70% (v/v) ethanol for 2 min. Slides were then placed under running tap water for 3 min to rehydrate the sections.

### **2.2.9.3 Haematoxylin and eosin staining**

Slides were immersed into a pot of premade Mayer's haematoxylin for 1 min, rinsed under running tap water until the water ran clear then immersed in eosin for 3 min. Slides were rinsed under running tap water again.

### **2.2.9.4 Dehydration of sections and mounting of cover slips**

Stained sections were dehydrated by immersion into a pot of 70% (v/v) ethanol for 5 sec, followed by 3 successive immersions into pots of 100% (v/v) ethanol for 1 min, 2 min and 3 min. Sections were then immersed twice in xylene for 10 min each time.

Cover slips were mounted to slides using a few drops of DPX mountant, pushing out any resultant bubbles. Slides were left to dry in a fume hood for a minimum of 12 h before visualizing using microscopy.


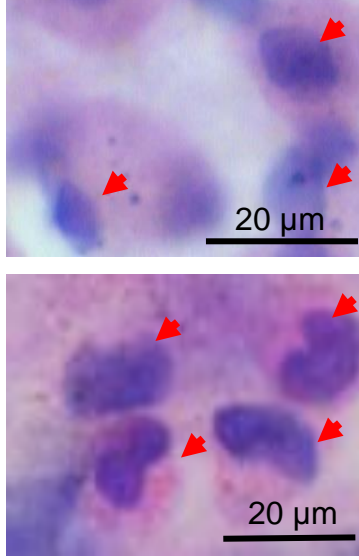
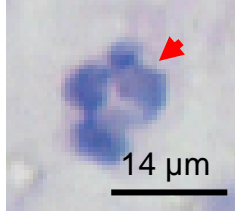
### **2.2.9.5 Light microscopy**

Slides were viewed under normal Köhler illumination using a Zeiss upright bright field microscope with oil immersion for higher magnification with a 63x objective lens. Images were captured using Zen software.

### **2.2.9.6 Identifying immune cells in histological sections**

Immune cells were identified within images captured from histological sections at 400x magnification by morphological features as described in Table 2.1.

**Table 2.1. Cell identification within H&E stained tissue sections.**

Cell type	Morphological description	Example of scoring (cell nuclei are labelled with red arrow heads)*
Lymphocyte**	Single round nucleus, very little cytoplasm	
Macrophage / monocyte***	Single round or kidney shaped nucleus, abundant cytoplasm; presence of engulfed material within cell	
Polymorphonuclear cells	Multi-lobed nucleus	

\*Images show appearance of H&E stained cells and are not scaled with respect to each other.

\*\*Any lymphocyte-like cells with an eccentric nucleus, which appeared to contain heterochromatin in a 'clockface' configuration were listed separately as plasma cells.

\*\*\*Any large, macrophage-like cells containing multiple nuclei surrounding particle(s) were listed separately as giant cells.



## **Chapter 3**

### **Development of a novel method to isolate wear particles from tissue**

#### **3.1 Background**

Isolation and subsequent analysis of wear particles from periprosthetic tissue has enabled an understanding of the wear, biological impact, and failure mechanisms of implants. It is therefore increasingly considered as an important tool for preclinical testing of new joint replacement materials (FDA, 2016). Previous methods have been used to isolate metal or ceramic particles from tissue by digesting the tissue with strong acids or bases or various enzymes, usually followed by rounds of centrifugation; however, these methods were not validated for sensitivity and sometimes yielded poor results due to protein contamination of the particles (Schmiedberg *et al.*, 1994; Margevicius *et al.*, 1994; Lerouge *et al.*, 1998; Doorn *et al.*, 1998; Schmiedberg *et al.*, 2006; Milosev and Remskar, 2008). Furthermore, the methods have not been developed with consideration for materials with dissolution properties, such as silicon nitride.

Lal *et al.* (2016) produced a method to isolate nanoscale SiN and CoCr particles from serum. The method omits the use of any corrosive chemicals, high temperature stages or low speed centrifugation steps which could lead to SiN dissolution or particle loss. Due to these desirable characteristics, this method could theoretically be adapted for application to tissue samples, and thus improve upon methods currently used to isolate particles from tissue.

#### **3.2 Aims**

The research outlined in this chapter aimed to develop and test a novel particle isolation method for application to tissues from an *in vivo* rat study, and later rabbit study, as part of the LifeLong Joints project. Due to the low particle volumes associated with the rat study, the method needed to be sensitive enough to isolate particle volumes of  $<0.018 \text{ mm}^3$ . In addition, due to low sample sizes of only three per test group available from each study, the

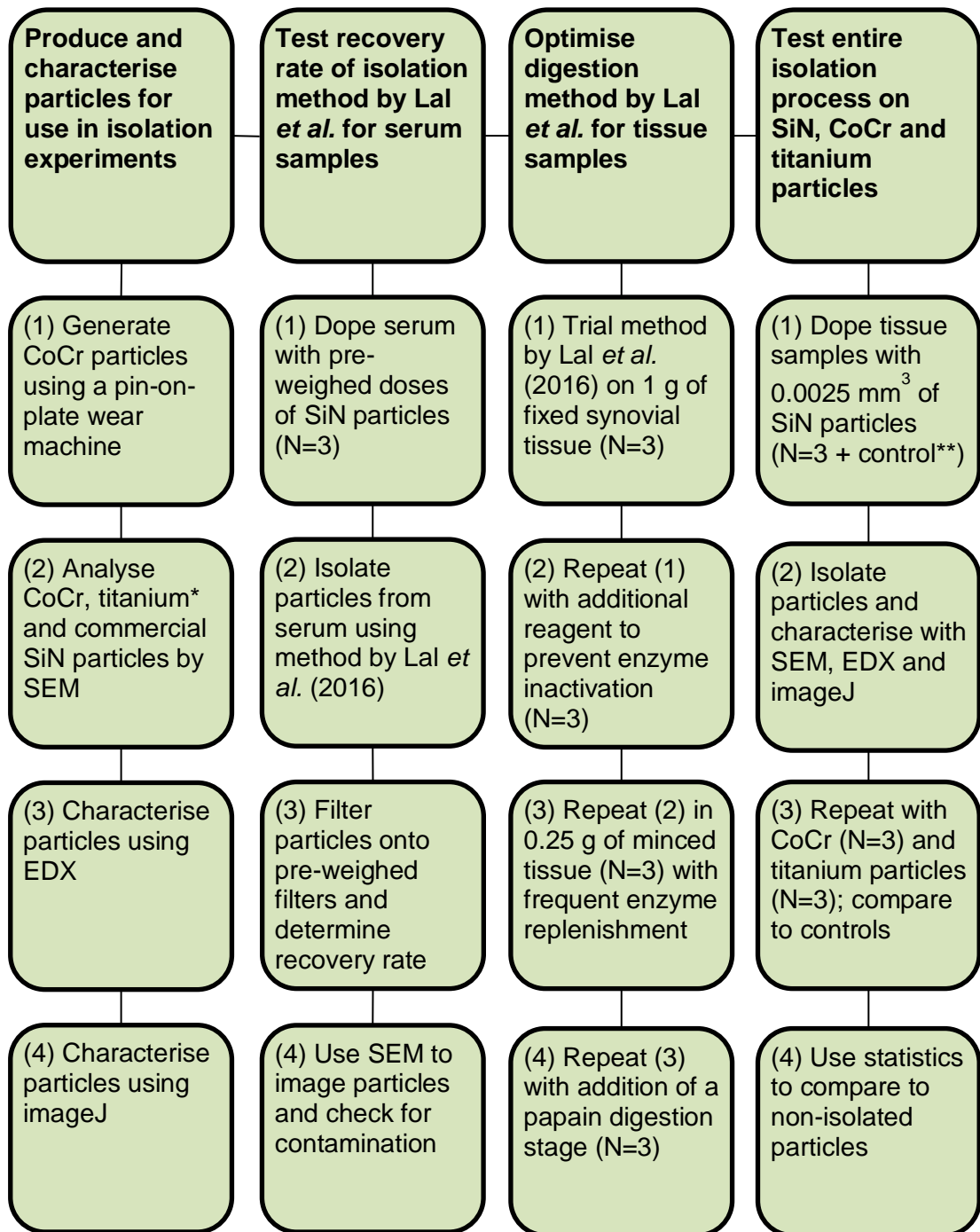
variation in results caused by the isolation method itself needed to be minimised.

Specific research objectives included:

- Testing the recovery rate of the isolation method developed by Lal *et al.* (2016) to establish whether the method is suitable for recovery of low particle volumes
- Adapting the digestion stage of the protocol to enable digestion of fixed tissue proteins
- Testing the method for the recovery of low volumes of SiN particles from tissue
- Testing the method in additional materials (CoCr and titanium) and ensuring that particle geometries are unchanged by the protocol

### **3.3 Overview of experiments**

An overview of the experiments included in this chapter is given in Figure 3.1. To validate the recovery rate of the method produced by Lal *et al.* (2016), serum samples were doped with particles and particle recovery was tested gravimetrically. Following testing of the serum isolation method, an alternative enzymatic digestion protocol was required to digest tissue. The digestion method was optimised prior to use as part of an isolation protocol. To validate sensitivity and efficacy of the isolation protocol, tissue samples were doped with low volumes of 0.0025 mm<sup>3</sup> of SiN particles, or 0.025 mm<sup>3</sup> of CoCr particles or titanium particles, and the particles were subjected to the isolation process and characterised. The results of particle characterisation before and after isolation were compared statistically to test whether the isolation method affected particle size or morphologies. The isolation method was then tested in rat cadavers injected with a volume of 0.018 mm<sup>3</sup> of SiN particles, in order to simulate realistic sample collection and preparation procedures prior to application of the method to a rat study, as part of the LifeLong Joints project.



**Figure 3.1. Overview of experiments detailed in this chapter.**

\*Titanium particles were generated by pin-on-plate by another researcher, Dr. Helen Lee.

\*\*Control refers to a tissue sample which was not doped with particles, but which was also subjected to the particle isolation process.

## **3.4 Materials and Methods**

Materials used throughout this chapter are given in Appendix A.

### **3.3.1 Creating a silicon nitride particle suspension**

Plastic bijous and commercial silicon nitride powder was acclimated in a measurements laboratory for a minimum of 48 h before at least three readings were recorded for each bijou using a Mettler XP250 microbalance. A weight of  $1 \pm 0.01$  mg of silicon nitride powder was added to pre-weighed bijous. The weighed particles were then used to create particle suspensions by diluting the particles in sterile water to  $1 \text{ mg.ml}^{-1}$  and mixing the suspension as described in 2.2.6.2.

### **3.4.1 Creating cobalt chromium and titanium particle suspensions**

Cobalt chromium particles were generated by pin-on-plate and collected as described in 2.2.3. Titanium particles were generated in the same way from medical grade titanium (Ti-6Al-4V) pins and plates by another researcher, Dr Helen Lee. Cleaned glass universals were pre-weighed by acclimation in the measurements laboratory for a minimum of 48 h before at least three readings were recorded for each universal using a Mettler XP205 microbalance. A volume of approximately 2.5 ml of particle suspension collected from each wear simulator station was added to separate pre-weighed universals and the universals were dried and sterilised in an oven ( $200^{\circ}\text{C}$ , 3 h). The universals were re-acclimated and re-weighed to calculate the mass of particles in each universal. Control universals, which were not filled with wear debris, were also weighed and the difference in weight deducted from the other readings. Particle suspensions were created as detailed in section 2.2.6.2.

### **3.4.2 Isolating particles from serum to quantify particle recovery**

#### **3.4.2.1 Preparation of particle doped serum samples to test particle recovery**

Commercial silicon nitride powder ( $\text{Si}_3\text{N}_4$ ; Sigma-Aldrich, spherical,  $<50 \text{ nm}$ ) and 30 ml SW32 centrifuge tubes were acclimated in the weighing room for seven days. Approximately  $1 \text{ mm}^3$  of silicon nitride powder was weighed into each of three separate ultracentrifuge tubes, noting the exact weight of silicon

nitride by taking three readings for each tube using a Mettler XP250 microbalance. A volume of 14 ml of 25% (v/v) foetal bovine serum (FBS) was added to each of these tubes, in addition to a fourth tube containing no particles as a control. The samples were sealed using parafilm and left on an orbital shaker at 37°C for a minimum of 12 h to allow proteins to adhere to particles. Serum samples were then made up to 30 ml by the addition of 25% (v/v) foetal bovine serum in sterile water and mixed as described in 2.2.6.2. Samples were added to SW32 ultracentrifuge tubes and were balanced by addition of 25% (v/v) FBS.

#### **3.4.2.2 Particle isolation from doped serum samples**

The samples were subjected to the isolation procedure as described by Lal *et al.* (2016). Briefly, samples were ultracentrifuged at 32,000 RPM (average RCF of 125,755 g) for three hours at 20°C in order to reduce the sample volume. After ultracentrifugation, 27 ml of the supernatant was carefully removed from each tube using a pipette. Samples were mixed again as described in section 2.2.6.2.

All volumes used in the digestion protocol were calculated based on a final volume of 5 ml. To each sample, 500 µl of 1 M HEPES buffer containing 30 mM CaCl<sub>2</sub> (made as described in section 2.2.4.1) was added to make a final concentration of 0.1 M HEPES and 3 mM CaCl<sub>2</sub>. A volume of 250 µl of 10% (v/v) SDS was added to each tube to make a final concentration of 0.5% SDS (v/v). Tubes were vortexed to mix. To each tube 125 µl of proteinase K stock was added to make a final concentration of 0.5 mg·ml<sup>-1</sup>. Sterile filtered water was added to each tube to make a final volume of 5 ml. The tubes were sealed and placed in an orbital shaker inside an incubator. The shaking speed was set to 320 rpm and the samples were incubated for 18 h at 50°C. After 18 h the digest was mixed as described in section 2.2.6.2. The proteinase K enzyme was replenished by addition of 150 µl of proteinase K stock to each tube; the tubes were vortexed, and digestion was continued at 50°C for a further 22 h. At the end of digestion, the samples were vortexed and sonicated as in section 2.2.6.2.

Density gradient ultracentrifugation and subsequent removal of SPT was carried out as detailed in sections 2.2.8.2 and 2.2.8.3 of the general methods section.

#### **3.4.2.3 Verifying particle isolation from serum by SEM analysis**

To ensure that recovery rates were not over-estimated due to protein adherence to particles, particles were re-suspended as described in 2.2.6.2. Aliquots of 10 µl were extracted and filtered and prepared for SEM analysis as described in section 2.2.6.3. The samples were imaged using SEM as described in section 2.2.6.4.

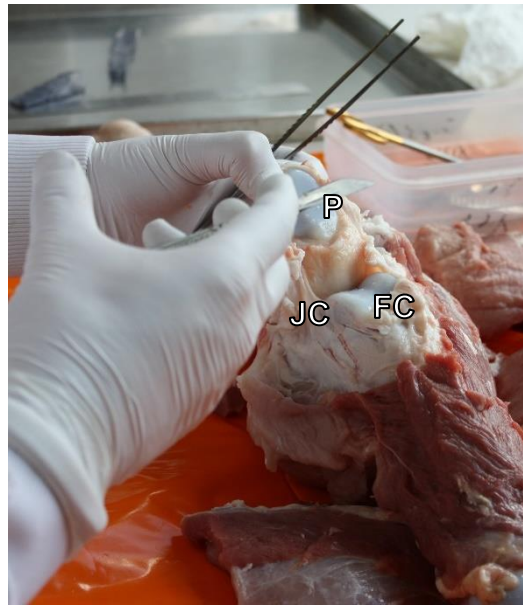
#### **3.4.2.4 Weighing particles for recovery rates**

Polycarbonate filters (25 mm) were pre-filtered with 70% (v/v) ethanol to remove any loose material and acclimated for 24 h in the measurements lab prior to weighing three times with a XP26 microbalance. The resuspended particle samples, in addition to the particle-free control sample, were filtered onto the pre-weighed filters using Millipore micro filter units as described in section 2.2.2, and the filters were re-acclimated in the measurements lab for 24 h. The filters were weighed to calculate the weight of particles deposited onto the filters. Control filters, which were not filtered with wear debris, were also weighed and the difference in weight deducted from the other readings.

#### **3.4.3 Preparation of tissue samples for tissue digestion and particle isolation experiments**

Porcine or ovine legs were supplied by local abattoirs within 24 h of slaughter. Pigs were aged approximately 6 months, sheep 8-12 months. Joints were dissected immediately using a scalpel as shown in Figure 3.2A. Synovial tissue including the intimal lining and surrounding ligament of each stifle joint was harvested (Figure 3.2B) and added to plastic bijous and covered with at least 20 times the volume of neutral buffered formalin. After 24 h fixation, the formalin was discarded, and the bijous were filled with 70% (v/v) ethanol. Tissues were stored at room temperature.

A



B



**Figure 3.2. Dissection and harvesting of synovial tissue from a porcine cadaver.** A. Surrounding muscle tissue was removed to expose the joint capsule and the patella was removed. B. Synovial tissue was then extracted from the patella.

JC = joint capsule, P = patella, ST = synovial tissue, FC = femoral condyle

### **3.4.4 Developing a method for effective digestion of tissue**

#### **3.4.4.1 Tissue digestion using a published method for serum proteins**

A wet weight of 1 g of fixed synovial tissue per sample (N=3) was added to a plastic universal and washed in sterile filtered water three times by filling each universal and immediately discarding each wash to remove residual fixative and ethanol. Tissue samples were digested as described by Lal *et al.* (2016), detailed in paragraph 2 of section 3.4.2.2.

#### **3.4.4.2 Tissue digestion method with added glycine**

The experiment described in section 3.4.4.1 was repeated; however, prior to making the digestion volume up to 5 ml, a 1 M stock of glycine was added to make an end concentration of 0.33 M. This digestion method was repeated using a 0.25 g sample of fixed tissue that was washed three times in sterile filtered water and minced to 1 mm<sup>3</sup> using a scalpel before addition of the digestion reagents.

#### **3.4.4.3 Tissue digestion method using more frequent enzyme replenishment**

Tissue samples were washed three times in sterile filtered water and minced to 1 mm<sup>3</sup> in a sterile culture dish using a scalpel. The samples were sonicated in an ice cooled water bath for 20 min prior to digestion. To each sample, 300 µl of 1 M HEPES buffer with CaCl<sub>2</sub> (pH 7.5), 1 ml of 1 M glycine solution and 150 µl of 10% (v/v) SDS, and 235 µl of proteinase K (20 mg.ml<sup>-1</sup> in sterile water) was added to each sample and the sample was vortexed gently to mix. Sterile water was added to a final volume of 3 ml and the end concentrations of HEPES, CaCl<sub>2</sub>, glycine, SDS and proteinase K were 0.1 M, 3 mM, 0.33 M, 0.5% (v/v) and 1.56 mg.ml<sup>-1</sup> respectively. The samples were incubated at 50 °C on an orbital shaker with moderate agitation.

After 6 h, the proteinase K was replenished by the addition of a volume of 150 µl proteinase K stock (prepared as described in section 2.2.4.4) and samples were gently vortexed. Samples were incubated at 50 °C overnight with moderate agitation, after which the proteinase K was replenished by an additional 150 µl of proteinase K, vortexing before and after the addition of proteinase K. Proteinase K replenishment was repeated after 6 h. Digestion was stopped after a total of 48 h.



#### **3.4.4.4 Final tissue digestion method using papain**

Fixed synovial tissue samples of 0.25 g were digested using a final protocol employing papain digestion followed by proteinase K digestion exactly as described in section 2.2.8.1.

#### **3.4.5 Testing the final particle isolation technique**

##### **3.4.5.1 Doping tissue samples with silicon nitride particles**

Fixed ovine synovial tissue was washed three times in sterile filtered water by filling the tube, vortexing, and immediately discarding each wash to remove traces of formalin, ethanol, and exterior contaminants. The tissue was then minced to 1 mm<sup>3</sup> pieces in a sterile culture dish, using sterile dissection equipment. Mincing was carried out in a class II cabinet. A wet weight of 0.25 g of minced tissue was added to round-bottomed plastic test tubes immediately and 1 ml of sterile water was added to each sample to prevent the tissue from drying out. A 1 mg.ml<sup>-1</sup> particle suspension (containing 1 ±0.01 mg of particles, as weighed using a high-resolution microbalance) was used to dope 0.25 g tissue samples with a particle volume of 0.0025 mm<sup>3</sup> particles, equivalent to 0.01 mm<sup>3</sup> of particles per gram. A volume of particle suspension was added to the desired concentration to each of three replica samples, and was not added to a fourth, particle-free control sample. The samples were placed on an orbital shaker at 37°C for 12 h to allow proteins to adhere to particles.

##### **3.4.5.2 Testing sensitivity and efficacy of the method for isolation of SiN particles**

The SiN-doped tissue samples were digested as described in 2.2.8.1 and subjected to density gradient ultracentrifugation and washing as described in 2.2.8.2 and 2.2.8.3. Samples were characterised and analysed statistically as described in 2.2.7. For the statistical analysis, the results of the repeats were pooled and compared to a control set of data from particles that were not subjected to the particle isolation process. A total of 450 isolated particles were characterised (150 isolated particles per repeat). The control sample consisted of 150 characterised particles.

### **3.4.5.3 Testing the method for isolation of cobalt chromium and titanium wear debris**

Tissue samples were doped with cobalt chromium or titanium particles at  $0.1 \text{ mm}^3.\text{g}^{-1}$  of tissue as described in section 3.4.5.1. The samples were then digested as described in section 2.2.8.1 and subjected to density gradient ultracentrifugation and washing as described in sections 2.2.8.2 and 2.2.8.3. Samples were characterised and analysed statistically as described in section 2.2.7. For the statistical analysis, the results of the three repeats were pooled and compared to the control set of data from particles that were not subjected to the particle isolation process. For cobalt chromium particles, 150 isolated particles per repeat were characterised (total 450 isolated particles). For titanium particles, 50 isolated particles per repeat were characterised (total 150 isolated particles). In both cases, control samples consisted of 150 characterised particles.

## **3.5 Results**

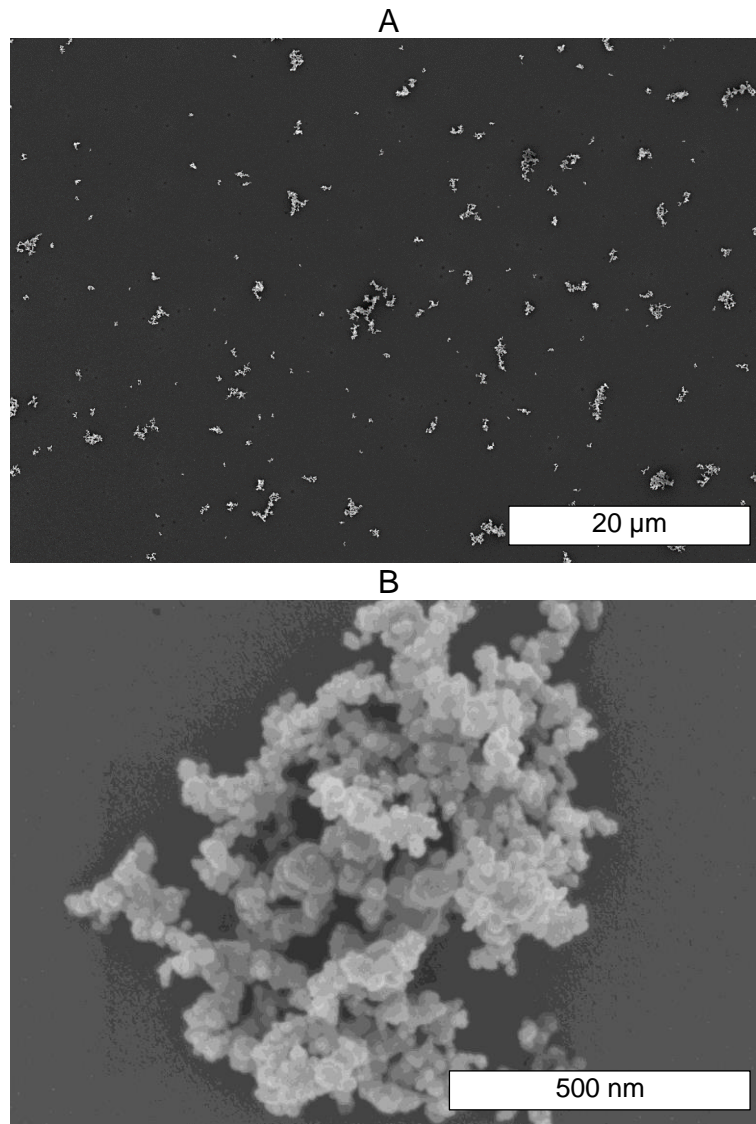
### **3.5.1 Characterisation of particles prior to isolation experiments**

#### **3.5.1.1 Characterisation of commercial silicon nitride particles**

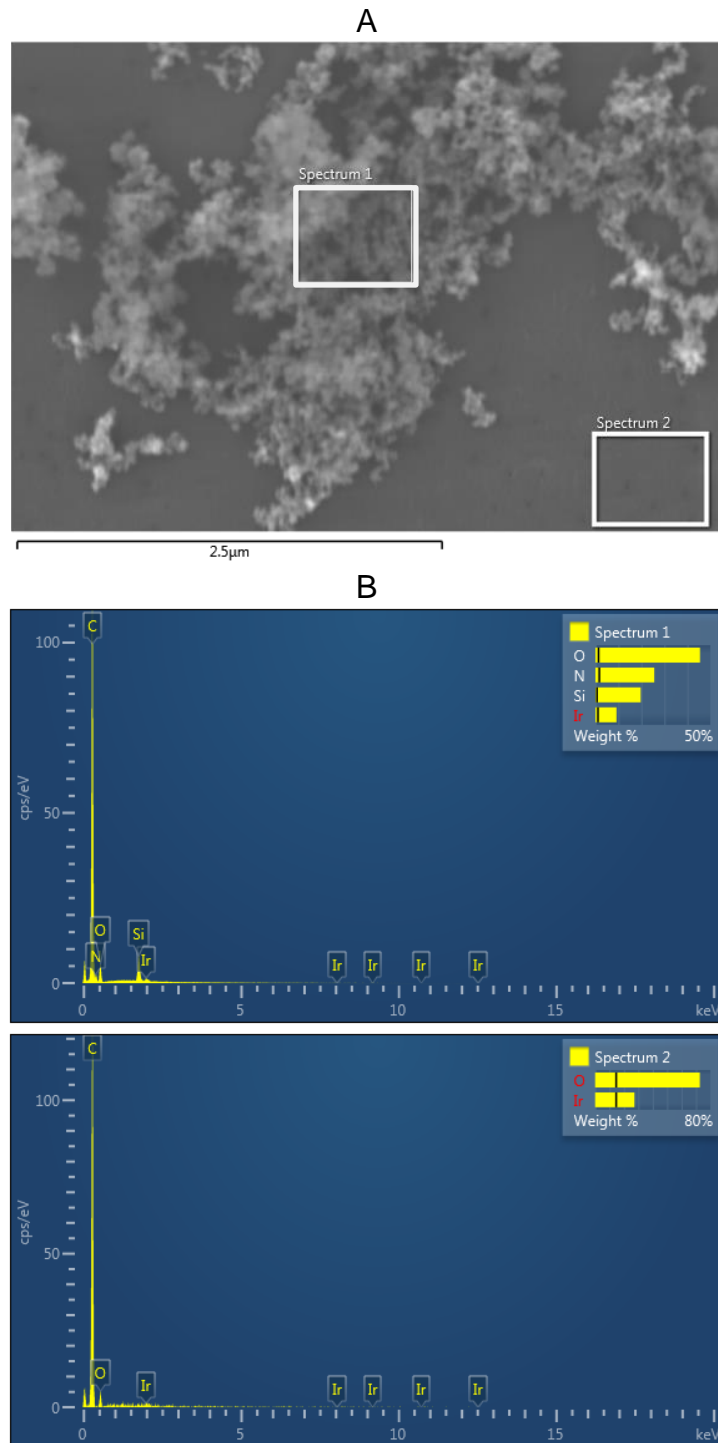
Commercial SiN particles (<50 nm) were filtered for observation by scanning electron microscopy (Figure 3.3), prior to isolation experiments. The SiN particles were observed as aggregates of approximately 0.2 - 2  $\mu\text{m}$  in size distributed across the filter membrane. The particles were relatively spherical, smooth in appearance and were nanoscale.

Elemental analysis was carried out on the particles as shown by EDX spectra (Figure 3.4A and B). Silicon, nitrogen, oxygen, carbon and iridium were detected. Silicon and nitrogen signals were detected exclusively in areas containing particles. Oxygen, iridium and carbon signals were shown to have originated from the polycarbonate filter membrane and sputter coating (Figure 3.4B). This was further demonstrated by elemental maps (Figure 3.5).

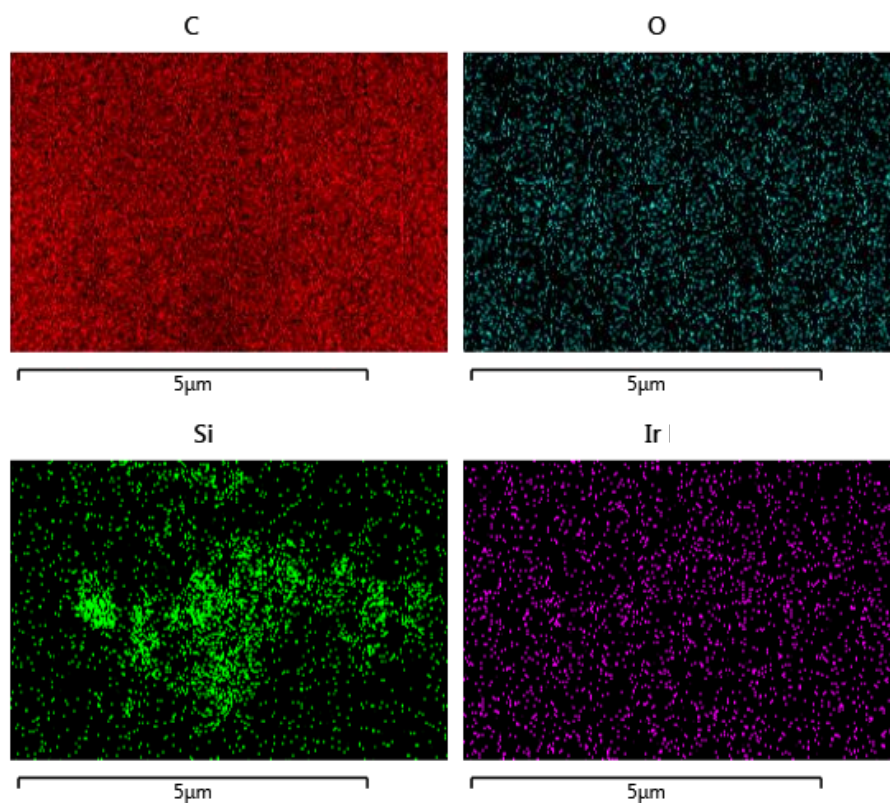
Particle characterisation showed that particles had a modal size range of 20-30 nm (Figure 3.6A), with an average particle size of 28 nm (Figure 3.6B). The low aspect ratio and high circularity indicated that particles were relatively spherical.



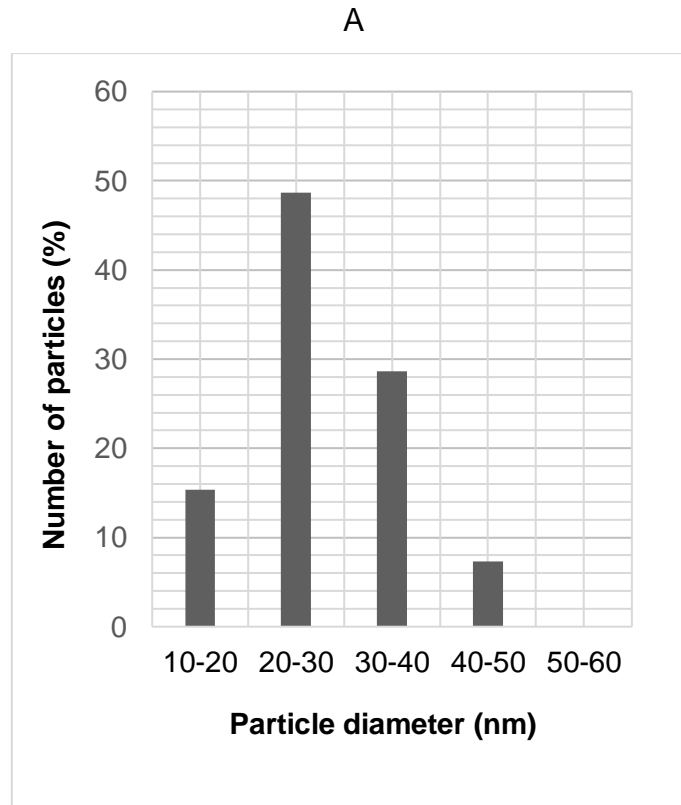
**Figure 3.3. Scanning electron micrograph of commercial SiN particles at (A) a magnification of 2,000x and (B) a higher magnification of 100,000x. The particles were sonicated in filtered water and filtered directly onto polycarbonate filter membranes.**



**Figure 3.4. Elemental analysis of commercial silicon nitride particles.** A. Scanning electron micrograph showing the area from the which the spectra were produced and the resultant spectra. B. Elemental maps. Samples were sputter coated with iridium and filtered onto polycarbonate filter membranes.



**Figure 3.5. Elemental mapping of commercial SiN particles, with the chemical symbol of the element above.** A volume of 0.01 mm<sup>3</sup> of particles was resuspended and filtered on 0.015 µm polycarbonate filter membranes; samples were iridium coated. Elements identified were carbon, silicon, oxygen, and iridium.



B

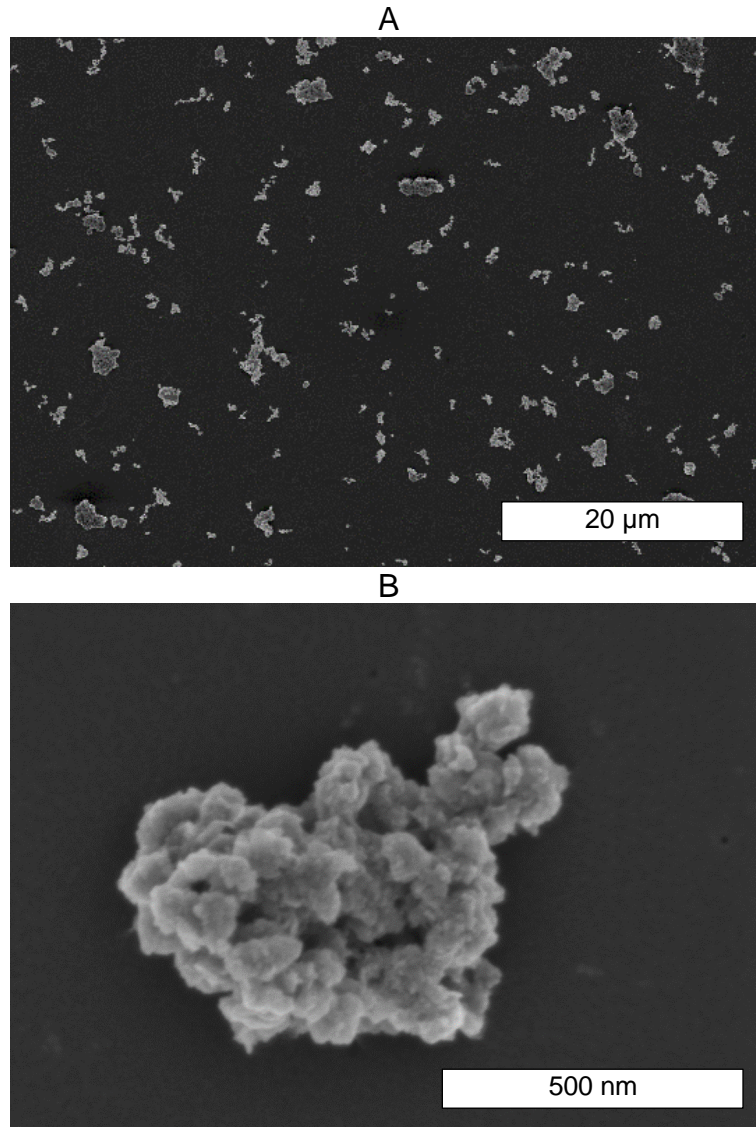
Parameter	Mean $\pm$ SD
Feret's diameter (nm)	28 $\pm$ 7
Aspect ratio	1.2 $\pm$ 0.1
Circularity	0.9 $\pm$ 0.0

**Figure 3.6. (A) The size distribution of commercial silicon nitride particles and (B) the average particle parameters.** The results are based on a sample of 150 particles which were characterised using scanning electron micrographs and imageJ software.

### **3.5.1.2 Characterisation of cobalt chromium and titanium particles for doping tissues**

Cobalt chromium particles generated by pin-on-plate were filtered for observation by scanning electron microscopy (Figure 3.7), prior to isolation experiments. CoCr particles were observed as large, dense aggregates of about 10  $\mu\text{m}$  in size, as well as small aggregates of approximately 0.2 - 2  $\mu\text{m}$

in size distributed across the filter membrane in a similar manner to the commercial SiN particles. The particles were also relatively spherical and were nanoscale; particles were too small to identify whether the particle surface was rough or smooth. Particles from three different stations were imaged; all three samples were similar.



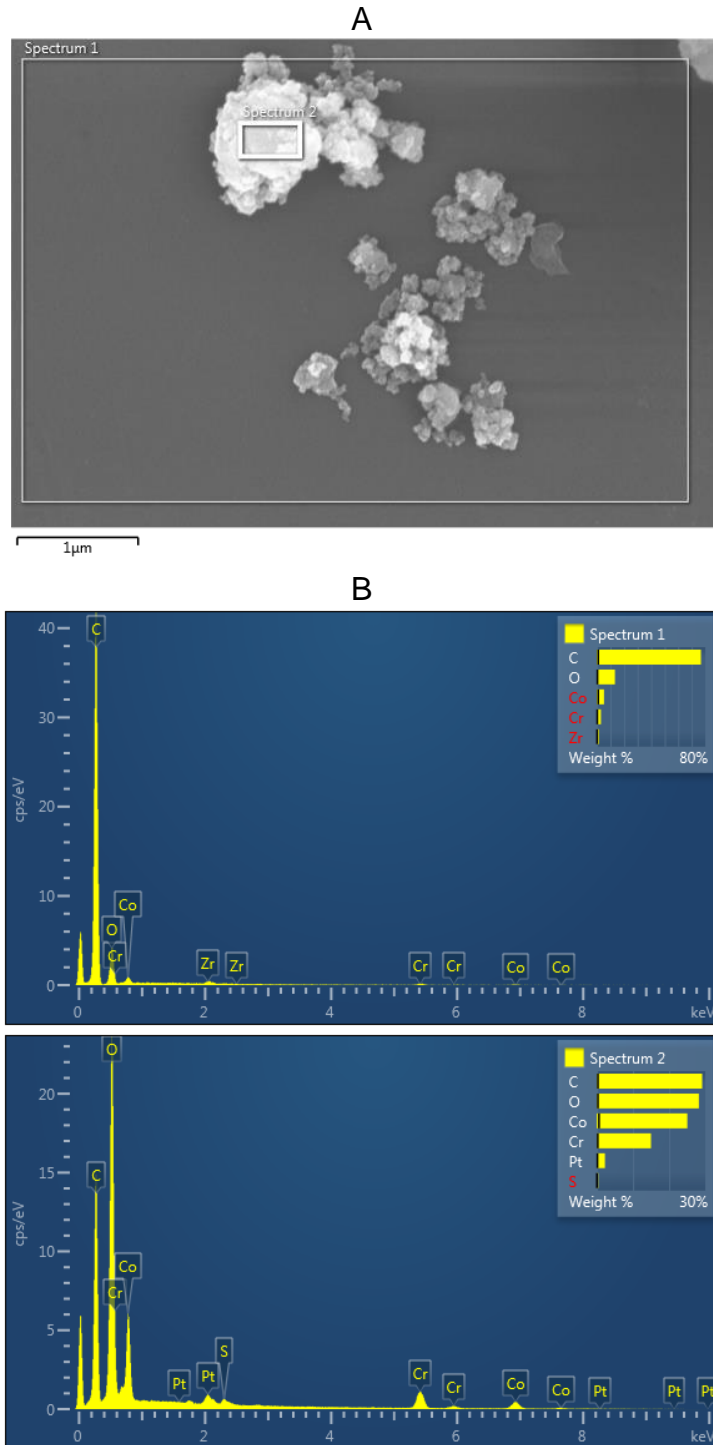
**Figure 3.7. Scanning electron micrograph of CoCr particles generated by pin-on-plate at (A) a magnification of 2,000x and (B) a higher magnification of 100,000x.** The particles were sonicated in filtered water and filtered directly onto polycarbonate filter membranes.

Elemental analysis was carried out on the particles as shown by EDX spectra (Figure 3.8). Chromium, cobalt, oxygen, carbon and platinum were detected. Oxygen, platinum and carbon signals were found to have originated from the

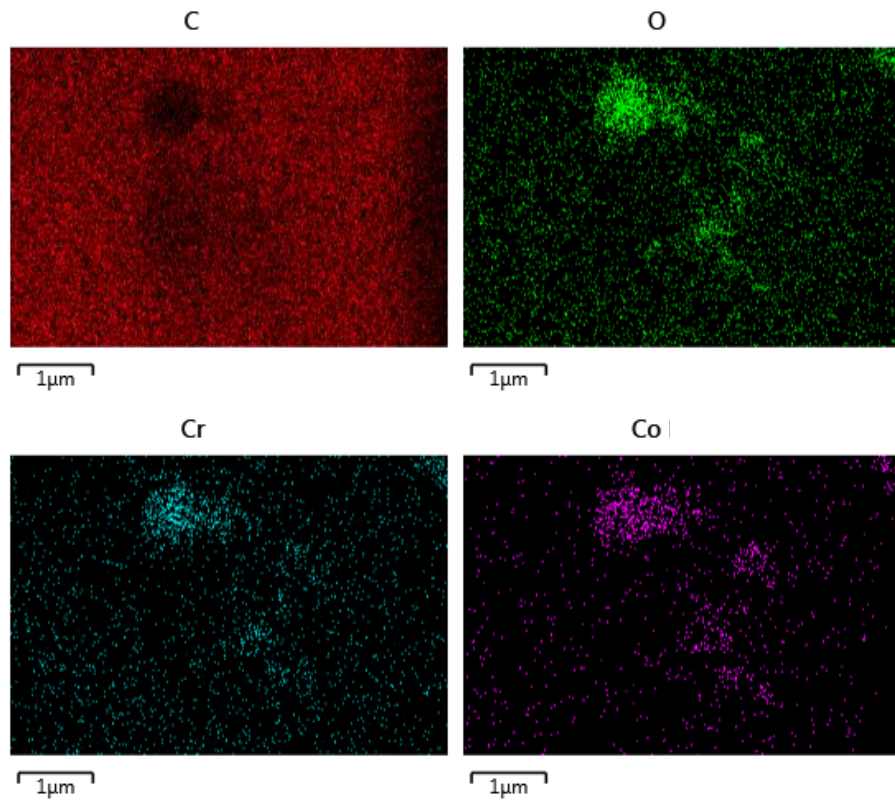
polycarbonate filter membrane and sputter coating while cobalt and chromium signals were detected exclusively in areas containing particles (Figure 3.9). However, oxygen was also detected within the particles, suggesting that particles were oxidized during filtration. This was not very apparent in the silicon nitride particles.

Particle characterisation showed that most particles were 10-30 nm (Figure 3.10A), with an average particle size of 23 nm (Figure 3.10B). Particles were therefore slightly smaller than the commercial SiN particles. The low aspect ratio and high circularity indicated that particles are relatively spherical, though less spherical than the commercial SiN particles.



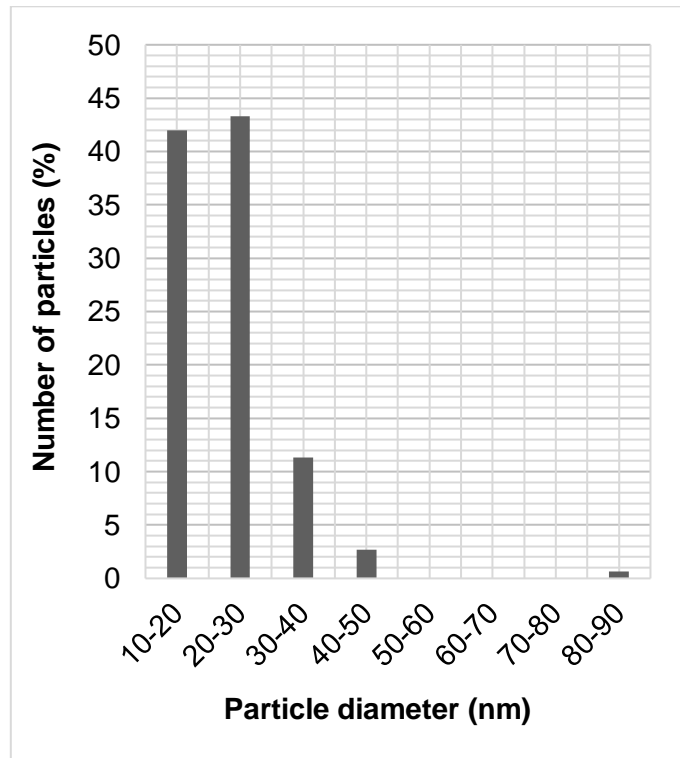


**Figure 3.8. Elemental analysis of CoCr particles generated by pin-on-plate.** A. Scanning electron micrograph showing the area from the which the spectra and elemental maps were produced. B. The corresponding spectra. Particles were sputter coated with a mix of platinum and palladium and filtered onto polycarbonate filter membranes.



**Figure 3.9. Elemental mapping of CoCr particles generated by pin-on-plate, with the chemical symbol of the element above.** Particles were resuspended and filtered on 0.015 μm polycarbonate filter membranes; samples were iridium coated. Elements identified were carbon, oxygen, chromium, and cobalt.

A



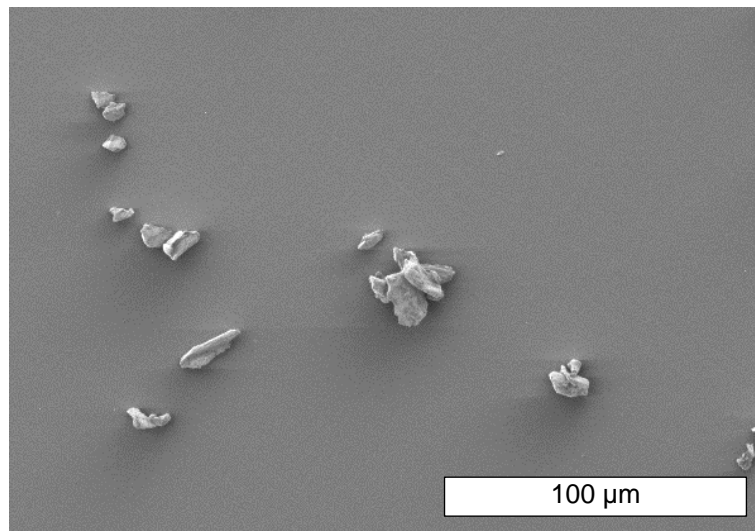
B

Parameter	Mean $\pm$ SD
Feret's diameter (nm)	23 $\pm$ 8
Aspect ratio	1.2 $\pm$ 0.2
Circularity	0.9 $\pm$ 0.0

**Figure 3.10. (A) Size distribution of CoCr particles and (B) average particle parameters.** The results are based on a sample of 150 particles which were characterised using scanning electron micrographs and imageJ software.

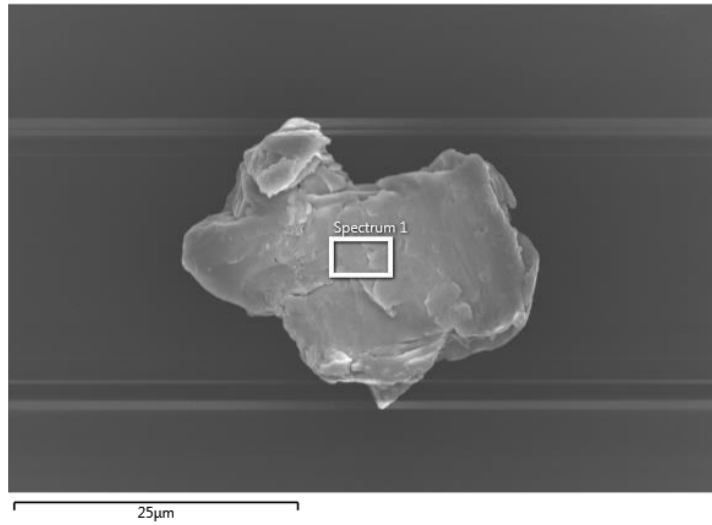
Titanium particles were generated by another researcher from medical grade Ti-6Al-4V alloy. The particles were filtered for observation by scanning electron microscopy (Figure 3.11), prior to isolation experiments. Unlike the SiN and CoCr particles, titanium particles showed no aggregation characteristics. The particles were micron scale and were less spherical in shape; the surface of the particles was rough. Particles were verified by

elemental analysis (Figure 3.12), which identified the presence of titanium, aluminium, vanadium, carbon, oxygen and iridium, the latter three of which were present in the polycarbonate filter and sputter coating. However, as with the cobalt chromium particles, some degree of particle oxidation occurred, as indicated by the elemental maps (Figure 3.13), which show oxygen signals produced by the particles. Characterisation of particles showed that the modal particle size was 10-15  $\mu\text{m}$  (Figure 3.14A), while average particle size was 15  $\mu\text{m}$  (Figure 3.14B). The aspect ratio was much higher than for SiN or CoCr particles, and the circularity was lower, indicating that particles were less spherical.

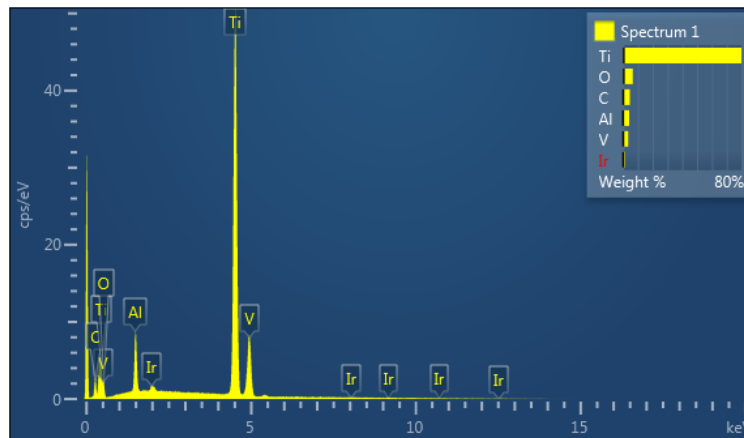


**Figure 3.11. Scanning electron micrograph of titanium particles generated by pin-on-plate, at a magnification of 500x.** The particles were sonicated in filtered water and filtered directly onto polycarbonate filter membranes.

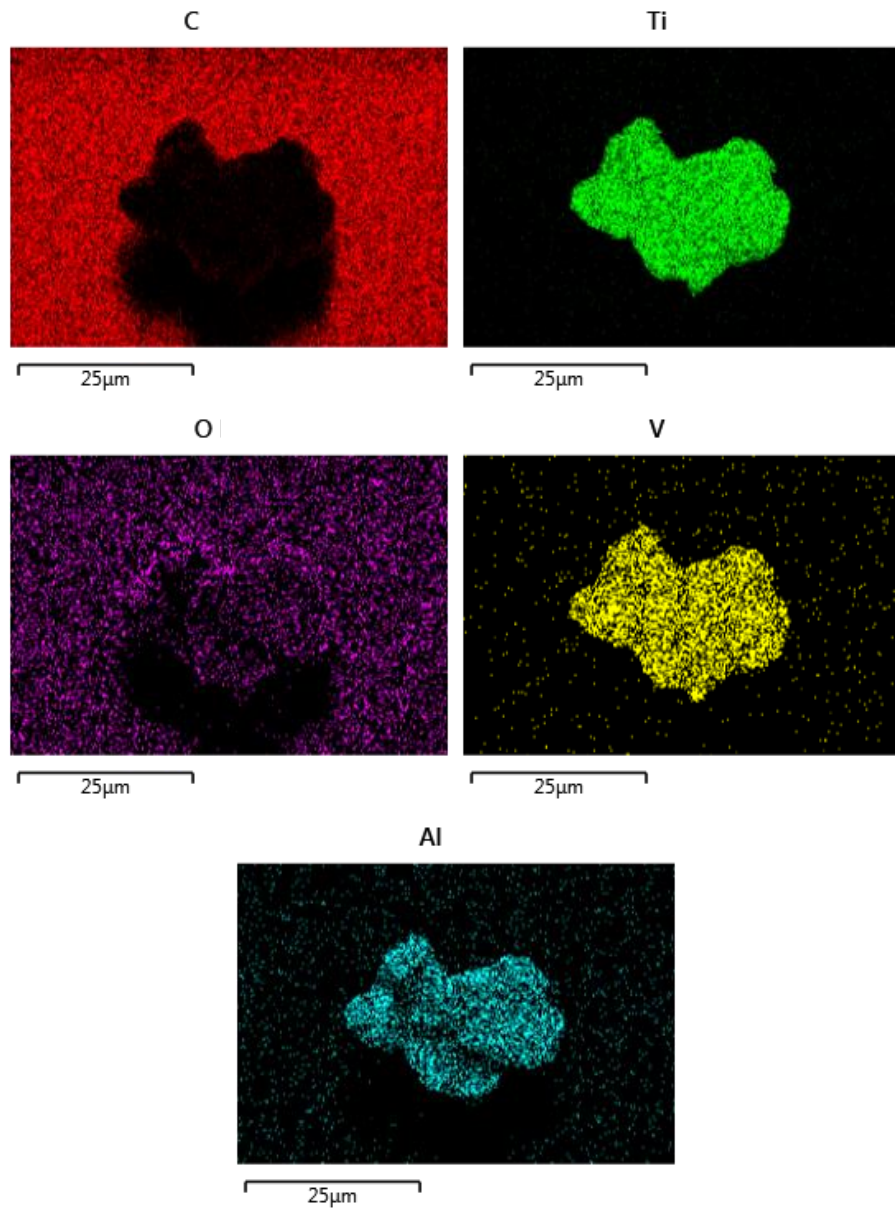
A



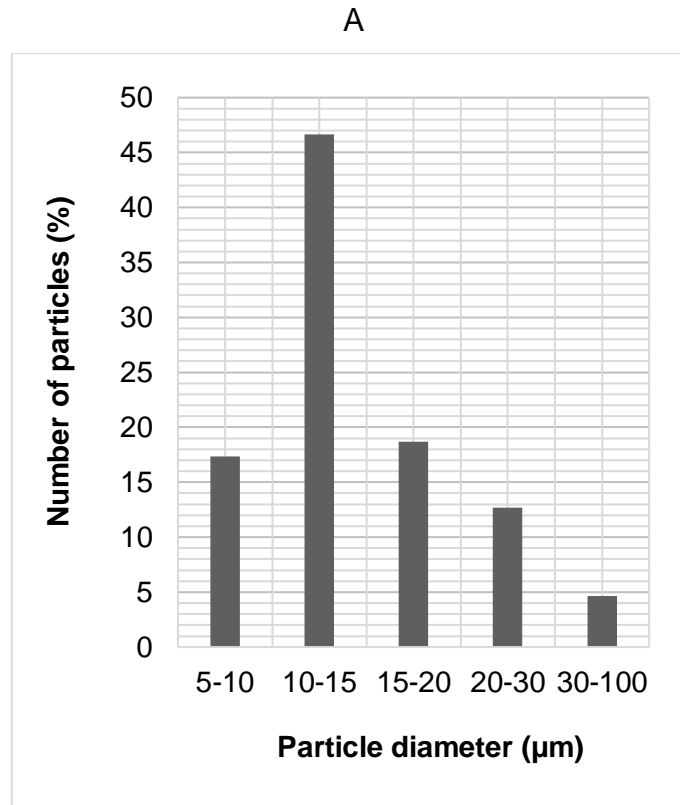
B



**Figure 3.12. Elemental analysis of titanium particles generated by pin-on-plate.** A. Scanning electron micrograph showing the area from the which the spectrum and was produced and (B) the corresponding spectrum. C. Particles were filtered onto polycarbonate filter membranes and sputter coated with iridium.



**Figure 3.13. Elemental mapping of titanium particles generated by pin-on-plate.** Particles were filtered onto polycarbonate filter membranes and sputter coated with iridium.



B

Parameter	Mean ± SD
Feret's diameter (µm)	15 ± 8
Aspect ratio	1.5 ± 0.5
Circularity	0.8 ± 0.1

**Figure 3.14. (A) Size distributions and (B) mean particle characteristics for titanium particles.** The results are based on a sample of 150 particles which were characterised using scanning electron micrographs and imageJ software.

### 3.5.2 Isolating particles from serum to quantify particle recovery

To test the particle isolation technique described by Lal *et al.* (2016), three replica commercial SiN-doped serum samples and a control serum sample, which consisted of particle-free serum, were subjected to the particle isolation procedure. The replica samples were doped with a relatively high particle dose ( $1 \text{ mm}^3$ , or 3.44 mg) to ensure that the volume was accurately detectable by a microbalance.

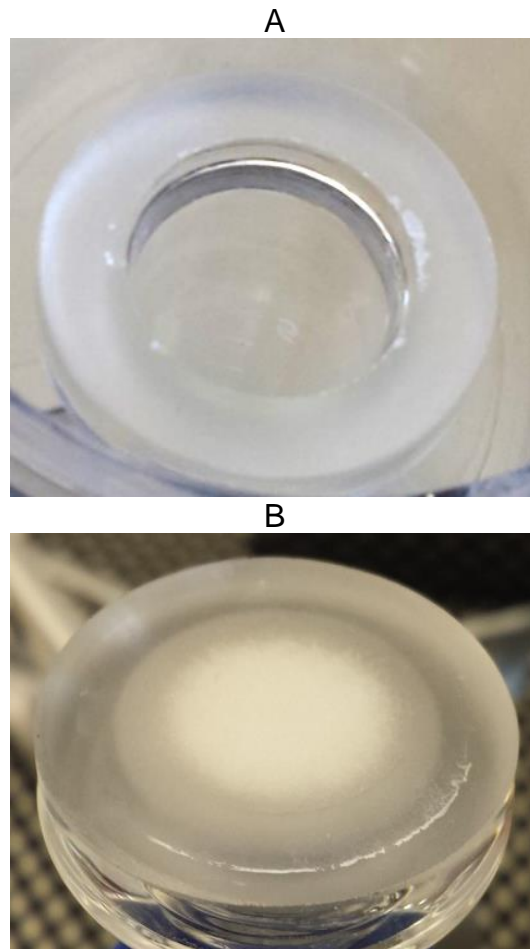
Following density gradient ultracentrifugation, a solid white pellet of SiN particles could be observed at the bottom of each replica sample, while no such pellet was observed in the control sample. SiN particles were also visually apparent following filtration of each sample (Figure 3.15) but were absent from the control sample. It must be noted that while the membrane was drying after filtration, static caused a small proportion of the filtered particles to move off of the membrane and into the surrounding mini culture dish. This likely had an impact on recovery weights.



**Figure 3.15. Filter membrane with isolated silicon nitride particles deposited on the surface, which have formed a cracked layer.** The initial doping volume was high ( $1 \text{ mm}^3$ ).

The control was filtered onto a pre-weighed filter and the difference in weight of the filter was used to calculate a weight of contaminants per sample, which was negligible ( $>0.01 \text{ mg}$ ). This weight was deducted from the other weight readings of the three filtered particle samples, giving recovery rates of 97.8%, 80.5% and 90.4%. The average particle recovery rate from three samples was therefore 89.6%. It was observed that particle loss occurred due to adherence of silicon nitride particles to the filtration equipment (Figure 3.16). The amount of adherence of particles to equipment was inconsistent, likely causing some of the variance in recovery rates.

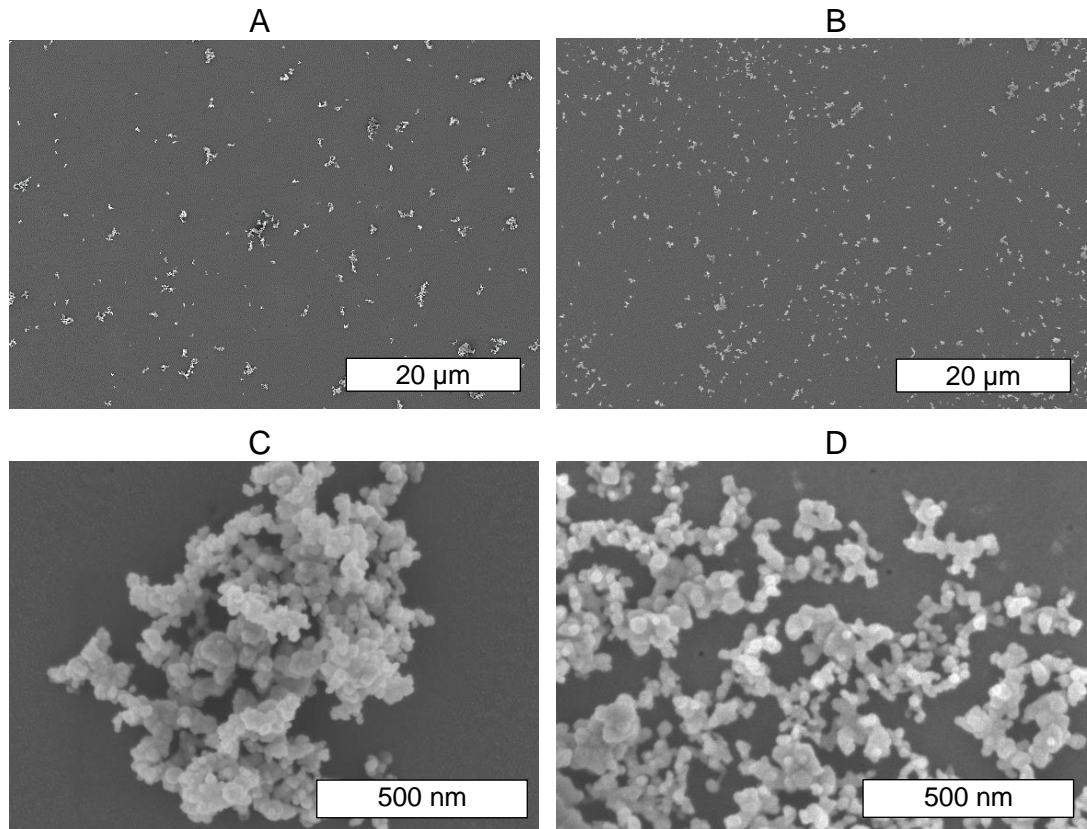




**Figure 3.16. Adherence of silicon nitride particles to filtration equipment.** (A) Bottom of filter column and (B) filter support. These areas of filtration equipment came into direct contact with the particle suspension and filter membrane.

### **3.3.2 Imaging of silicon nitride particles isolated from serum**

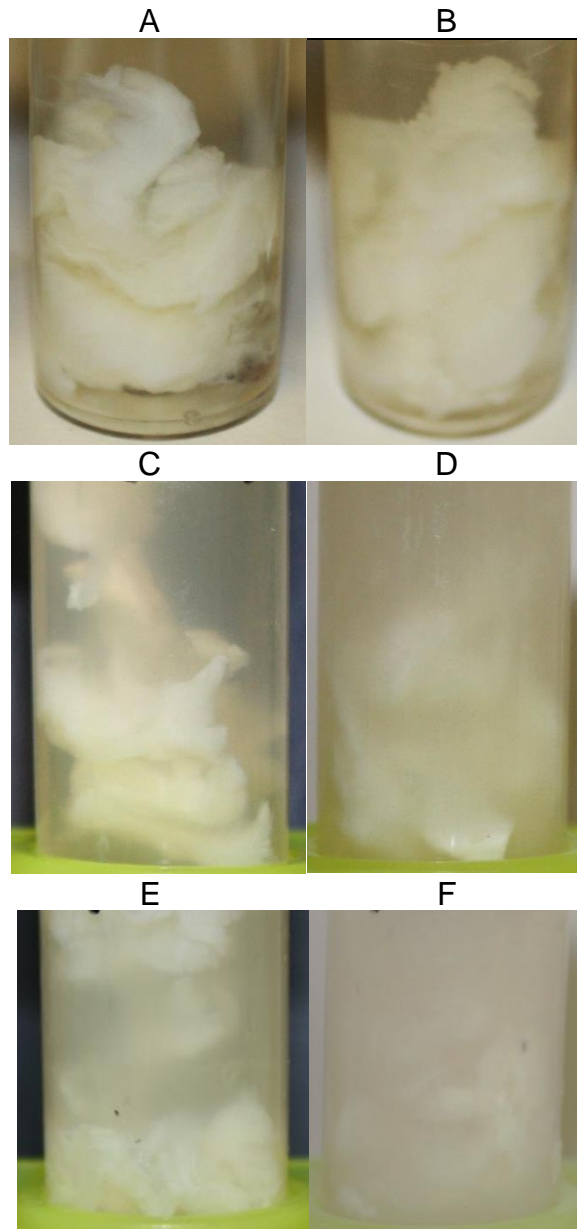
SEM analysis of isolated particles revealed no observable contamination and total removal of protein (Figure 3.17); the particles were similar to the imaged non-isolated particles described in 3.5.1 and there were also no marked differences between replicas. Inspection of the control filter by SEM revealed very few contaminants and no observable protein film.



**Figure 3.17. Commercial SiN particles at (A and B) a magnification of 2,000x and (C and D) a high magnification of 100,000x, before (A and C) and after (B and D) isolation. Particles were sonicated in filtered water and filtered onto polycarbonate filter membranes.**

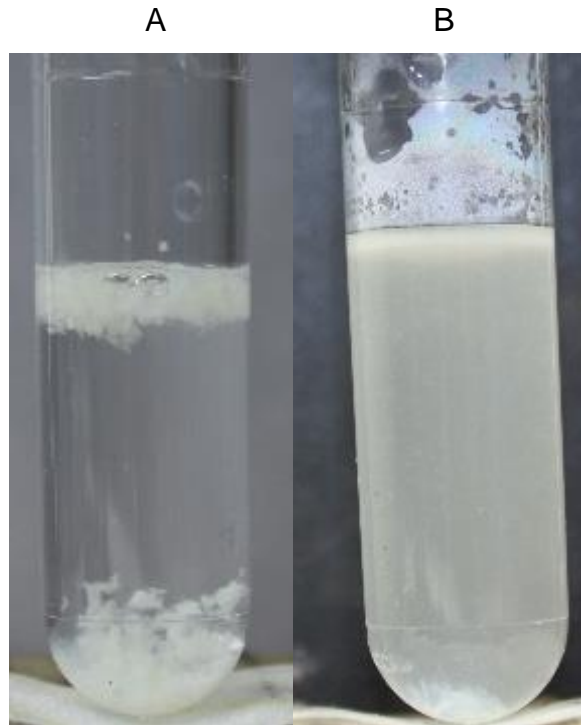
### **3.3.3 Developing a method for effective digestion of tissue and initial particle isolation experiments from tissue**

The first tissue digestion experiment was carried out similarly to the method for digestion of serum proteins given in Lal et al. (2016). However, this resulted in little to no observable change to any of the three replica tissue samples (Figure 3.18A and B). The experiment was therefore repeated with the addition of glycine, to bind to and inactivate any residual formalin (Takeichi *et al.*, 2009). This resulted in a clearly observable change to the tissue, as the surrounding solution became cloudy in appearance and the tissue volume appeared to be slightly reduced (Figure 3.18C and D). Improving efficiency by mincing tissue and reducing tissue amount was still insufficient to ensure complete digestion (Figure 3.18E and 5F).



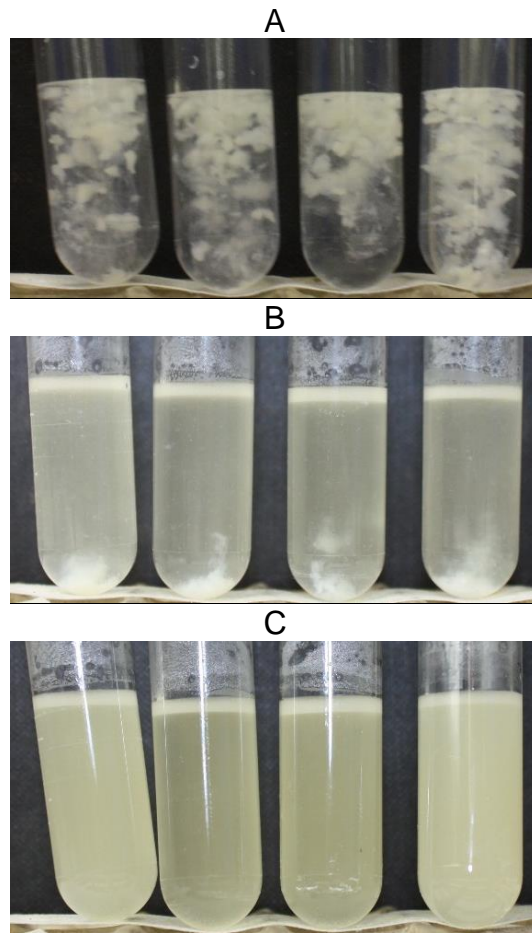
**Figure 3.18. Appearance of tissues during initial digestion experiments,** using a published method for the digestion of serum proteins with proteinase k. Tissue sample after 24 h digestion (left) and after at 48 h (right), without the use of glycine (A and B) and with the use of glycine (C-F). Tissue was either digested whole (A-D) or minced prior to digestion (E and F).

The method was further adapted to improve tissue digestion. This included more frequent proteinase K replenishment, which resulted in almost complete tissue digestion (Figure 3.19).



**Figure 3.19. (A) Tissue sample prior to digestion, and (B) after 48 h of a digestion protocol involving frequent proteinase K replenishment in the presence of glycine.** The tissue was 0.25 g of fixed porcine stifle joint synovial tissue, minced to 1 mm<sup>3</sup>.

Finally, the method was adapted to include a digestion stage with papain prior to addition of proteinase K. The method included the use of glycine and frequent replenishment of enzyme. This method was tested on 0.25 g samples of fixed porcine stifle joint synovial tissue, minced to 1 mm<sup>3</sup>. Tissue digestion appeared successful by 48 h (Figure 3.20).

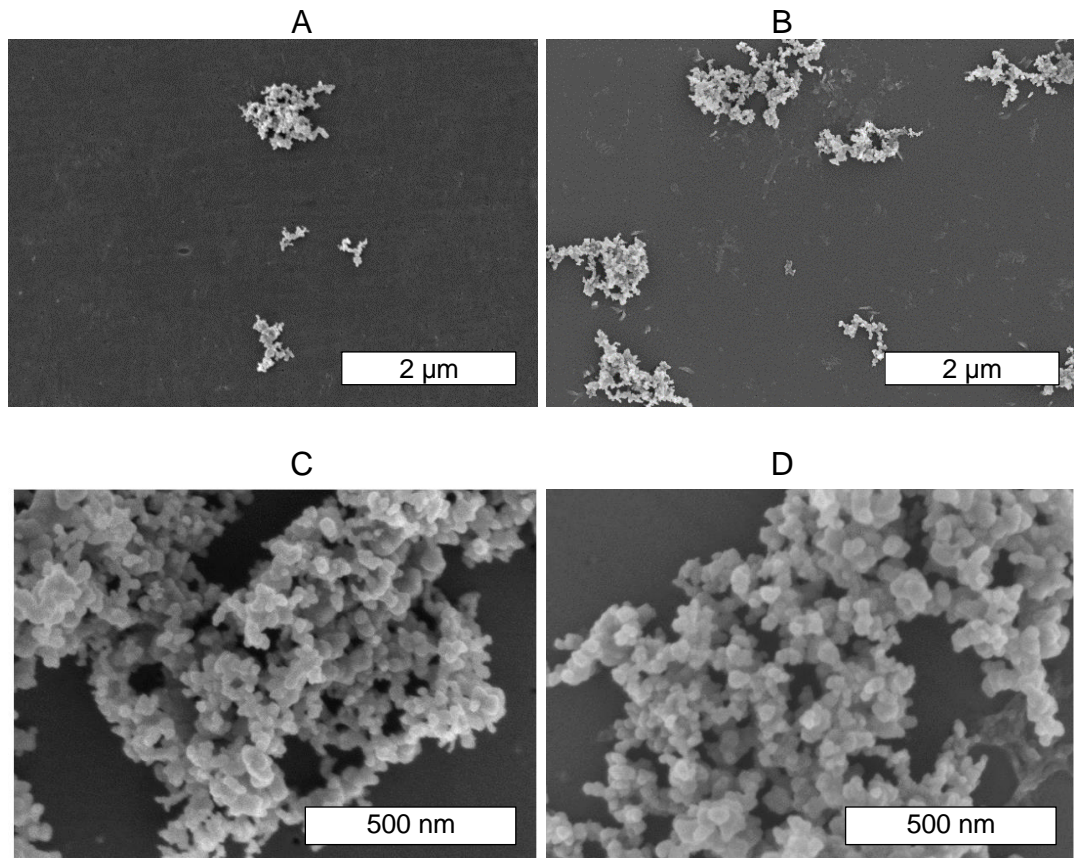


**Figure 3.20. Appearance of tissue samples during a tissue digestion experiment using papain and proteinase K. (A) Before digestion, (B) after 24 h and (C) at 48 h.**

### **3.5.3 Testing the final isolation protocol**

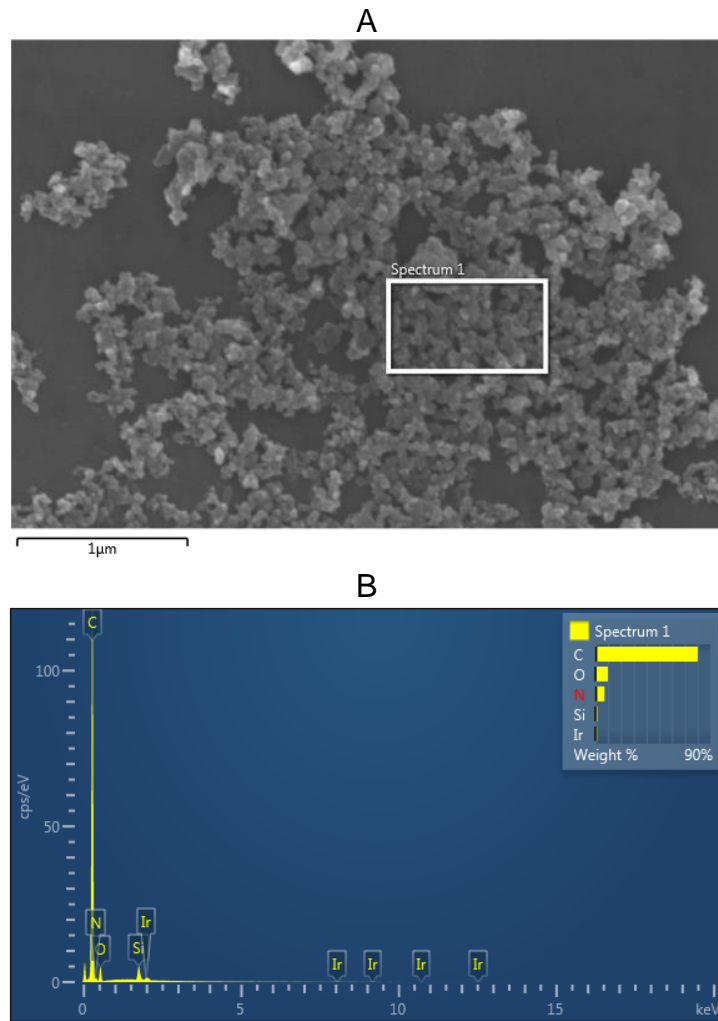
The final digestion method was applied to fixed synovial tissue samples doped with  $0.01 \text{ mm}^3$  of SiN particles per gram of tissue, in addition to a particle-free control tissue sample. Following the digestion protocol, the samples were visibly homogeneous, with no remaining pieces of tissue. The samples were subjected to the entire particle isolation process. Following density gradient ultracentrifugation, no particle pellet was found in any tube, including the control, most likely due to the very low volume of particles being isolated. After the washing stage of the protocol, the particle samples were resuspended and filtered. Analysis of the filters using SEM revealed that samples were largely free of protein contamination and isolated particles were visibly similar to particles not subjected to the recovery process. Each replica was similar. Particles were absent from the control sample.



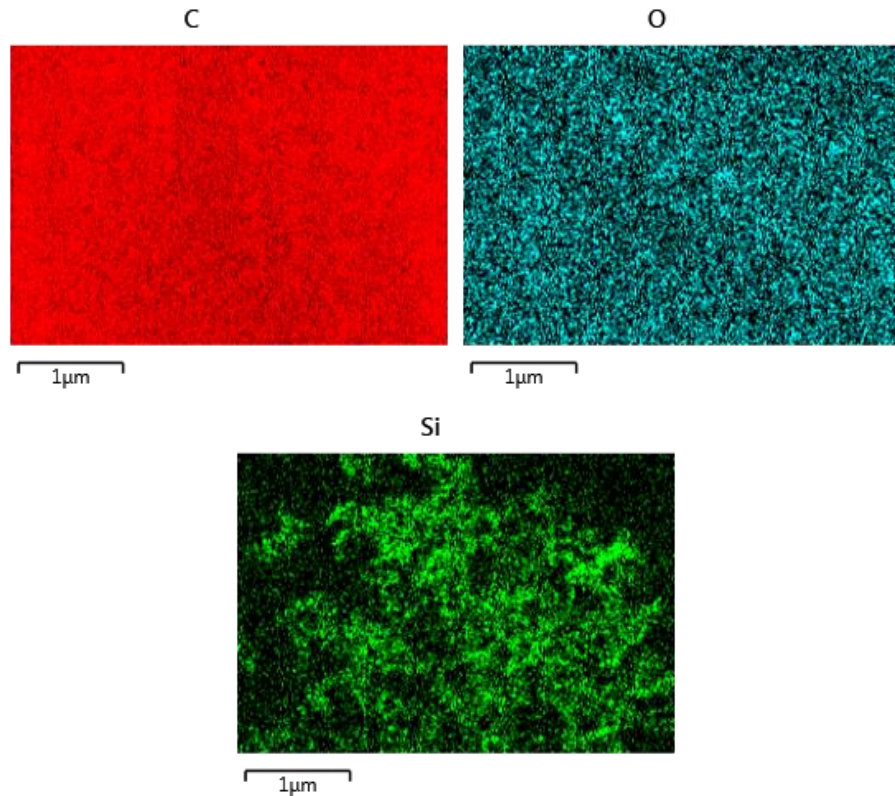


**Figure 3.21. Commercial silicon nitride particles (A and C) before isolation, and (B and D) following isolation from tissue using the final method, at (A and B) a magnification of 20,000x and (C and D) a higher magnification of 100,000x. The particles were resuspended and filtered on 0.015  $\mu\text{m}$  polycarbonate filter membranes; samples were iridium coated.**

Elemental analysis was carried out on the isolated particles in the same way as the non-isolated particles (Figure 3.22 and Figure 3.23). The spectra and elemental mapping produced similar results, with silicon and nitrogen found exclusively in areas containing particles. Oxidation was not very apparent in the particles (Figure 3.23).



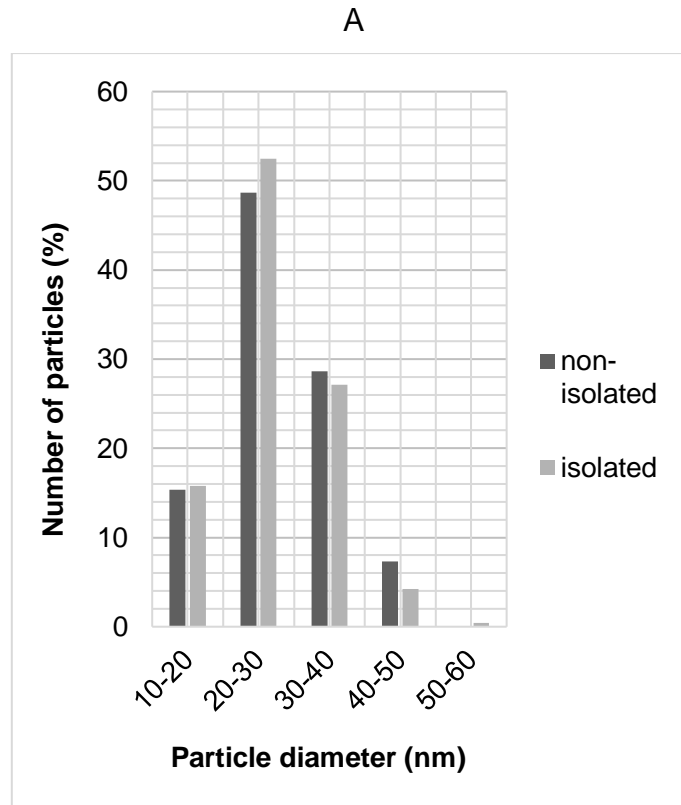
**Figure 3.22. Elemental analysis of commercial silicon nitride particles.** A. Scanning electron micrograph showing the area from the which the spectrum was produced. B. Spectrum taken from the silicon nitride particles. The particles were resuspended and filtered on 0.015 μm polycarbonate filter membranes; samples were iridium coated.



**Figure 3.23. Elemental mapping of isolated SiN particles, with the chemical symbol of the element above.** The particles were resuspended and filtered on 0.015 μm polycarbonate filter membranes; samples were iridium coated. Elements identified were carbon, silicon, oxygen, and iridium.

Particle characterisation was carried out to ensure that particles were not changed in terms of size or morphology (N=3 isolated particle samples plus 1 control sample of non-isolated particles; each sample was comprised of 150 particles). Particle size distribution, average size, aspect ratio and circularity were similar before and after isolation (Figure 3.24). This was confirmed by statistical analysis using Kolmogorov-Smirnov tests comparing data for each parameter (size, aspect ratio, circularity) of the non-isolated particles versus the isolated particles.





B

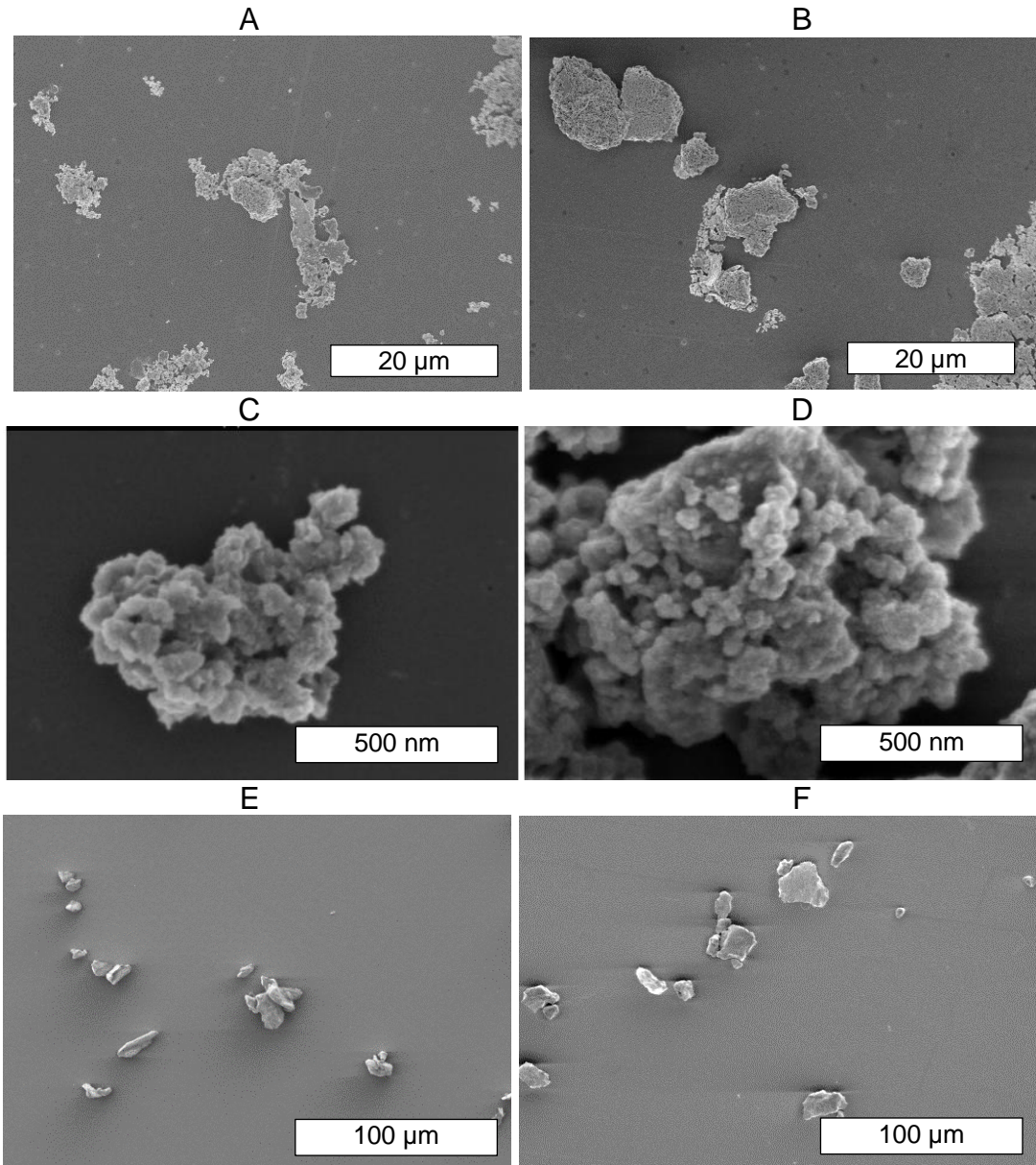
Parameter	Non-Isolated Particles (mean ± SD)	Isolated Particles (mean ± SD)
Feret's diameter (nm)	28 ± 7	27 ± 7
Aspect ratio	1.2 ± 0.1	1.2 ± 0.1
Circularity	0.9 ± 0.0	0.9 ± 0.0

**Figure 3.24. (A) Size distributions of commercial silicon nitride particles prior to and after isolation from tissue and (B) average particle parameters.** Data for isolated particles is the average of three repeat experiments, each consisting of 150 particles.

### 3.5.4 Testing the final particle isolation technique in cobalt chromium and titanium particles

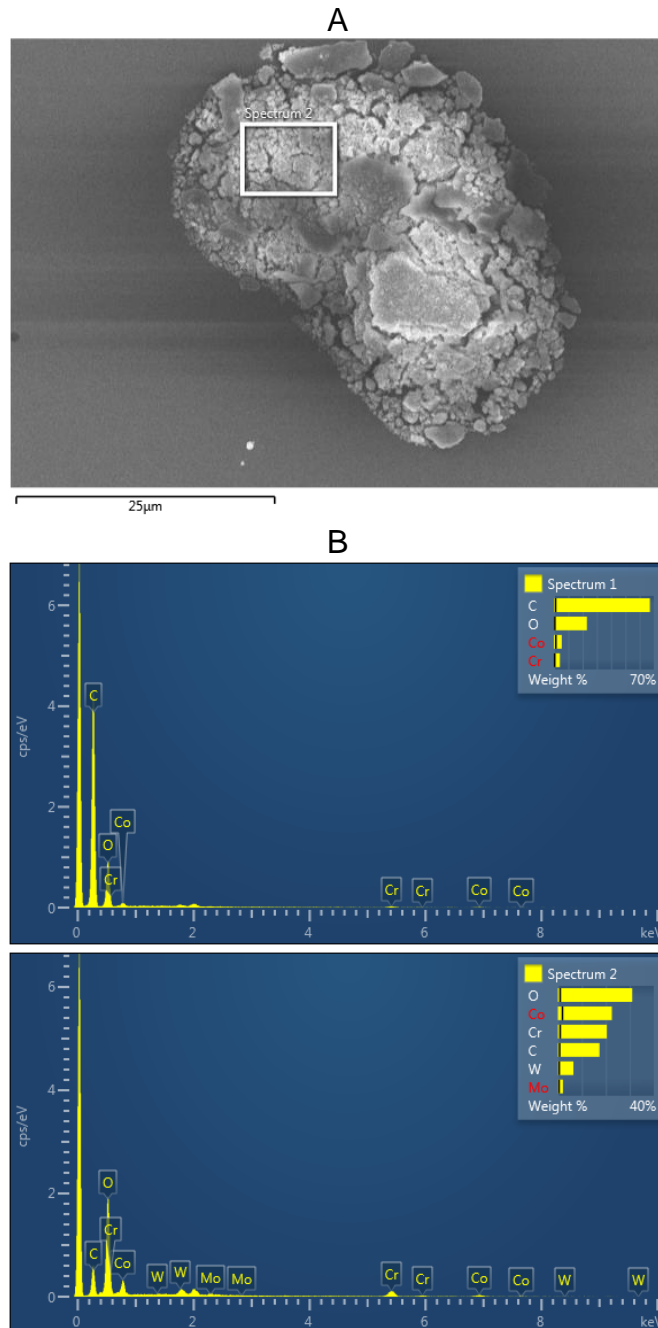
The particle isolation method was tested in alternative orthopaedic materials, including cobalt chromium and titanium. Samples again consisted of three particle-doped replicas and a particle-free tissue sample to use as a control

for contamination. Cobalt chromium particles were isolated from all three replica samples, with no noticeable difference between replicas. The same was also true of the titanium samples. The particles were similar in appearance before and after isolation (Figure 3.25).

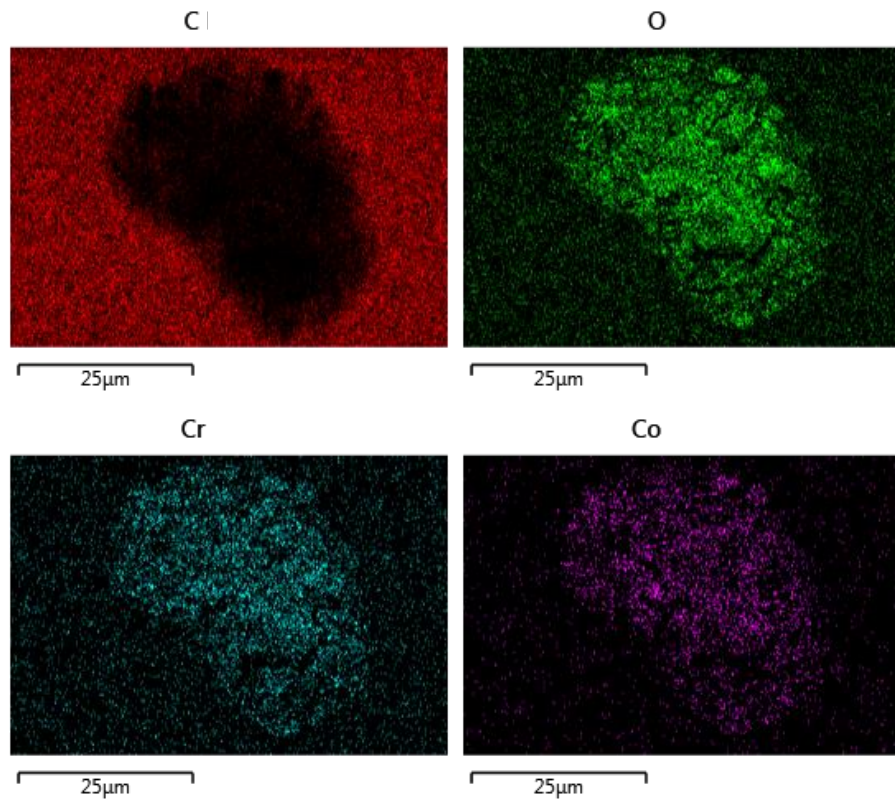


**Figure 3.25. Scanning electron micrographs of CoCr particles (A-D), at magnifications of 2,000x (A and B) and 100,000x (C and D), and titanium particles at a magnification of 500x (E and F), not subject to isolation (left) and after isolation (right). The particles were resuspended and filtered on 0.015 μm polycarbonate filter membranes; samples were iridium coated.**

Elemental analysis largely confirmed a lack of contamination in the isolated particles (Figure 3.26 - Figure 3.29), though traces of tungsten were identified on CoCr particles (Figure 3.26). Oxidation of CoCr particles and to a lesser extent titanium particles was apparent (Figure 3.27 and Figure 3.29).

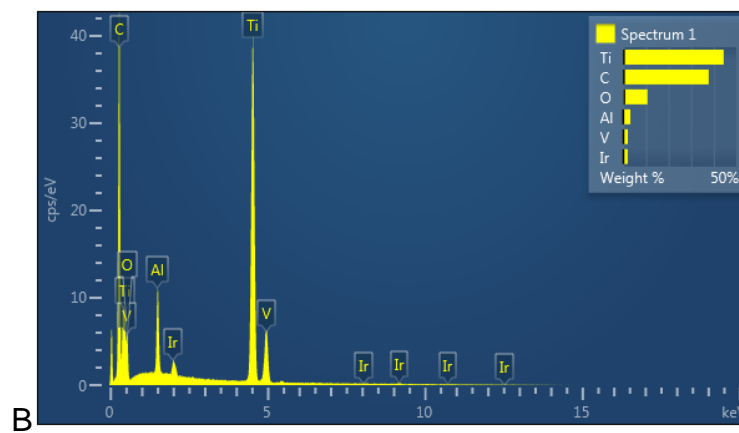
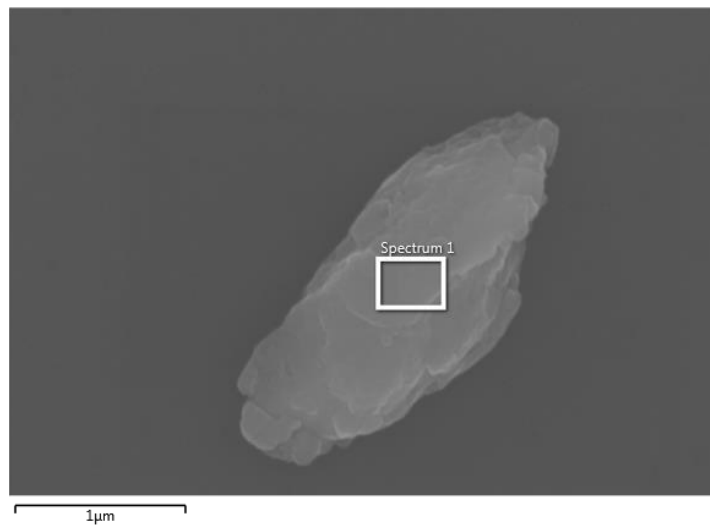


**Figure 3.26. Elemental analysis of isolated CoCr particles.** A. Scanning electron micrograph showing areas from the which the spectra were produced. B. Spectra (spectrum 1 was the entire micrograph). The particles were resuspended and filtered on 0.015 μm polycarbonate filters; samples were sputter coated with iridium to prevent charging of the sample.



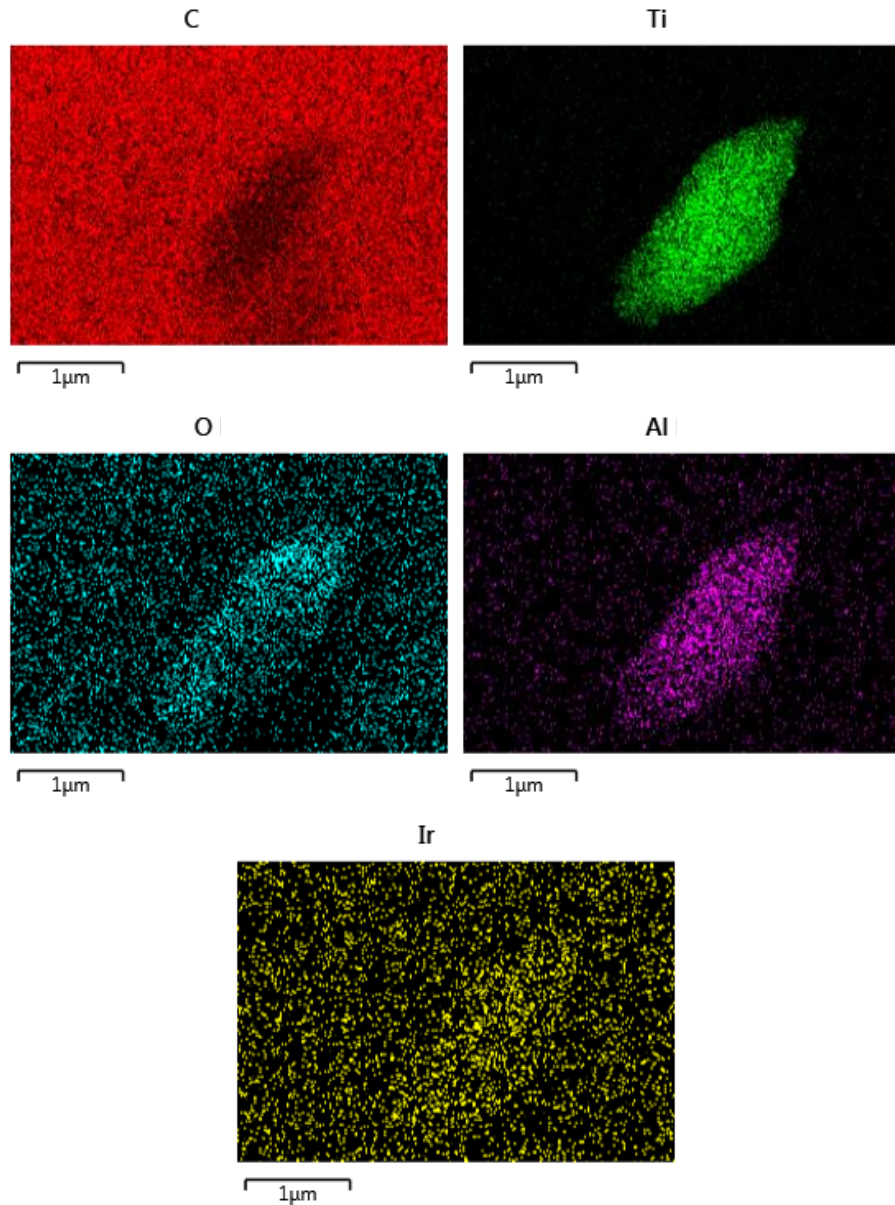
**Figure 3.27. Elemental mapping of isolated cobalt chromium particles.** The particles were resuspended and filtered on 0.015 µm polycarbonate filter membranes; samples were iridium coated. The elements identified included carbon, oxygen, chromium and cobalt.

A



**Figure 3.28. Elemental analysis of isolated titanium particles.** A. Scanning electron micrograph showing the area from the which the spectrum was produced. B. Elemental spectrum. The particles were resuspended and filtered on 0.015  $\mu\text{m}$  polycarbonate filter membranes; samples were iridium coated.

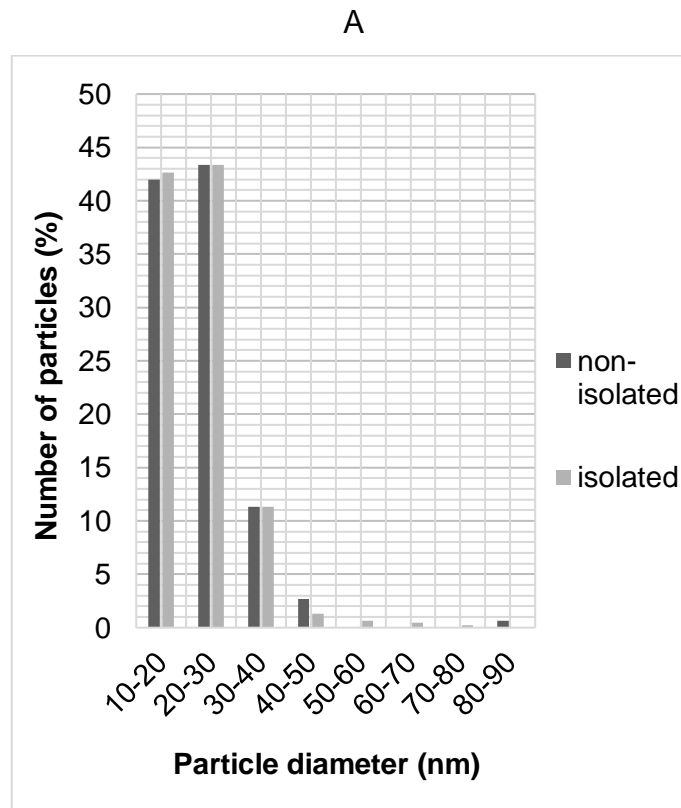




**Figure 3.29. Elemental mapping of isolated titanium particles.** The particles were resuspended and filtered on 0.015  $\mu\text{m}$  polycarbonate filter membranes; samples were iridium coated. The elements identified included carbon, oxygen, titanium, aluminium and iridium.

Particle sizes, aspect ratios and circularities were similar before and after isolation for both materials (Figure 3.30 and Figure 3.31), indicating that the isolation method did not affect particle geometry. This was confirmed by statistical analysis using Kolmogorov-Smirnov tests comparing data for each parameter (size, aspect ratio, circularity) of the non-isolated particles versus the isolated particles (For both CoCr and titanium, N=3 isolated particle

samples plus 1 control sample of non-isolated particles; each control sample was comprised of 150 particles and each isolated particle sample consisted of 150 CoCr particles or 50 titanium particles).

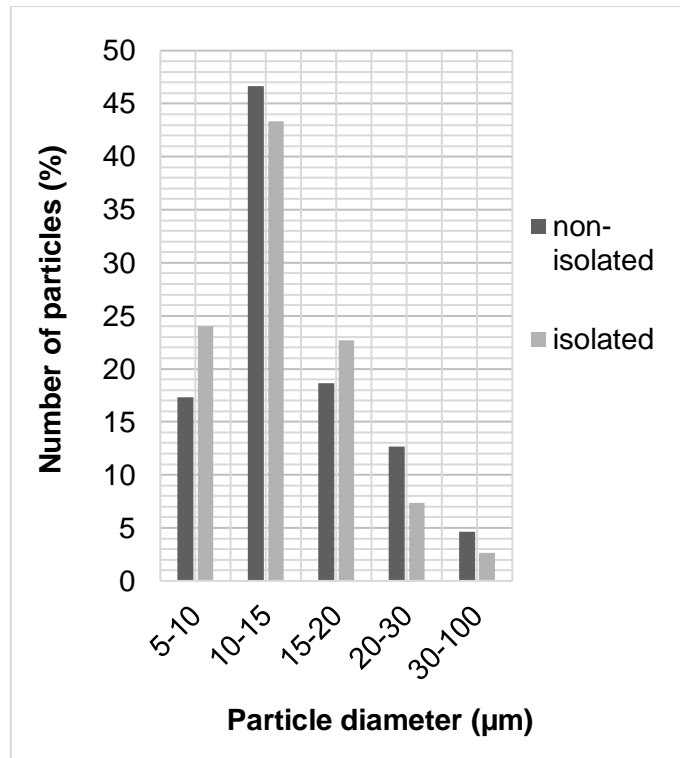


B

Parameter	Non-Isolated Particles (mean ± SD)	Isolated Particles (mean ± SD)
Feret's diameter (nm)	23 ± 8	23 ± 8
Aspect ratio	1.2 ± 0.2	1.2 ± 0.1
Circularity	0.9 ± 0.0	0.9 ± 0.0

**Figure 3.30. (A) Particle size distributions and (B) mean particle characteristics for CoCr, for both isolated and non-isolated particles.** Data for isolated particles is the average of three repeat experiments, each consisting of 150 particles.

A



B

Parameter	Non-Isolated Particles (mean ± SD)	Isolated Particles (mean ± SD)
Feret's diameter (µm)	15 ± 8	14 ± 6
Aspect ratio	1.5 ± 0.5	1.4 ± 0.3
Circularity	0.8 ± 0.1	0.8 ± 0.1

**Figure 3.31. (A) Particle size distributions and (B) mean particle characteristics for titanium, for both isolated and non-isolated particles.** Data for isolated particles is the average of three repeat experiments, each consisting of 50 particles.



### 3.5.5 Summary of results

The main results of this chapter were as follows:

- The average recovery rate for the method developed by Lal et al. (2016) was determined to be  $89.6\% \pm 7.1\%$  (SD).
- A particle isolation method was developed by adapting the method developed by Lal et al. (2016) and successfully applied to tissue samples doped with  $0.0025 \text{ mm}^3$  of SiN particles per sample.
- The method was demonstrated to have no effect on SiN particle geometries.
- The method was also applied to volumes of  $0.025 \text{ mm}^3$  of titanium or CoCr particles, with no effect on particle geometries.
- Particles were relatively pure following the isolation process, with no substantial changes to particle composition.

### 3.6 Discussion

The research outlined in this chapter validated a recently developed method (Lal *et al.*, 2016) for the isolation of particles from serum through the use of gravimetric recovery rates. In addition, this research study has taken the initial progress made by Lal *et al.* (2016) forward by adapting the isolation process for a new application – the isolation of particles from tissue samples. This has involved changes to the method including sample preparation, the removal of certain stages of the protocol, and optimisation of the digestion protocol specifically for fixed tissue samples. In addition, the isolation process had not been tested on micron-scale particles, only nanoscale particles, and had also not been used to isolate titanium particles. Particles were shown not to contain significant levels of contamination through SEM and EDX analysis, and particle geometries were shown not to be significantly affected by the isolation procedure. The method was highly reliable as particles were isolated from all three samples from each material group. Initial particle volumes were very low in the SiN group, suggesting that the technique is highly sensitive. The isolated particles were not irreversibly bound to any surface, so particles

isolated using the method have the potential to be used in further studies; for example, with nanoparticle-tracking analysis.

The particle recovery experiments produced an average recovery rate of  $89.6\% \pm 7.1\%$  (SD), which is similar to that deduced by the nanoparticle tracking analysis used by Lal et al. (2016). Since analysis of isolated particles by SEM revealed a lack of visible contamination, and control particle-free samples produced a negligible weight change to filters, it is unlikely that recovery rates were overestimated as a result of contamination.

The current method was tested in particle-doped tissue samples at starting volumes as low as  $0.0025 \text{ mm}^3$  per sample of tissue. A very low volume was chosen for these experiments since particle concentration in any given explant tissue sample could vary substantially, for example depending on the location from which tissue was extracted, the performance of an implant, and the clearance rate of particles within the tissue. Particle amounts could therefore be extremely low, especially in well-functioning ceramic-on-ceramic bearings which may produce less than  $0.5 \text{ mm}^3$  of wear per year *in vivo* (Hatton *et al.*, 2003). Although the quantities of tissue available from the LifeLong Joints animal studies were expected to be less than 250 mg, such an amount of tissue is often available from human explant samples; the particle isolation method was therefore tested on initial tissue masses of 250 mg.

Another major part of the research outlined in this chapter is the production of an effective tissue digestion stage. Glycine was used as previous research has shown it improves formalin-fixed tissue digestion with proteinase K, possibly by preventing inactivation of the enzyme or protein re-crosslinking, by inactivating the formyl group of formaldehyde (Takeichi *et al.*, 2009). The results of this analysis support the use of glycine and the use of papain for increasing the efficiency of tissue digestion. More frequent enzyme replenishment rather than larger but less frequent doses was also more effective, possibly due to gradual loss of enzyme activity. Scanning electron microscopy (SEM) was chosen rather than transmission electron microscopy (TEM) for particle characterisation to enable the surface characteristics of

particles to be analysed, and because preparation for TEM would likely damage the particles.

During the particle isolation protocol, transfer of samples between tubes was minimised to two tube changes, and any sample tubes were washed in sterile water three times whilst sonicating the tube, and these washes were added to samples, to prevent particle loss. Previous work has shown no particle loss during removal of supernatant following ultracentrifugation (Lal *et al.*, 2016), and low speed centrifugation steps were omitted from the current protocol. It is also worth noting that this method required only 4 days of processing time (excluding filtration for SEM), did not require any specialist equipment, had relatively few stages and was cost effective, making it easier and quicker to perform than current methods (Brown *et al.*, 2006; Catelas *et al.*, 2001).

Steps were taken throughout the study to ensure that the particle isolation method was effective and could be in future be used for periprosthetic tissue samples. Samples were formalin-fixed as this is the conventional way to preserve explant samples for biological analysis; subsequent storage of samples in 70% (v/v) ethanol also prevents bacterial contamination of samples. Where possible all solutions used during particle characterisation and isolation were filtered using 0.02 µm pore-size filters prior to use to prevent extraneous particle contamination or bacterial contamination. To minimise variations in particle aggregation, samples were re-suspended and filtered using the same protocol and to prevent bias during imageJ measurements, images were randomised, and all the particles that were visible in each image were measured. Manual sizing of individual particles was used rather than automatic sizing functions, which may inaccurately define particle boundaries.

The CoCr and titanium particles used in this study were similar in size and shape to those retrieved from tissue and generated by physiological hip simulators (Tipper *et al.*, 2001; Brown *et al.*, 2006; Bohler *et al.*, 2000; Grosse *et al.*, 2015). The model SiN particles used were similar in size to recently published data on nanoscale SiN debris produced by a coating adhered to a CoCr substrate (Pettersson *et al.*, 2016), though particles up to a few microns

in size were also identified. The nanoscale particles were also spherical and aggregated. Measuring particle parameters also showed that particle dissolution did not occur during the isolation process to a detectable extent. Measuring the chosen parameters – size, aspect ratio and circularity - for the particles was important due to their significance to the biological activity of particles. For example, based on a murine model involving injected particles, nanoscale and not micron scale CoCr particles were genotoxic at 40 weeks *in vivo* (Brown *et al.*, 2013). Additionally, UHMWPE particles in the 0.1–1  $\mu\text{m}$  size range have been found to be more biologically active in terms of osteolytic cytokine release than particles above 1  $\mu\text{m}$  in size, and it was found that particles of a size below approximately 50 nm failed to elicit a proinflammatory response in primary cells (Liu *et al.*, 2015). Size-related differences in particle biocompatibility may be due to how readily cells are able to phagocytose particles. Aspect ratio may also affect cellular uptake of particles (Chithrani *et al.*, 2006); UHMWPE particles with a more elongated shape are more inflammatory (Yang *et al.*, 2002). Further, spherical nanoparticles with a circularity of greater than 0.7, when taken up by cells, may have different biological effects than less spherical particles, since particles with rough edges may break through endosomal or lysosomal membranes and thus reside more frequently in cytoplasm (Chu *et al.*, 2014).

There were, however, several limitations to the current study. During the particle recovery rate experiments, it was found that particles were lost through adherence to particle filtration equipment. This may explain the variation between recovery readings between the three samples. To enable accurate gravimetric analysis within the limits of available equipment, an ultra-high volume of SiN particles was required to dope samples; lower volumes of particles may have different recovery rates. Despite the limitations, the recovery measurements used had advantages over nanoparticle tracking analysis, since such analysis measures the number of particle aggregates, which may change depending on exact conditions used to re-suspend particles. A limitation of the particle isolation experiments from tissue was that particles were incubated with tissue for 12 hours and were introduced via pipetting a particle suspension; particles produced by a prosthesis may have

differing particle aggregation and protein corona characteristics, since it has been suggested that a hard protein corona is formed after 48 hours (Casals *et al.*, 2010). During elemental analysis of isolated particles, traces of tungsten were found on CoCr particles, though this did not affect particle sizes or morphologies. This may reflect a chemical affinity between CoCr and tungsten. Particles of less than 10 nm in size were not measured due to the resolution limit of the SEM equipment. The measurements of the particles were also limited due to their aggregated nature, which meant that larger particles may be obstructed by smaller particles and vice versa, and particle boundaries were not always clearly visible. Overall the isolation technique showed potential but needs to be validated in *in vivo* samples, which contained particles for a longer period.

## Chapter 4

### In vivo investigation of silicon nitride nanoparticles using a rat model

#### 4.1 Background

As described in Chapter 1, ceramic materials including silicon nitride have a generally favourable biocompatibility profile. Silicon nitride has been investigated in bulk form through animal studies (Howlett *et al.*, 1989) and its clinical use in cervical spacers and spinal fusion implants (Taylor *et al.*, 2010). It has also been analysed in either bulk or particulate form through cell studies (Mazzochi and Belosi, 2008; Neuman *et al.*, 2004; Zhang *et al.*, 2011). These studies have suggested that silicon nitride is non-cytotoxic and does not negatively affect cell viability. However, the biocompatibility of silicon nitride is still disputed, as high doses of silicon nitride particles have been shown to stimulate TNF- $\alpha$  secretion (Zhang *et al.*, 2011), and there are still very few studies on silicon nitride particles. Furthermore, to the author's knowledge, there were no publications detailing the response to silicon nitride particles *in vivo* at the time of this research study. Therefore, there is currently no information with regard to soft tissue reactions to silicon nitride particles, which would be required for pre-clinical testing of a silicon nitride coated joint implant. Additionally, studies thus far have not taken into account potential changes to particle geometries, as well as chemical changes, which may occur *in vivo*. These are of interest as they would affect the biocompatibility of the material and are especially critical for the evaluation of silicon nitride, which has dissolution properties. Dissolution of silicon nitride could potentially minimise chronic inflammatory reactions to particles. One study has suggested an *in vivo* dissolution rate of silicon nitride particles of 0.33 - 2 nm per day, depending on the characteristics of the particles (Maloney, 2005); however, the study involved subcutaneous implants coated with silicon nitride rather than particles. Dissolution of silicon nitride coatings have also been estimated at 0.2 – 1.4 nm per day; however, *in vivo* conditions were simulated using 25% foetal bovine serum and a 37°C incubator (Pettersson *et al.*, 2016). Thus, the dissolution of particles within a joint may differ. Overall, the lack of

available information warrants an *in vivo* investigation into the biological reaction to silicon nitride particles. This would be necessary to ensure the safety of the material prior to the commencement of any longer-term *in vivo* studies involving an implant.

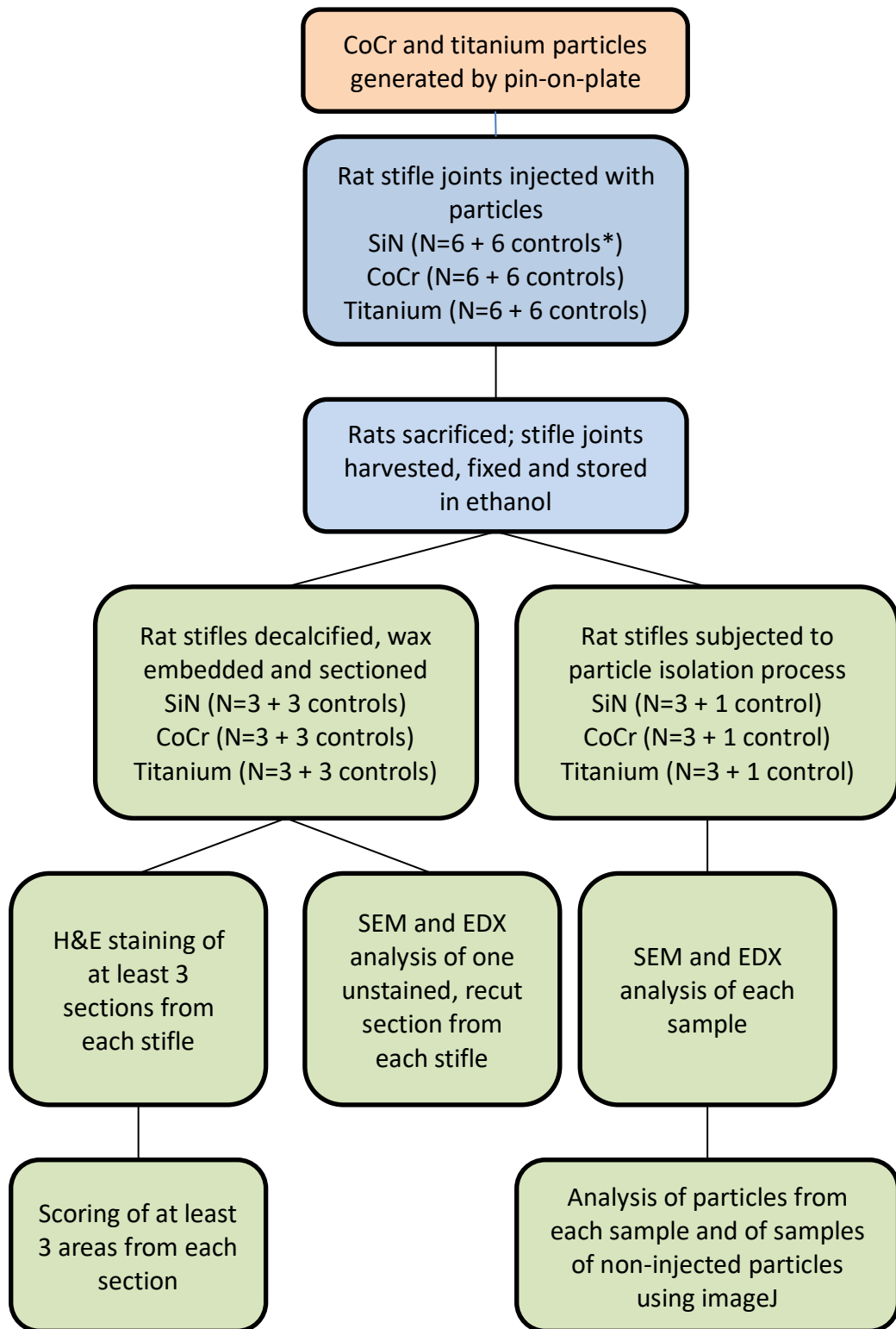
## **4.2 Aims**

The overall aim of the research outlined in this chapter was to evaluate the biocompatibility of silicon nitride particles *in vivo*. This was achieved using a rat model whereby particles were injected into rat stifle joints for a seven-day period, using cobalt chromium and titanium particles as reference materials. Specific objectives included:

- Implementation of the particle isolation method developed in Chapter 3 to isolate the particles from the rat tissues following the seven-day period, and thus assess whether any changes to particle geometries or chemical composition occurred *in vivo*.
- To evaluate the *in vivo* response to silicon nitride particles through histology. In particular, the objectives were to characterise inflammatory cell infiltrates and morphological changes to joint tissues, such as synovial thickening.

## **4.3 Overview of experiments**

To investigate silicon nitride particle biocompatibility, an animal study was carried out in collaboration with the University of Zurich. Briefly, this involved the generation of particles using a pin-on-plate wear tester, subsequent sterilisation of the particles, and a protocol for injection of the particles into rat stifle joints, carried out by Dr Saurabh Lal. The overall study design, including type of animal, number of animals, and time points were developed and the animal study was carried out by researchers at the University of Zurich. Samples consisting of intact stifle joints were sent to the University of Leeds for histological evaluation and particle isolation, which is the focus of this chapter. An overview of the animal model and subsequent experiments is given in Figure 4.1.



**Figure 4.1. Overview of experiments outlined in this chapter.** Orange boxes describe work carried out in Leeds by Dr. Saurabh Lal. Blue boxes describe experiments carried out at the University of Zurich, while green boxes describe work carried out at the University of Leeds by the current author. \*Control samples refer to the contralateral, non-injected joint of each animal.



## 4.4 Materials and Methods

Materials used throughout this chapter are given in Appendix A.

### 4.4.1 Generation of particle suspensions for injection into rat stifle joints

Experiments described in this subsection (4.4.1 only) were carried out by another researcher at the University of Leeds, Dr. Saurabh Lal. Cobalt chromium or titanium wear debris were generated by a pin-on-plate wear tester as described in section 2.2.5. A PBS stock solution was produced by dissolving one Dulbecco's PBS tablet in 100 ml of sterile filtered water. The solution was used immediately. In addition to commercially available silicon nitride particles (Sigma-Aldrich, <50 nm), the cobalt chromium and titanium particles were sterilised by heat treatment at 180 °C for 4 h and resuspended at a concentration of 1.8 mm<sup>3</sup>.ml<sup>-1</sup> in sterile water. The particle suspensions were diluted 50% (v/v) in the PBS solution to give a final particle suspension concentration of 0.9 mm<sup>3</sup>.ml<sup>-1</sup> for injection. Details of the materials used and an overview of the animal model are given in Table 4.1.

**Table 4.1. Particles used for injection into rat stifle joints and overall in vivo study design including groups, time points and animal numbers.**

Material group	Details	Volume of particles injected	Time (injection to sacrifice)	Number of rats
SiN	Si <sub>3</sub> N <sub>4</sub> , commercially available nanopowder (<50nm, Sigma-Aldrich, UK)	0.018 mm <sup>3</sup>	seven days	six
CoCr	Particles generated by pin-on-plate in house (high carbon; >0.2 %, (ASTM, F1537))	0.018 mm <sup>3</sup>	seven days	six
Titanium	Particles generated by pin-on-plate in house (medical grade Ti-6Al-4V alloy)	0.018 mm <sup>3</sup>	seven days	six

#### **4.4.2 Characterisation of particle suspensions**

Three aliquots of 20 µL of each particle suspension described in section 4.4.1 were analysed by SEM and characterised as described in 2.2.6 prior to injection into rats. This was to verify particle purity and to ensure that particles were of a clinically relevant size and shape. CoCr and SiN particles were expected to be nanoscale and approximately spherical or oval, while titanium particles were expected to be micron scale and irregular in shape. Particles were also characterised in order to serve as control samples against which to compare later samples of isolated particles. Particle characterisation included elemental analysis using energy dispersive X-ray spectroscopy, as described in 2.2.6.5 and ImageJ measurements of 150 particles from each sample, except for titanium particles, where a minimum of 100 particles from each sample were measured, as described in 2.2.6.6; measurements included size, aspect ratio and circularity, as defined in 2.2.6.6.

#### **4.4.3 Animal model**

Experiments and the design of the animal model described in this section were carried by researchers at the University of Zurich until the point where the samples were shipped to Leeds. The animal model consisted of male Han Wistar rats (outbred, supplied by Charles River), 8-12 weeks old and with weights ranging from 297-342 grams. Guidelines contained in EU Directive 2010/63/EU for animal experiments were followed. Details of food, housing and environment are given in Appendix B. The study involved a total of 18 rats, consisting of three material groups (Table 4.1). Tail marks were placed on the rats on arrival into the facility and the health of each rat was subsequently examined; animals with any visible signs of illness were excluded from the study. The rats were acclimatised for at least 8 days under test conditions prior to the study. Stifle joints were chosen for treatment to allow a greater degree of accuracy and repeatability compared to injection of the hip joints (based on personal communication with veterinary surgeons at University of Zurich). Prior to immediate use, the particle suspensions were vortexed and sonicated for 20 min three times to ensure homogenous dispersion of particles. Rats were anaesthetised by a subcutaneous injection

of ketaminhydrochloride ( $20 \text{ mg.kg}^{-1}$ ). Anaesthesia was prolonged by Isofluran/O<sub>2</sub> inhalation via a facemask. The anaesthetised rat was placed in dorsal recumbency. The stifle joint region was clipped prior to injection. The surgical site was cleaned and disinfected. The surgery procedure was performed under sterile conditions. The injection procedure was performed by placing the needle between the medial and lateral condyles from the anterior aspect of the joint. Rats were injected in the right stifle joint using a glass Hamilton syringe (23 gauge) containing 20  $\mu\text{l}$  of particle suspension (SiN, CoCr or Titanium). This equated to a dose of  $0.018 \text{ mm}^3$  of particles per rat. This was chosen as a relatively high dosage volume (Brown *et al.*, 2013), to allow feasibility of wear debris extraction, as well as cause a sufficient biological response for analysis. After injection, the needle was withdrawn and the rat allowed to recover from anaesthesia. The left stifle joints were not injected and were used as untreated control joints. Thereafter rats were monitored daily over a seven-day period, at which point animals were euthanised with a rising CO<sub>2</sub> concentration. Excess muscle tissue was removed from the stifle joints using a scalpel, taking care not to open the joint compartment by leaving the pericapsular ligament intact. The intact rat stifle joints (both treated and non-treated) were excised by bisection shears midway through the femur, tibia and fibula (Figure 4.2).



**Table 4.2. Dissected wistar rat, in which the left intact stifle joint has been removed. SLF superior to left femur PL patella ligament T tibia**

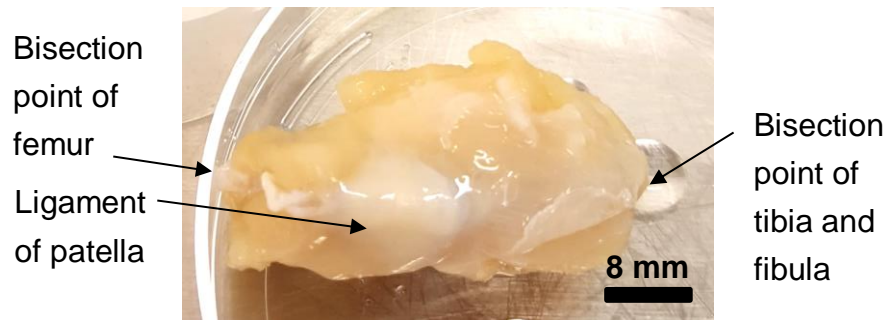
The stifle joints were immediately formalin-fixed at room temperature for a period of 48 h by placement into sterile, screw cap 50 ml plastic tubes filled with 10 % (v/v) NBF. The joints were fixed in their natural configuration, i.e. the degree of flexion in the joints was not altered. The stifle joints were stored at room temperature by discarding the NBF and refilling with 70% (v/v) ethanol. Samples were shipped at room temperature to Leeds within 48 h. For shipment it was necessary to temporarily remove the ethanol and cover samples in medical gauze soaked in 70% (v/v) ethanol. On arrival at Leeds the gauze was discarded and samples were briefly examined to ensure no drying out of tissue had occurred. Tubes containing the samples were then immediately refilled with 70% (v/v) ethanol.

#### **4.4.4 Particle isolation from injected rat stifle joints**

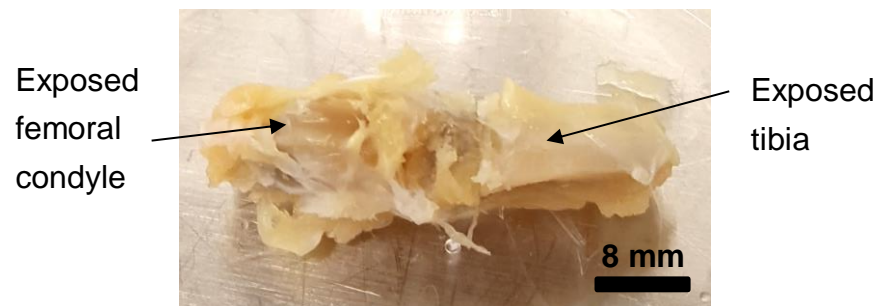
##### **4.4.4.1 Harvesting and preparation of tissue**

The intact rat stifle joints were washed three times in sterile filtered water by filling the tube, vortexing the tube for five seconds, and immediately discarding each wash to remove traces of formalin, ethanol, and exterior contaminants. As the joints were intact, this would not have led to loss of particles. The patellar ligament, patella, fat pad and synovial tissue continuous with the fat pad was carefully excised as one intact piece using clean, sterile dissection equipment in a class II cabinet (Figure 4.2). The patella was discarded, and the tissue was weighed to give approximately 150 mg (wet weight) of tissue for digestion. The tissue was minced to 1 mm<sup>3</sup> sized pieces in a sterile culture dish and added to round-bottomed plastic test tubes. A volume of 1 mL of sterile filtered water was added to each sample to prevent the tissue from drying out. Dissection equipment was cleaned by sonication in 70% (v/v) ethanol for 5 minutes between samples to prevent sample cross contamination.

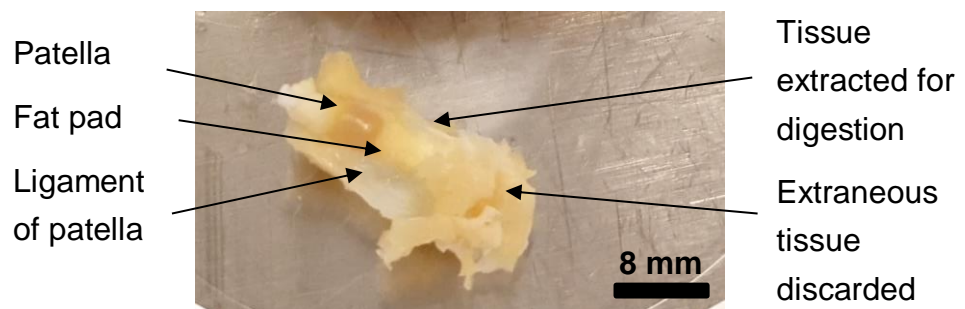
A



B



C



**Figure 4.2. Dissection and harvesting of rat stifle joint tissue for particle isolation.** (A) Appearance of intact stifle joint. (B) Following excision of the patella, associated ligament and fat pad as one intact piece. The synovium was removed with the fat pad, as demonstrated by the lack of tissue on the femoral condyles. (C) The patella, along with tissue above the patella, was discarded, as well as excess muscle tissue below the fat pad.

#### 4.4.4.2 Particle isolation and characterisation

Immediately following harvesting and tissue preparation as described in 4.4.4.1, tissue was subjected to the tissue digestion procedure as described in section 2.2.8.1, density gradient ultracentrifugation as described in 2.2.8.2,

and sodium polytungstate was removed from samples as described in 2.2.8.3. Isolated particles were stored at -20 °C prior to SEM analysis and characterisation as described in 2.2.6. Similarly to the particle suspensions that were characterised prior to injection, which is outlined in section 4.4.2, characterisation of isolated particles included elemental analysis and ImageJ measurements of 150 particles from each sample, except for titanium particles, where a minimum of 100 particles from each sample were measured. Particles were chosen by capturing a random area of the filter containing particle aggregates, and as many particles from each image as possible were measured.

#### **4.4.5 Statistical analysis comparing non-injected particles with particles post-isolation from tissues**

SiN and CoCr particle samples, before injection and after isolation from injected rat stifles joints, were analysed statistically as described in section 2.2.7. Each Kolmogorov-Smirnov test consisted of the raw data from one isolated sample compared to the raw data from a non-injected, control particle sample. The measurements included particle size (maximum ferret's diameter), aspect ratio and circularity as described in section 2.2.6.6. A different control sample was used for each comparison, and the null hypothesis which was tested was that there were no significant differences between size, aspect ratio and circularity for non-injected particles and particles post-isolation, other than those due to chance, with a significance level of  $p < 0.05$ .

#### **4.4.6 Histology of rat stifle joints**

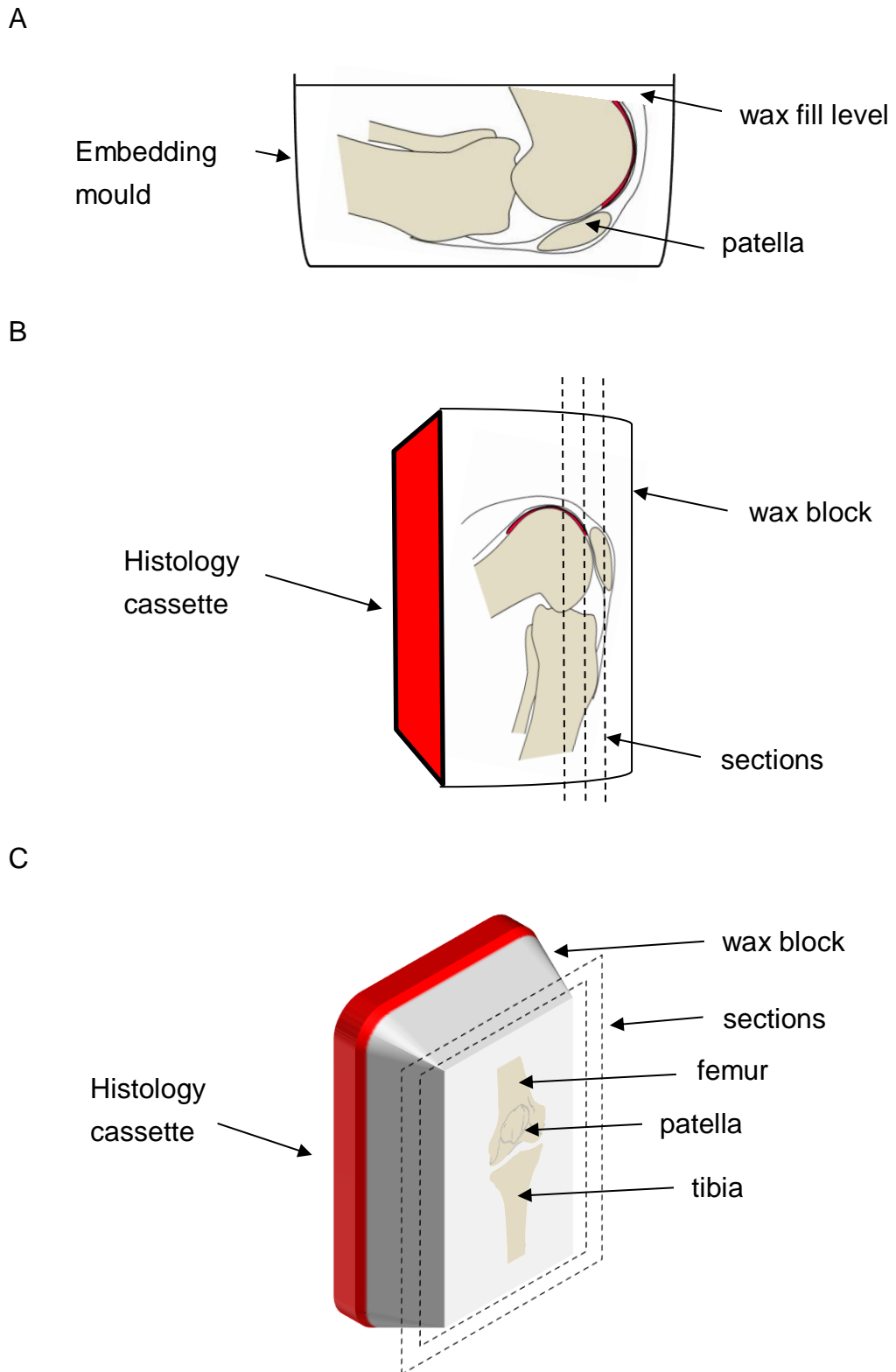
Histological analysis was carried out on three injected rat stifle joints from each material group, in addition to the three non-injected, contralateral stifle joints, which were used as untreated controls. Briefly, this required decalcification of the bone to enable the tissues to be soft enough for thin sectioning; following this, the intact stifle joints were embedded in wax, sectioned, and selected sections were stained with haematoxylin and eosin (H&E) to allow observation of tissue structures and cells using light microscopy. The particles and any biological reactions were analysed.

#### 4.4.6.1 Decalcification, wax embedding and sectioning

Concentrated EDTA (12.5 % (w/v)) was prepared by dissolving 250 g of EDTA in 1750 mL of distilled water with a magnetic stirrer. A mass of 25 g of sodium hydroxide pellets was added to the EDTA solution. Following total dissolution of the EDTA and sodium hydroxide pellets, the pH of the solution was adjusted to 7.0 using premade 6 M HCL or 6 M NaOH. The solution was stored for up to one year at room temperature. Prior to decalcification, excess bone and muscle tissue was trimmed away using scissors. Samples were added to individual 150 ml pots and the pots were filled with the EDTA solution. The pots were sealed and placed horizontally on an orbital shaker in a 37 °C incubator. The EDTA solution within each pot was discarded and replaced with fresh EDTA solution every 2-3 days for a period of five weeks. Tissues were processed within individual, labelled plastic cassettes using a tissue processor and programme given in Table 4.3. Within 12 h of completion of the tissue programme, tissues were wax embedded as described in section 2.2.9.1, using the embedding and cutting orientations shown in Figure 4.3.

**Table 4.3. Programme used for histological processing of intact rat stifle joints prior to embedding in paraffin wax.**

<b>Solution</b>	<b>Time</b>
70% (v/v) Ethanol	2 h
90% (v/v) Ethanol	2 h
100% Ethanol	1 h
100% Ethanol	1 h
100% Ethanol	2 h
100% Ethanol	2 h
100% Xylene	2 h
100% Xylene	2 h
100% Xylene	2 h
100% Molten wax	3 h
100% Molten wax	3 h
<b>TOTAL</b>	<b>22 h</b>



**Figure 4.3. Schematic representation of embedding and cutting orientation of the intact stifle joints.** (A) Representation of stifle joint placement within embedding mould. (B) Representation of lateral view of sectioning plane. (C) 3D model showing cross sections of the joint from a frontal plane.



The wax blocks were chilled on ice for 10 min prior to sectioning and every 15 min during sectioning. Sections were set to 5  $\mu\text{m}$ , with a blade angle of  $0.5^\circ$ , and the slides were labelled sequentially with their approximate depth into the sample. The sections were floated on a water bath filled with deionised water at a temperature of  $40^\circ\text{C}$  and applied to charged slides. The slides were drained of excess water by tapping the edge on paper tissue and the slides were placed on a hot plate at  $55\text{-}60^\circ\text{C}$  for 2 h. Approximately 40 serial sections were taken from both injected and control stifle joints, from the frontal part of each joint. This consisted of approximately the first 1.5 mm of each joint, containing the fat pad, patella, one or both femoral condyles, the tibia and some of the patella ligament.

#### **4.4.6.2 Haematoxylin and eosin staining of sections and slide mounting**

A minimum of three sections per sample, each approximately 100  $\mu\text{m}$  apart (depth), were dewaxed and hydrated as described in section 2.2.9.2, stained with H&E as described in section 2.2.9.3, and dehydrated and mounted with coverslips as described in section 2.2.9.4.

#### **4.4.6.3 Observation of stifle joint sections using light microscopy and scoring biological reactions by counting raw cell and blood vessel numbers**

Stifle joint sections were observed using light microscopy as described in section 2.2.9.5. Tiled images were created using a 2.5x objective lens to capture entire stifle joint sections. Any particles and tissue reactions to particles were captured at higher magnifications for analysis. For vascularisation scoring, a customised scoring method was used; a 10x objective lens was used to capture three areas from the fat pad of each section, containing the highest numbers of blood vessels, the lowest numbers of blood vessels and an intermediate number of blood vessels; blood vessels were identified by a ring of endothelial cells surrounding erythrocytes. The resultant score was the raw number of blood vessels in each image. The total number of cells in selected areas of the fat pad, and numbers of macrophages, lymphocytes and polymorphonuclear cells, were also counted to quantify the inflammatory infiltrates. For this scoring, a 40x objective lens was used to

capture three areas from the fat pad of each tissue sample section, containing the highest number of inflammatory cells, the lowest number of inflammatory cells, and an intermediate number of inflammatory cells. A description of how immune cells were recognised is given in section 2.2.9.6. For scoring of synovial thickness, a customised scoring method was required, similar to that used by Baeten *et al.*, 2000; a 40x objective lens was used to capture three areas from the synovium of each section (or 20x if the synovium was especially thick), consisting of the thickest part of the synovium, the thinnest part of the synovium, and a part of the synovium that was of intermediate thickness. The images were used to count the number of cells in the synovial lining. For each parameter, results were presented as raw numbers.

#### **4.4.6.4 Additional scoring of raw cell numbers by independent researchers**

Two independent researchers were asked to score a randomised selection of the same histology images measured in section 4.4.6.3 for total cell number in the fat pad and numbers of polymorphonuclear cells, macrophages and lymphocytes, using the same methods described in section 4.4.6.3. This was to verify the results, since cell identification using nucleus morphology may be considered subjective to some degree. The researchers were blinded with regard to which group each image belonged to in order to prevent any biases. One image from each injected stifle, and one image from a control stifle, were scored to give a total of 10 scores from each researcher.

#### **4.4.6.5 Statistical analysis of raw cell numbers and blood vessel numbers**

The parameters that were measured as described in section 4.4.6.3 were analysed statistically using the raw data for:

- total cell numbers
- synovial thickness
- numbers of macrophages
- numbers of lymphocytes
- numbers of blood vessels

In each case,  $N \geq 12$  images per material group for each parameter, and  $N \geq 3$  images per stifle joint. In addition, the scores made by all three researchers on a selection of images, as described in section 4.4.6.4, were also analysed statistically ( $N=10$  per researcher). All analysis was carried out using SPSS (v 23). A Shapiro-Wilkes test was first used on the dataset for each animal and each material group, and for the data from second scoring, to determine whether data were normally distributed. Data that was not normally distributed was analysed using a Kruskal Wallis test. Tests were performed by comparing material groups, by comparing individual animals to each other, and by comparing the scores between individual researchers. If any significant differences were detected ( $p < 0.05$ ), Dunn's post hoc tests were performed with Bonferroni correction.

#### 4.4.6.6 Conversion of raw cell numbers into semi-quantitative scores

Raw cell numbers that were measured as described in section 4.4.6.3 were converted to semi-quantitative scores using a method described in ISO 10993-6 (2016). Firstly, tissues were scored from 1-4 based on the raw number of each cell present in a given high-powered (400x) field as shown in Table 4.4.

**Table 4.4. Semiquantitative scoring of inflammatory cell infiltrates, adapted from ISO 10993-6 (2016).**

Cell type/response	Score				
	0	1	2	3	4
Polymorpho-nuclear cells	0	Rare, 1 to 5 phf*	5 to 10 phf	Heavy infiltrate	Packed
Lymphocytes					
Plasma cells					
Macrophages					
Giant cells		Rare, 1 to 2 phf	3 to 5 phf		Sheets
Necrosis	None	Minimal	Mild	Moderate	Severe

\*Number of cells present per high-power field (400x)

Tissue responses, including vascularisation, fibrosis and any fatty infiltration was scored using another histological evaluation system given in ISO 10993-6 (2016), as shown in Table 4.5. Scoring for the number of blood vessels was carried out per 100x field. Fibrosis and fatty infiltration was assessed in the whole section.

**Table 4.5. Semiquantitative scoring of vascularisation, fibrosis and fatty infiltration, adapted from ISO 10993-6 (2016).**

Response	Score				
	0	1	2	3	4
Vascularisation	0	Minimal capillary proliferation, 1 to 3 buds	Groups of 4 to 7 capillaries with supporting fibroblastic structures	Broad band of capillaries with supporting fibroblastic structures	Extensive band of capillaries with supporting fibroblastic structures
Fibrosis	0	Narrow band	Moderately thick band	Thick band	Extensive band
Fatty infiltrate	0	Minimal amount of fat associated with fibrosis	Several layers of fat and fibrosis	Elongated and broad accumulation of fat cells about material	Extensive fat completely surrounding material

The scores were totalled using a system adapted from ISO 10993-6 (2016). Scores from inflammatory cell infiltrates and necrosis were weighted more by doubling, and scores for controls were subtracted from test specimens (Table 4.6). Based on this scoring method, materials were considered a:

- non-irritant (average total scores of 0,0 up to 2,9)
- slight irritant (average total scores of 3,0 up to 8,9)
- moderate irritant (average total scores of 9,0 up to 15,0)
- severe irritant (average total scores > 15)

**Table 4.6. Semiquantitative scoring of overall tissue reaction to a material, adapted from ISO 10993-6 (2016).**

	Test Sample			Control Sample		
Sample number:						
Polymorphonuclear cells						
Macrophages						
Lymphocytes						
Plasma cells						
Giant cells						
Necrosis						
SUBTOTAL (x2)						
Neovascularization						
Fibrosis						
Fatty infiltrate						
SUBTOTAL						
TEST - CONTROL						
AVERAGE TOTAL SCORE						

#### **4.4.6.7 SEM and EDX analysis of histological sections**

From each rat stifle joint, a serial section adjacent to the H&E section which was observed using light microscopy to contain the highest number of particles was placed into a slide holder and dewaxed by immersion in xylene for 10 min, then in fresh xylene for a further 10 min. Sections were then immersed into successive pots of 100% (v/v) ethanol for 3 min, 2 min and 2 min. Slides were stored at room temperature for up to 24 h and were then cut to fit large SEM stubs and adhered to the stubs with carbon adhesives. The edges of the glass slides and stubs were painted with carbon paint and the samples were dried at room temperature for 10 minutes and then carbon

coated to a thickness of 15 nm. Slides were imaged and analysed by scanning electron microscopy using a Hitachi SU8230 Cold FEG SEM, with and without the use of a back scattered electron detector to enhance the contrast between the tissue and the particles. Elemental analysis was carried out using EDX as described in 2.2.6.5.

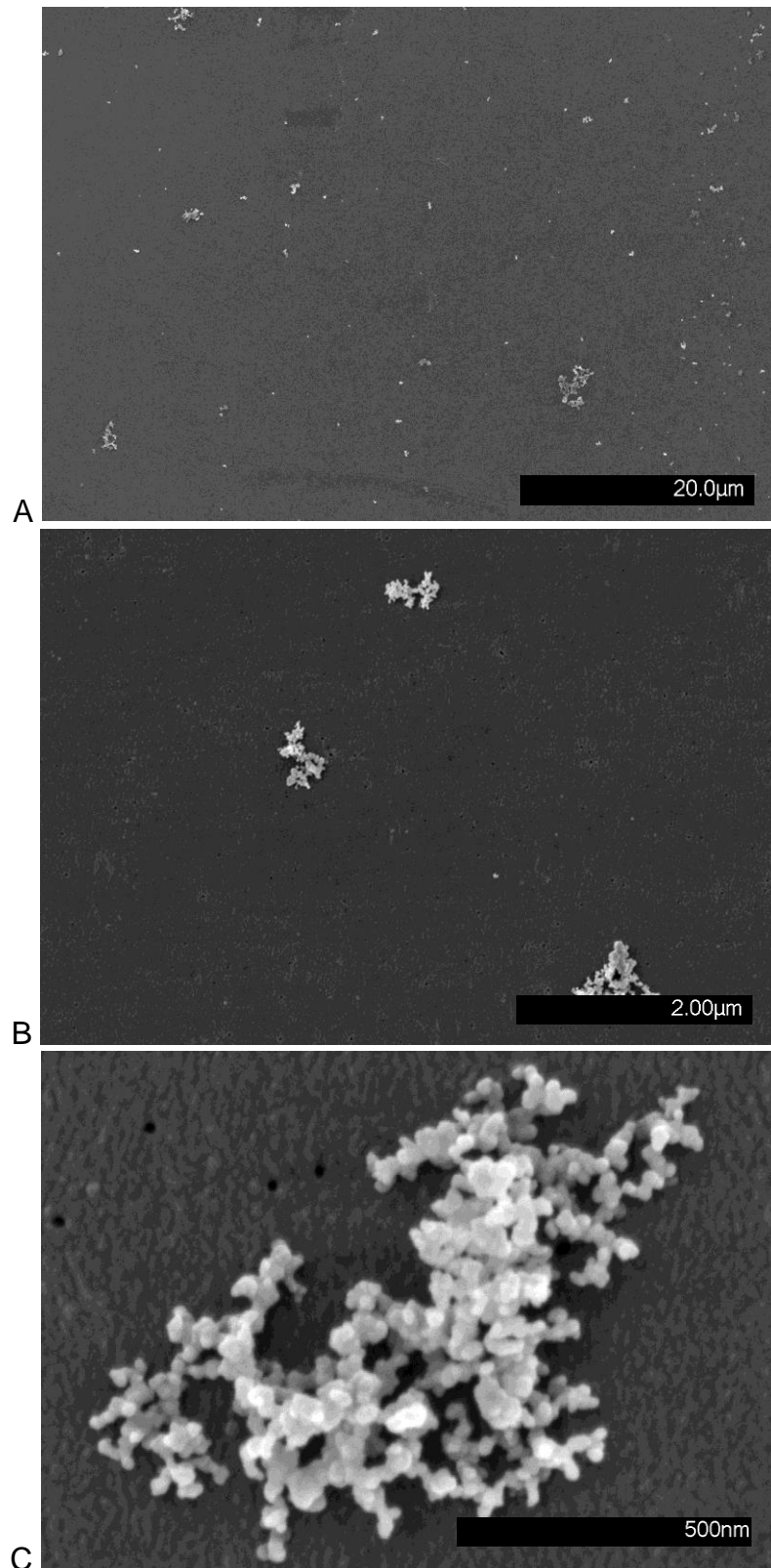
## **4.5 Results**

### **4.5.1 Characterisation of particle suspensions prior to injection into rat stifle joints**

Prior to injection into rat stifle joints, particle suspensions were characterised using scanning electron microscopy, EDX and image analysis. Although commercial SiN particles (Sigma-Aldrich, <50 nm), CoCr and Titanium particles were characterised in Chapter 3, it was necessary to repeat particle characterisation to provide a minimum of three control sets of data per material group to compare to the data obtained for the isolated particles, in order to determine whether any significant changes in terms of particle size, aspect ratio or circularity occurred *in vivo*. In addition, the CoCr and Titanium particles used in the rat study were produced by a different pin-on-plate wear test and therefore particles could have varied slightly due to changes in experimental conditions. It was also important to filter a volume of 0.018 mm<sup>3</sup> of particles to replicate the particle injections as closely as possible, since higher or lower particle volumes may affect particle aggregation, and hence particle size measurements.

#### **4.5.1.1 Scanning electron microscopy of SiN particles**

The SiN particles, when directly suspended in sterile water by sonication and filtered, were observed as aggregates of approximately 0.2 - 2 µm in size distributed across the filter membrane (Figure 4.4A, B). The aggregates formed a branched pattern and particles were nanoscale, spherical and smooth in appearance (Figure 4.4C).



**Figure 4.4. Scanning electron micrographs of non-injected commercial SiN particles.** (A) At 2000x magnification, (B) at 20,000x magnification and (C) at 100,000x magnification. A volume of 0.018 mm<sup>3</sup> of particles was resuspended and filtered on the 0.015 μm polycarbonate filter membranes prior to imaging.

#### **4.5.1.2 Elemental analysis of silicon nitride particles**

##### 4.5.1.2.1 Elemental mapping of silicon nitride particles

Elemental mapping using EDX and Aztec 3.3 software was carried out on a dense cluster of SiN particle aggregates (Figure 4.5A); this produced a map showing that carbon was ubiquitously present (Figure 4.5B), likely due to overlapping signals from the polycarbonate membrane. Iridium signals were also ubiquitous although less intense than carbon signals, and varied slightly in intensity, possibly indicating slight variations in sputter coating thickness. Oxygen signals were also ubiquitous. Silicon signals were much more intense in areas where particles were present and were absent in areas of filter membrane where particles were absent; nitrogen signals followed a similar pattern to silicon signals although were less intense.

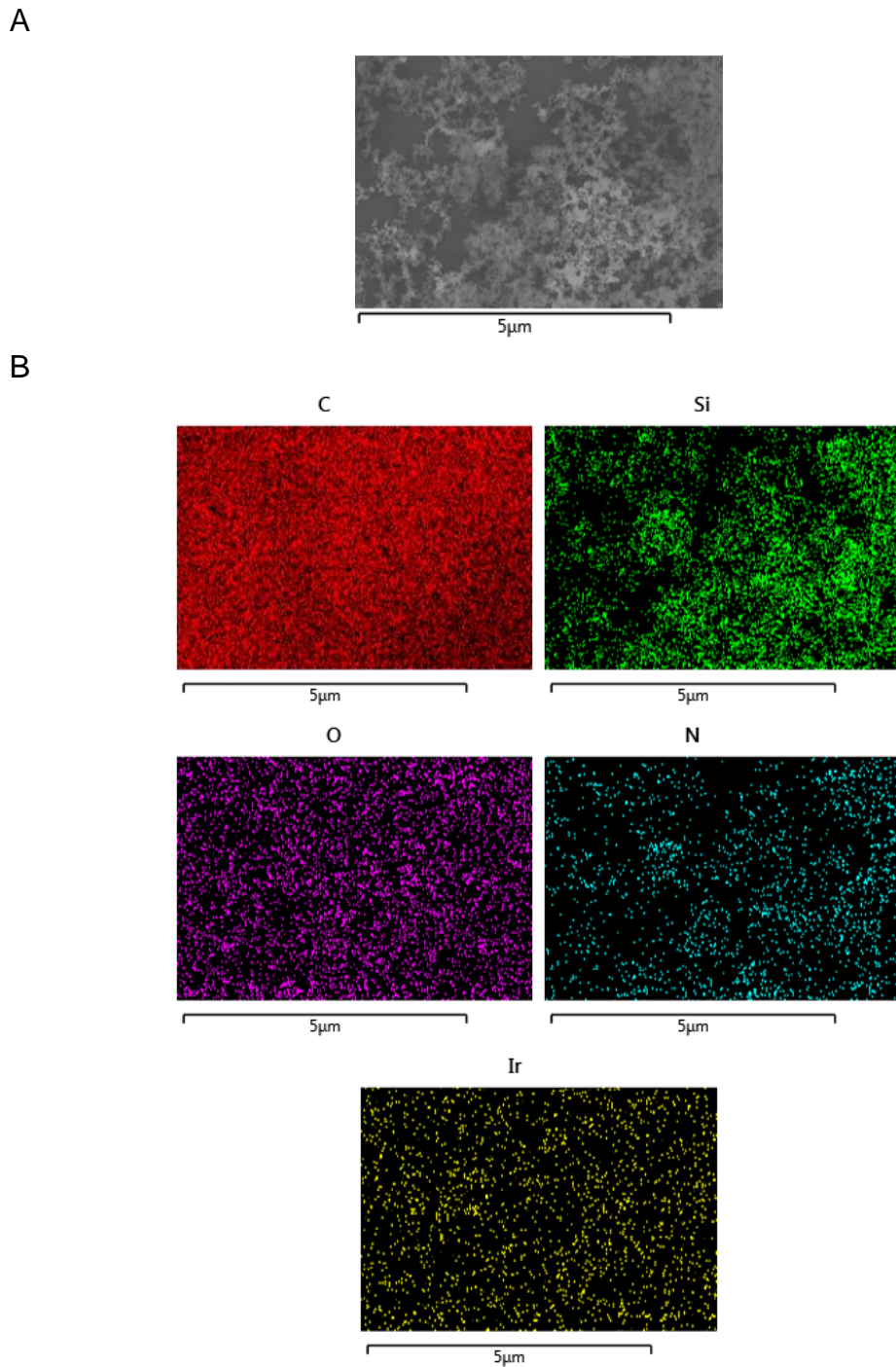
##### 4.5.1.2.2 Spectrum analysis of silicon nitride particles

Spectrum analysis using EDX and Aztec 3.3 software was used to carry out more detailed elemental analysis over smaller areas of the filter. An area containing particles was selected and compared to an area containing no particles (Figure 4.6A). In the area containing particles, elements detected were, from the highest to lowest intensity, carbon, oxygen, nitrogen, silicon and iridium (Figure 4.6B). In the area not containing particles, elements detected were, from the highest to lowest intensity, carbon, oxygen and iridium (Figure 4.6C). This confirmed that carbon, oxygen and iridium were present as background signals from the polycarbonate filter membrane and iridium sputter coating.

#### **4.5.1.3 Characterisation of SiN particles using image analysis**

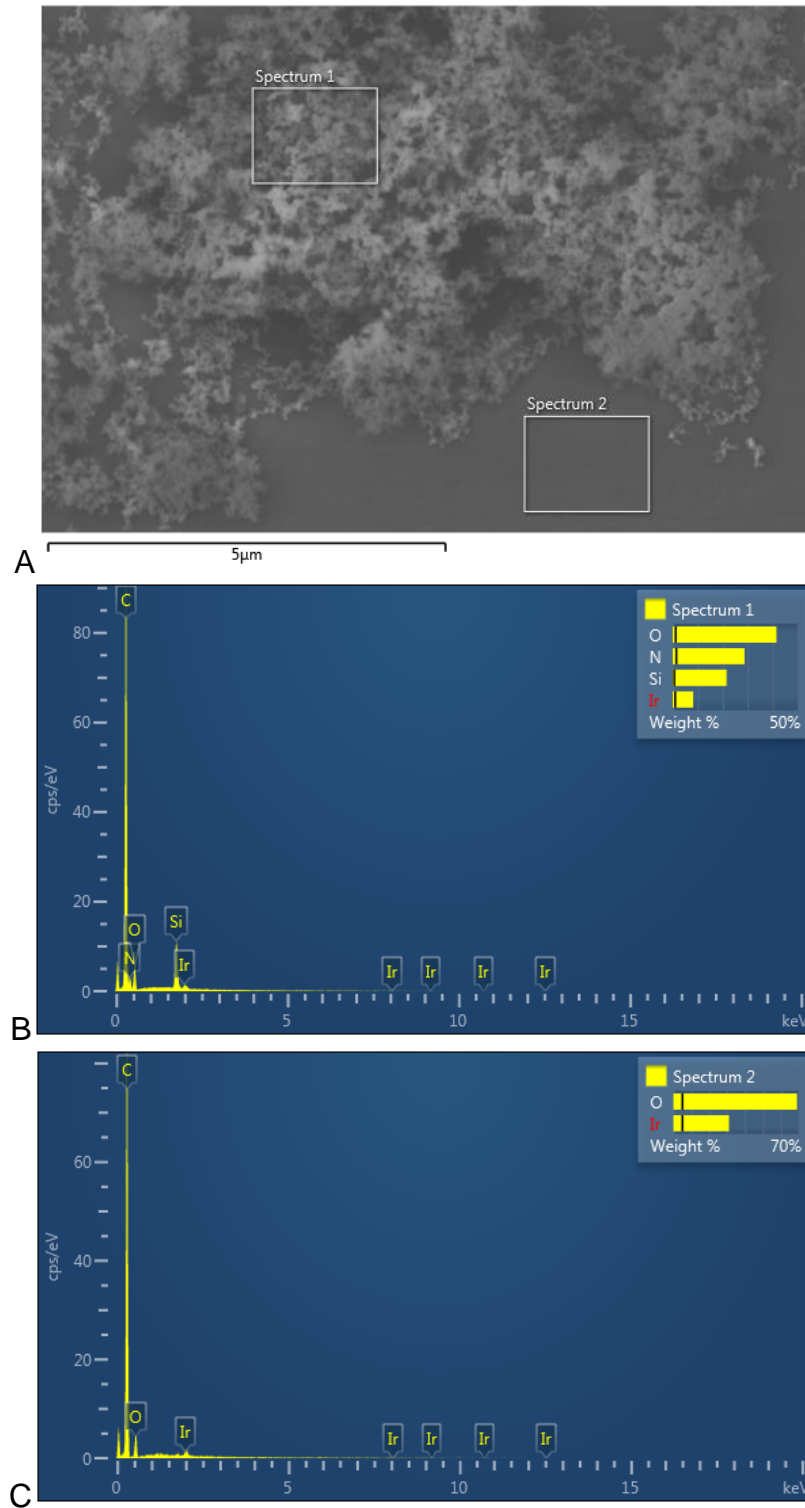
SiN particle sizes ranged from 10-60 nm in size (Figure 4.7A). SiN particles had a modal particle size of 20-30 nm, and an average particle size of 26 nm  $\pm$  1 (SD) (Figure 4.7B). Particles were relatively spherical or oval, with a low aspect ratio of 1.2  $\pm$  0.0 (SD), and a circularity of 0.9  $\pm$  0.0 (SD). Variation in aspect ratio, circularity and size between the repeat samples was low, based on the standard deviation of the measurements.





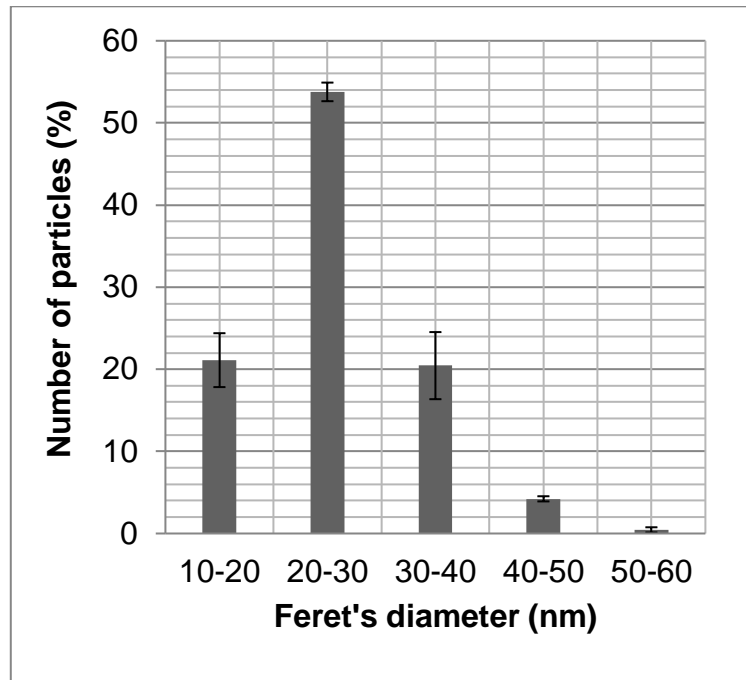
**Figure 4.5. Elemental mapping of non-injected commercial SiN particles.**

(A) Scanning electron micrograph showing the area from the which the elemental maps were produced. (B) The corresponding elemental maps, with the chemical symbol of the element above. A volume of  $0.018 \text{ mm}^3$  of particles was resuspended and filtered on  $0.015 \text{ }\mu\text{m}$  polycarbonate filter membranes; samples were iridium coated. Elements identified were carbon, silicon, oxygen, nitrogen and iridium.



**Figure 4.6. Elemental spectra of non-injected commercial SiN particles.** A volume of 0.018 mm<sup>3</sup> of particles was resuspended and filtered on to a 0.015 μm polycarbonate filter membrane; samples were iridium coated. (A) Scanning electron micrograph showing the area from the which the spectra were produced, (B) a corresponding spectrum from a particle aggregate, and (C) a corresponding spectrum from an area of filter membrane that contained no particles.

A



B

Parameter	Mean ± SD (N=3)
Feret's diameter (nm)	26 ± 1
Aspect ratio	1.2 ± 0.0
Circularity	0.9 ± 0.0

**Figure 4.7. (A) Size distribution of non-injected commercial silicon nitride particles and (B) average particle parameters.** Values are based on the average ImageJ measurements of three samples of 150 particles (total of 450 particles). Error bars on the graph show standard deviation between the three samples.

#### 4.5.1.4 Scanning electron microscopy of cobalt chromium particles

Similar to the SiN particles, when directly suspended in sterile water by sonication and filtered, CoCr particles were observed as aggregates of approximately 0.2 - 2  $\mu\text{m}$  in size distributed across the filter membrane (Figure 4.8A, B). The aggregates however were denser in appearance and less branched compared to the SiN particles. Particles were nanoscale and

spherical in appearance and were smaller than the SiN particles. The particles were too small to identify whether the particle surfaces were rough or smooth (Figure 4.8C).

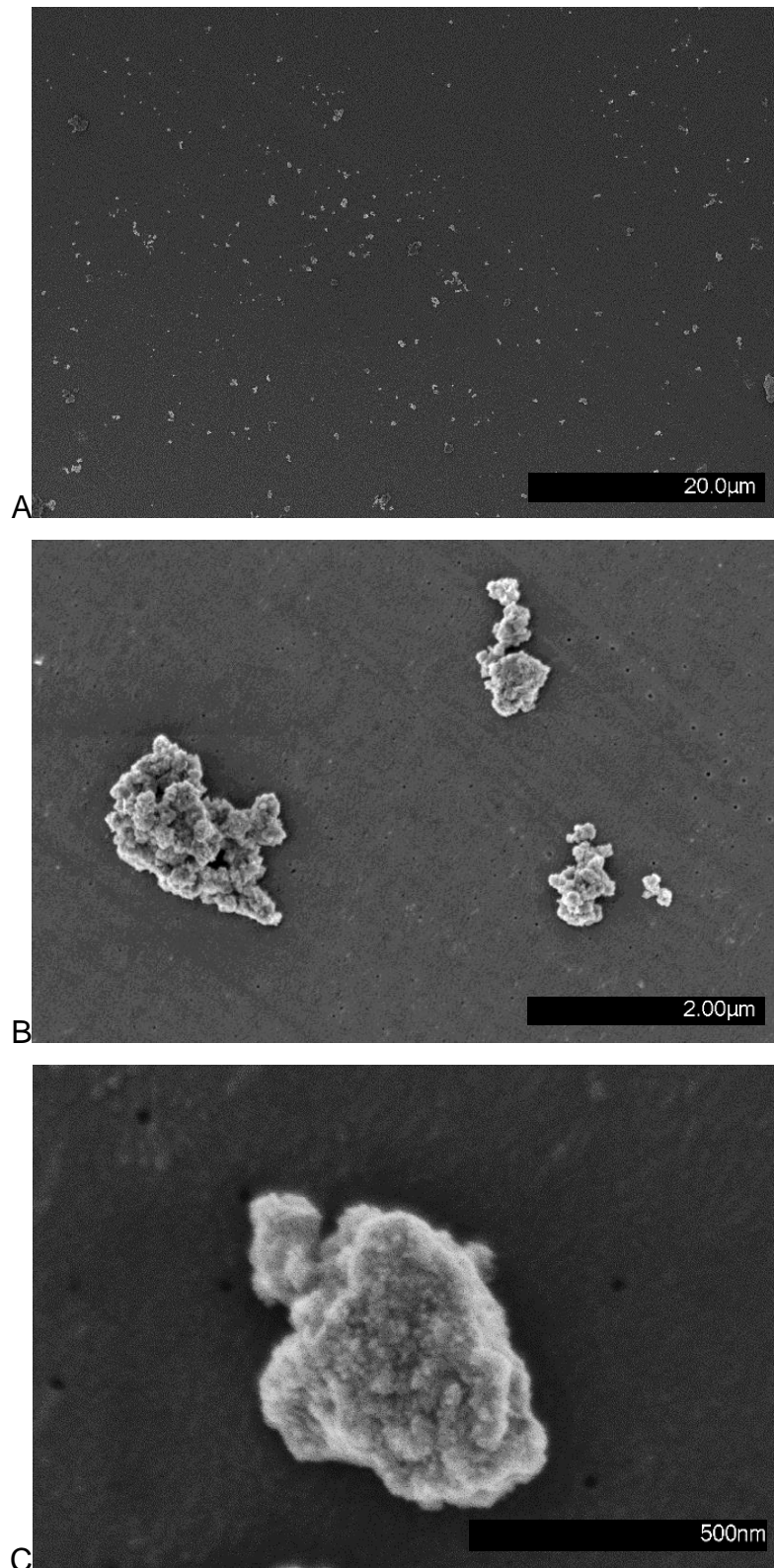
#### **4.5.1.5 Elemental analysis of cobalt chromium particles**

##### 4.5.1.5.1 Elemental mapping of cobalt chromium particles

Elemental mapping using EDX and Aztec 3.3 software was carried out on several CoCr particle aggregates (Figure 4.9A). As with mapping of the SiN particles, carbon was ubiquitously present, with a slightly less intense signal in the area containing particles (Figure 4.9B). Iridium signals were also ubiquitous and were slightly more intense in the area containing particles. Oxygen signals were also ubiquitous, with much higher intensity signals found in the area containing the particle aggregates, suggesting oxidation of particles. Chromium signals were less intense than oxygen signals and were concentrated in areas where particles were present and were absent in areas of the filter membrane containing no particles. Cobalt signals followed a similar pattern to the chromium signals.

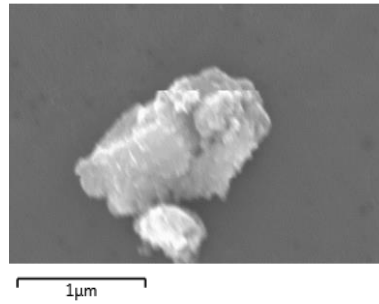
##### 4.5.1.5.2 Spectrum analysis of cobalt chromium particles

As with the SiN particles, spectrum analysis was used to carry out more detailed elemental analysis over smaller areas of the filter; an area containing particles was selected and compared to an area containing no particles (Figure 4.10A). In the area containing particles, elements detected were, from the highest to lowest intensity, carbon, oxygen, cobalt, chromium, iridium and molybdenum (Figure 4.10B). In the area not containing particles, elements detected were, from the highest to lowest intensity, carbon, oxygen and iridium (Figure 4.10C). This confirmed that carbon, oxygen and iridium were present as background signals from the polycarbonate filter membrane and iridium sputter coating.

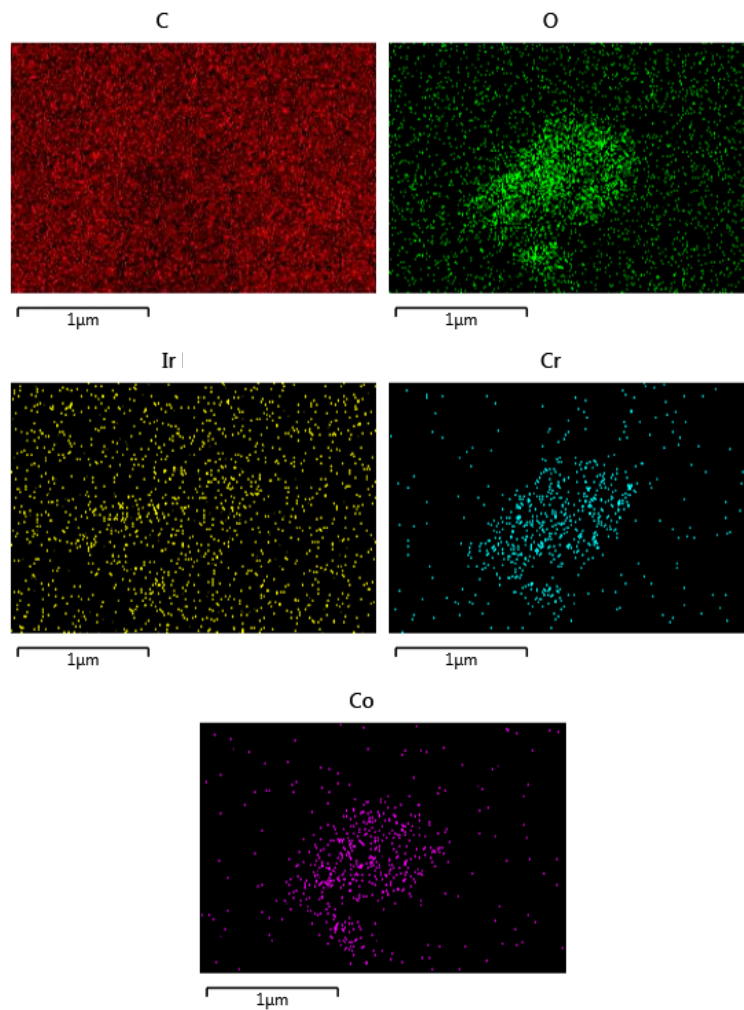


**Figure 4.8. Scanning electron micrographs of non-injected CoCr particles.** (A) At 2000x magnification, (B) at 20,000x magnification and (C) at 100,000x magnification. A volume of 0.018 mm<sup>3</sup> of particles was resuspended and filtered on the 0.015 µm polycarbonate filter membranes prior to imaging.

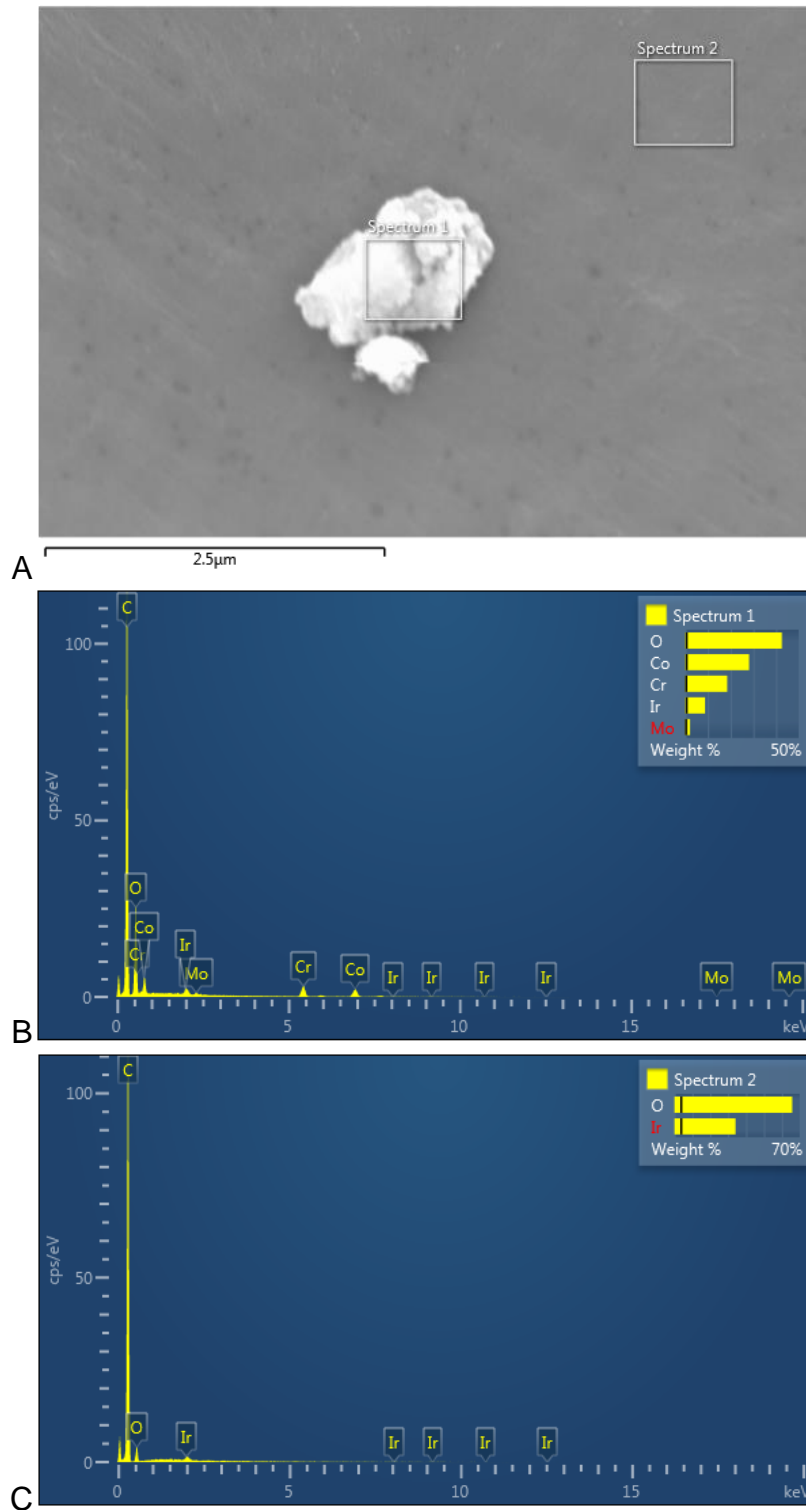
A



B



**Figure 4.9. Elemental analysis of non-injected CoCr particles generated by pin-on-plate.** (A) Scanning electron micrograph showing the area from the which the elemental maps were produced. (B) The corresponding elemental maps, with the chemical symbol of the element above. A volume of  $0.018 \text{ mm}^3$  of particles was resuspended and filtered on  $0.015 \text{ }\mu\text{m}$  polycarbonate filter membranes; samples were iridium coated. Elements identified were carbon, oxygen, iridium, chromium and cobalt.

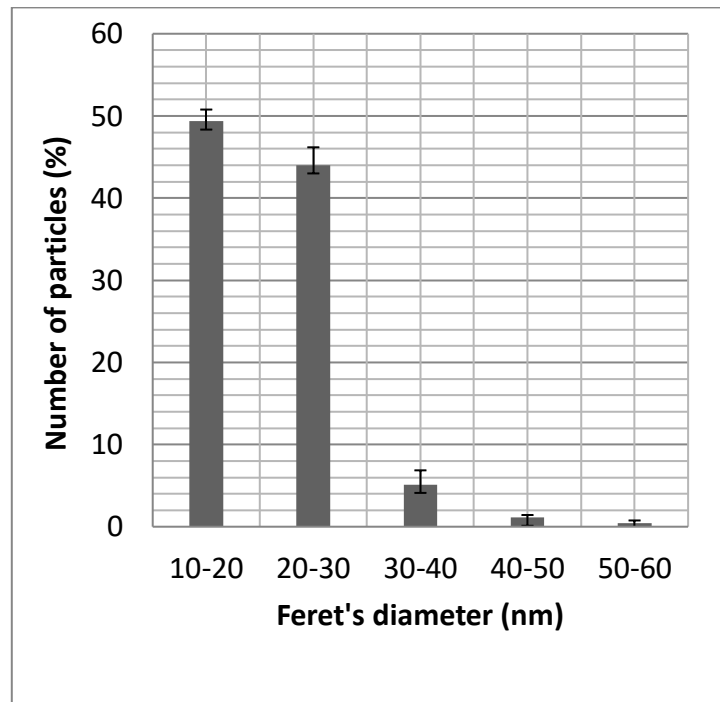


**Figure 4.10. Elemental analysis of non-injected CoCr particles generated by pin-on-plate.** A volume of 0.018 mm<sup>3</sup> of particles was resuspended and filtered onto a 0.015 μm polycarbonate filter membrane; the sample was iridium coated. (A) Scanning electron micrograph showing the area from the which the spectra were produced, (B) a corresponding spectrum from a particle aggregate, and (C) a corresponding spectrum from an area of filter membrane not containing particles.

#### 4.5.1.6 Characterisation of CoCr particles

Similar to SiN particles, CoCr particle sizes ranged from 10-60 nm (Figure 4.11), however CoCr particles had a modal particle size of 10-20 nm, and an average particle size of 21 nm  $\pm$  0 (SD). Particle size thus varied less than SiN particle size. Particles were also spherical or oval, with an aspect ratio of 1.3  $\pm$  0.0 (SD), and a circularity of 0.9  $\pm$  0.0 (SD).

A



B

Parameter	Mean $\pm$ SD (N=3)
Feret's diameter (nm)	21 $\pm$ 0
Aspect ratio	1.3 $\pm$ 0.0
Circularity	0.9 $\pm$ 0.0

**Figure 4.11. (A) Size distribution of non-injected CoCr particles generated by pin-on-plate wear testing and (B) average particle parameters.** Values are based on the average ImageJ measurements of three samples of 150 particles (total of 450 particles). Error bars on the graph show standard deviation between the three samples.



#### **4.5.1.7 Scanning electron microscopy of titanium particles**

Unlike the SiN and CoCr particles, when directly suspended in sterile water by sonication and filtered, titanium particles did not form aggregates and instead individual, micron-scale particles were observed distributed across the filter membrane (Figure 4.12A, B). The particles were much larger and less spherical in appearance than CoCr and SiN particles, and the surface of the particles was rough (Figure 4.12C).

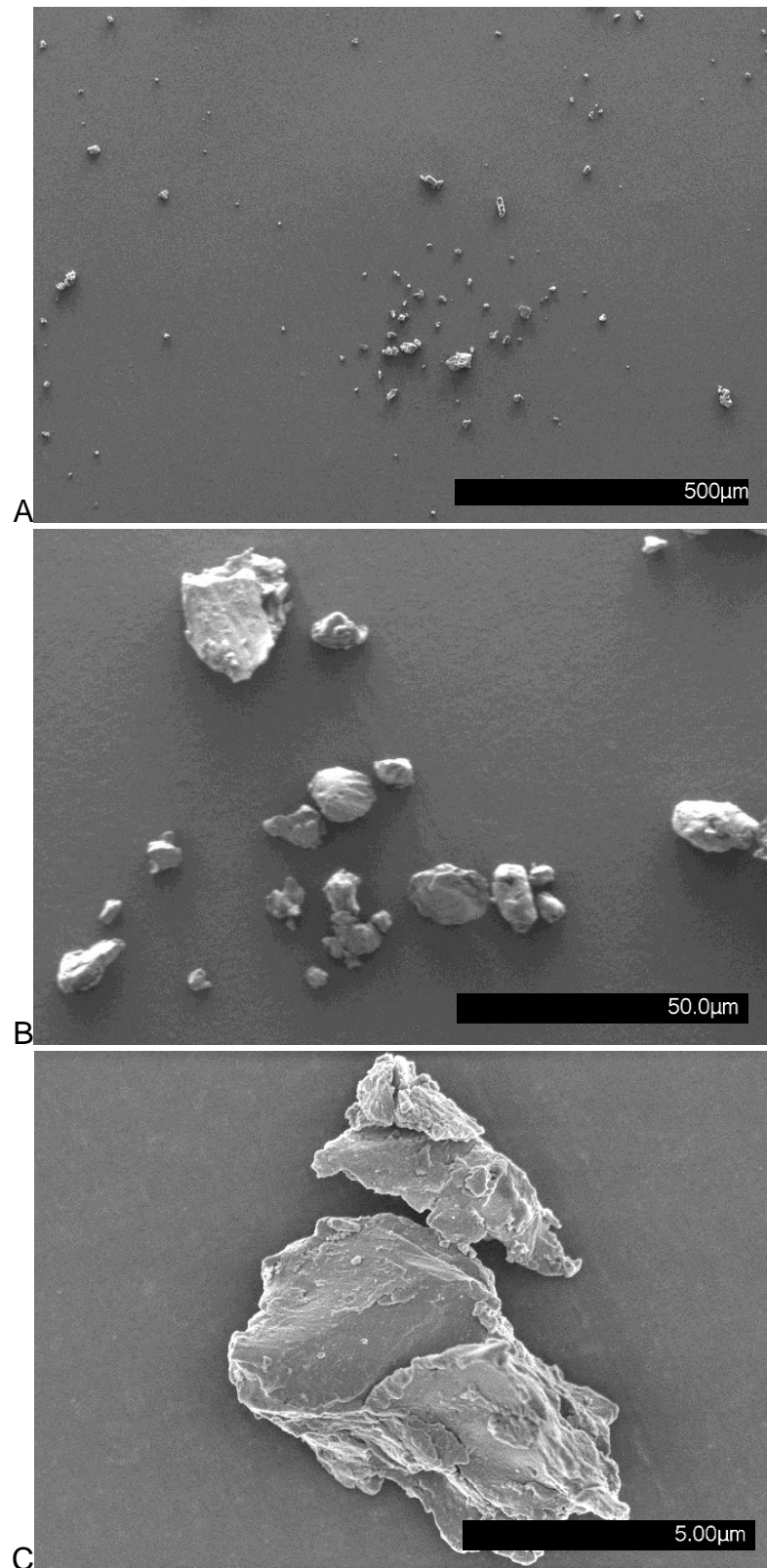
#### **4.5.1.8 Elemental analysis of titanium particles**

##### 4.5.1.8.1 Elemental mapping of titanium particles

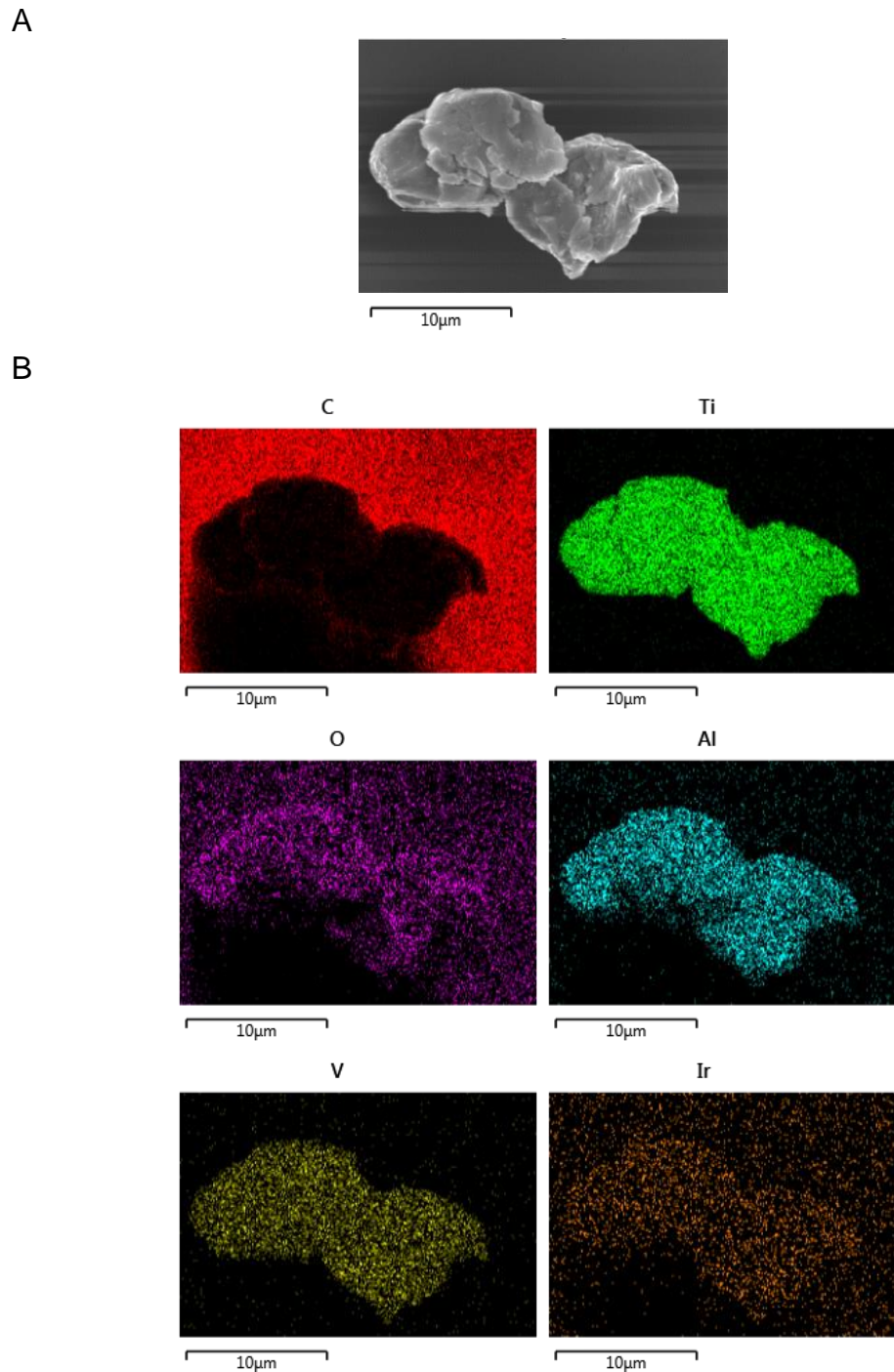
Elemental mapping was carried out on titanium particles (Figure 4.13A); this showed that carbon was ubiquitous in the background but absent from the area containing particles (Figure 4.13B). Iridium signals were also ubiquitous in the background but were also present in higher intensity in the area containing particles, as were oxygen signals, suggesting oxidation of particles. Titanium, aluminium and vanadium signals (in order of decreasing intensity) were concentrated in the areas where particles were present and were absent in areas of the filter membrane which contained no particles.

##### 4.5.1.8.2 Spectrum analysis of titanium particles

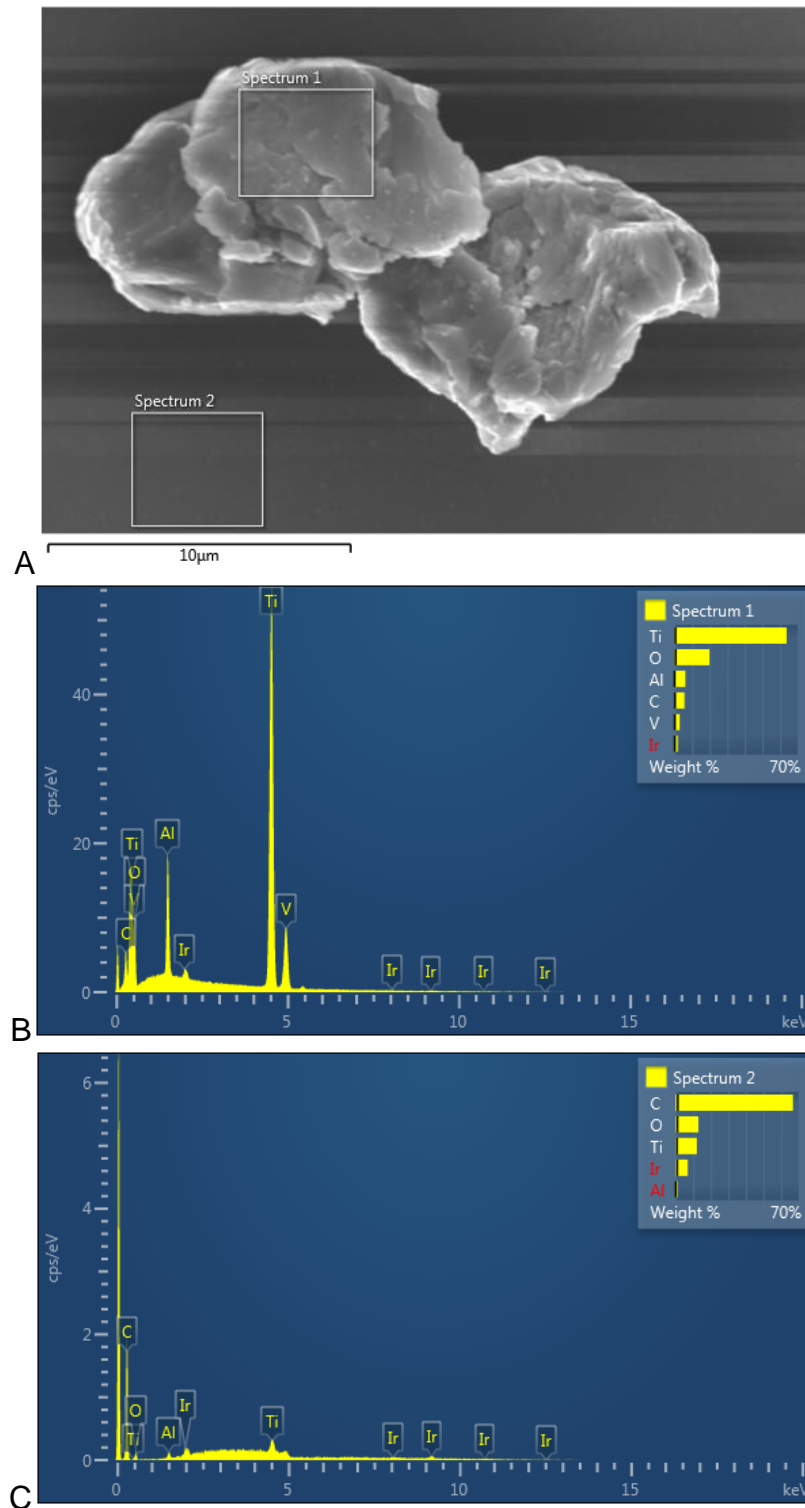
As with the SiN and CoCr particles, spectrum analysis was used to carry out more detailed elemental analysis over smaller areas of the filter; an area containing particles was selected and compared to an area containing no particles (Figure 4.14). In the area containing particles, elements detected were, in order from the highest to lowest intensity, titanium, oxygen, aluminium, carbon, vanadium and iridium. In the area not containing particles, elements detected were, in order from the highest to lowest intensity, carbon, oxygen, titanium, iridium and aluminium. This confirmed that carbon, oxygen and iridium were present as background signals from the polycarbonate filter membrane and iridium sputter coating. The presence of titanium and aluminium signals in the background is likely due to spectral overlap from nearby areas of the membrane. Since oxygen and not carbon was the second most abundant element in the area containing particles, the analysis confirmed that particle oxidation likely occurred.



**Figure 4.12. Scanning electron micrograph of non-injected titanium particles.** (A) 100x magnification, (B) 1,000x magnification and (C) 10,000x magnification. Particles were generated by pin-on-plate by another researcher. A volume of 0.018 mm<sup>3</sup> of particles was resuspended and filtered on 0.015 μm polycarbonate filter membranes.



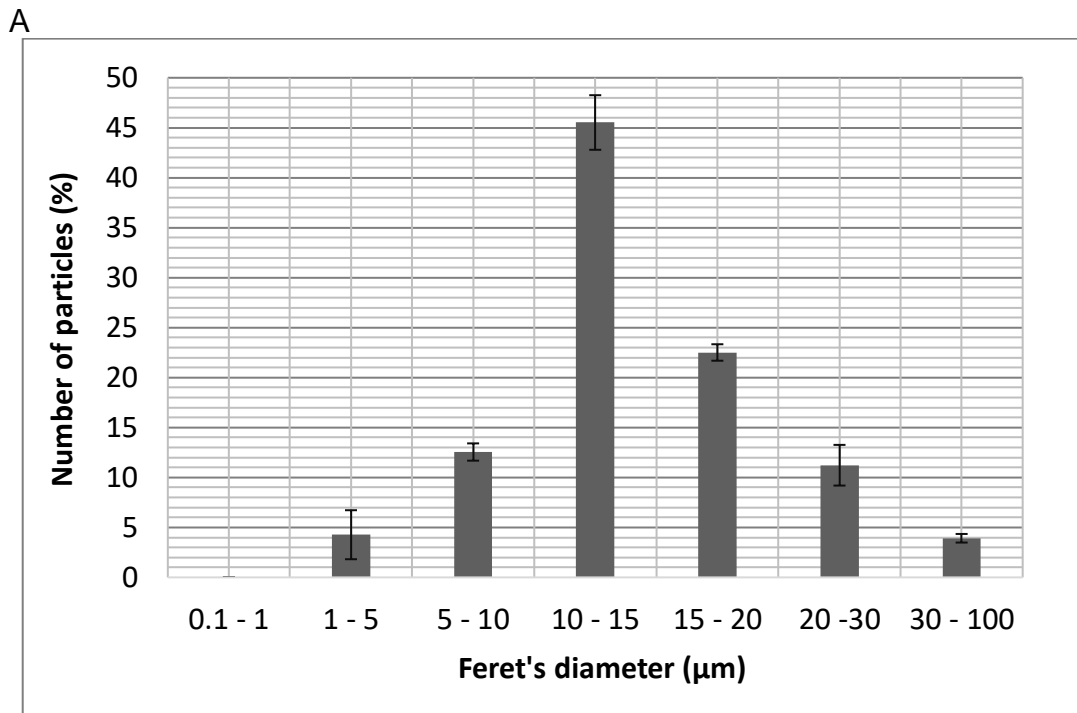
**Figure 4.13. Elemental analysis of non-injected titanium particles generated by pin-on-plate wear testing.** (A) A scanning electron micrograph showing the area from the which the elemental maps were produced and (B) the corresponding elemental maps, with the chemical symbol of the element above. A volume of 0.018 mm<sup>3</sup> of particles was resuspended and filtered on 0.015  $\mu$ m polycarbonate filter membranes; samples were iridium coated. Elements identified included carbon, titanium, oxygen, aluminium, vanadium and iridium.



**Figure 4.14. Elemental analysis of non-injected CoCr particles generated by pin-on-plate.** A volume of 0.018 mm<sup>3</sup> of particles was resuspended and filtered onto a 0.015 µm polycarbonate filter membrane; the sample was iridium coated. (A) Scanning electron micrograph showing the area from the which the spectra were produced, (B) a corresponding spectrum from a particle, and (C) a corresponding spectrum from an area of the filter membrane not containing particles.

#### 4.5.1.9 Characterisation of titanium particles

Titanium particles exhibited a much wider size distribution than SiN or CoCr particles, with sizes ranging from 1 - 100  $\mu\text{m}$  (Figure 4.15A). Titanium particles had a modal particle size of 10 - 15  $\mu\text{m}$ , and an average particle size of 15  $\mu\text{m} \pm 0$  (SD). Particles were thus much larger than SiN or CoCr particles. Particles were also less spherical, with an aspect ratio of  $1.6 \pm 0.0$ , and a circularity of  $0.8 \pm 0.0$ . Particle aspect ratio thus also varied more than for SiN or CoCr particles.



B

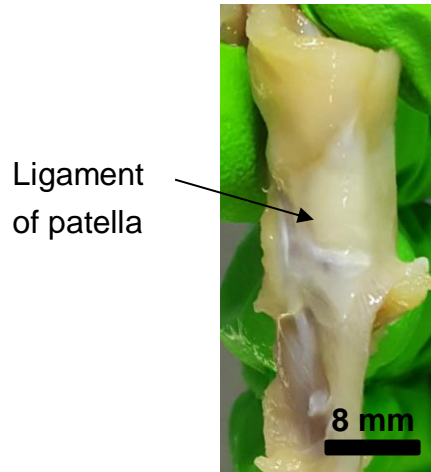
Parameter	Mean $\pm$ SD (N=3)
Feret's diameter ( $\mu\text{m}$ )	15 $\pm$ 0
Aspect ratio	1.6 $\pm$ 0.0
Circularity	0.8 $\pm$ 0.0

**Figure 4.15. (A) Size distribution of non-injected titanium particles generated by pin-on-plate wear testing and (B) average particle parameters.** Values are based on the average ImageJ measurements of three samples of <100 particles. Error bars on the graph show standard deviation between the three samples.

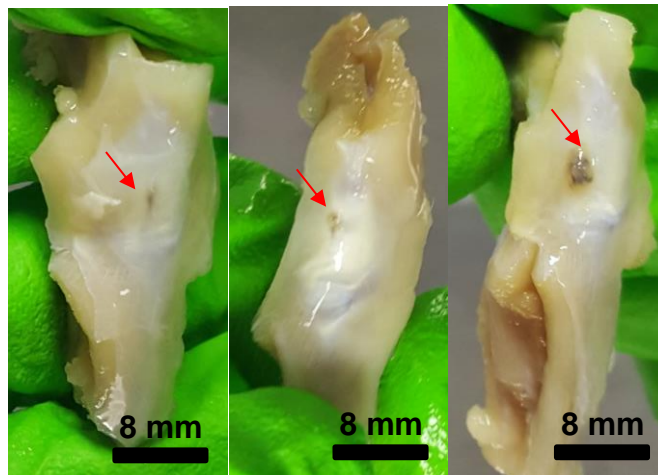
#### **4.5.2 Observations of rats and rat stifle joints prior to and after sacrifice**

Based on communications with the University of Zurich, there were no behavioural or physiological observations in the live rats indicative of a response to the particles. Following sacrifice and shipment of the excised stifle joints, macroscopic observation of the intact SiN and titanium injected joints gave no indications of inflammation or any other biological reaction and were similar in appearance to the control joints (Figure 4.16A). The intact CoCr injected stifle joints showed signs of darkened tissue within the patella ligament (Figure 4.16B). Such darkened areas were apparent to varying degrees in all of the CoCr injected stifle joints and were completely absent in other joints.

A



B



**Figure 4.16. Appearance of intact stifle joints following formalin fixation and storage in 70% (v/v) ethanol.** (A) Untreated control stifle joint from CoCr material group. (B) Darkened tissue in three different CoCr-injected stifle joints, indicated by red arrows.

#### **4.5.3 Particle isolation from injected rat stifle joints**

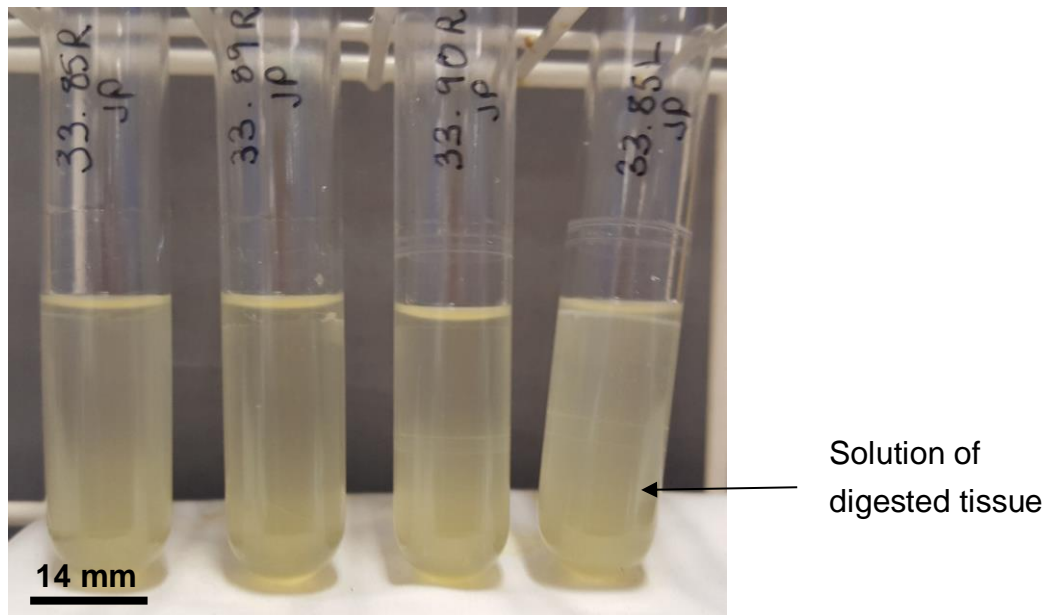
Animals were assigned identification numbers, which were used to label samples throughout the particle isolation process (Table 4.7).

**Table 4.7. Identification numbers used for each animal sample for particle isolation.**

Animal number	Group	Details of materials injected*	Additional details
33.85	Silicon nitride	Si <sub>3</sub> N <sub>4</sub> , commercially available nanopowder (<50nm, Sigma-Aldrich, UK)	All animals were injected with a volume of 0.018 mm <sup>3</sup> of particles for an <b><i>in vivo</i></b> exposure time of seven days prior to sacrifice
33.89			
33.90			
33.76	Cobalt chromium	Particles generated by pin-on-plate in house (high carbon >0.2 % medical grade alloy; (ASTM, F1537))	
33.77			
33.78			
33.79	Titanium	Particles generated by pin-on-plate in house (medical grade Ti-6Al-4V alloy)	
33.80			
33.81			

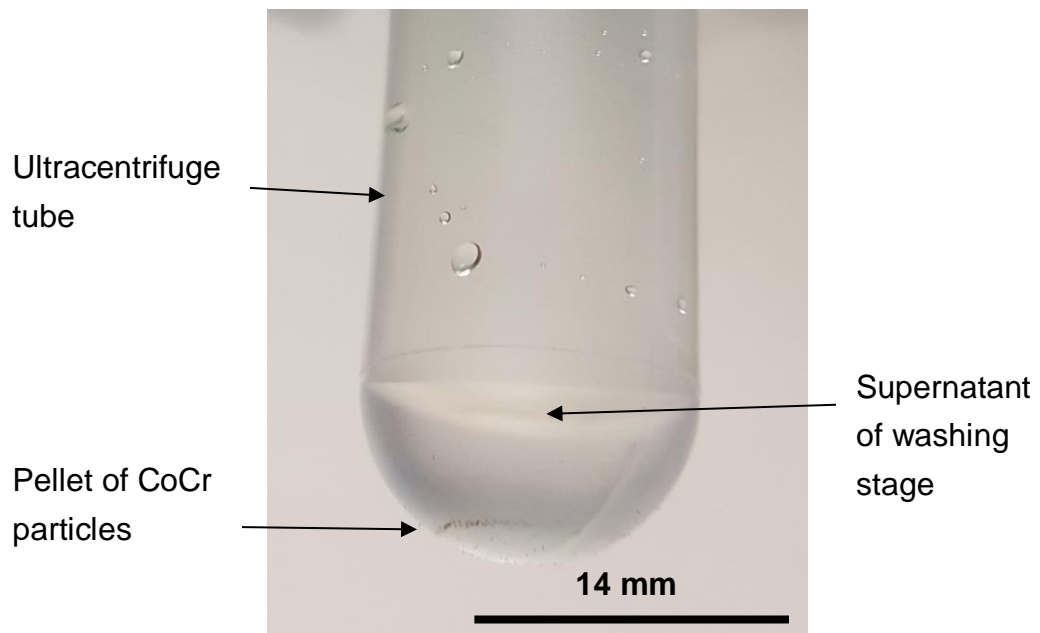
Tissues from each injected joint, in addition to a non-injected control, were minced and digested enzymatically as part of the particle isolation process. Digested tissues formed a cloudy solution (Figure 4.17), with no visible pieces of tissue. The control digested sample was similar in appearance to the other samples.





**Figure 4.17. Appearance of SiN injected rat tissue samples, and an untreated control rat tissue sample from a contralateral stifle joint (last tube on right), post-digestion.** Each sample consisted of approximately 150 mg (wet weight) of tissue. Digested tissue samples from the CoCr and titanium groups were similar (data not shown).

Digested tissues samples were subjected to density gradient ultracentrifugation. Following density gradient ultracentrifugation of samples and each washing stage of the protocol, CoCr-injected tissue samples formed a visible circular pellet at the bottom of each ultracentrifuge tube (Figure 4.18). A visible pellet did not form in SiN or titanium injected tissue samples, or untreated control tissues samples.



**Figure 4.18. Pellet of CoCr particles isolated from a CoCr injected rat stifle joint (33.76) during the washing stages of the particle isolation protocol, following each ultracentrifugation step. A visible pellet was absent from the control samples and from the other material groups.**

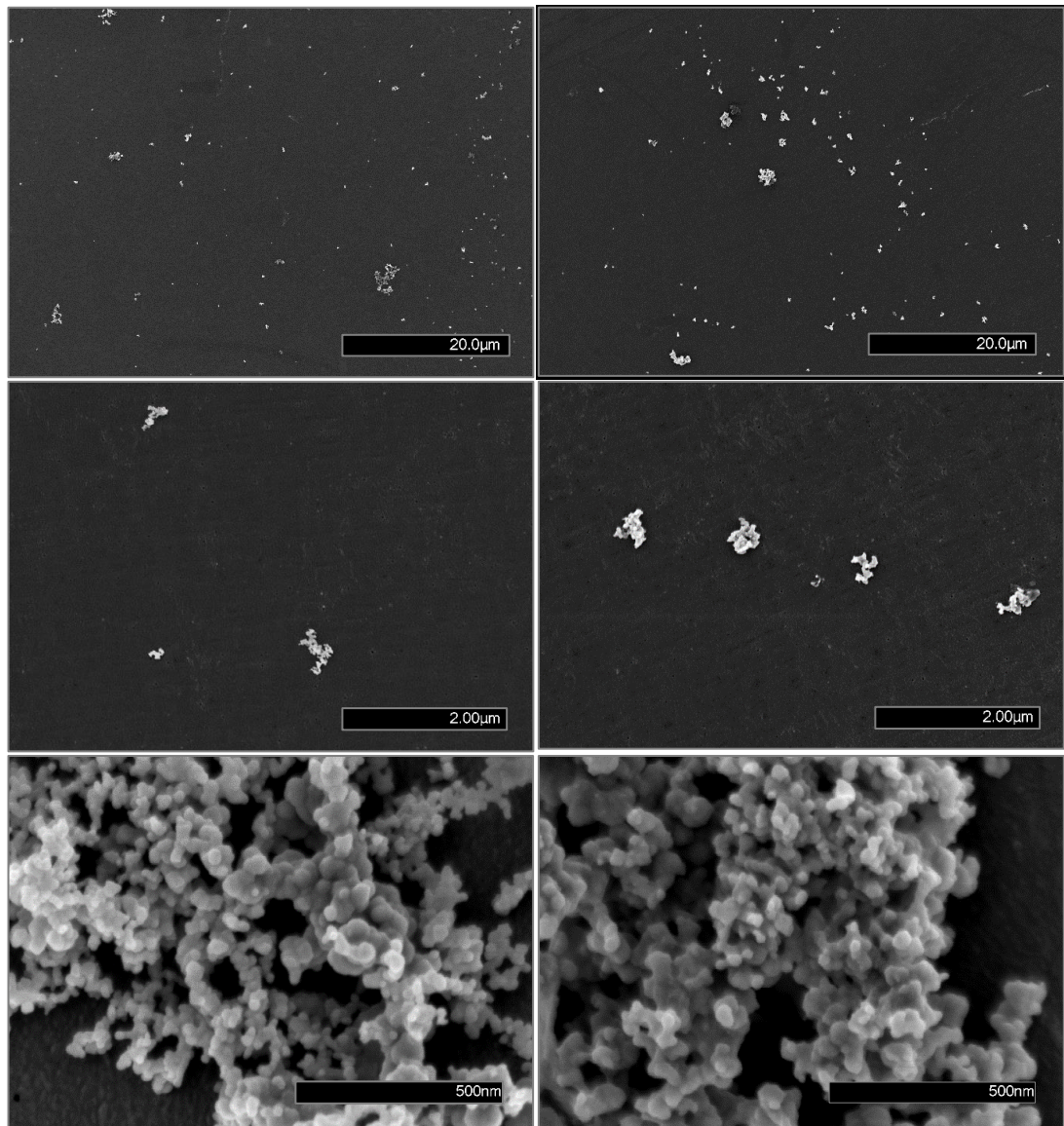
#### **4.5.4 Visual observation of isolated particles using SEM**

Isolated particles were resuspended, filtered and then analysed by SEM. Particles were successfully isolated from each particle-injected stifle joint that was subjected to the isolation process (three per material group). A control sample, which consisted of an untreated contralateral stifle joint was also subjected to the isolation process for each material group (total of three controls) and these controls did not contain any particles and were largely free from contaminants. In addition, none of the samples contained any visible traces of protein or bacteria. In each case, the results of all three repeat isolations were similar, in terms of particle aggregation, particle size and morphologies, and all lacked visible traces of protein or bacterial contamination.

#### **4.5.5 Comparison of SEM images of isolated particles with non-injected particles**

Similar to SiN particles before injection, isolated particles were observed as aggregates of approximately 0.2 - 2  $\mu\text{m}$  in size distributed across the filter

membrane (Figure 4.19). The aggregates once again had a branched pattern and particles were nanoscale, spherical and smooth in appearance. Results were similar in each sample (N=3).

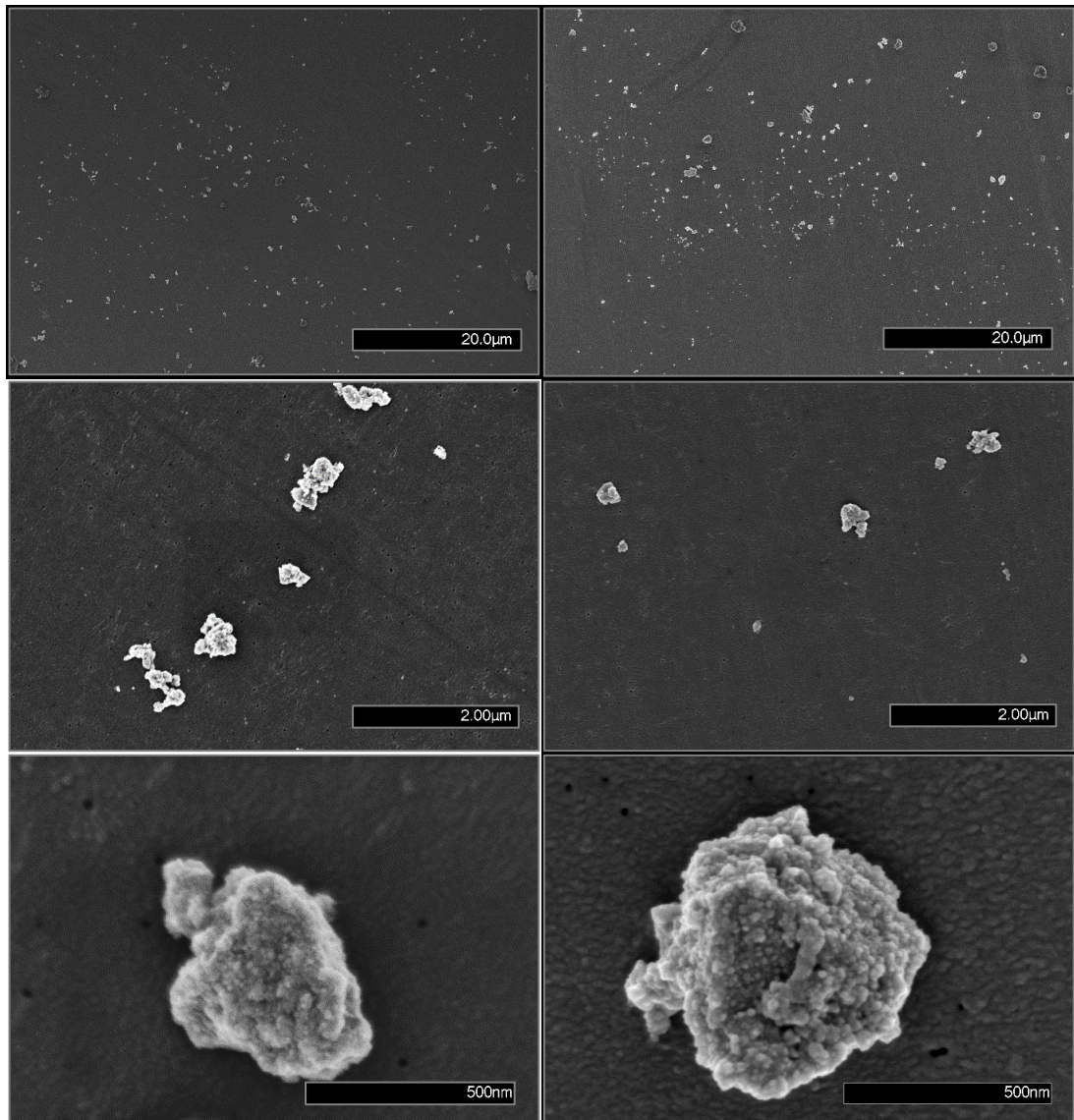


**Figure 4.19. Commercial silicon nitride particles (<50nm, Sigma) imaged by high resolution scanning electron microscopy.** Left: Particles before subjection to the recovery procedure (control 1). Right: following isolation from an injected rat stifle joint (33.89R), after a 7-day *in vivo* time point. Top: at 2,000x magnification. Middle: at 20,000x magnification. Bottom: at 100,000x magnification.

Isolated CoCr particles were also similar in appearance to the non-injected CoCr particles; they formed dense aggregates of approximately 0.2 - 2 µm in size distributed across the filter membrane (Figure 4.20). Particles were



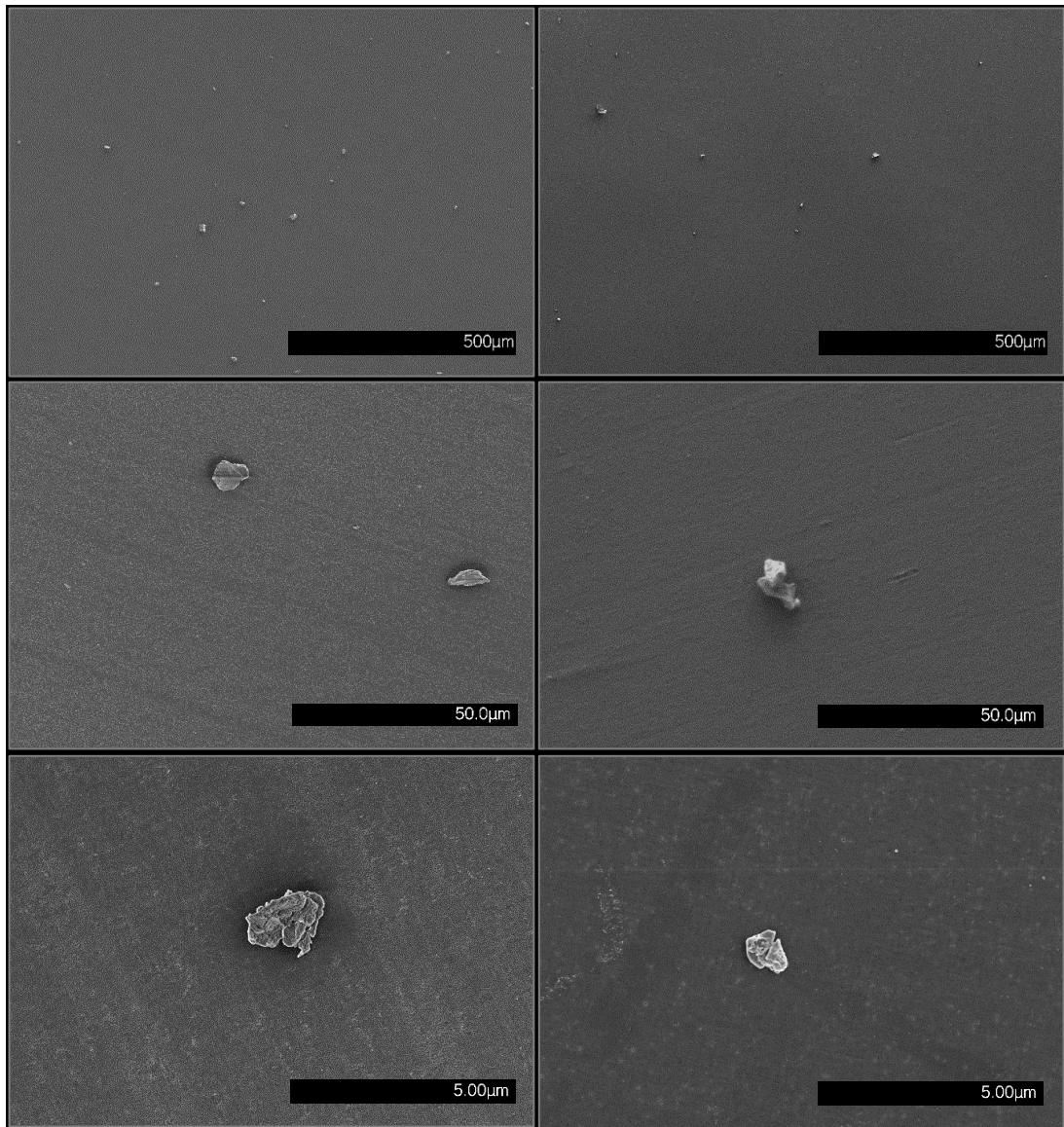
nanoscale and spherical in appearance. Results were similar in each sample (N=3).



**Figure 4.20. Clinically relevant CoCr particles generated using a pin-on-plate wear tester, filtered onto polycarbonate filter membranes at a volume of 0.018 mm<sup>3</sup>, and imaged by high resolution scanning electron microscopy. Left: particles before subsection to the recovery procedure (control 1). Right: following isolation from an injected rat stifle joint (33.76R), after a 7-day *in vivo* time point. Top: at 2,000x magnification. Middle: at 20,000x magnification. Bottom: at 100,000x magnification.**

Titanium particles were also similar before injection and post-isolation. Isolated titanium particles did not form aggregates; individual, micron-scale particles were observed distributed across the filter membrane (Figure 4.21). The particles were much larger and less spherical in appearance than CoCr

and SiN particles, and the surface of the particles was rough. Results were similar for in each of the three samples.



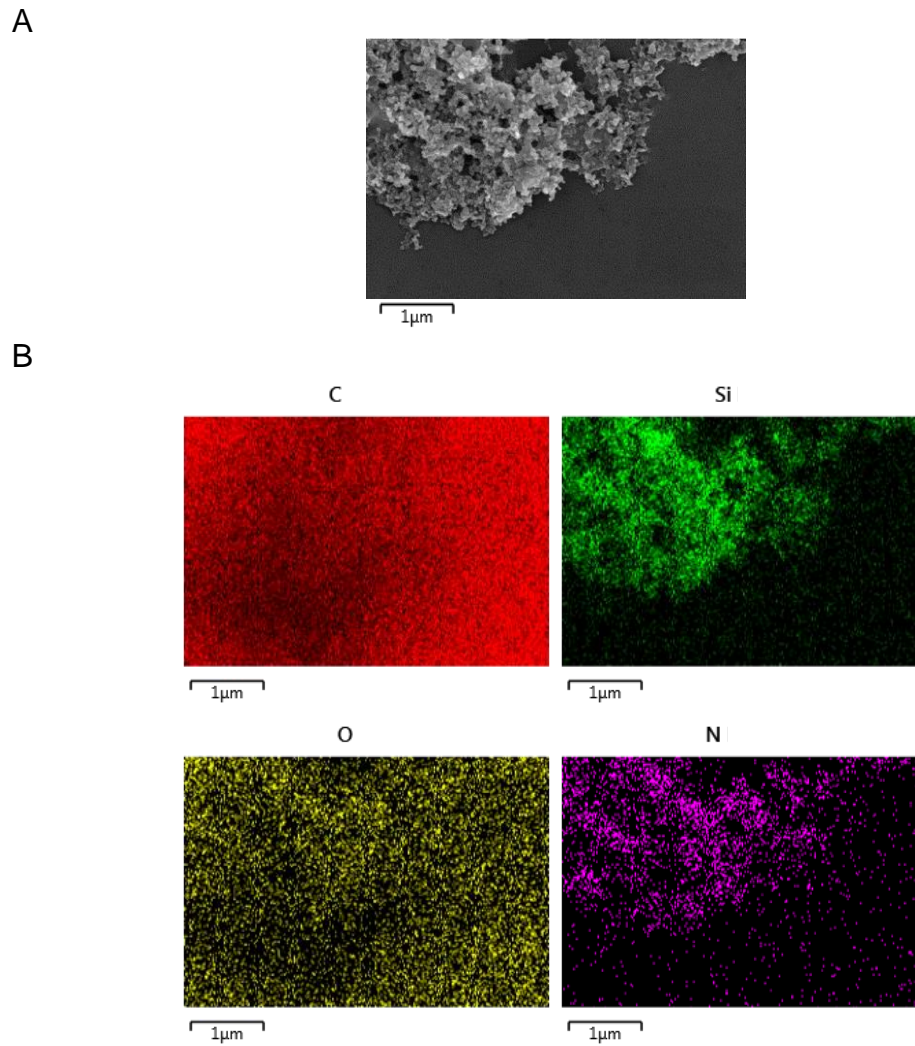
**Figure 4.21. Clinically relevant titanium particles generated using a pin-on-plate wear tester, filtered onto polycarbonate filter membranes at a volume of 0.018 mm<sup>3</sup>, and image by high resolution scanning electron microscopy. Left: particles before subsection to the recovery procedure (control 1). Right: following isolation from an injected rat stifle joint (33.81R), after a 7-day *in vivo* time point. Top: at 2,000x magnification. Middle: at 20,000x magnification. Bottom: at 100,000x magnification.**

#### **4.5.6 Elemental analysis of isolated particles**

Elemental mapping and spectrum analysis was performed in the same way as for the non-injected particles, using EDX and Aztec 3.3 software during SEM analysis.

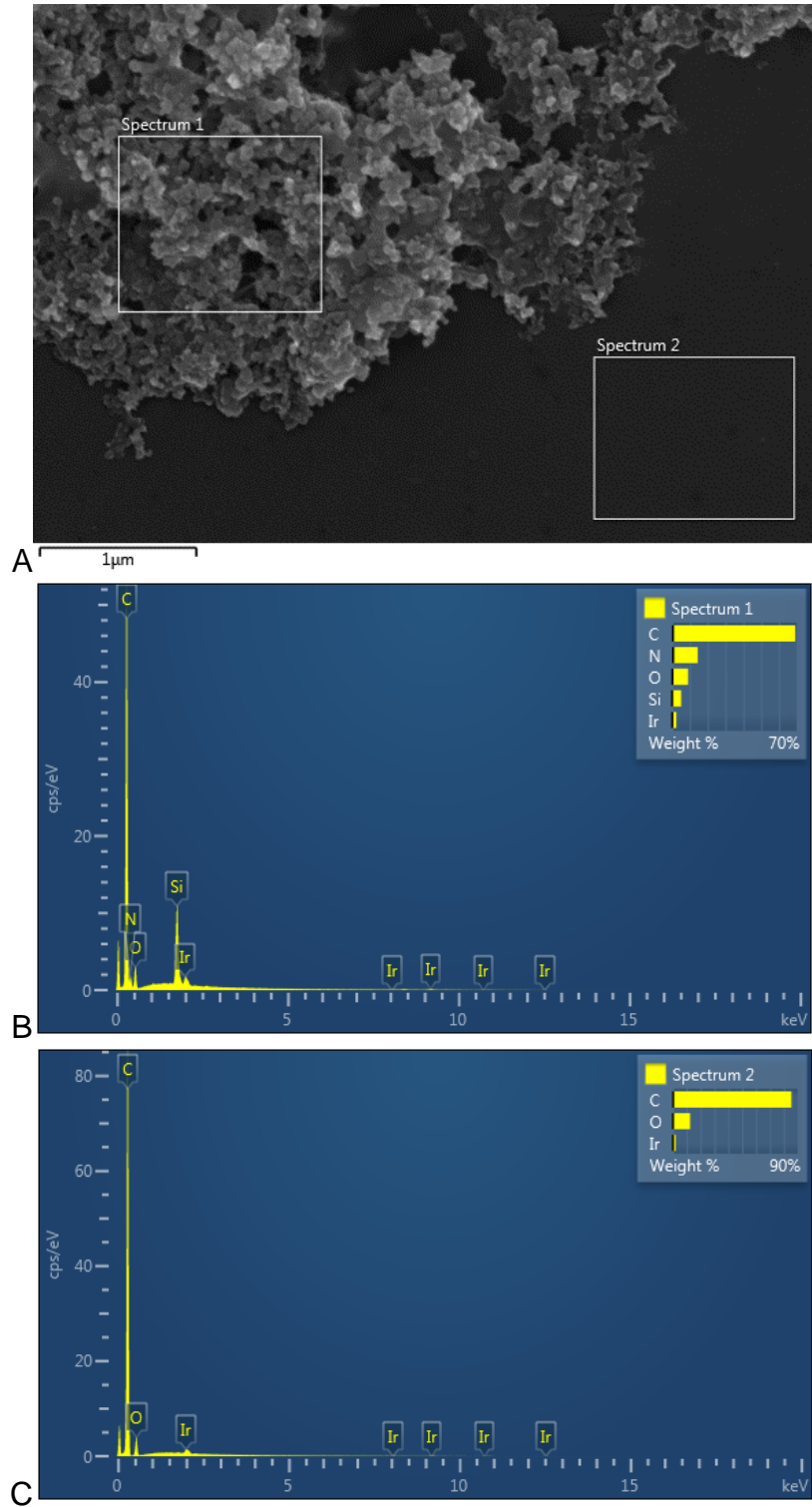
Elemental mapping of a dense cluster of isolated SiN particle aggregates produced very similar results to those of non-injected SiN particles (Figure 4.22A,B); carbon and oxygen signals were ubiquitous across the filter due to the polycarbonate membrane. Silicon signals, and to a lesser extent nitrogen signals, were concentrated in areas containing particles. This suggests that SiN particles were not chemically changed by the isolation process.





**Figure 4.22. Elemental analysis of SiN particles isolated from an injected rat stifle (33.90R).** A. Scanning electron micrograph showing the area from the which the elemental maps were produced and (B) the corresponding elemental maps, with the chemical symbol of each element given above. A volume of  $0.018 \text{ mm}^3$  of particles was resuspended and filtered on  $0.015 \mu\text{m}$  polycarbonate filter membranes; samples were iridium coated. Elements identified included carbon, silicon, oxygen and nitrogen.

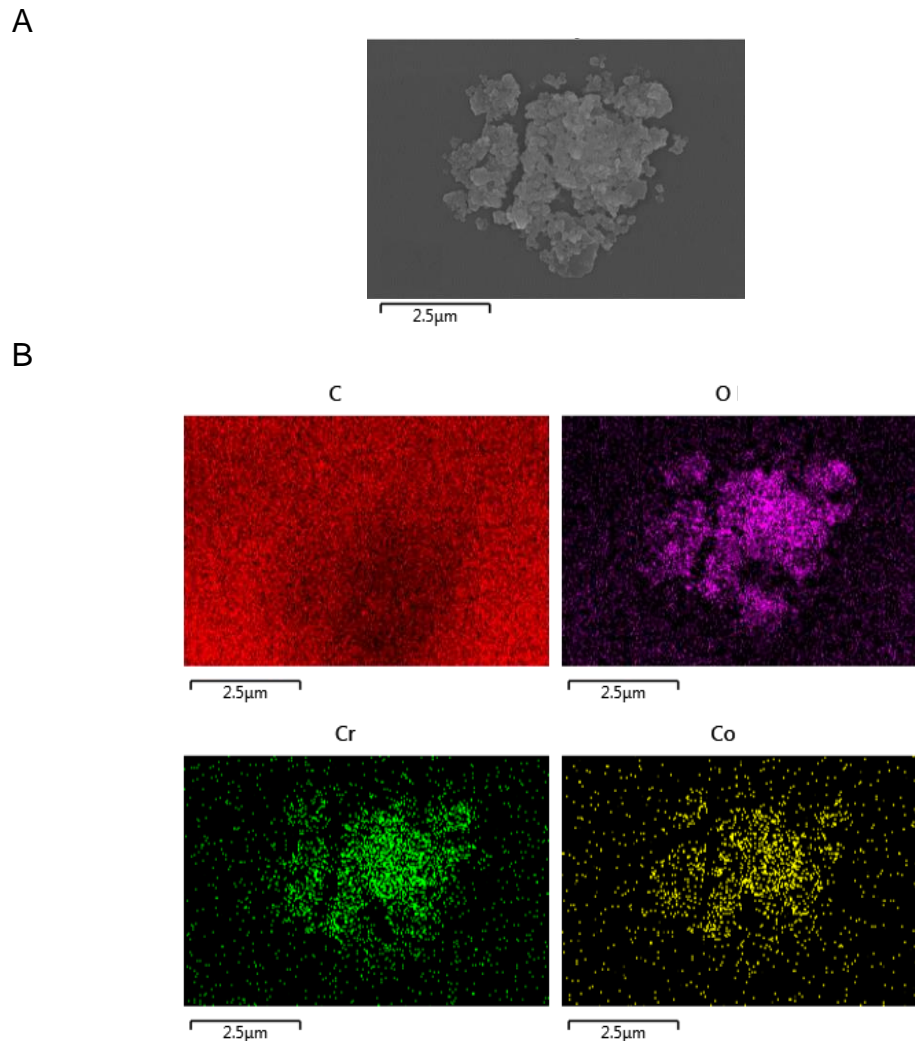
Spectrum analysis was again used to carry out more detailed elemental analysis over smaller areas of the filter (Figure 4.23A - C); results differed from non-injected particles only in the spectrum taken directly over a particle aggregate, in which nitrogen was more prevalent than oxygen (Figure 4.23B).



**Figure 4.23. Elemental spectra of SiN particles isolated from an injected rat stiffl joint (33.85R).** A volume of 0.018 mm<sup>3</sup> of particles was resuspended and filtered on 0.015 μm polycarbonate filter membranes; samples were iridium coated. (A) Scanning electron micrograph showing the area from the which the spectra were produced, (B) a corresponding spectrum from a particle, and (C) a corresponding spectrum from an area of blank filter membrane.



Isolated CoCr particles produced similar elemental maps to those of CoCr particles before injection (Figure 4.24A, B); however, the ratio of cobalt to chromium shifted, with more chromium present than cobalt post-isolation. Carbon was ubiquitous across the filter membrane but produced a less intense signal in areas containing particles. Oxygen signals were also ubiquitous, with higher intensity signals found in the area containing the particle aggregates, suggesting oxidation of particles. Chromium signals were again less intense than oxygen signals and were concentrated in areas where particles were present and were absent in areas of filter membrane containing no particles; cobalt signals followed a similar pattern to chromium signals, though were less intense.



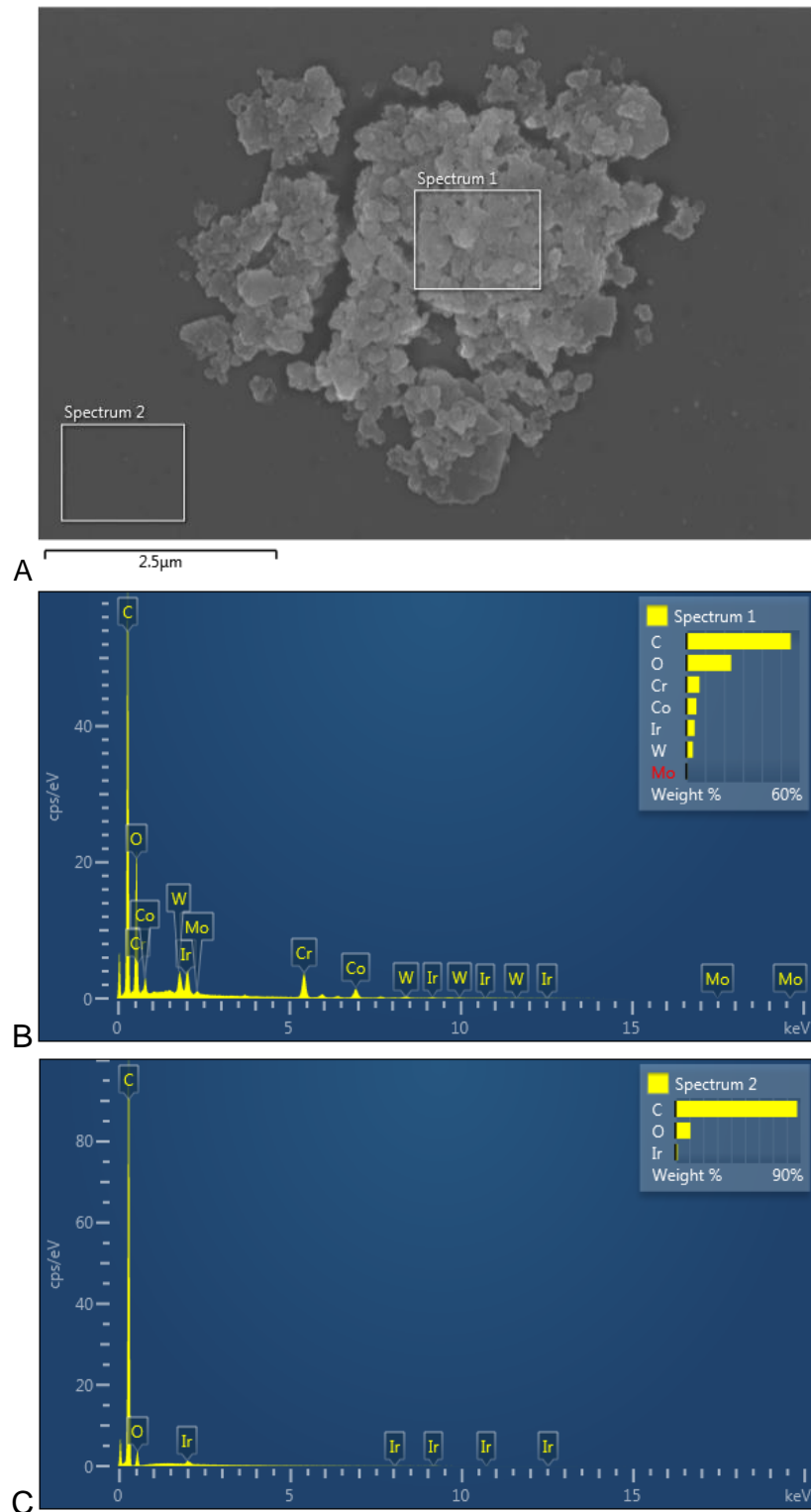
**Figure 4.24. Elemental analysis of CoCr particles isolated from an injected rat stifle (33.76R).** A. Scanning electron micrograph showing the area from the which the elemental maps were produced and (B) the corresponding elemental maps, with the chemical symbol of each element given above. A volume of 0.018 mm<sup>3</sup> of particles was resuspended and filtered on 0.015 μm polycarbonate filter membranes; samples were iridium coated. Elements identified included carbon, oxygen, chromium and cobalt.

Spectrum analysis was similar in the spectrum taken over the blank filter membrane, and in the spectrum taken over the CoCr particles (Figure 4.25). Once again chromium was more abundant than cobalt; however, tungsten was also present.

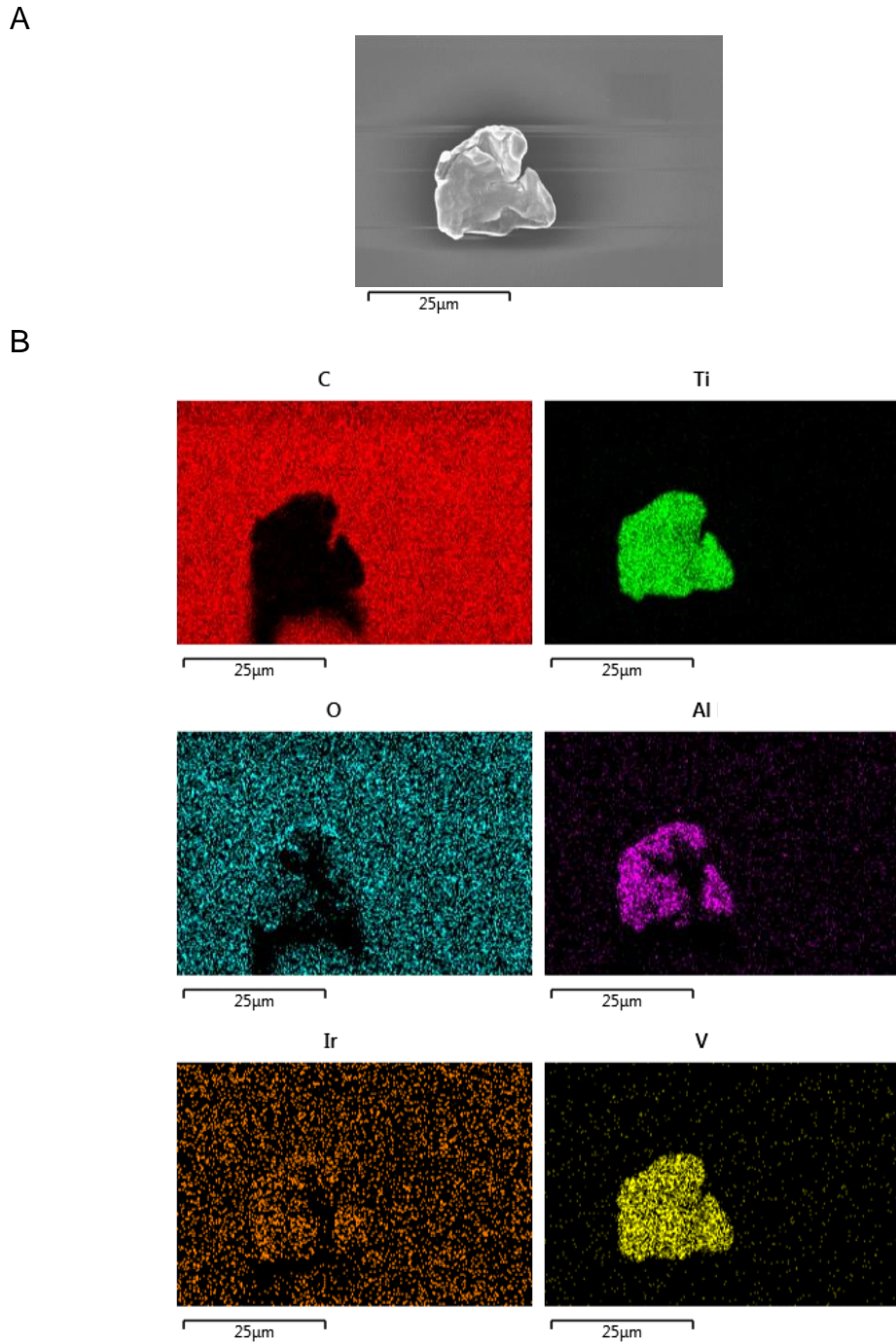
Elemental mapping carried out on several titanium particles gave similar results to those of the non-injected titanium particles (Figure 4.26A); this produced a map which showed that carbon was ubiquitous in the background

but absent from the area containing particles (Figure 4.26B). Iridium signals were also ubiquitous in the background but were also present in the area containing particles. Oxygen signals, were present in both the background and within particles, suggesting oxidation of particles. Titanium, aluminium and vanadium signals were concentrated in areas where particles were present and were absent in areas where particles were absent.

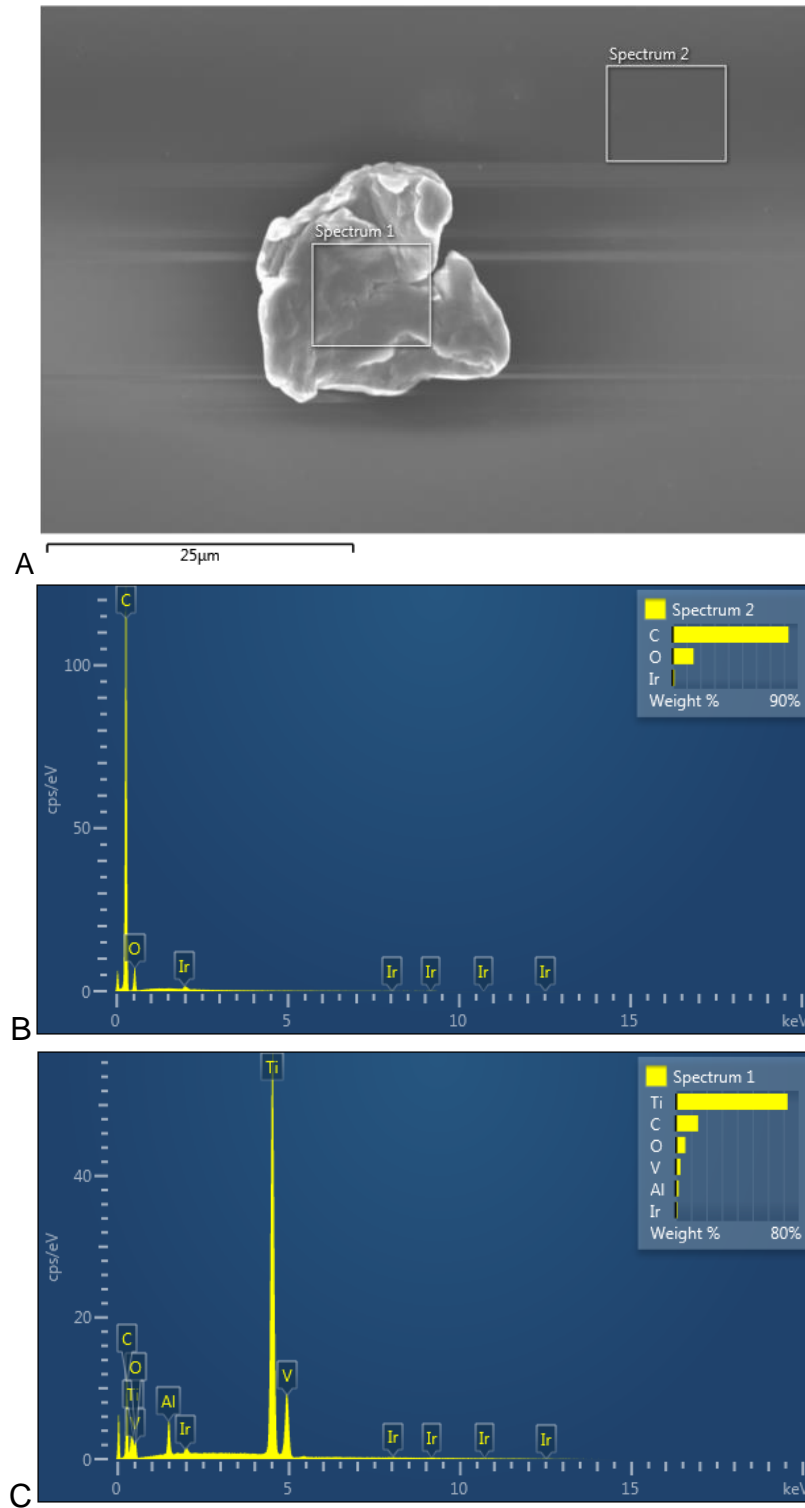
Spectra analysis also yielded similar results to the non-injected particles (Figure 4.27A-C); however, in the spectrum taken directly over the titanium particles, the relative amounts of each element varied; in particular, vanadium was more abundant than aluminium (Figure 4.27A-C). This may reflect *in vivo* changes to particles; however, the differences between the amounts of each element may have been too low to accurately differentiate which was more abundant.



**Figure 4.25. Elemental spectra of CoCr particles isolated from an injected rat stifle joint (33.76R).** A volume of 0.018 mm<sup>3</sup> of particles was resuspended and filtered onto a 0.015 µm polycarbonate filter membrane; the sample was iridium coated. (A) Scanning electron micrograph showing the area from the which the spectra were produced, (B) a corresponding spectrum from a particle aggregate, and (C) a corresponding spectrum taken over an area of filter membrane containing no particles.



**Figure 4.26. Elemental analysis of titanium particles isolated from an injected rat stifle joint (33.81R).** (A) Scanning electron micrograph showing the area from the which the elemental maps were produced and (B) the corresponding elemental maps, with the chemical symbol of each element given above. A volume of  $0.018 \text{ mm}^3$  of particles was resuspended and filtered on  $0.015 \text{ }\mu\text{m}$  polycarbonate filter membranes; samples were iridium coated. Elements identified included carbon, titanium, oxygen, aluminium, iridium and vanadium.

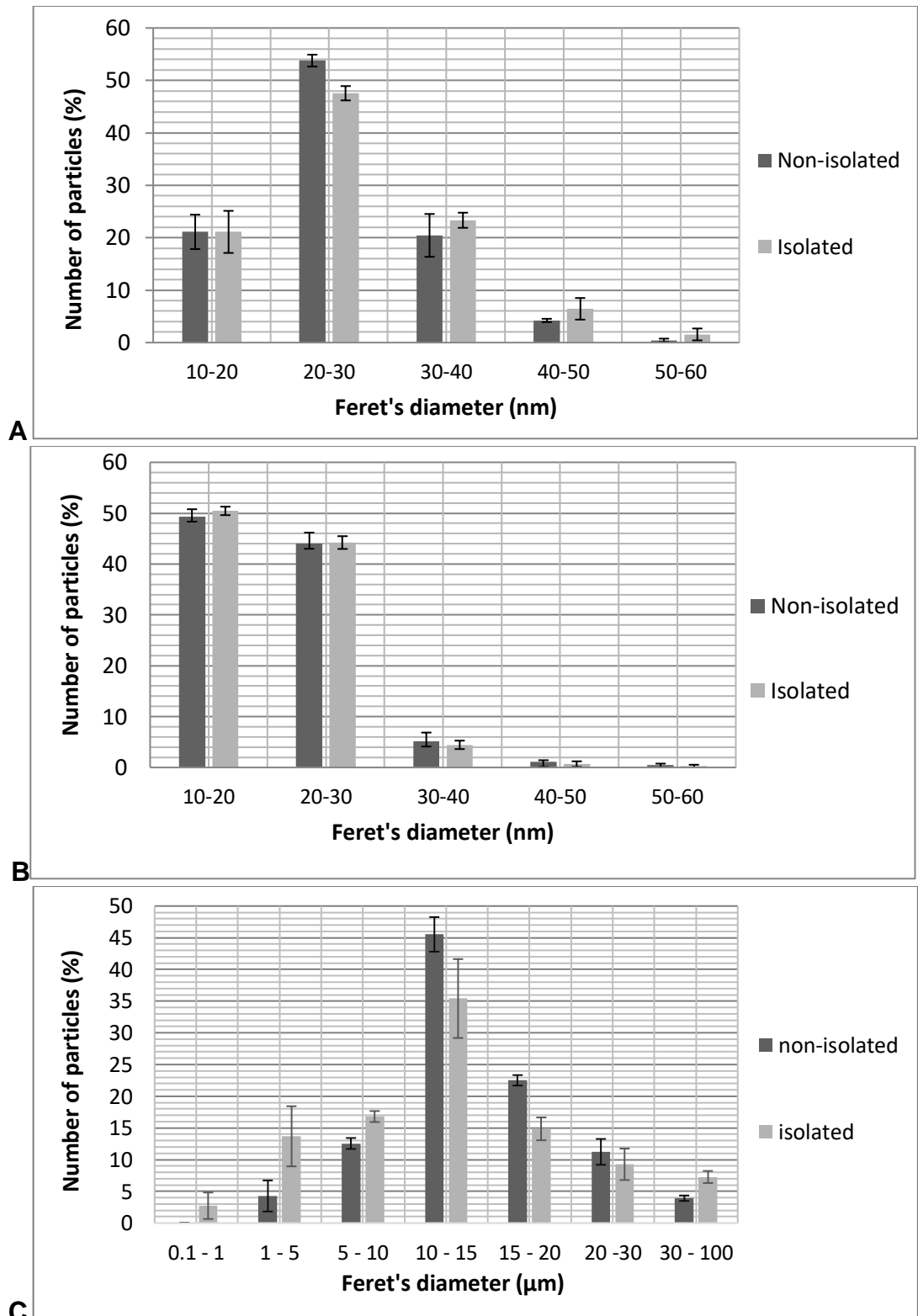


**Figure 4.27. Elemental spectra of titanium particles isolated from an injected rat stifle joint (33.81R).** A volume of 0.018 mm<sup>3</sup> of particles was resuspended and filtered onto a 0.015 μm polycarbonate filter membrane; the sample was iridium coated. (A) Scanning electron micrograph showing the area from the which the spectra were produced, (B) a corresponding spectrum from a particle, and (C) a corresponding spectrum taken over an area of filter membrane that did not contain any particles.

#### **4.5.7 Characterisation of isolated particles with image analysis and comparisons with non-injected particles**

Isolated and non-injected SiN, CoCr and titanium particles had similar size distributions, suggesting that the isolation process recovered particles of various sizes equally successfully, for each material (Figure 4.28A-C). For isolated SiN particles and isolated CoCr particles, sizes ranged from 10-60 nm, which was the same for non-injected particles. Both non-injected and isolated SiN particles had a modal particle size of 20 - 30 nm, while CoCr particles had a modal size of 10 - 20 nm both before injection and post-isolation. Titanium particles exhibited a broader size distribution from 0.1 to 100  $\mu\text{m}$ , with a modal particle size of 10 - 15  $\mu\text{m}$  before injection and post-isolation. Average particle sizes, aspect ratios and circularities for each material were also similar before injection and post isolation (Table 4.8), though like the non-injected titanium particles, there was a high degree of variation in each of the particle parameters measured for isolated titanium particles. Based on their low aspect ratios and high circularities, SiN and CoCr particles were considered spherical. Due to the higher aspect ratio and lower circularity, titanium particles were considered oval or irregular in shape. Overall results demonstrated that particles of all three materials were largely unchanged by *in vivo* exposure during the seven-day period; either in terms of particle size or shape.

The data were analysed by performing a test of normality (Shapiro-Wilk) using SPSS software; this showed that for each parameter (size, aspect ratio and circularity), and for each sample, the data were not normally distributed. Therefore, a nonparametric test (Kolmogorov-Smirnov, or KS) was used to compare the geometric measurements of control particles to isolated particles. This confirmed that the differences in SiN and CoCr particle size distributions and morphologies between particles before and after isolation were not significant (KS test,  $p > 0.05$ ). Titanium particles were not analysed statistically, since it was not feasible to measure the minimum of 150 particles recommended in (ISO 17853, 2011).



**Figure 4.28. Size distributions for non-injected particles, and particles isolated from injected rat stifle joints, for (A) SiN (B) CoCr and (C) Titanium material groups.** Values are based on the average ImageJ measurements of three samples of 150 particles (approx.100 titanium particles per sample). Error bars give standard deviation between the three samples (+/-). A different x-axis was used for titanium particles as they were micron-scale.



**Table 4.8. Average parameters for non-injected particles, and particles isolated from injected rat stifle joints, for SiN, CoCr and Titanium material groups.** Values are based on the average ImageJ measurements of three samples of 150 particles (approx.100 titanium particles per sample) +/- standard deviation between the three particle samples.

Material:	SiN		CoCr		Titanium	
Particle type:	Non-Isolated	Isolated	Non-Isolated	Isolated	Non-Isolated	Isolated
Feret's diameter	26 +/- 1	27 +/- 1	21 +/- 0	21 +/- 0	15 +/- 0	14 +/- 1
Aspect ratio	1.2 +/- 0.0	1.2 +/- 0.0	1.3 +/- 0.0	1.2 +/- 0.0	1.6 +/- 0.0	1.7 +/- 0.1
Circularity	0.9 +/- 0.0	0.9 +/- 0.0	0.9 +/- 0.0	0.9 +/- 0.0	0.8 +/- 0.0	0.7 +/- 0.0

#### 4.5.8 Analysis of decalcified stifle joint sections

In addition to particle isolation, stifle joints from the animal study described in section 4.4.3 were decalcified for histological analysis. As with the samples for particle isolation, each animal was ascribed a unique identification number by researchers at the University of Zurich; these were used to label samples during histological processing (Table 4.9).

**Table 4.9. Identification numbers used for each animal sample for histological analysis.**

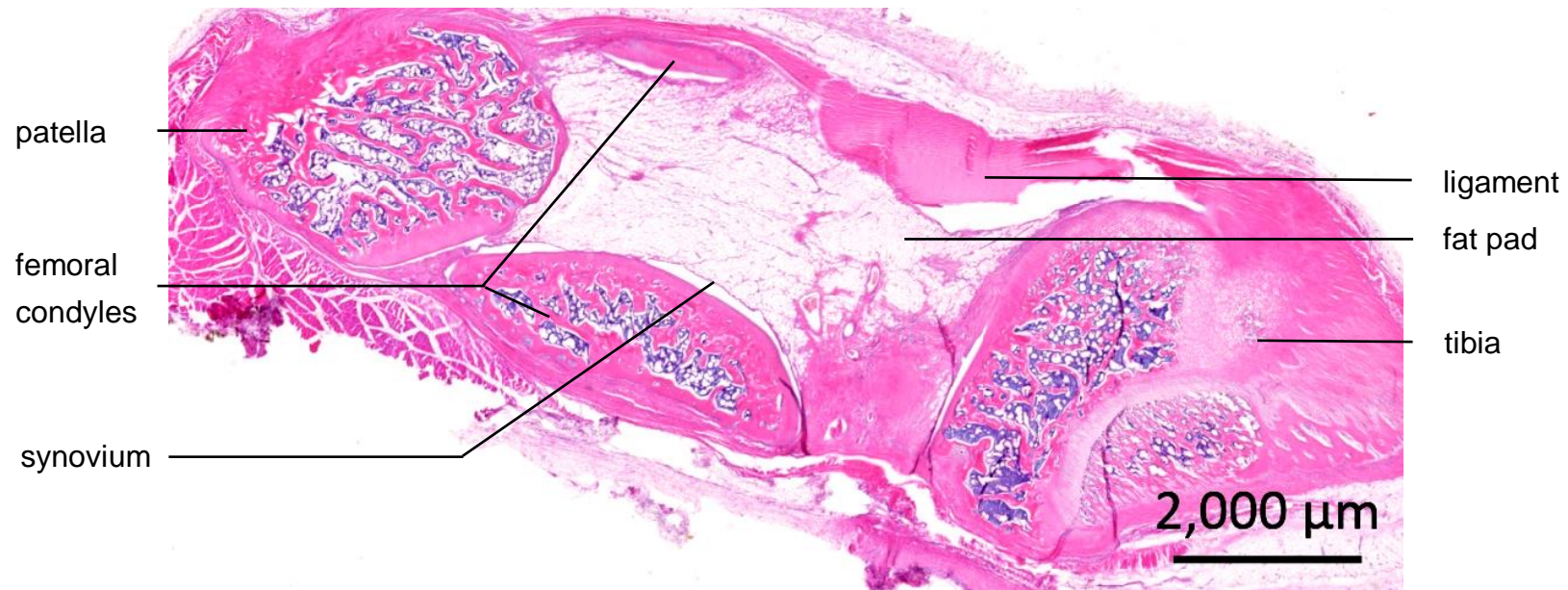
Animal number	Group	Details of materials injected*	Additional details
33.86	Silicon nitride	Si <sub>3</sub> N <sub>4</sub> , commercially available nanopowder (<50nm, Sigma-Aldrich, UK)	All animals were injected with a volume of 0.018 mm <sup>3</sup> of particles for an <i>in vivo</i> exposure time of seven days prior to sacrifice
33.87			
33.88			
33.73	Cobalt chromium	Particles generated by pin-on-plate in house (high carbon >0.2 % medical grade alloy; (ASTM, F1537))	
33.74			
33.75			
33.82	Titanium	Particles generated by pin-on-plate in house (medical grade Ti-6Al-4V alloy)	
33.83			
33.84			

Following fixation and transport from the University of Zurich, six stifle joints from each material group, consisting of three injected joints and the corresponding contralateral non-treated joint, were decalcified for five weeks in concentrated EDTA as described in section 4.4.6.1. The joints were then processed for histology, embedded in paraffin wax and 5 µm sections were collected from each joint as described in section 4.4.6.1.

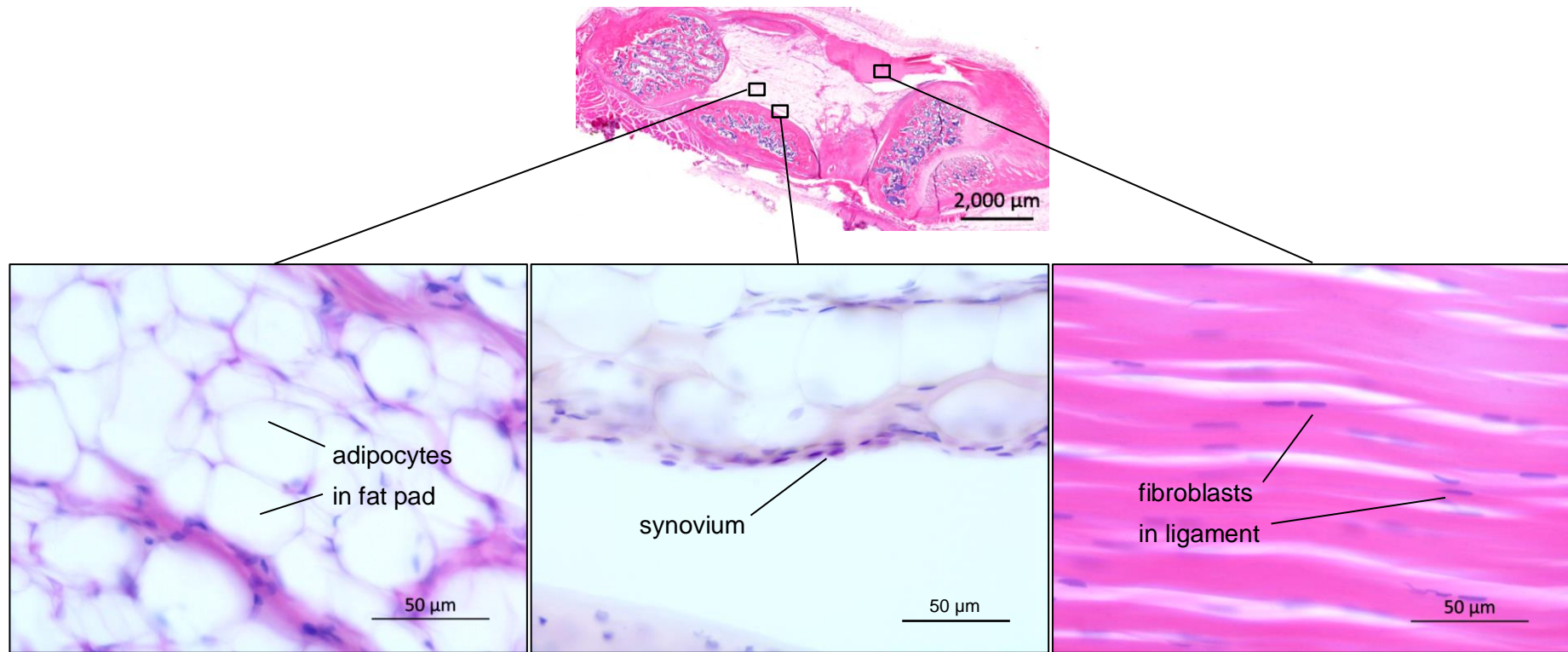
#### **4.5.8.1 Observations of tiled and high magnification images of control stifle joint sections**

**Contralateral, non-treated stifle joint sections were stained with H&E as described in section 4.4.6.2 and a tiled image of the whole section was created as described in section 4.4.6.3 to reveal the overall joint morphology (Figure 4.29**

Figure 4.29). Sections from a frontal plane from the anterior part of each joint consisted of the patella, fat pad, parts of the femur and tibia, and contralateral ligament. Some initial sections also contained parts of the ligament of the patella. Higher magnification views using a 40x objective lens were captured from each section in order to analyse the cell types present within the fat pad, synovium and ligament of each joint as described in section 4.4.6.3 (Figure 4.30). Within the fat pad, nearly all of the cells were visually identified as adipocytes, with a few fibroblasts present. The synovium consisted of cells with fibroblast and macrophage morphologies, and was approximately 1-2 cells thick, though in some areas the synovium was up to about 6 cells thick. Ligaments contained regular layers of fibroblasts. All control stifle joints were similar in appearance and did not contain particles or inflammatory cell infiltrates.



**Figure 4.29. Whole joint section taken from a depth of up to 1500 μm into the joint capsule, from a non-treated contralateral rat stifle joint (animal 33.86; control joint), stained with H&E.** The joint was formalin fixed, decalcified, paraffin embedded and sectioned such that cross sections were taken from an frontal plane. The image was captured under normal Köhler illumination by capturing multiple views with a 2.5x objective lens and stitching the individual images together.



**Figure 4.30. Images of histological sections taken from a depth of up to 1500 μm into the joint capsule of a non-treated contralateral rat stifle joint (33.86L), stained with H&E.** High magnification images were captured at 400x magnification from selected areas of the soft tissue. The joint was formalin fixed, decalcified, paraffin embedded and sectioned such that cross sections were taken from an frontal plane.

#### **4.5.8.2 Observations of tiled images of particle-injected stifle joint sections**

For all of the stifle joints injected with SiN, CoCr or titanium particles, tiled images of entire stifle joint sections stained with H&E were created in the same way as the controls. These images showed that the overall joint morphology of each particle-injected stifle joint was similar to that of the control stifle joints; large scale changes such as thickening of the entire joint capsule were absent. However, small areas of inflammation, synovial thickening and particle deposits were evident (Figure 4.31-Figure 4.33). The extent and location of these features varied between the sections and animals within each material group, indicating a non-uniform dispersion of particles, and possibly differences in the immune reaction to the material between individual animals. Beyond a depth of approximately 1500 µm into each joint, there were no observable particle deposits or morphological changes, suggesting that particles did not disperse to a greater depth into the joint tissue.

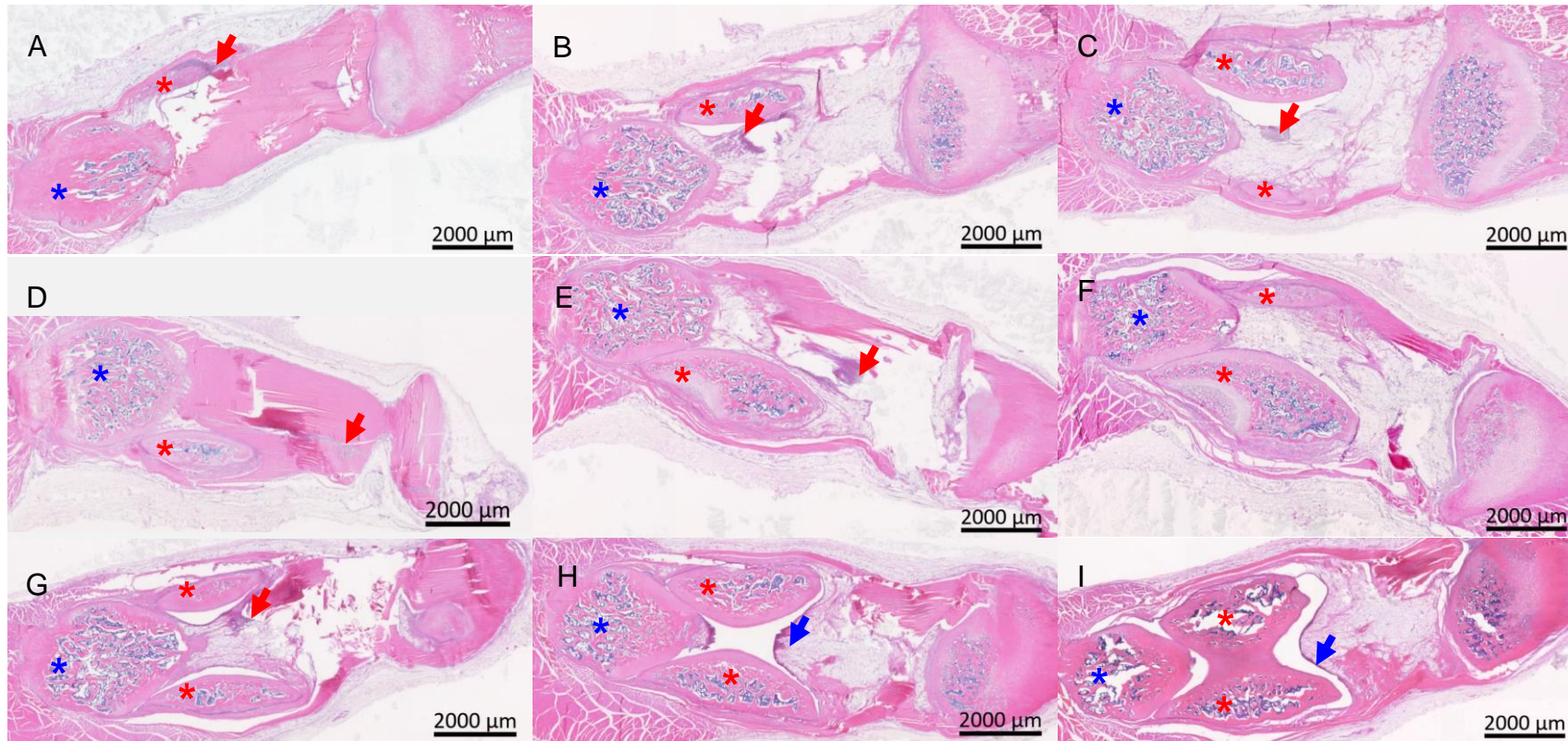
In the SiN-injected stifle joints, SiN particle aggregates were barely visible at magnifications of 25x, which were used to create the tiled images (Figure 4.31). Sections from rat 33.86 contained particles deposited adjacent to one of the femoral condyles with accompanying inflammatory cell infiltrates (Figure 4.31A – C). Inflammatory cells and particles were also present in the centre of the patella ligament and fat pad of rat 33.87 (Figure 4.31D – E). Inflammation was less apparent in a stifle joint section taken from a greater depth from rat 33.87 (Figure 4.31F). Inflammatory infiltrates (Figure 4.31G) and a thicker synovium (Figure 4.31H - I) were observed in sections from rat 33.88.

In the CoCr group, inflammation was apparent in each section from rats 33.73 and 33.74 (Figure 4.32A – F). Particle deposits which were dark brown in appearance were apparent to varying degrees within multiple CoCr injected stifle joint sections (Figure 4.32B – D). The deposits confirmed that CoCr particles did not disperse uniformly through the joints. In rat 33.73 particles were found within the ligament and centre of the fat pad while in rat 33.74 particles were highly concentrated almost exclusively in the centre of the fat pad, where inflammation was particularly extensive surrounding the particles.

Particle deposits were not as evident in sections from rat 33.75 (Figure 4.32G – I), though inflammation was also present in the centre of the fat pad. Areas of increased thickness of synovium were also observed, particularly in rat 33.74 (Figure 4.32D – F). Overall, the extent of inflammation appeared to be greater in CoCr injected stifle joints compared to SiN injected stifle joints.

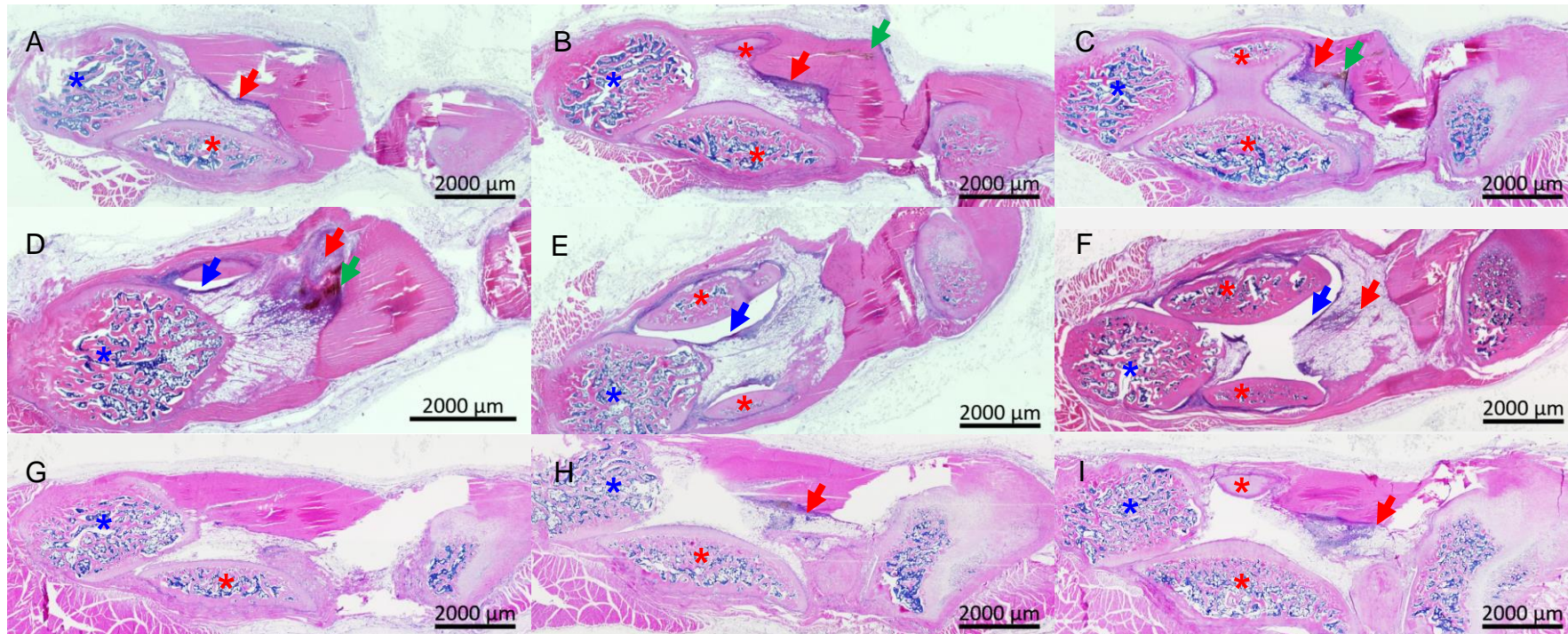
Titanium injected joints showed lower levels of inflammation than CoCr injected joints (Figure 4.33). Synovial thickening was not apparent at the magnification of 25x used to create the tiled images. Inflammation was largely absent in rat 33.82 (Figure 4.33A - C), although particles were observed within the ligament of a section (Figure 4.33B). Inflammation was present within sections from rat 33.83 (Figure 4.33D – F), although particle deposits were not apparent within the tiled images. A section from rat 33.84 contained an area of inflammation within the fat pad (Figure 4.33G), and a large particle deposit was also apparent in a section at a greater depth (Figure 4.33H), with some surrounding inflammation. Particles and reactions were not apparent within a section taken from further towards the centre of the joint of rat 33.84 (Figure 4.33I).





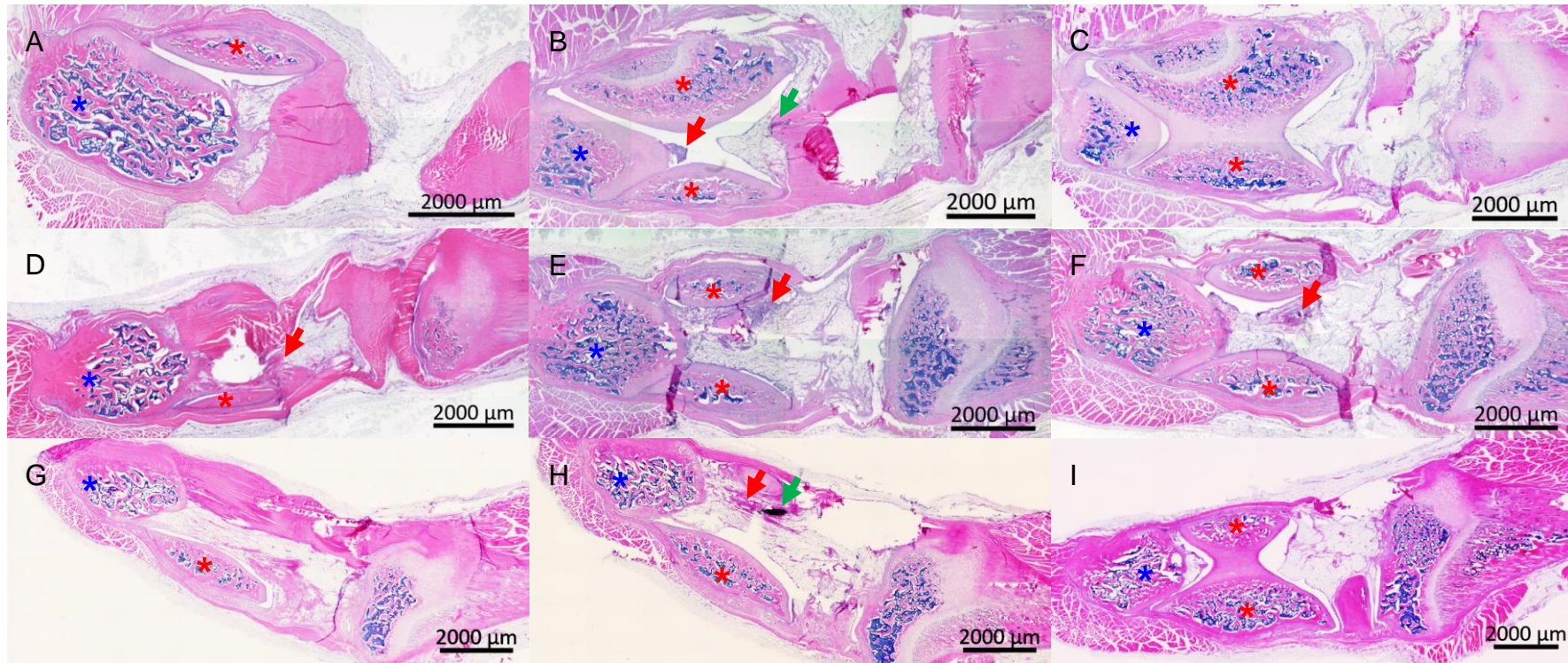
**Figure 4.31. Whole joint sections taken from depths of up to 1500  $\mu\text{m}$  into the joint capsule, from SiN-injected rat stifles, stained with H&E.** Sections are the three most inflamed from rat 33.86 (A-C), rat 33.87 (D-F) and rat 33.88 (G-I). The joints were formalin fixed, decalcified, paraffin embedded and sectioned such that cross sections were taken from an frontal plane. Tiled images were created with a 2.5x objective lens under normal Köhler illumination. Red and blue arrow heads indicate inflammatory cell infiltrates and thickened synovium respectively. Red and blue asterix indicate the femoral condyles and the patella respectively.





**Figure 4.32. Whole joint sections taken from depths of up to 1500  $\mu\text{m}$  into the joint capsule, from CoCr-injected rat stifle joints, stained with H&E.** Sections are the three most inflamed from rat 33.73 (A-C), rat 33.74 (D-F) and rat 33.75 (G-I). The joints were formalin fixed, decalcified, paraffin embedded and sectioned such that cross sections were taken from a frontal plane. Tiled images were created with a 2.5x objective lens under normal Köhler illumination. Red, blue and green arrow heads indicated inflammatory infiltrates, areas of thickened synovium, and deposits of particles respectively. Red and blue asterix indicate the femoral condyles and the patella respectively.





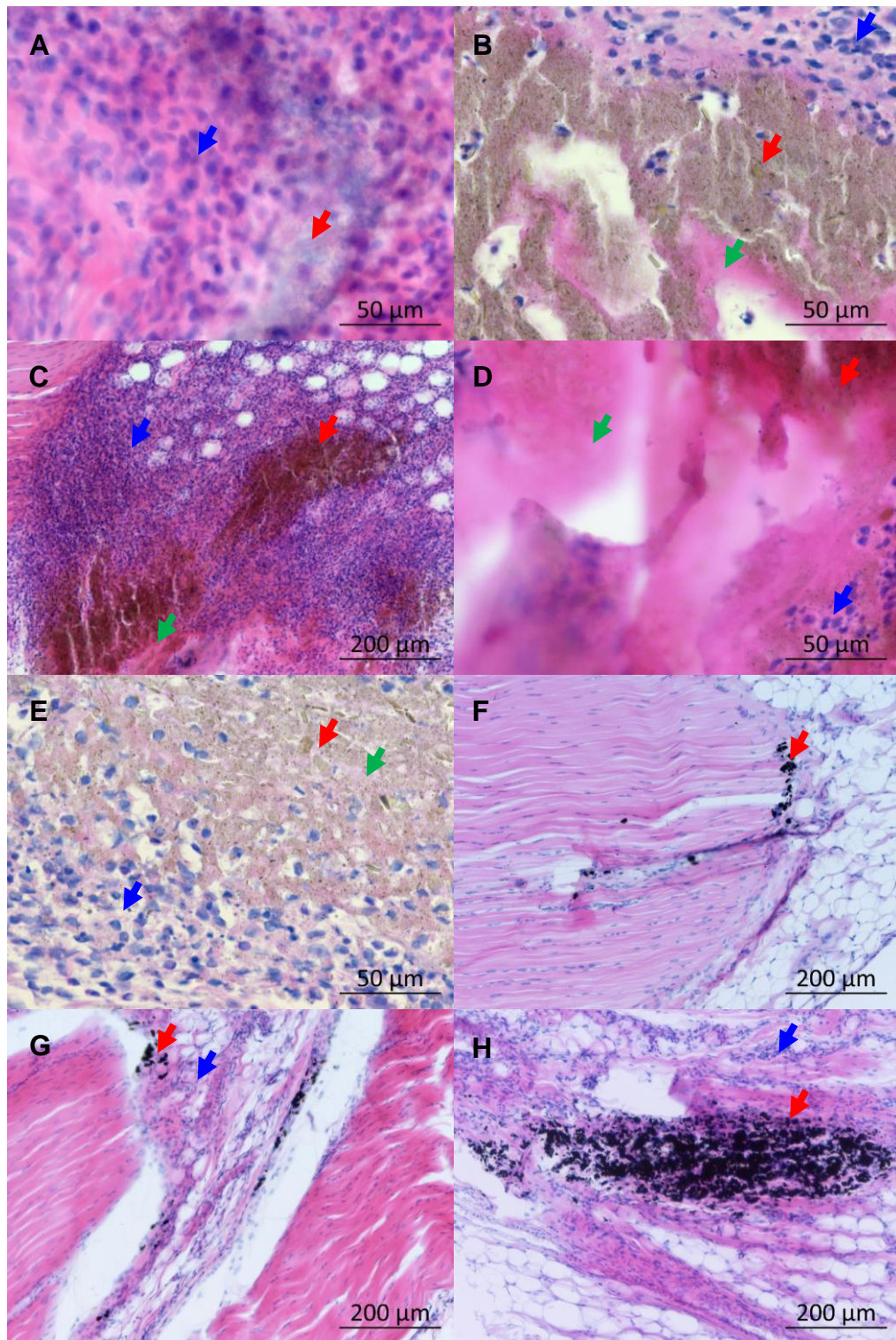
**Figure 4.33. Whole joint sections taken from depths of up to 1500  $\mu\text{m}$  into the joint capsule, from titanium-injected rat stifle joints, stained with H&E.** Sections are the three most inflamed from rat 33.82 (A-C), rat 33.83 (D-F) and rat 33.84 (G-I). The joints were formalin fixed, decalcified, paraffin embedded and sectioned such that cross sections were taken from a frontal plane. Tiled images were created with a 2.5x objective lens under normal Köhler illumination. Red and green arrow heads indicate inflammatory cell infiltrates and particle deposits respectively. Red and blue asterixis indicate the femoral condyles and the patella respectively.

#### **4.5.8.3 Observations of high magnification images of particles within injected stifle joint sections**

High magnification views of the H&E stained stifle joint sections taken with a 10x, 20x, 40x or 63x objective lens showed that there were slight variations in section thickness (Figure 4.34); images often contained multiple layers of cells indicating a section thickness of greater than the intended 5  $\mu\text{m}$  thickness (Figure 4.34A).

Within the SiN-injected rat stifles, certain areas of tissue were grey and granular in appearance; these areas were located in sites containing inflammatory cell infiltrates within a section from rat 33.86 (Figure 4.34A) and a section from rat 33.87; these areas appeared to contain particle aggregates. However, most often the particles were barely visible or absent within sections. Areas of inflammation in the absence of observable particle deposits were also present; such areas were also observed in CoCr injected stifle joint sections. However, dark brown areas which appeared to contain particulate matter were highly visible in nearly all of the CoCr injected rat stifle joint sections at higher magnifications and were variably dispersed through large areas of the fat pad and in certain areas of ligament (Figure 4.34B - E). In most cases these dark areas were surrounded by inflammatory cells. However, cytoplasmic staining in the absence of cell structures or nuclei were also present in CoCr injected stifle joint sections, suggesting a necrotic reaction to particles (Figure 4.34B - E). Necrosis was present in all three of the CoCr injected rats and was absent in the SiN injected stifle joint sections. Particles were observed within multiple sections from each titanium-injected rat at high magnifications (Figure 4.34F - H); however, particles accumulated in small areas of the fat pad and patella ligament and were completely absent throughout most of each section, suggesting limited particle dispersion. Inflammation was observed to limited degrees directly surrounding particles but was otherwise absent in titanium-injected stifle joint sections (Figure 4.34F - H). Necrosis was also absent in sections from the titanium injected group. Other types of reactions, such as giant cell formation or fibrosis, were not observed within any of the material groups.

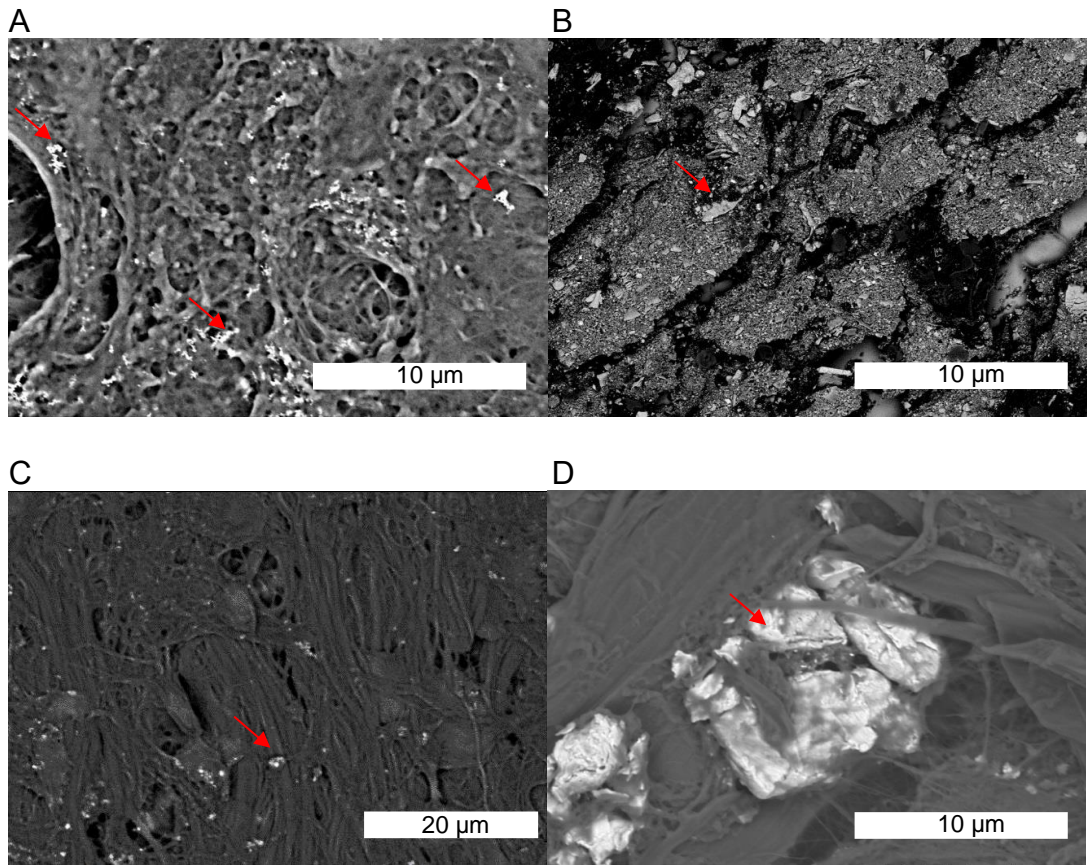




**Figure 4.34 Images of particles within H&E stained sections.** SiN-injected rat 33.86 (A), CoCr-injected rats 33.73 (B), 33.74 (C and D) and 33.75 (E), and titanium-injected rats 33.82-33.84 (F-H). The joints were formalin fixed, decalcified, paraffin embedded and sectioned; cross sections were taken from a frontal plane. The images were captured under normal Köhler illumination with a 10x or 40x objective lens. Red arrow heads indicate particles; blue arrow heads indicate inflammatory cells; green arrow heads indicate necrosis.

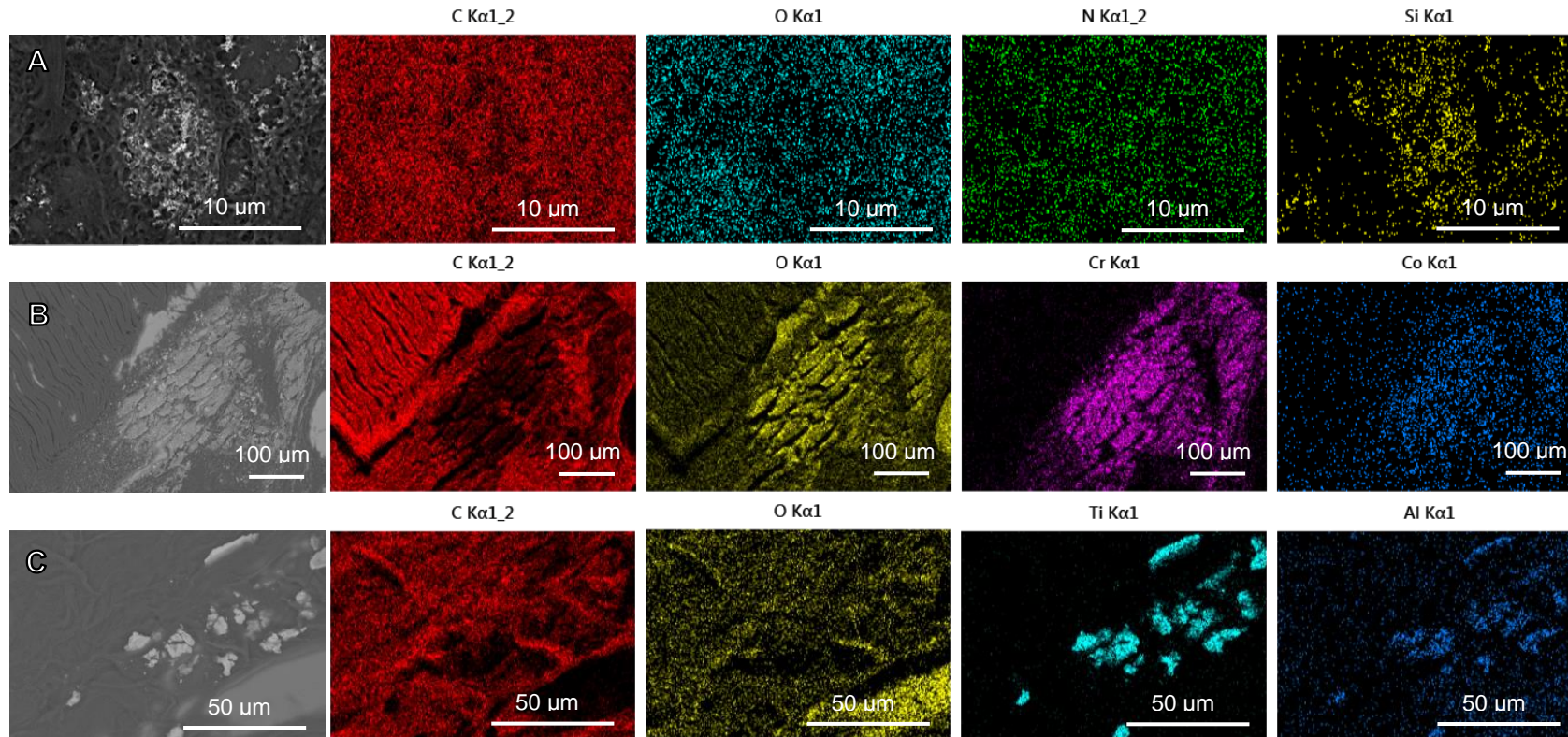
#### **4.5.8.4 Analysis of particles within tissue sections using scanning electron microscopy and elemental analysis**

Serial sections were taken from areas of each stifle joint thought to contain particles, deparaffinised and observed using SEM at magnifications of 2,000x and 5,000x (Figure 4.35). These high magnification images of unstained tissue did not allow cells to be easily distinguished, and particles appeared to be partially covered by the extracellular matrix; however, particles could be detected within the tissue using a back scattered electron detector, which was used to show particles as bright against a dark background. The analysis revealed that SiN particles were aggregated in a similar way to those that were not subjected to *in vivo* exposure (Figure 4.35A). In contrast to CoCr particles which were directly filtered for SEM analysis, the CoCr particles within tissue sections were either present as large deposits (Figure 4.35B) or dispersed aggregates (Figure 4.35C). Titanium particles were similar in appearance to titanium particles that were not subjected to *in vivo* exposure (Figure 4.35D). The analyses confirmed the histological findings that particles were located mainly in the patella ligament and fat pad of each rat for each material group. Elemental analysis confirmed the composition of the particles (Figure 4.36; Table 4.10), with silicon and nitrogen present in the SiN group (Figure 4.36A), cobalt and chromium present in the CoCr group (Figure 4.36B), and titanium and aluminium present in the titanium group (Figure 4.36C). In spectrum analysis, vanadium was also identified exclusively in titanium particles, and molybdenum was identified exclusively in CoCr particles. This analysis confirmed initial observations that the sections contained the injected particles, and that the particles were not contaminants or tissue artefacts. Elemental mapping indicated a higher ratio of chromium to cobalt in the areas containing CoCr particles (Figure 4.36B). CoCr particles appeared to be oxidized, as significant oxygen signals were detected in the CoCr particles (Figure 4.36B); this was not apparent in SiN or titanium particles. This differs slightly to SiN and titanium particles post-isolation, in which oxidation was apparent (Table 4.10).



**Figure 4.35. Images captured from a whole joint section from (A) a SiN injected rat stifle joint, (B) and (C) a CoCr injected joint and (D) a titanium injected joint.** The tissue sections were dehydrated in ethanol, carbon coated and imaged by scanning electron microscopy using back scattered electrons, to enable heavier elements to be distinguished by their brighter appearance. Particle aggregates are indicated by red arrows.





**Figure 4.36. Elemental analysis of tissue sections from rat stifle joints injected with (A) SiN, (B) CoCr and (C) titanium.** The sections were dehydrated in ethanol, carbon coated and imaged by scanning electron microscopy with back scattered electrons (grayscale images); elements were detected by energy dispersive X-ray spectroscopy to produce corresponding elemental maps of each imaged area (coloured images). Carbon, oxygen and nitrogen were ubiquitous in the tissue. Signals originating from the glass slide were omitted.

**Table 4.10. Elemental components of particles detected by energy dispersive X-ray spectroscopy within tissue sections and post-isolation from tissue.**

Elements present in detectable quantities*	Si <sub>3</sub> N <sub>4</sub> particles		CoCr particles		Titanium particles	
	Within tissue section	After isolation	Within tissue section	After isolation	Within tissue section	After isolation
Aluminium					X	X
Cobalt			X	X		
Chromium			X	X		
Molybdenum			X	X		
Nitrogen	X	X				
Oxygen		X**	X	X		X
Silicon	X	X				
Titanium					X	X
Tungsten				X		
Vanadium					X***	X

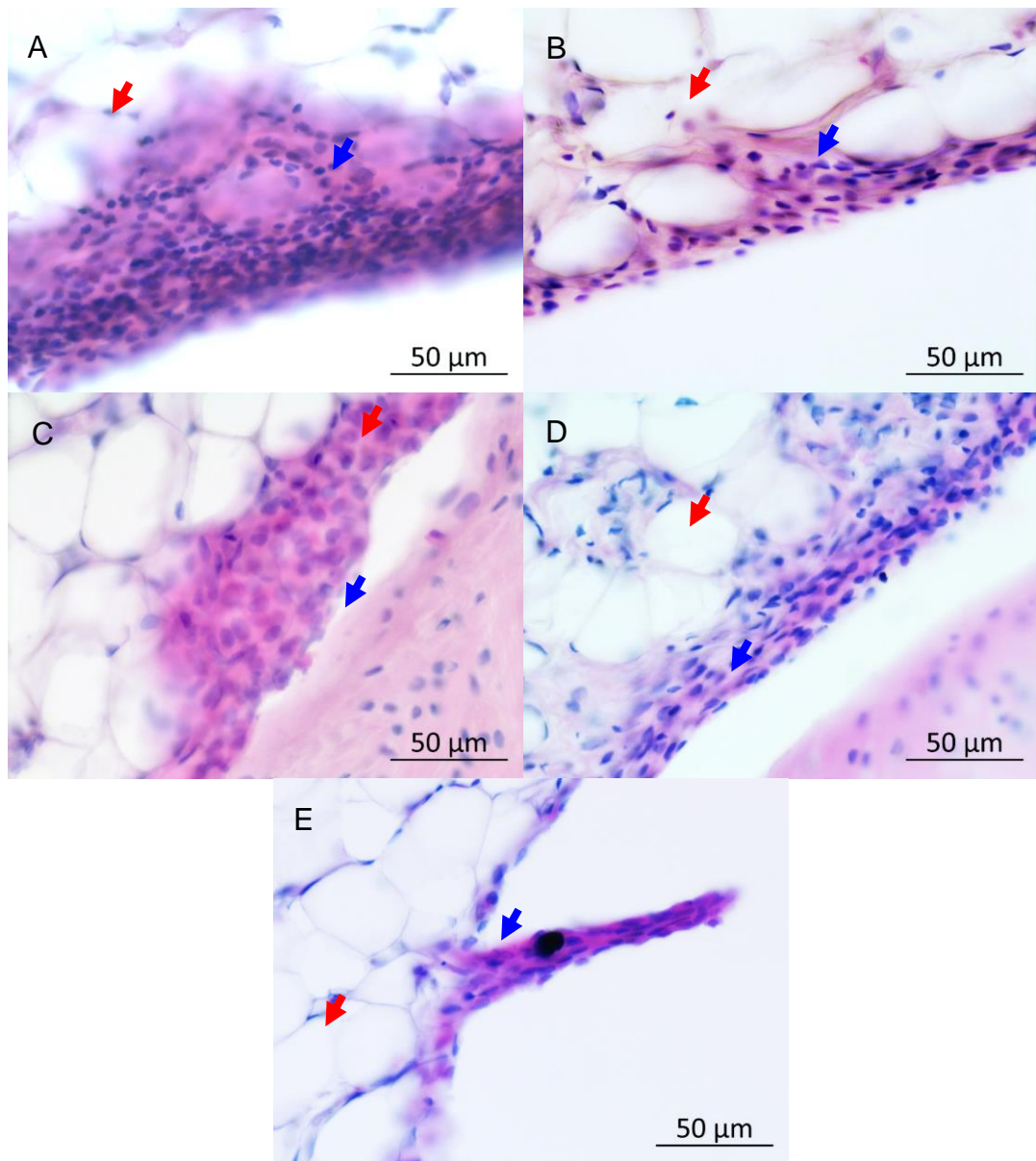
\*Elements present in the background (such as iridium from the sputter coating) have been excluded. \*\*Likely from background (polycarbonate filter membrane). \*\*\*Detected during spectrum analysis. Silicon and metal elements were not detected in control tissue from an untreated stifle joint.

#### **4.5.8.5 Analysis of soft tissue reactions within high magnification images of H&E stained tissue sections**

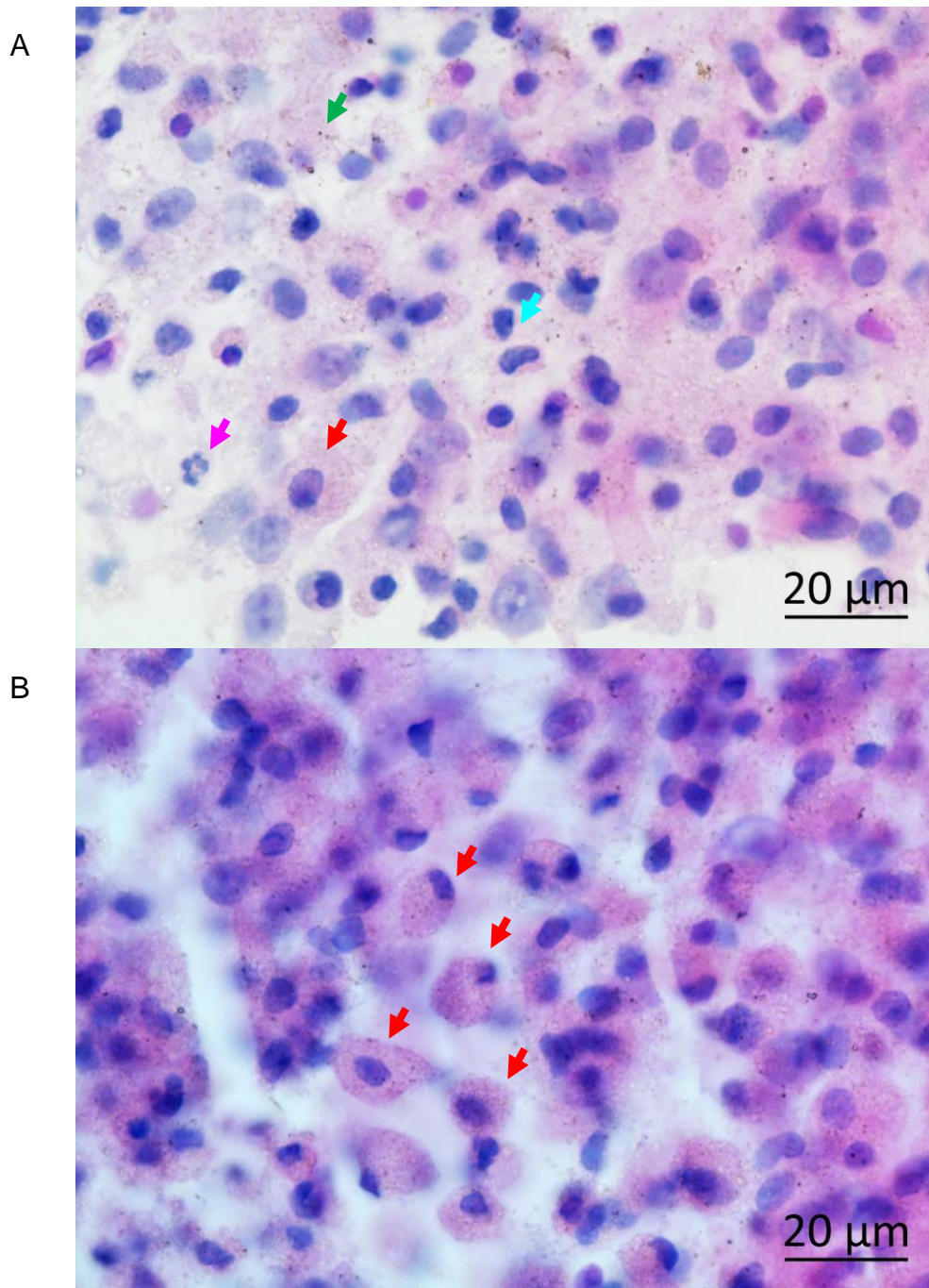
Images were taken of the synovium in H&E stained stifle joint sections at a high magnification of 400x; this demonstrated that there were morphological differences in the synovia between particle-injected and control stifle joints (Figure 4.37). In comparison to the synovium from an untreated stifle joint (Figure 4.37A), the synovium within the contralateral SiN-injected stifle joint was typically thicker due to greater numbers of synovial cells in localised areas of the synovium (Figure 4.37B). Increases in synovial cell numbers were observed to a greater extent in CoCr-injected stifle sections (Figure 4.37C), and to a lesser extent in titanium-injected stifle sections (Figure 4.37D). Finger-like projections also formed in response to titanium particles in animal 33.84 (Figure 4.37E). However, variations in synovial cell numbers were apparent within sections, between sections, between animals, and between material groups, making direct comparisons between material groups difficult. It was also not possible to recognise cell types within the synovium based on nucleus morphology, due to cell layers overlapping.

High magnification images taken with a 63x objective lens of inflammatory cell infiltrates in the fat pad of H&E stained SiN-injected rat sections demonstrated that a variety of cell types including macrophages, lymphocytes and polymorphonuclear cells were present (Figure 4.38A); these cells could be identified based on nucleus and cell morphology as described in section 4.4.6.3, although in some areas cell types were hard to identify due to the presence of overlapping cell layers. Macrophages and lymphocytes were abundant while polymorphonuclear cells were rare. Particles were also present and appeared to be engulfed by macrophages (Figure 4.38B).





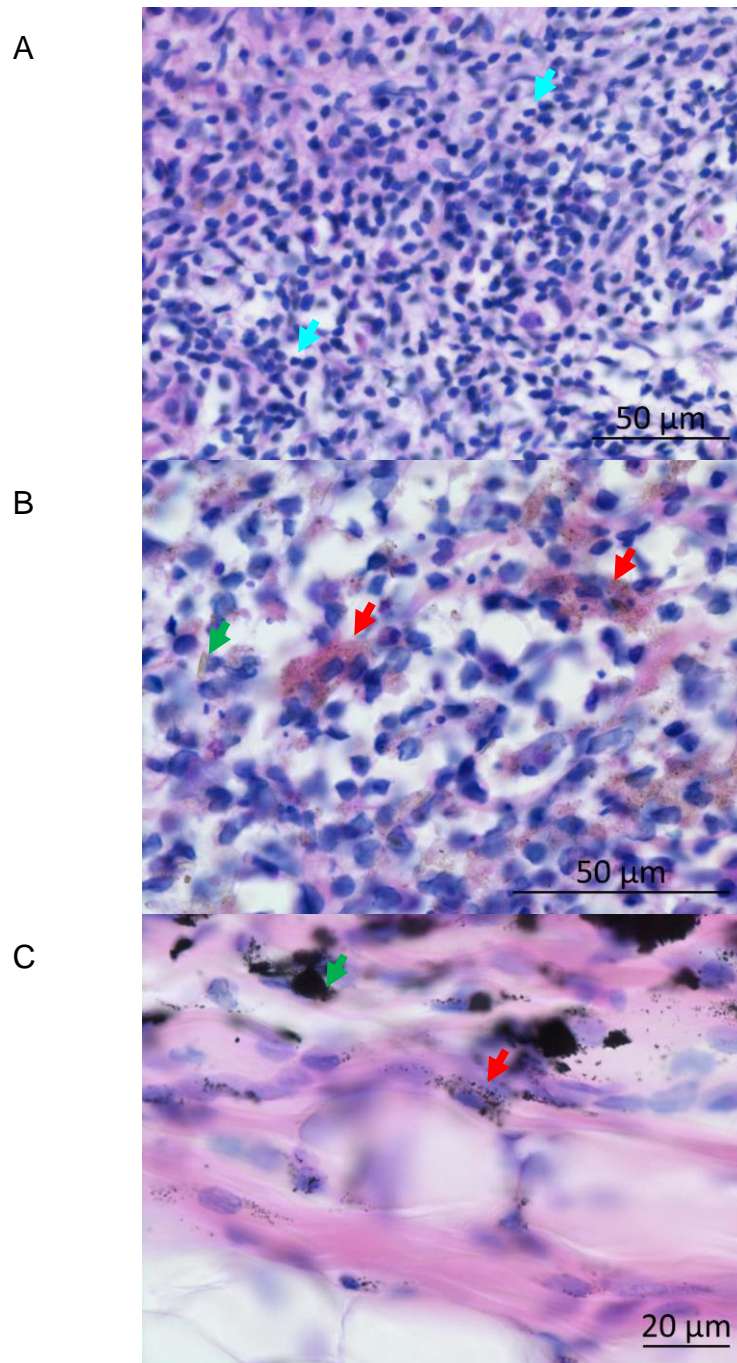
**Figure 4.37. Images of synovium taken from H&E stained sections from depths of up to 1500 μm into rat stifle joint capsules.** (A) Control stifle joint 33.86L. (B) SiN-injected stifle joint 33.86R (depth of 1200 μm). (C) CoCr-injected stifle joint 33.74R. (D) Titanium-injected stifle joint 33.83R. (E) Titanium-injected stifle joint 33.84R. The joints were formalin fixed, decalcified, paraffin embedded and sectioned such that cross sections were taken from a frontal plane. The images were captured under normal Köhler illumination with a 40x objective lens. Red arrow heads show adipocytes of the fat pad; blue arrow heads indicate cells of the synovium.



**Figure 4.38. Images of inflammatory cell infiltrates within the fat pad taken from H&E stained sections from depths of up to 1500 μm into a SiN-injected rat stifle joint capsule (33.87).** The joints were formalin fixed, decalcified, paraffin embedded and sectioned such that cross sections were taken from a frontal plane. The images were captured under normal Köhler illumination with a 63x (oil immersion) objective lens. Arrow heads show particles (green), lymphocytes (blue), neutrophils (pink) and macrophages containing engulfed particles (red).

Macrophages and lymphocytes were also observed in H&E stained sections from CoCr-injected rat stifles (Figure 4.39). Lymphocytes were present in large clusters in each rat (Figure 4.39A); macrophages containing engulfed particles were found within and between these clusters (Figure 4.39B). Polymorphonuclear cells were also present but rare. Overall fewer inflammatory cells were observed surrounding titanium particles; macrophages, lymphocytes and polymorphonuclear cells were all relatively rare in the titanium injected stifle joint sections. The few macrophages that were observed clearly contained engulfed particles (Figure 4.39C). The titanium and CoCr groups also contained areas where cell types were hard to recognise due to the presence of overlapping cell layers.





**Figure 4.39.** Images of inflammatory cell infiltrates and engulfed particles taken from H&E stained sections of CoCr-injected rat stifle joints (A and B; 33.74 and 33.75 respectively) and a titanium-injected rat stifle joint (C; 33.84). The joints were formalin fixed, decalcified, paraffin embedded and sectioned such that cross sections were taken from a frontal plane. The images were captured under normal Köhler illumination with a 63x (oil immersion) objective lens. Arrow heads show particles (green), lymphocytes (blue) and macrophages containing engulfed particles (red).

#### **4.5.8.6 Scoring of rat stifle joint sections by counting raw cell numbers and blood vessels**

Images of the synovium were taken at 400x magnification for each H&E stained stifle joint section and these were used to count the number of cell layers in the synovium. In each case, the synovium of control groups was on average  $4 \pm 1$  (SD) cells thick (Figure 4.40A). However, the average synovial thickness of particle-injected stifle joints was higher than the control in each material group; in the SiN group, synovial thickness increased to an average of  $9 \pm 2$  (SD) cells thick, while in the CoCr group, synovial thickness increased to  $12 \pm 9$  (SD) cells thick. The average synovial thickness in the titanium-injected group was  $6 \pm 1$  (SD) cells thick. Statistical analysis using a Kruskal-Wallis test revealed that synovial thickness differed significantly by treatment group ( $p < 0.05$ ). Post-hoc tests using Dunn's tests with Bonferroni correction showed that only the CoCr-injected stifles differed significantly to the contralateral controls. There was no significant difference between the synovial thickness of SiN-, CoCr- or titanium-injected joints ( $p > 0.05$ ).

Images of the fat pad were taken at 100x magnification for each H&E stained stifle joint section and these were used to count the total number of blood vessels present in the average 100x magnification field of view ( $3,345 \mu\text{m}^2$ ) of the fat pad, as described in 4.4.6.3. In the SiN group, the number of blood vessels was slightly higher in injected joints compared to control joints ( $5 \pm 0.4$  (SD), vs  $3 \pm 0.6$  (SD)) while in the CoCr group there was no difference between the averages (Figure 4.40B). In the titanium group there was also a higher number of blood vessels in the injected group compared to the control group ( $7 \pm 6$  (SD) vs  $5 \pm 1$  (SD)). A Kruskal-Wallis test showed that the differences in blood vessel number were not statistically significant for any material ( $p > 0.05$ ).

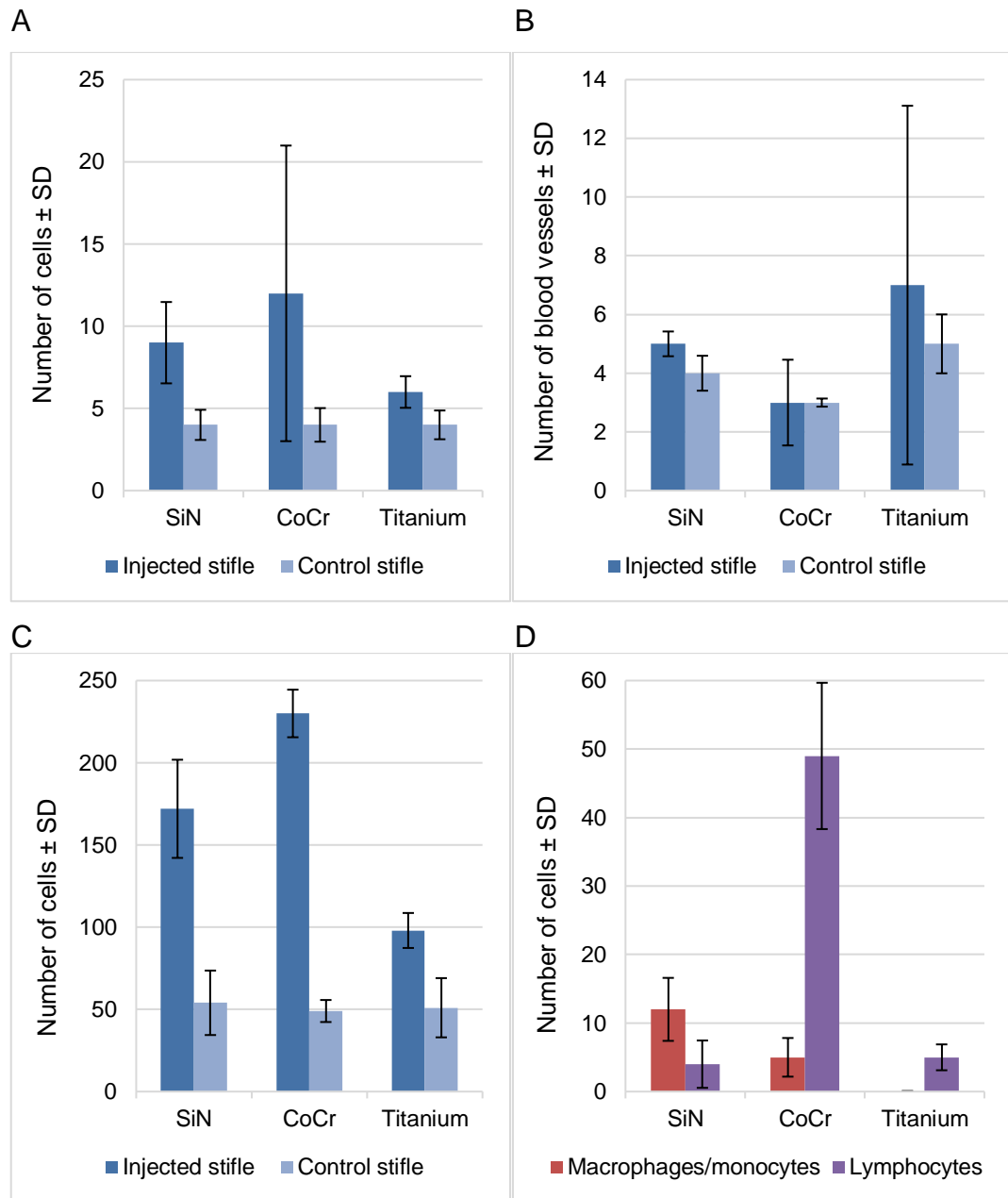
Images of each H&E stained stifle joint section were also used to count the total number of cells present in the average 400x magnification field of view ( $836 \mu\text{m}^2$ ) of the fat pad; this demonstrated that for the three control groups of stifle joints, the average number of cells was  $49-54 \pm 7-20$  (SD) (Figure 4.40C). However, SiN injected stifles contained on average  $172 \pm 30$  (SD) cells, while CoCr injected joints contained on average  $230 \pm 14$  (SD) cells. Titanium-injected stifle joints contained on average  $98 \pm 11$  (SD) cells. Statistical analysis using a Kruskal-Wallis test revealed that total cell number within the

fat pad differed significantly by treatment group ( $p < 0.05$ ). Post-hoc tests using Dunn's test with Bonferroni correction showed that both the CoCr and SiN-injected stifles differed significantly to their respective contralateral controls. However, there was no statistically significant difference between total cell numbers in the injected stifles of the SiN, CoCr or titanium groups ( $p > 0.05$ ).

The average number of macrophages/monocytes and lymphocytes within a given 400x field of view ( $836 \mu\text{m}^2$ ) of the fat pad in sections from particle-injected stifle joints differed between material groups (Figure 4.40D). The data indicated that macrophages were most frequent in SiN-injected stifles, with an average of  $12 \pm 5$  (SD) macrophages present per field of view; in comparison an average of  $5 \pm 3$  (SD) macrophages were present in CoCr-injected stifles. In titanium injected stifles, macrophages were too rare to be counted (average of  $< 1$  per field of view in all animals). Lymphocytes were most frequent in the CoCr-injected stifles, with an average of  $49 \pm 11$  (SD); this was approximately ten times higher than the average number of lymphocytes in the titanium-injected group ( $5 \pm 2$  SD cells). In the SiN group, the average number of lymphocytes was similar to the titanium group, at  $4 \pm 3$  (SD) cells. In control groups, numbers of any immune cell were negligible (average of  $< 1$  in all animals). Kruskal-Wallis tests showed that there was an overall significant difference in both the number of macrophages and the number of lymphocytes between injected groups and control groups ( $p < 0.05$ ). Post-hoc tests using Dunn's test with Bonferroni correction showed that both the CoCr- and SiN-injected stifles differed significantly in terms of number of macrophages compared to their respective contralateral controls. However, there was no statistically significant difference in macrophage numbers between the injected stifles of the different material groups ( $p > 0.05$ ). Post-hoc tests using Dunn's test with Bonferroni correction also showed that both the CoCr- and titanium-injected groups differed significantly in terms of number of lymphocytes compared to their respective contralateral controls. However, there was no statistically significant difference in lymphocyte numbers between the injected groups ( $p > 0.05$ ). Numbers of polymorphonuclear cells and plasma cells are not shown but were  $< 2$  in each particle-injected animal and were thus present in insufficient quantities for statistical analysis between animals or material groups.

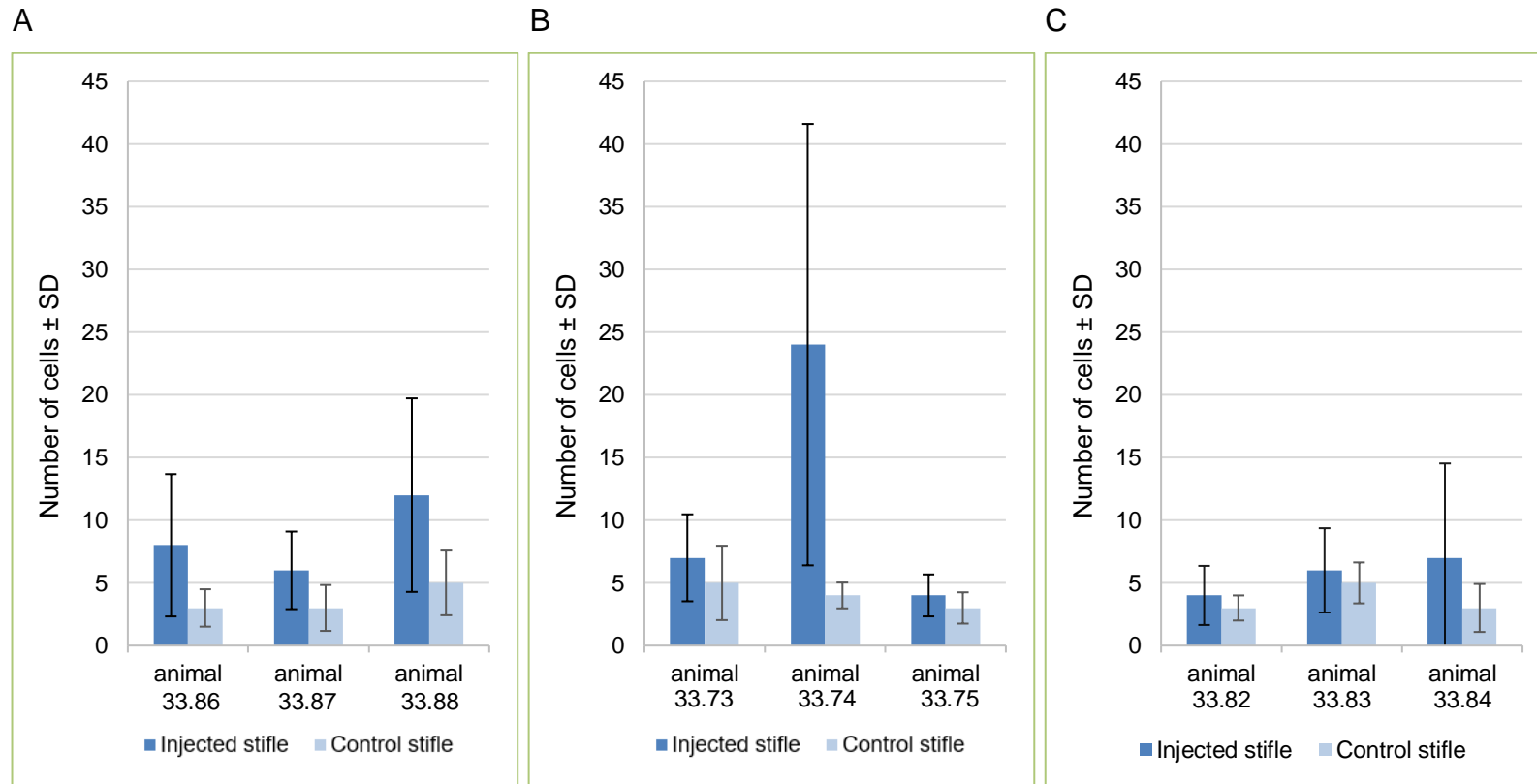
Variations between sections and animals were apparent for most of the histological scoring (Figure 4.41 - Figure 4.44). In terms of synovial thickness, animal 33.88 (SiN group) exhibited a greater average number of cells in both the control (untreated) and particle-injected stifle compared to the other animals ((Figure 4.41A). The injected stifle had an average synovial thickness of  $12 \pm 8$  (SD) cells, compared to  $8 \pm 6$  (SD) and  $6 \pm 3$  (SD) for the injected stifles of animals 33.86 and 33.87 respectively. Furthermore, animal 33.74 (CoCr group) showed a much greater increase in synovial thickness in the injected stifle than the other two rats, with an average synovial thickness of  $24 \pm 18$  (SD) cells, compared to  $7 \pm 3$  (SD) and  $4 \pm 2$  (SD) in the injected stifles of animals 33.73 and 33.75, respectively (Figure 4.41B). The increase in thickness was unequal between different locations of the stifle, as shown by the high degree of variation in the synovial thickness scoring. Variation of synovial thickness of injected stifles varied less between animals in the titanium group (Figure 4.41C). Despite the apparent variations between animals of the same group, pairwise comparisons of the stifles using a Kruskal-Wallis test followed by post-hoc tests using Dunn's test with Bonferroni correction showed that stifles within the same group did not differ significantly ( $p > 0.05$ ).

Histological scoring of vascularisation demonstrated a similar average number of blood vessels of  $4-5 \pm 3-5$  (SD) between animals in the SiN group (Figure 4.42A). However, there was a high degree of variation between different locations of each injected stifle. Differences between animals in the CoCr group were low (Figure 4.42B); however, in the titanium group the injected stifle of animal 33.82 contained a much greater number of blood vessels compared to the other two animals, with an average of  $17 \pm 15$  (SD) compared to  $4 \pm 3-4$  (SD) cells (Figure 4.42C). A Kruskal Wallis test revealed that the differences were not significant between any stifle joint ( $p > 0.05$ ).

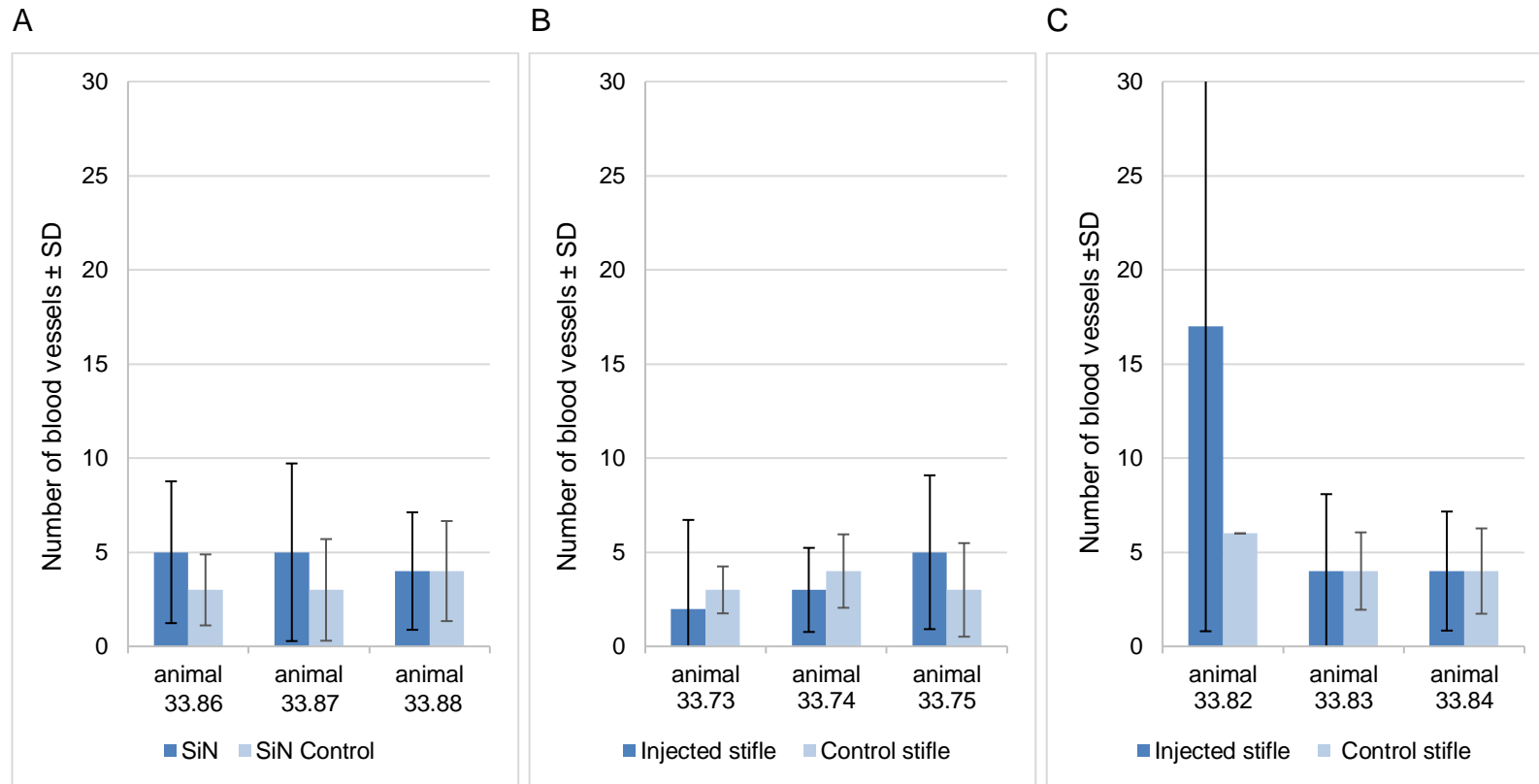


**Figure 4.40. Histological scoring of rat stifle joint sections, showing differences between material groups and controls.** (A) The average thickness of the synovium in terms of cell number. (B) The average number of blood vessels within the fat pad in a 100x field of view (3,345  $\mu\text{m}^2$ ). (C) The average total number of cells within a 400x field of view (836  $\mu\text{m}^2$ ). (D) The average number of macrophages/monocytes and lymphocytes within a given 400x field of view in sections from particle-injected stifle joints; numbers of these cell types were negligible in control stifle joints. Error bars show standard deviation for the three animals within each material group. All scoring was carried out on formalin fixed, decalcified, paraffin embedded rat sections (5  $\mu\text{m}$  thickness) stained with H&E (N  $\geq$ 12 images for each group).





**Figure 4.41. Histological scoring of synovial thickness in terms of average cell number in rat stifle joint sections, showing variations between individual animals.** (A) SiN group, (B) CoCr group and (C) titanium group. Error bars show standard deviation for the scoring of individual sections from each animal. All scoring was carried out on formalin fixed, decalcified, paraffin embedded rat sections (5  $\mu$ m thickness) stained with H&E. N  $\geq$ 12 images for each group.

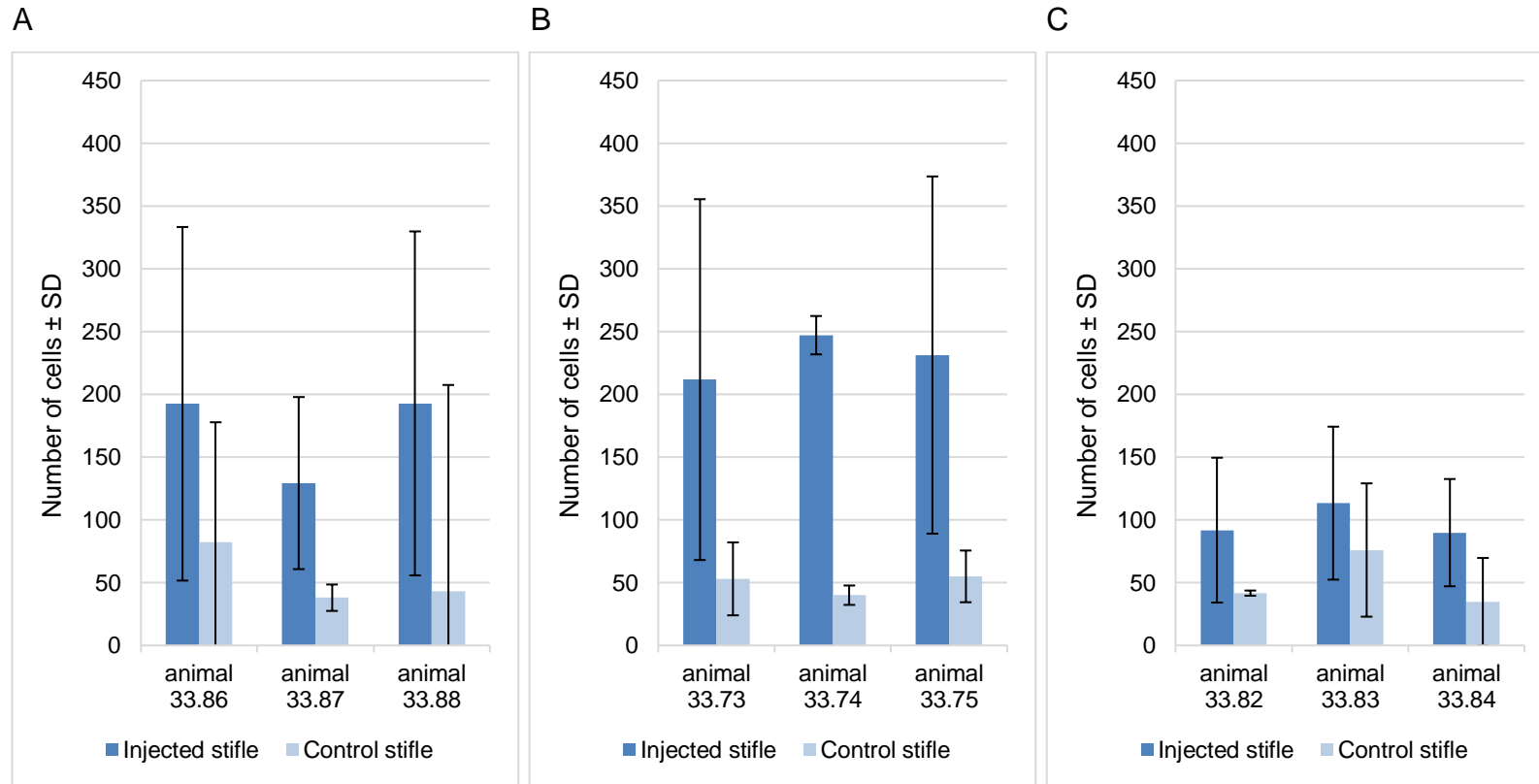


**Figure 4.42. Histological scoring of vascularisation in rat stifle joint sections, showing variations between individual animals.**

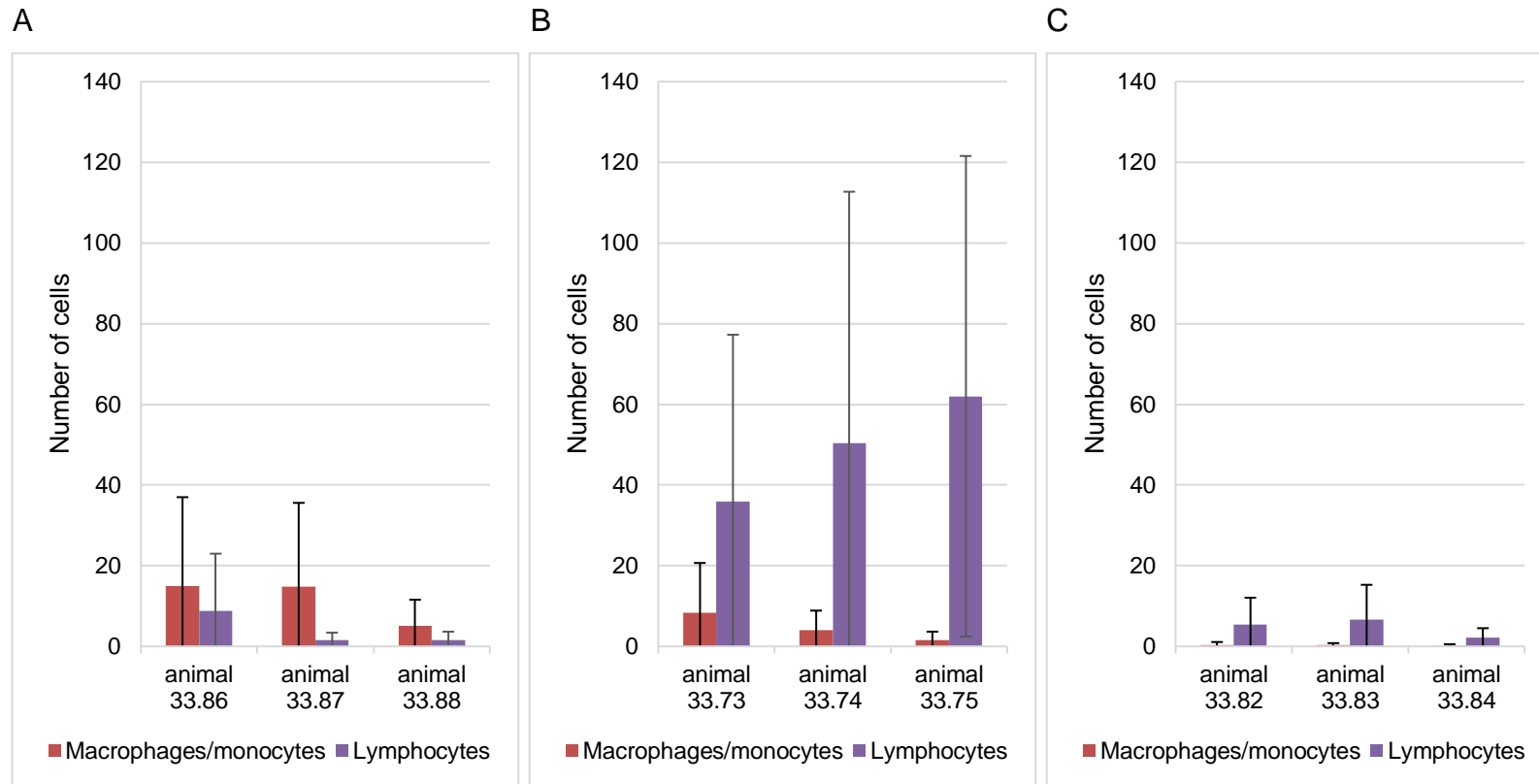
(A) SiN, (B) CoCr and (C) titanium group. Scores were based on the average number of blood vessels within the fat pad in a 100x field of view. Error bars show standard deviation for the scoring of individual sections from each animal. All scoring was carried out on formalin fixed, decalcified, paraffin embedded rat sections (5  $\mu$ m thickness) stained with H&E. N  $\geq$ 12 images for each group.

Counting the total number of cells present in the average 400x magnification field of view of the fat pad also revealed animal specific differences (Figure 4.43). Variation within each fat pad was high in most of the animals. In the SiN group, the control fat pad of animal 33.86 contained more cells on average than either of the other two control fat pads ( $82 \pm 69$  (SD) compared to  $38 \pm 11$  (SD) and  $43 \pm 15$  (SD) in the other two stifle joints) (Figure 4.43A). In addition, the average number of cells in the treated fat pad was lower in animal 33.87 compared to the other two animals ( $129 \pm 96$  compared to  $193 \pm 141$ - $143$  (SD)). Variation in the treated fat pad of each animal was similarly high in the CoCr and titanium groups (Figure 4.43B and C). Pairwise comparisons of the stifles using a Kruskal-Wallis test followed by post-hoc tests using Dunn's test with Bonferroni correction showed that stifles within the same group did not differ significantly ( $p > 0.05$ ).

There were also animal specific differences in the numbers of macrophages and lymphocytes involved in the cellular response to particles in treated stifle joints (Figure 4.44). In the SiN group (Figure 4.44A), animal 33.86 contained a greater average number of lymphocytes in the fat pad ( $9 \pm 14$  (SD) compared to  $2 \pm 2$  (SD)). In addition, the fat pad from animal 33.88 contained approximately 3 times fewer macrophages compared to the other two animals. In the CoCr group (Figure 4.44B), animals 33.73 - 33.75 differed slightly in the proportions of lymphocytes and macrophages; the data suggested a possible inverse correlation between the number of lymphocytes and macrophages. In the titanium group (Figure 4.44C), numbers of both cell types were low. Variation in the numbers of lymphocytes in the CoCr group and the number of macrophages in animals 33.86 and 33.87 of the SiN group was high. However, once again pairwise comparisons of the stifles using a Kruskal-Wallis test followed by post-hoc tests using Dunn's test with Bonferroni correction showed that stifles within the same group did not differ significantly, either in macrophage numbers or lymphocyte numbers ( $p > 0.05$ ).

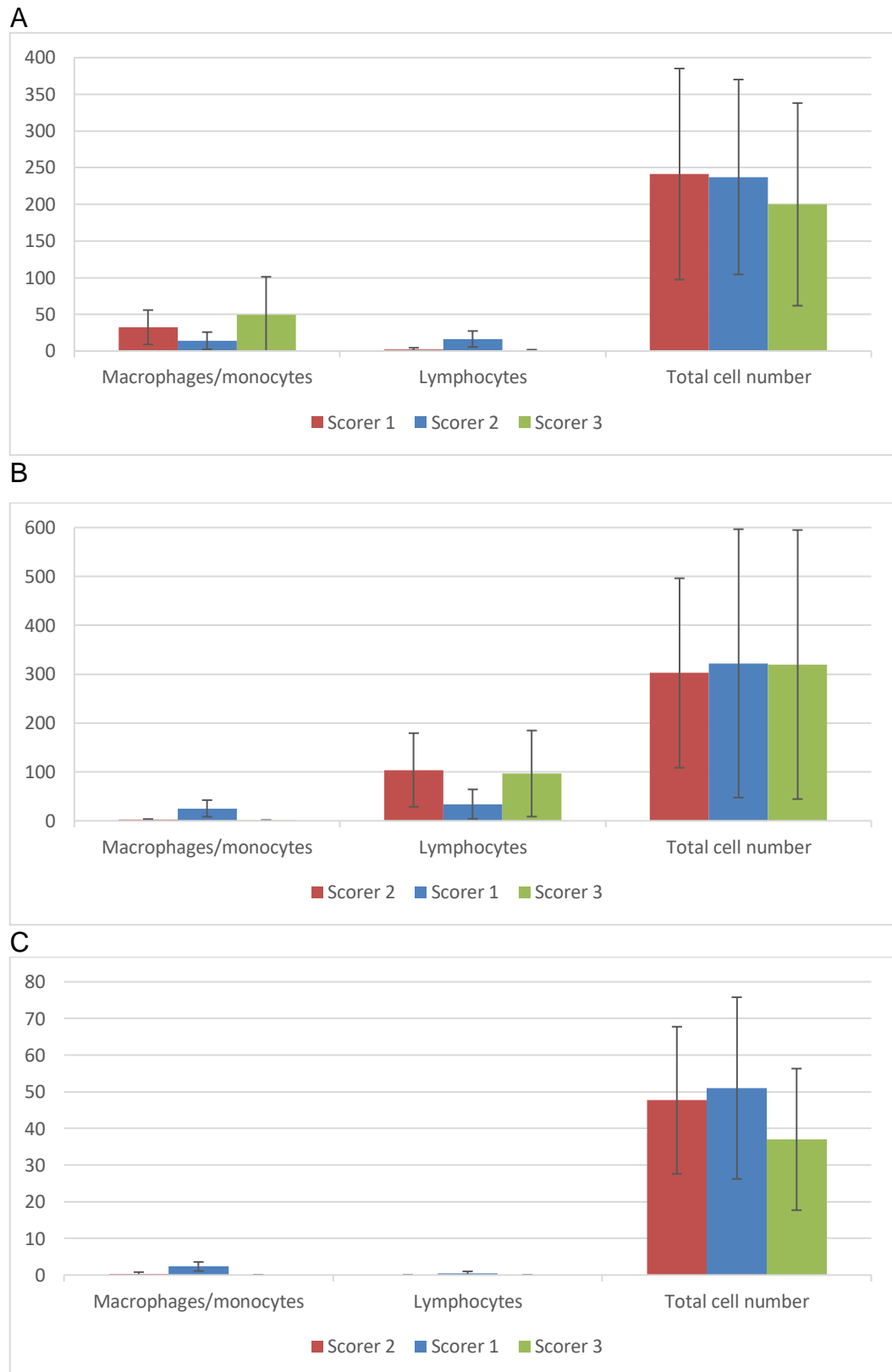


**Figure 4.43. Histological scoring of the average total number of cells within a 400x field of view of the fat pad, showing variations between individual animals. (A) SiN, (B) CoCr and (C) titanium group. All scoring was carried out on formalin fixed, decalcified, paraffin embedded rat sections (5  $\mu$ m thickness) stained with H&E. N  $\geq$ 12 images for each group.**



**Figure 4.44. Histological scoring of the average number of macrophages and lymphocytes within a 400x field of view of the fat pad, showing variations between individual animals. (A) SiN, (B) CoCr and (C) titanium group. Numbers of these cell types were negligible in control stifle joints. Error bars show standard deviation for the scoring of individual sections from each animal. All scoring was carried out on formalin fixed, decalcified, paraffin embedded rat sections (5  $\mu$ m thickness) stained with H&E.**

To ascertain the degree of subjectivity in cell counting, a selection of images (1 image from each injected stifle, and 1 image from an untreated stifle) were scored in terms of average number of cells per 400x magnification field of view by two other researchers, Dr. Saurabh Lal and Dr. Stacy-Paul Wilshaw and compared to the scoring carried out by the current author (Figure 4.45). Both additional scorers were blinded to prevent bias in scoring. The comparisons demonstrated that, for the SiN group (Figure 4.45A), scoring of macrophage numbers was, on average,  $14 \pm 12$  (SD),  $32 \pm 23$  (SD) and  $49 \pm 51$  (SD) cells for each of the three scorers. Scoring of lymphocytes was on average  $1 \pm 1$  (SD),  $2 \pm 2$  (SD) and  $16 \pm 11$  cells for each of the three scorers. Total cell number varied from an average of  $200 \pm 138$  (SD),  $237 \pm 133$  (SD) and  $241 \pm 144$  (SD) cells for each of the three scorers. Two researchers scored greater numbers of macrophages/monocytes than lymphocytes, while one researcher scored similar numbers of both. In the CoCr group, two researchers scored very low numbers of macrophages, while one researcher gave a score of  $25 \pm 17$  (SD) (Figure 4.45B). Scoring of lymphocytes by all three researchers was higher in the CoCr group than in the SiN group and was on average  $34 \pm 30$  (SD),  $97 \pm 88$  (SD) and  $104 \pm 75$  (SD). Scoring of total cell number by all three researchers was also higher in the CoCr group than in the SiN group. In the titanium group, all three researchers gave similarly low scores for both macrophage and lymphocyte numbers, and all three counted much lower total cell numbers of, on average,  $37 \pm 19$  (SD),  $48 \pm 20$  (SD) and  $51 \pm 25$  (SD). Variation in total cell number between different images of the same material group was high for each researcher, as shown by the standard deviations. Statistical analysis was performed using a Kruskal-Wallis test, which showed that total cell number and numbers of lymphocytes in the fat pad were not significantly different ( $p < 0.05$ ). Although there was a significant difference overall for scoring of macrophage numbers, post-hoc analysis using Dunn's test with Bonferroni correction did not show a significant difference between any pair of scorers ( $p > 0.05$ ).



**Figure 4.45. Histological scoring of injected stifle joints, including the average number of macrophages and lymphocytes and the average total number of cells within a 400x field of view of the fat pad, showing variations between different scorers. (A) SiN, (B) CoCr and (C) titanium group. Error bars show standard deviation for the scoring of each animal.**

#### **4.5.8.7 Conversion of raw cell numbers into semi-quantitative scores**

The raw numbers of cells and blood vessels which were counted during histological scoring of H&E stained sections were converted into semi-quantitative scores based on methods adapted from ISO 10993-6 (2016), as described in section 4.4.6.6. Based on this scoring method, materials were considered a:

- non-irritant (0,0 up to 2,9)
- slight irritant (3,0 up to 8,9)
- moderate irritant (9,0 up to 15,0)
- severe irritant (> 15)

For SiN particles, the overall semi-quantitative score was 10, which under the conditions of this scoring method, would qualify the SiN particles as a moderate irritant (Table 4.11). This score was mainly due to the numbers of macrophages counted within SiN treated stifle joints. CoCr particles scored an average of 16, which would classify the particles as a severe irritant, due mainly to the large numbers of lymphocytes present in CoCr-treated stifle joints (Table 4.12). Titanium particles scored 4 on average and would be considered a slight irritant (Table 4.13). However, in animal 33.84 of the titanium group, the reaction score was 2. Thus, in animal 33.84 titanium was a non-irritant.



**Table 4.11. Semi-quantitative score of the overall reaction to SiN particles, based on methods adapted from ISO 10993-6 (2016).** Cell scoring is based on the average raw number of cells counted per high-powered field (400x), while scores for vascularisation are made based on the average number of blood vessels per 100x field. Other tissue reactions are scored qualitatively based on descriptions given in ISO 10993-6.

	Test Sample (SiN)			Control Sample (untreated)		
Animal number:	33.86	33.87	33.88	33.86	33.87	33.88
Polymorphonuclear cells	0	1	1	0	0	0
Macrophages	3	3	2	0	0	0
Lymphocytes	2	1	1	0	0	0
Plasma cells	0	0	0	0	0	0
Giant cells	0	0	0	0	0	0
Necrosis	0	0	0	0	0	0
SUBTOTAL (x2)	10	10	8	0	0	0
Neovascularization	2	2	2	1	1	2
Fibrosis	0	0	0	0	0	0
Fatty infiltrate	0	0	0	0	0	0
SUBTOTAL	12	12	10	1	1	2
TEST - CONTROL	11	11	8			
AVERAGE	10					
CLASSIFICATION	Moderate reaction					

**Table 4.12. Semi-quantitative score of the overall reaction to CoCr particles, based on methods adapted from ISO 10993-6 (2016).** Cell scoring is based on the raw number of cells counted per high-powered field (400x), while scores for vascularisation are made based on the number of blood vessels per in a 100x field. Other tissue reactions are scored qualitatively based on descriptions given in ISO 10993-6.

	Test Sample (CoCr)			Control Sample (untreated)		
Animal number:	33.73	33.74	33.75	33.73	33.74	33.75
Polymorphonuclear cells	0	1	0	0	0	0
Macrophages	2	1	1	0	0	0
Lymphocytes	4	4	4	0	0	0
Plasma cells	0	0	0	0	0	0
Giant cells	0	0	0	0	0	0
Necrosis	2	3	2	0	0	0
SUBTOTAL (x2)	16	18	14	0	0	0
Neovascularization	1	1	2	1	2	1
Fibrosis	0	0	0	0	0	0
Fatty infiltrate	0	0	0	0	0	0
SUBTOTAL	17	19	16	1	2	1
TEST - CONTROL	16	17	15			
AVERAGE	16					
CLASSIFICATION	Severe reaction					

**Table 4.13. Semi-quantitative score of the overall reaction to titanium particles, based on methods adapted from ISO 10993-6 (2016).** Cell scoring is based on the raw number of cells counted per high-powered field (400x), while scores for vascularisation are made based on the number of blood vessels per in a 100x field. Other tissue reactions are scored qualitatively based on descriptions given in ISO 10993-6.

	Test Sample (Titanium)			Control Sample (untreated)		
Animal number:	33.82	33.83	33.84	33.82	33.83	33.84
Polymorphonuclear cells	0	1	0	0	0	0
Macrophages	0	0	0	0	0	0
Lymphocytes	2	2	1	0	0	0
Plasma cells	0	0	0	0	0	0
Giant cells	0	0	0	0	0	0
Necrosis	0	0		0	0	0
SUBTOTAL (x2)	4	6	2	0	0	0
Neovascularization	3	2	2	2	2	2
Fibrosis	0	0	0	0	0	0
Fatty infiltrate	0	0	0	0	0	0
SUBTOTAL	7	8	4	2	2	2
TEST - CONTROL	5	6	2			
AVERAGE	4					
CLASSIFICATION	Slight reaction					

## **4.5.9 Summary of results**

### **4.5.9.1 Summary of particle isolation results**

The main results of the isolation experiments detailed in this chapter were as follows:

- Rat stifle joint tissue samples were successfully digested using the particle isolation method developed in Chapter 3.
- Particles were successfully isolated from all 9 particle-injected stifle joints.
- Particles were relatively free from contamination.
- The composition of CoCr particles was altered by in vivo exposure.
- Particle geometries did not differ significantly.

### **4.5.9.2 Summary of main results of histology and scoring of rat stifle joints**

The main results of the histological analysis detailed in this chapter were as follows:

- Overall, differences were identified between control and treated joints.
- Although large scale morphological changes to joints were minimal, thickening of the synovium was observed, which was only significant in CoCr-injected joints.
- The reaction to SiN particles was characterised by inflammatory cell infiltrates of predominantly macrophages in the fat pad.
- CoCr particles caused larger infiltrates of inflammatory cells, consisting of predominantly lymphocytes, and smaller numbers of macrophages.
- Titanium particles caused a mild reaction, mainly involving lymphocytes; macrophages were present but rare.
- Macrophages often contained engulfed particles in all three particle-treated groups.
- Particles were observed within sections by SEM and EDX, which confirmed that the particles identified using light microscopy were not present in slides due to contamination and were not histological or biological artefacts.

- Necrosis was present in treated stifles of the CoCr group and was absent in the other material groups.
- Particles were not dispersed uniformly through the joints, causing a large degree of variation between different sections / locations of each stifle.
- There were variations in the response to particles between individual rats, though differences were not significant.

## **4.6 Discussion**

### **4.6.1 Isolation of particles from injected stifle joints**

Prior to application of the particle isolation method developed in Chapter 3 to an *in vivo* study, the method was trialled on rat cadavers (Appendix C). The results indicated that particle isolation from small amounts of rat tissue is feasible, and chemical fixation of the tissue using formalin did not produce any observable changes to particles.

The method was therefore applied to a rat study. The study successfully isolated low volumes of micron-scale and nanoscale particles from tissue, without discrimination to particle size or morphology, from a total of nine different animal samples. The animals were injected with either SiN (N=3), CoCr (N=3) or titanium (N=3), demonstrating that the isolation method is effective in a variety of different materials. Initial particle volumes were 0.018 mm<sup>3</sup>, suggesting that the technique is highly sensitive. Particles were demonstrably unchanged in terms of size, aspect ratio or circularity by the isolation procedure. Proteins were effectively removed, and the elemental analysis demonstrated that the isolated particles were relatively pure.

The use of an *in vivo* model also enabled histological analysis of injected particles within tissue sections, scanning electron microscopy and elemental analysis of particles within tissues. Particles were located within histological tissue sections with a previously used technique (Esposito et al., 2013) to enable accurate tissue harvesting prior to particle isolation. Elemental analysis of isolated particles demonstrated a degree of particle oxidation in the CoCr and titanium particles. Since particle oxidation was also identified in CoCr particles within tissue sections, it is likely that oxidation of the CoCr

particles occurred *in vivo*; however, in titanium particles, oxidation was only evident post-isolation and thus likely occurred during the filtration of particles prior to SEM analysis. Prior to isolation, a higher ratio of cobalt to chromium was evident from spectrum analysis; this would be expected since the alloy used was cobalt with 28% chromium, 6% molybdenum and approximately 0.2% carbon (ASTM F1537, 2011). However, following seven days of *in vivo* exposure there was a higher ratio of chromium to cobalt, both in tissue sections and post-isolation, which is likely due to *in vivo* changes. These findings suggest the displacement of cobalt and formation of chromium oxides, which have been documented to occur *in vivo* (Paustenbach *et al.*, 2014). This may have led to the necrosis identified in the rat tissues, as elevated levels of cobalt are known to cause tissue necrosis (Catelas *et al.*, 2005). It has been suggested that corrosion of the particles occurs within phagolysosomes, leading to toxic levels of metal ions (Haynes *et al.*, 2000).

Rats were chosen rather than mice to allow a sufficient dose of particles to be injected and to enable an appropriate amount of tissue to be harvested for particle isolation; in addition, the joints were still small enough for whole-joint histological analysis to be feasible. The volume of injected particles was 0.018 mm<sup>3</sup>, which is lower than the volume of particles that would normally be recovered from an explant tissue sample, since the volume of particles per gram of tissue from a failed hip prosthesis has been estimated at 0.37 mm<sup>3</sup> (Ingham *et al.*, 2003). Failed ceramic-on-ceramic bearings may produce 1–5 mm<sup>3</sup> of wear per year (Nevelos *et al.*, 1999). The *in vivo* exposure time of seven days was the maximum time point that could enable protein binding to particles before a large volume of particles would be lost through dissemination. It has previously been shown that following injection of mice stifle joints with nanoscale and micron scale CoCr particles, approximately 60–70% of the injected metal was no longer present in the peri-articular tissue after seven days, and particles were found to disseminate via lymph nodes (Brown *et al.*, 2013). In this study, the darkened tissue which was visibly apparent on the surface of CoCr-injected stifle joint tissues may have been due to metallosis within the ligament, possibly due to particles and/or metal ions diffusing out of the joint space through the injection site.

The CoCr and titanium particles used in this study were similar in size and shape to those retrieved from periprosthetic tissues and those generated by physiological hip simulators (Bohler *et al.*, 2000; Brown *et al.*, 2006; Tipper *et al.*, 2001; Firkins *et al.*, 2001 and Grosse *et al.*, 2015). Our results suggest that SiN particles may dissolve less quickly *in vivo* than has been previously suggested by simulations of *in vivo* conditions (Pettersson *et al.*, 2016), since there were no detectable changes to particle size or shape. Additionally, results suggest that corrosion of particles, which may occur within macrophages, did not affect a significant number of particles within the given time frame. Surface characteristics of the particles also appeared to be unchanged. Surface characteristics play a crucial role in how particles interact with proteins and thus in the overall biocompatibility of a material (Aggarwal *et al.*, 2009).

There were several limitations to the current study. Particle adhesion to the glass syringe may have occurred during injection, and hence there may have been slightly lower actual volumes of particles delivered intra-articularly. Since particles were *in vivo* for a period of seven days, and were introduced via an injection, particles produced by a prosthesis may have differing particle aggregation and protein corona characteristics, though it has been suggested that a hard protein corona is formed after just 48 h (Casals *et al.*, 2010). In addition, particles may not have dispersed as they would in an *in vivo* scenario where particles are continuously produced. It is also possible that there were subtle changes to particle geometries that could not be detected due to the resolution limit of the SEM equipment; however, international guidelines for minimum magnifications were followed (ISO 17853, 2011; ASTM F1877, 2016). The measurements of the particles were also limited due to their aggregated nature, which meant that manual particle sizing was required. This limited the number of particles that it was feasible to size, though international guidelines were also followed with regard to minimum particle numbers for statistical analysis of particle characteristics. Another possible limitation of the current study is that during elemental analysis of isolated particles, tungsten was identified on CoCr particles. However, this had no detectable effect on particle size or morphology and the tungsten could likely be removed by further rounds of ultracentrifugation, as described in the washing stages of the

protocol. Furthermore, elemental analysis demonstrated a lack of any other contaminating elements on particles, suggesting that particles were relatively pure.

The isolation technique reported here represents an improvement to current particle isolation methods from tissue, due to its more effective removal of proteins and greater sensitivity. This work could be valuable to future animal and explant studies evaluating ceramic or metal particles, especially as the latest generation of orthopaedic materials are highly wear-resistant, and thus there may be a need to isolate increasingly lower volumes of particles.

#### **4.6.2 Histological analysis of stifle joint sections**

Histological analysis of intact stifle joints enabled the collection and subsequent H&E staining of whole joint cross-sections. Particles were successfully located within tissue sections, and confirmed by elemental analysis of unstained, re-cut sections. Accompanying inflammatory cell infiltrates, as well as changes to joint morphology, could be analysed in a semi-quantitative way by counting cells within specific locations. The data were analysed statistically, and this demonstrated significant differences between controls and treated stifle joints. Overall, the results indicated that all three materials elicited a biological reaction. CoCr, but not SiN or titanium particles, caused necrosis, and CoCr elicited a more severe biological response involving larger inflammatory cell infiltrates than either of the other materials.

To minimise any biases in cell counting, three areas from each section were chosen for scoring, consisting of a low, intermediate and high number of cells. This prevented inflammatory cell infiltrates from being missed, which may have occurred if a completely randomised method was used. In addition, scoring of multiple areas per section was carried out to account for any differences within sections.

To establish the validity of the cell counting technique, two additional researchers scored a blinded and randomised selection of the same images. There was no statistically significant difference between any of the scores for any pair of researchers, though a general difference was found with respect to macrophage scoring. This may reflect a difference in the relative histological



experience of different researchers, or the qualitative nature of histological scoring, which is a limitation of the current study.

Although sample numbers were highly limited ( $N \geq 12$  images per material group for each parameter, and  $N \geq 3$  images per stifle joint), it was useful to perform statistics to aid interpretation of the results of histological scoring. Overall, this demonstrated that there was a statistically significant difference in the synovial thickness of CoCr-injected stifle joints compared to the controls. It has been shown that the synovium thickens in response to injury or disease and following joint replacement (Kung *et al.*, 2015). Thickening of the synovium appeared to be due to proliferation of cells in the intimal layer, although inflammatory cell infiltration of the sub-synovial layer may have contributed to the number of cells counted. The formation of finger-like projections (villi) into the joint space, which was observed in a titanium-injected rat, has also been reported to contribute to synovial thickening (Kung *et al.*, 2015). It has previously been difficult to deduce whether these changes occur solely as a result of injury during the hip replacement procedure, or also as a response to wear debris. These results suggest that certain wear debris may directly impact synovial thickness, though it is also possible that a greater degree of injury was caused to CoCr-treated stifle joints during the injection procedure by experimental variation. SiN- and CoCr- injected joints differed to their respective untreated controls in terms of the number of cells in the fat pad, and in terms of the number of macrophages. Additionally, CoCr- and titanium-injected joints differed to their untreated controls in terms of number of lymphocytes. Overall, this indicates that an inflammatory response occurred with respect to all three materials. This agrees with previous reports that an innate, predominantly macrophage-driven immune response occurs in response to ceramic materials (Bylski *et al.*, 2009; Roualdes *et al.*, 2010). A more lymphocyte dominated response to CoCr particles has also been established (Watters *et al.*, 2010). Titanium particles have been described most extensively as eliciting a macrophage-driven response (Warashina *et al.*, 2003), though there is some contention with regard to the biological effects of titanium particles. In addition, reactions to titanium particles appeared to be more localised in comparison to the other materials, since inflammation was only present directly surrounding particles and was absent from the sections

that contained no particles. Giant cells were not found in any of the samples despite evidence of giant cell reactions to large particles; it is possible that under the conditions of this study, a longer time point would be required for this type of reaction to occur. Although the statistical analysis comparing material groups to their respective controls suggest that biological responses differed between materials, no statistically significant differences were found between treated material groups (SiN vs CoCr, SiN vs titanium, or CoCr vs titanium) for any of the biological reactions measured. It is likely that the sample numbers were too few to establish any significant differences. Differences between any pair of animals within the same material group were also not significant, likely due to the same reason. Since a non-inbred strain of rats was used, it is likely that at least some of the variation observed between animals is significant and reflects individual-specific differences. Although neovascularisation may occur within days of an inflammatory stimulus (Curseifen *et al.*, 2006), CoCr particles may also interfere with wound healing and block angiogenesis. Our results suggest that a significant degree of neovascularisation did not occur within the seven-day timeframe. However, it is probable that variations within animals was too high to enable effective statistical comparisons between animals and groups.

Observation of particles within tissue sections demonstrated that particles were successfully delivered into the joint space. Silicon nitride particles were less apparent in tissue sections, most likely as a result of dissolution during the five-week decalcification procedure, which was performed at 37°C with agitation. However, dispersion was limited to the anterior part of each joint, directly beneath the patella, with few particles identified in the central part of each joint. Particle dispersion was more limited in the titanium group, possibly due to the size of the titanium particles, which likely prevented particle diffusion and transportation by macrophages. Studies have shown that particles eventually disseminate throughout the joint space (Catelas *et al.*, 2001; Doorn *et al.*, 1998), suggesting that development of the injection method to enable greater dispersion of the particles within the seven-day timeframe may improve the clinical relevance of the animal model.

Apart from statistical analysis of the raw cell numbers, materials were classified based on a semi-quantitative scoring method adapted from ISO

10993-6 (2016). Although this helped to grade the severity of the reaction and give an indication of the relative biocompatibility of each material, this approach had several limitations. Firstly, the method focusses on implants, and thus certain scores, e.g. fatty infiltration were less suitable for the rat model used. It was noted that the presence of a single cell type could increase scores from zero to one, which could influence the classification of a material. Since immune cells are present even in most healthy tissues to some extent, a higher scoring threshold of more than one cell might be more relevant. Scores such as that for necrosis are relatively qualitative in the methods given in ISO 10993-6 (2016). Further, the classification method does not take into consideration the conditions of the study, i.e., scores cannot be adjusted to take different time points or doses into consideration, which limits its use as a comparative tool to other studies. Finally, the method scores all cell types equally; thus, a nonspecific reaction involving predominantly macrophages would have an identical score to a lymphocyte-driven response involving the same number of lymphocytes. There is evidence that nonspecific immune responses are associated with more biocompatible materials (Ingham and Fisher, 2000); thus, the score of 'moderate irritant' attributed to SiN may not be a true reflection of the biocompatibility of the material.

Other limitations to the study included the fact that no sham injection was carried out in the contralateral, untreated stifle joint. This would have enabled any biological effects from the injury of the injection to be excluded. However, researchers at the University of Zurich have indicated that based on previous experience involving a similar study (Mirsaidi *et al.*, 2014), injury to the injection is resolved within the first 2-3 days. Further, the relatively few polymorphonuclear cells found within sections indicates that the general response to injury had subsided. Another limitation is that although microtome sectioning was set to 5  $\mu\text{m}$ , in some areas sections appeared to contain overlapping layers of cells. It is possible that as the pre-chilled wax block reached room temperature, the wax block and sample expanded slightly, resulting in thicker sections. This may have caused more cells to be counted in certain areas – for example, the intimal lining of the synovium was slightly thicker in certain areas than the 1-2 cells normally described in the literature (Kung *et al.*, 2015). Additionally, the non-uniform dispersion of particles meant

that some sections contained a greater volume of particles than others, which could have caused experimental variation in the results. It is also possible that certain cell types were easier to recognise than others, leading to possible biases in scoring.

## Chapter 5

# Investigation of the biocompatibility of silicon nitride coatings using an *in vivo* rabbit model

### 5.1 Background

Ceramic coatings are being investigated for application to bearing surfaces to enhance the function of orthopaedic implants (Khanna *et al.*, 2017). The advantages of using ceramic coatings over the use of the ceramic material in bulk form include the possibility of retaining a ductile substrate material, such as CoCr, whilst preventing incidences of fracture and catastrophic failure, which occur in bulk ceramic implants (Hamilton *et al.*, 2010). Coatings may be used to improve implant function by enhancing the wear-resistance, and by reducing the volume of wear debris released. Ceramic coatings may also have a more favourable biocompatibility profile compared to typical metal substrate materials (Bal and Rahaman, 2012); thus, the wear debris are not only lesser in volume but also elicit a less harmful biological reaction. Silicon nitride (SiN) is of particular interest as a coating material due to its dissolution properties and a generally favourable biocompatibility profile (Bal and Rahaman, 2012; Pettersson *et al.*, 2016). SiN coatings may also have the potential to be highly wear resistant (Olofsson *et al.*, 2012).

The *in vivo* biocompatibility of model (commercially available) SiN particles was investigated in Chapter 4 through a seven-day study involving the injection of particles into rat stifle joints. However, an *in vivo* study using an actual SiN-coated prosthesis would be required to analyse the biocompatibility of a specific coating. This is important since injection of particles could differ significantly from the natural release of wear debris, and since a time point of longer than seven days is required to better evaluate the chronic reaction to coating debris. In addition, the longer time point may enable particle dissolution to take place, which would theoretically reduce chronic reactions to particles. Further, the model particles used in Chapter 4 had a narrow, nanoscale size range, while coating particles could potentially include larger-diameter particles. Finally, particle reactions may vary between species, since there are known phylogenetic variations in the structure and function of the

immune system (Haley, 2003). Thus, data from different animal models needs to be gathered to gain a better understanding of the biocompatibility of SiN coating particles.

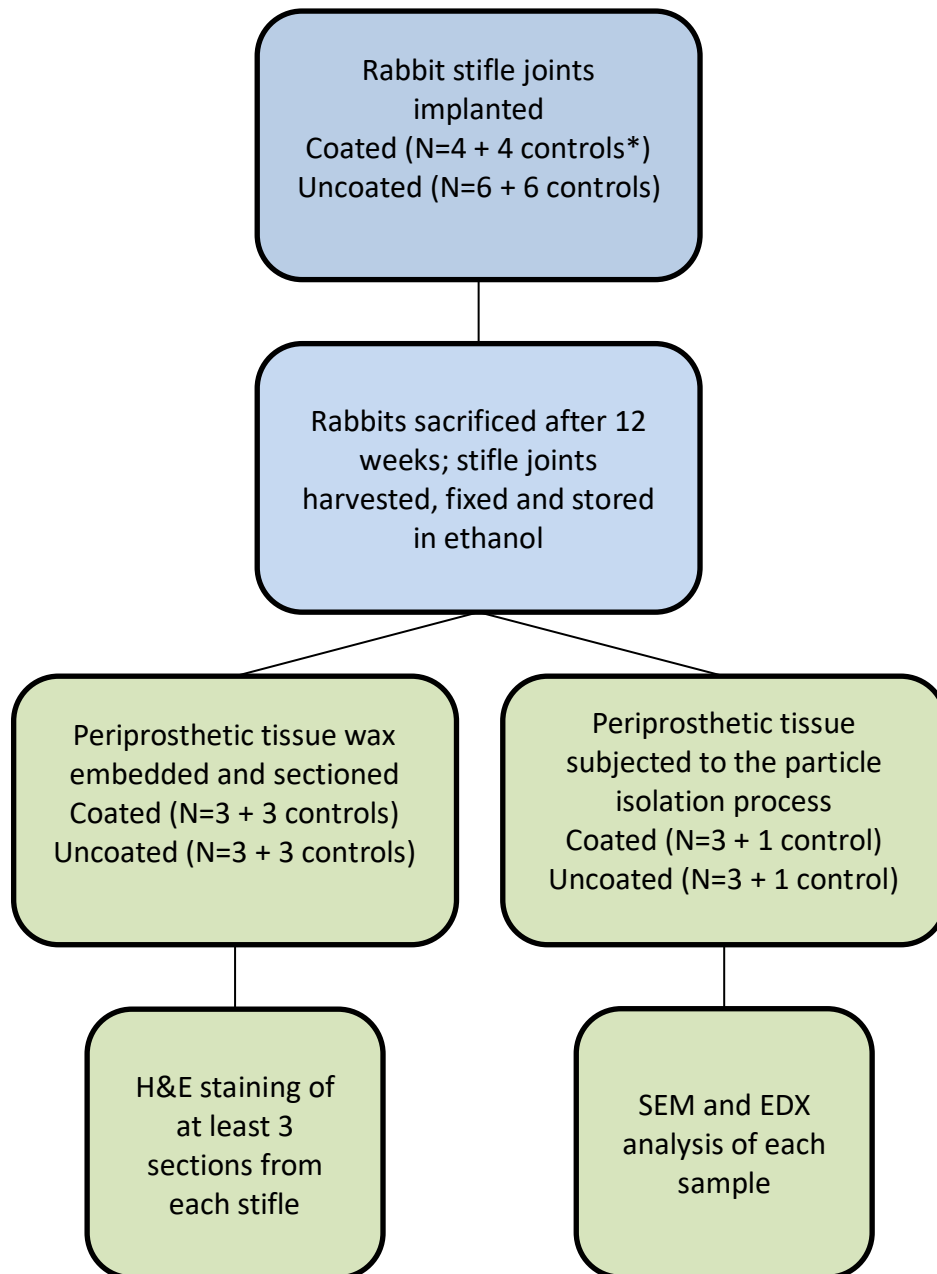
## **5.2 Aims**

The aim of research outlined in this chapter was to investigate the biocompatibility of SiN coatings *in vivo*. This was achieved using a rabbit model whereby SiN-coated stifle joint prostheses manufactured from CoCr were implanted for a period of three months; uncoated CoCr prostheses were also implanted into a separate group of rabbits for the same time period to serve as controls. Specific objectives included:

- Isolation and characterisation of particles produced by the coating, as well as particles produced by the uncoated control prostheses, from the periprosthetic tissue of implanted rabbit stifle joints
- Histological analysis of periprosthetic tissue from implanted rabbit stifles to assess changes to joint morphology including synovial thickness and vascularisation and characterise any inflammatory cell infiltrates.

## **5.3 Overview of experiments**

To investigate the biocompatibility of a silicon nitride coating, an *in vivo* study was carried out in collaboration with the University of Zurich. Briefly, this involved the manufacture and subsequent coating of rabbit stifle joint prostheses, which were surgically implanted into rabbits at the University of Zurich. As with the rat study, the overall study design, including type of animal, number of animals, and time points were developed and the animal study was carried out by researchers at the University of Zurich. Samples consisting of intact rabbit stifle joints, or dissected periprosthetic tissues, were sent to the University of Leeds for histological evaluation and particle isolation, which is the focus of this chapter. An overview of the animal model and subsequent experiments is given in Figure 5.1.



**Figure 5.1. Overview of experiments outlined in this chapter.** Blue boxes describe experiments carried out at the University of Zurich, while green boxes describe work carried out at the University of Leeds by the current author. \*Control samples refer to the contralateral, non-implanted joint of each animal. In the coated group, tissue samples taken from two stifle joints were split to enable both histology and particle isolation to be carried out. In the uncoated group, tissue samples were not split since a greater number of animals were available for analysis.

## 5.4 Materials and methods

Materials used throughout this chapter are given in Appendix A.

### 5.4.1 In vivo model

The study involved a total of 10 rabbits, consisting of a coated and uncoated group (Table 5.1). Experiments and the design of the animal model described in this section were carried out by researchers at the University of Zurich (Prof Brigitte von Rechenberg and Dr Karina Klein) until the point where the samples were shipped to Leeds.

**Table 5.1. Details of samples from animal study.**

Implant type	Number of rabbits	Number of intact joints sent to Leeds after three-month implantation time	Number of histology samples sent to Leeds
Uncoated cobalt chrome molybdenum alloy (ISO 5832-12)	Six – labelled as follows: 34.01 34.03 34.04 34.06 34.07 34.08	Six in total (three treated and three untreated joints from rabbits 34.03, 34.04 and 34.08)	Six in total (three treated and three untreated samples from rabbits 34.01, 34.06 and 34.07)
Silicon nitride coated cobalt chrome molybdenum alloy (ISO 5832-12)	Four – labelled as follows: 34.14 34.17 34.22 34.24	Six in total (three treated and three untreated joints from rabbits 34.17*, 34.22 and 34.24*)	Two (treated and untreated sample from rabbit 34.14)

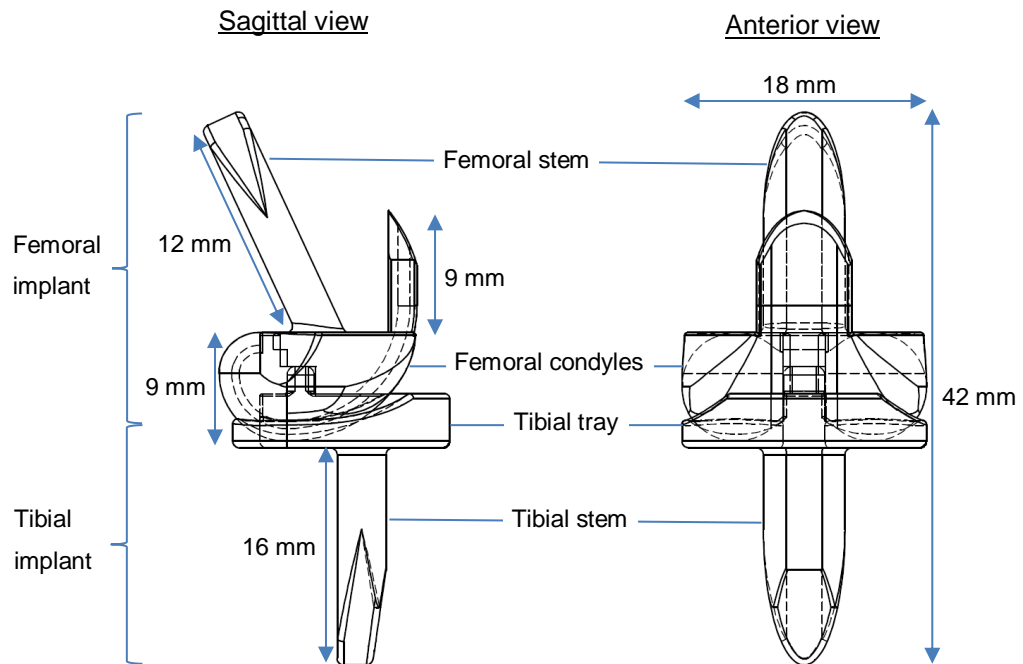
\* Samples split for histological analysis as well as particle isolation



The *in vivo* model consisted of female New Zealand White rabbits (outbred; supplied by Charles River), 5-12 months old and with weights ranging from 3-5 kg. Guidelines contained in EU Directive 2010/63/EU for animal experiments were followed. Details of food, housing and environment are given in Appendix B. Ear tattoos and transponders were placed on the rabbits on arrival into the facility. The rabbits were physically examined and acclimatised for at least seven days under test conditions prior to the study; during this time animals were checked for viability and any clinical signs of abnormality twice daily. Animals with any signs of illness were excluded from the study, while healthy animals were randomly assigned to one of the study groups. Animals were also weighed to ensure accurate dosage of medications. Stifle joints were chosen for treatment due to the ease of access of the stifle, to enable comparisons to the rat study (which involved the stifle joint), and due to the ability to use a customised interphalangeal prosthesis as an effective stifle joint prosthesis. The left stifle joints were not implanted and were used as untreated control joints.

#### **5.4.2 Prosthesis design**

The design of the rabbit stifle joint prostheses was adapted from a human interphalangeal joint prosthesis by researchers at ETH Zurich (Prof Stephen Ferguson and Mr. Remo Affentranger) and consisted of a femoral implant with a stem and a tibial implant with a stem (Figure 5.2). The implants were produced by CNC machining from CoCr alloy with molybdenum (ISO 5832-12) and polished to a surface roughness of  $0.049 \mu\text{m} \pm 0.005 \mu\text{m}$  Ra by Jossi Orthopedics (Islikon, Switzerland). The surface coating was carried out by Ionbond (Olten, Switzerland). Implants were sterilised at the University of Zurich at  $134^{\circ}\text{C}$  using a medical device steam steriliser.



**Figure 5.2. Design of rabbit stifle joint prostheses.**

### **5.4.3 Coating details**

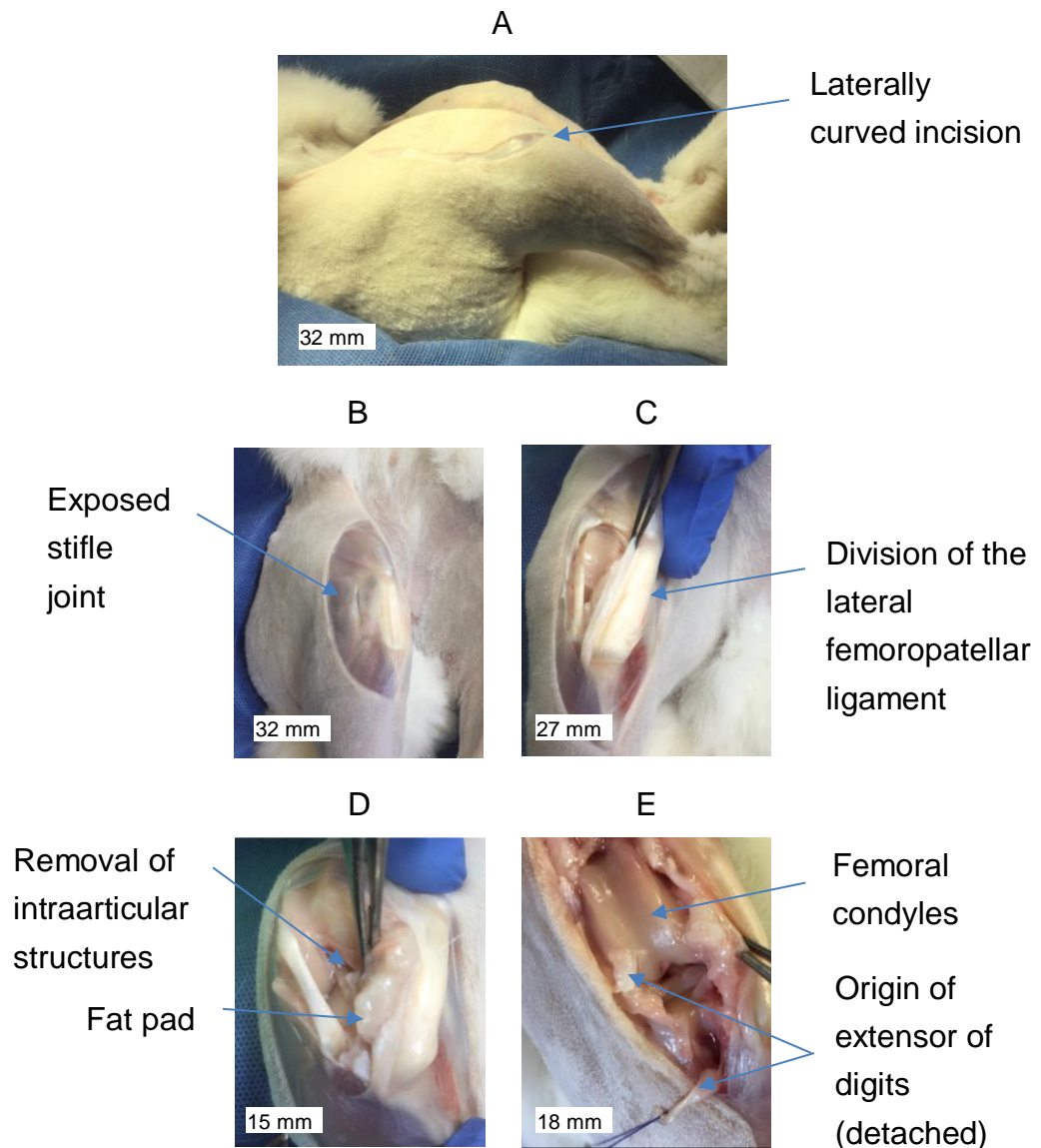
The rabbit implants were coated in two batches. Prior to the deposition, the substrates were cleaned by glow discharge in an Ar/H<sub>2</sub> mixture at up to -900V. After this, a Cr adhesion layer was deposited, followed by about 0.8 μm of CrN and 0.8 μm of a transition layer of CrN – SiN. The top layer was 5.5 - 6.1 μm of SiN. The depositions were done at -150 V at 6.0 × 10<sup>-3</sup> mbar. The Cr-magnetrons were run in unbalanced magnetron sputtering mode whereas the Si was provided by HIPIMS sputtering. All magnetrons (2× Cr, 2× Si) were run at 5 kW. The deposition process used Argon as a sputtering gas for Cr deposition and a mix of Ar and N<sub>2</sub> (60% v/v Ar) for the nitrides (CrN and SiN).

### **5.4.4 Surgical implantation of the stifle joint prostheses**

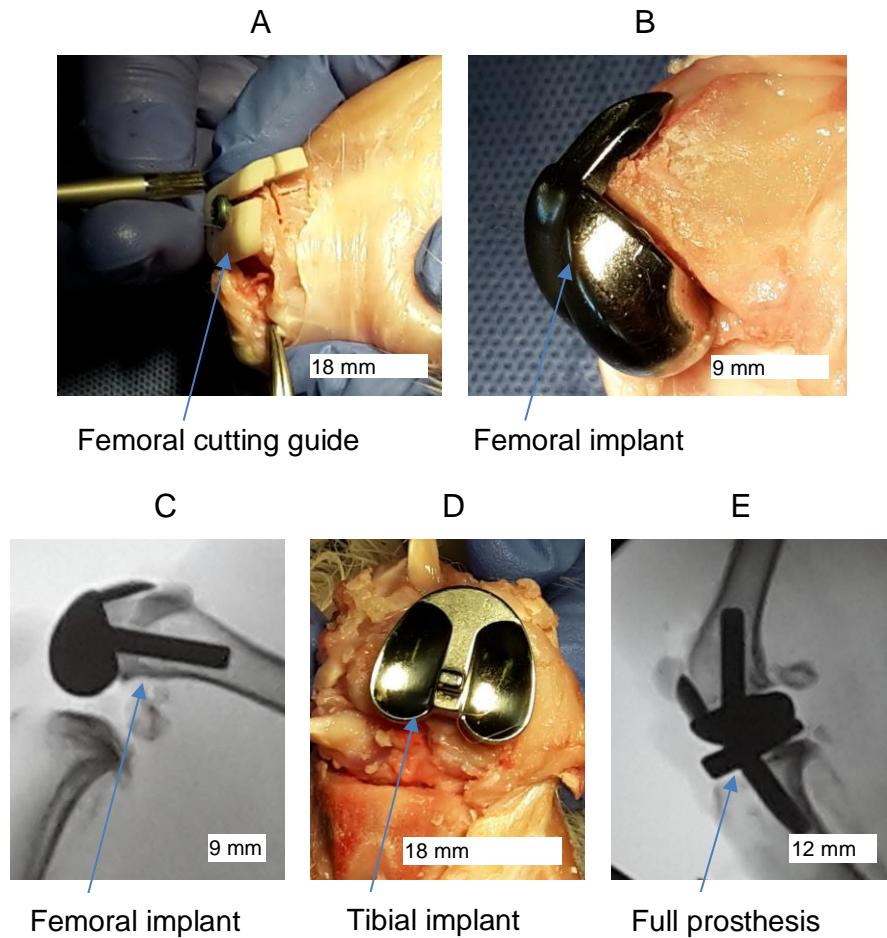
The surgical method provided here has been adapted from information supplied by the University of Zurich. Stainless steel surgery instruments and a saw plate were made of Synthes 519.150 stainless steel; cutting guides were made from VisiJet© M3 crystal polymer. Under general anaesthesia each rabbit was placed in dorsal recumbency with the thorax and the head slightly tilted to the non-operated side. The right hind limb was shaved and the stifle joint region including the proximal part of the lower leg and the distal part of the upper leg was disinfected. The surgical site was isolated with sterile drapes to avoid contamination of the incision, instruments and supplies. A 5-

8 cm laterally curved incision of the skin was made to the stifle joint region (Figure 5.3A). The skin and subcutis were dissected to expose the stifle joint and the patella. The distal part of the fascia lata and the distal, tendinous part of the femoral biceps muscle was incised to gain lateral joint access (Figure 5.3B). The patella was dislocated medially by dividing the lateral femoropatellar ligament (Figure 5.3C). The cruciate ligaments were divided and all intraarticular structures (menisci) were excised (Figure 5.3D). The fat pad was left in place. To fully expose the knee joint, the patellar tendon and the cranial tibial muscle was partially detached from the tibial tuberosity/plateau. The origin of the long extensor of digits was detached from the lateral femoral condyle and tagged using a suture for later refixation (Figure 5.3E). To find the correct position for the cutting guide on the femoral condyles and thus to ensure a correct osteotomy direction, a small pin was inserted in the medullary cavity and the position was verified using fluoroscopy. Different drill bits with increasing size (2.5, 3.5 and 4.5 mm) were used to slowly enlarge the medullary cavity and prepare a hole for the holding pin for the cutting guide. The size of the holding pin was chosen such that the stem of the femoral implant fit the same hole. Using the cutting guide and an oscillating saw, the femoral condyles and a part of the patellar groove were resected (Figure 5.4A). The femoral implant was inserted, ensuring adequate stability was achieved and the position was checked using fluoroscopy (Figure 5.4B and C). For preparing the tibial part, the implant was removed. Similar to the femoral implant, a pin was placed in the medullary cavity of the tibia using fluoroscopy to enable correct positioning for the tibial cutting guide. Again, different drill bits with increasing size (2.5, 3.5 and 4.5 mm) were used to slowly enlarge the medullary cavity and prepare a hole for the holding pin for the cutting guide. The size of the holding pin was chosen such that the stem of the tibial implant fit the same hole. Correct positioning of the cutting guide was verified using fluoroscopy. The tibia plateau was then dissected by cutting perpendicular to the medullary cavity of the tibia (parallel to the tibial plateau). The prosthesis was inserted until adequate stability was achieved (Figure 5.4D). Motion through the full articular range was tested with both implants in place and positioning of the overall implant was verified by fluoroscopy (Figure 5.4E). Both implants were removed and bone cement (Refobacin© bone

cement R with gentamycin) was applied into both of the drilled cavities in the distal part of the femoral shaft and the proximal part of the tibial shaft. The prosthesis parts were re-implanted and once again, positioning was verified by fluoroscopy.

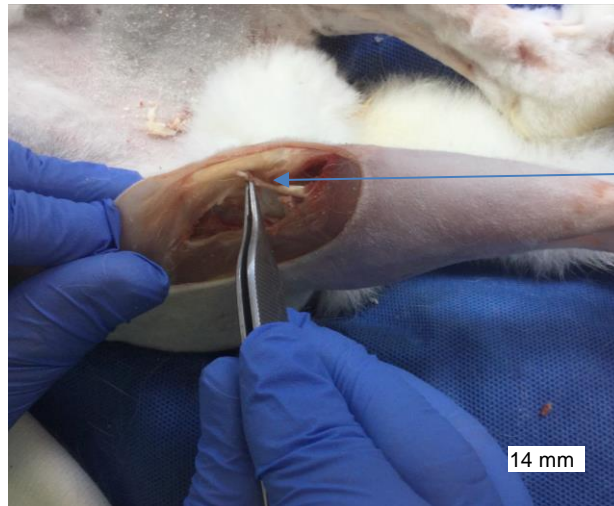


**Figure 5.3. Surgical procedure to open the joint compartment for prosthesis implantation.** (A) A 5-8 cm laterally curved incision of the skin was made to the stifle joint region. (B) The distal part of the fascia lata and the distal, tendinous part of the femoral biceps muscle was incised to gain lateral joint access. (C) The patella was dislocated medially by dividing the lateral femoropatellar ligament. (D) The cruciate ligaments were divided and all intraarticular structures (menisci) were excised. (E) The origin of the long extensor of digits was detached from the lateral femoral condyle and tagged using a suture for later refixation.



**Figure 5.4. Surgical fitting of the rabbit stifle joint prosthesis parts.** A. Application of the cutting guide with the holding pin to enable accurate cutting of the femur. B. Appearance of distal end of the femur following femoral implantation, showing cut parts of the bone. C. Fluoroscopic observation of the position of the femoral implant. D. Appearance of tibial component following implantation. E. Fluoroscopic observation of the position of both prosthesis parts.

Following the implantation, the origin of the lateral digital extensor muscle was sutured to the patella ligament (Figure 5.5). The lateral femoropatellar ligament, the fascia lata and the distal tendinous part of the femoral biceps muscle were repaired using resorbable suture material. The skin was closed with an intracutaneous continuous suture using resorbable suture material. The incision site was protected with waterproof wound spray.



Repair of the extensor of digits muscle

**Figure 5.5. Surgical procedure to repair stifle joint function and close the joint compartment.** The origin of the lateral digital extensor muscle was sutured to the patella ligament, and the joint compartment and skin was closed by suturing.

#### **5.4.5 In-life phase of the rabbit study**

Post-operative analgesia was administered subcutaneously in the form of buprenorphine ( $0.01-0.05 \text{ mg.kg}^{-1}$ ) every 6-8 hours on the day of surgery. In addition, meloxicam ( $1 \text{ mg.kg}^{-1}$ ) was given subcutaneously once daily for at least 7 days. Additional analgesia was provided as required. Prophylactic antibiotic therapy was administered by giving enrofloxacin ( $7.5 \text{ mg.kg}^{-1}$  intravenously or subcutaneously) once daily on the day of surgery and for 5-7 days thereafter. Ranitidine was given twice daily (before and after surgery,  $1-2 \text{ mg.kg}^{-1}$  intravenously or subcutaneously) as an antacid on the day of surgery and as required thereafter. Animals were checked for viability and any clinical signs of abnormality at least three times in the two-hour postoperative recovery period and twice daily for the three-month observation period.

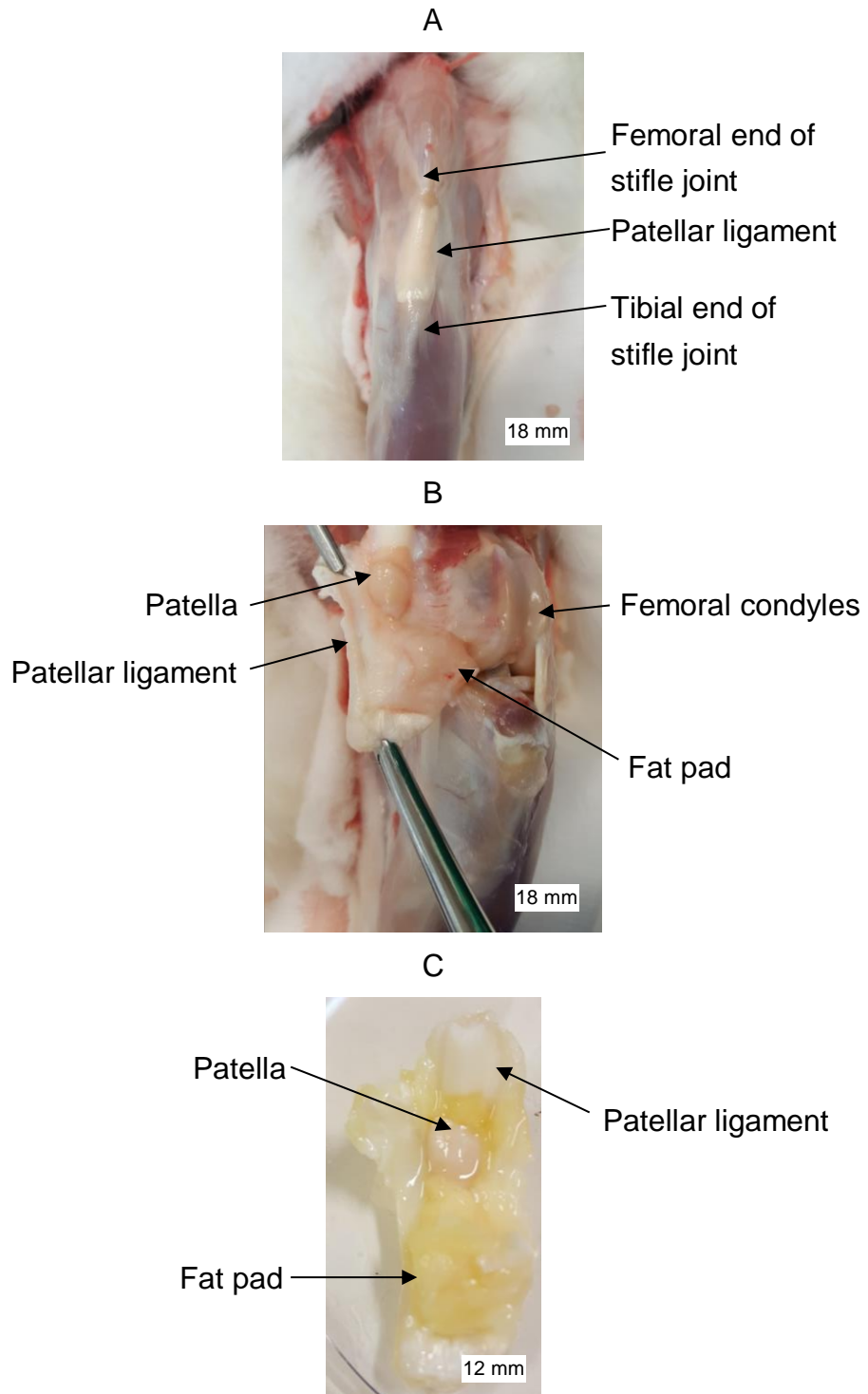
#### **5.4.6 Euthanasia and dissection**

At the end of the observation period, euthanasia was carried out by first sedating the rabbits with alphaxalone ( $3-5 \text{ mg.kg}^{-1}$ ). After sedation, the animals were euthanized with pentobarbital ( $150-300 \text{ mg.kg}^{-1}$ ). Rabbits were dissected immediately following sacrifice. Stifle joints were either left intact to prevent contamination of tissue prior to particle isolation or dissected for histology. The tissues for histology were extracted by first dissecting the skin

and subcutis to expose the stifle joint (Figure 5.6A). This was followed by opening the joint compartment with a scalpel (Figure 5.6B) and carefully shearing the joint compartment above the patella, below the fat pad, and parallel to the contralateral ligaments to provide one whole piece of tissue consisting of the patellar ligament, patella, fat pad and part of the synovium. These tissues were immediately formalin-fixed at room temperature for a period of 24 h by placement into sterile, plastic tubes filled with 10 % (v/v) NBF (Figure 5.6C). For the intact joints, excess muscle tissue was removed from the stifle joints using a scalpel, taking care not to open the joint compartment by leaving the pericapsular ligament intact. The intact rabbit stifle joints (both treated and non-treated) were excised by bisection with shears midway through the femur, tibia and fibula. The stifle joints were immediately formalin-fixed at room temperature for a period of 10 days by placement into sterile, plastic tubes filled with 10 % (v/v) NBF. The joints were fixed in their natural configuration, i.e. the degree of flexion in the joints was not altered.

Following the fixation period, stifle joints and histology tissue samples were stored at room temperature by discarding the NBF and refilling with 70% (v/v) ethanol. Samples were shipped at room temperature to Leeds within 48 h. For shipment it was necessary to temporarily remove the ethanol and cover samples in medical gauze soaked in 70% (v/v) ethanol. On arrival at Leeds the gauze was discarded, and samples were briefly examined to ensure no drying out of the tissue had occurred. Tubes containing the samples were then immediately refilled with 70% (v/v) ethanol and stored at room temperature prior to further analysis.





**Figure 5.6. Dissection of rabbit stifle joints for histology.** A. Appearance of the exposed stifle joint (untreated) following dissection of the skin and subcutis. B. Opening of the joint compartment. C. Appearance of harvested tissue following fixation and storage in 70% (v/v) ethanol, part of which was processed for histology.



## **5.4.7 Particle isolation from periprosthetic tissue of rabbit stifle joints**

### **5.4.7.1 Harvesting and preparation of tissue**

Dissection of the stifle joints and subsequent particle isolation from dissected tissues was carried out for all six implanted stifle joints (N=3 from the uncoated group and N=3 from the SiN-coated group). In addition, two untreated joints which served as particle-free control tissue samples were subjected to the same particle isolation methodology. The intact rabbit stifle joints were washed three times in sterile filtered water by filling the tube, vortexing the tube for five seconds, and immediately discarding each wash to remove traces of formalin, ethanol, and exterior contaminants. The excised tissues were dissected in a similar way to the histology samples (Figure 5.6); the joint compartment was opened and the patellar ligament, patella, fat pad and synovial tissue continuous with the fat pad was carefully excised as one intact piece using clean, sterile dissection equipment in a class II cabinet. The patella and any tissue exterior to the joint compartment were discarded and a 250 mg (wet weight) sample of tissue from the fat pad immediately beneath the patella was extracted for particle isolation. For animals 34.17 and 34.24 from the SiN-coated group, the rest of the fat pad was used for histological analysis. The 250 mg tissue samples were minced to 1 mm<sup>3</sup> sized pieces in a sterile culture dish and added to round-bottomed plastic test tubes. A volume of 1 ml of sterile filtered water was added to each sample to prevent the tissue from drying out. Dissection equipment was cleaned by sonication in 70% (v/v) ethanol for 5 minutes between samples to prevent sample cross contamination.

### **5.4.7.2 Particle isolation and characterisation**

Immediately following harvesting and tissue preparation as described in 5.4.7.1, tissues were subjected to the tissue digestion procedure as described in section 2.2.8.1. Samples were then subjected to density gradient ultracentrifugation as described in 2.2.8.2, and sodium polytungstate was removed from samples as described in 2.2.8.3. Isolated particles were stored at -20 °C prior to SEM analysis. Particles were filtered as described in 2.2.2.

SEM imaging and elemental analysis was carried out on the filtered particles as described in sections 2.2.6.4 and 2.2.6.5.

#### **5.4.8 Histological analysis of periprosthetic tissues**

Histological analysis was carried out on tissue samples from three treated rabbit stifle joints from both the coated and uncoated groups, in addition to three untreated contralateral stifle joints from both groups, which were used as controls. Briefly, this required the tissue samples to be embedded in paraffin wax; samples were then sectioned, and selected sections were stained with haematoxylin and eosin (H&E) to allow observation of tissue structures and cells using light microscopy. The particles and any inflammatory cell infiltrates were analysed.

##### **5.4.8.1 Tissue processing, wax embedding and sectioning**

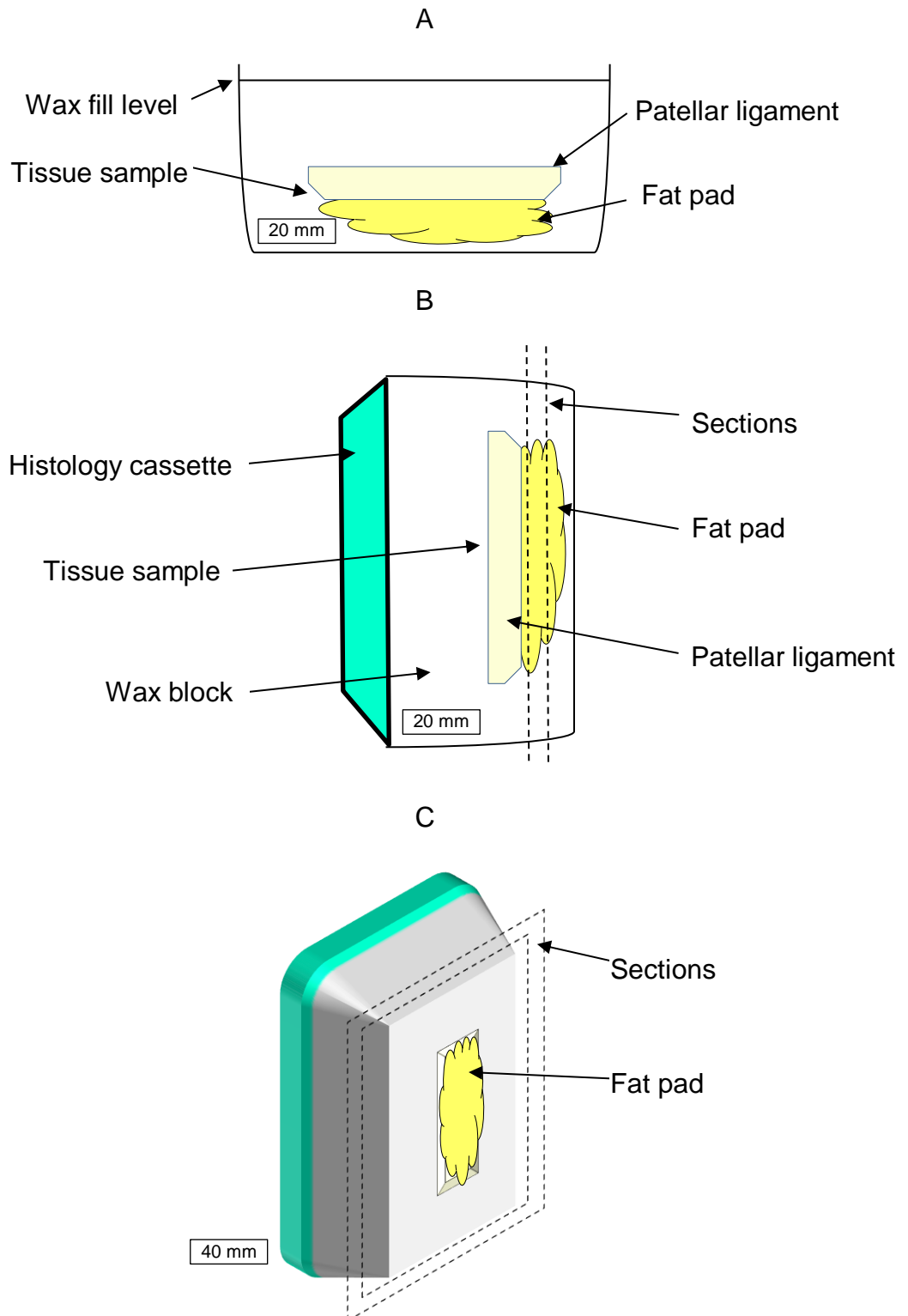
Rabbit stifle joint tissues were trimmed to leave only the distal part of the fat pad and associated patellar ligament. Tissues were processed within individual, labelled plastic cassettes using a tissue processor (Table 5.2).

**Table 5.2. Programmes used for rabbit tissue samples.**

<b>Solution (v/v)</b>	<b>Soft tissue samples</b>
70% ethanol	1 hr
90% ethanol	1 hr
100% ethanol	30 m
100% ethanol	30 m
100% ethanol	1 hr
100% ethanol	1 hr
100% xylene	1 hr
100% xylene	1 hr
100% xylene	1 hr
100% Molten wax	2 hr
100% Molten wax	1 hr
<b>TOTAL</b>	<b>11 hr</b>

Within 12 hours of completion of the tissue programme, the tissue samples were embedded as described in section 2.2.9.1, using the embedding and

cutting orientations shown in Figure 5.7A and B. This orientation was chosen to allow cross sections of the fat pad to be observed by light microscopy.



**Figure 5.7. Embedding and cutting orientation of rabbit histological samples.** (A) Representation of tissue sample placement within an embedding mould. (B) Representation of the lateral view of the sectioning plane. (C) 3D model showing cross-sections of the tissue from a frontal plane.

Approximately 30 serial sections were taken from both treated and untreated joints. The wax blocks were chilled on ice for ten minutes and sectioned to 5 µm with a blade angle of 3°. The sections were floated on a water bath filled with deionised water at a temperature of 45-50°C and applied to charged slides. The slides were drained of excess water by tapping the edge on paper tissue and the slides were placed on a hot plate set to 55-60°C for 2 h.

#### **5.4.8.2 Haematoxylin and eosin staining of sections and slide mounting**

A minimum of three sections per sample, each approximately 100 µm apart (depth), were dewaxed and re-hydrated as described in section 2.2.9.2, stained with H&E as described in section 2.2.9.3, and dehydrated and mounted with coverslips as described in section 2.2.9.4.

#### **5.4.8.3 Observation of stifle joint sections using light microscopy**

Stifle joint sections were observed using light microscopy as described in section 2.2.9.5. Inflammatory cells were identified based on cell and nucleus morphology as described in section 2.2.9.6.

### **5.5 Results**

#### **5.5.1 In-life observations and surgical complications**

Details of in-life observations or surgical complications for each of the rabbits described in this section (5.5.1) were reported by the University of Zurich. In the uncoated group, the majority of the surgeries were successful. However, in rabbit 34.03, the tibial component of the prosthesis subluxated caudomedially after surgery. This caused stiffness in the treated joint; the degree of flexion was <90° at sacrifice. Maximum stifle joint flexion at sacrifice for rabbits 34.01, 34.04 and 34.08 was approximately 165°, 130° and 95°, respectively, in the treated joints. In rabbits 34.06 and 34.07 the degree of mobility in the treated joints was not affected (maximum flexion was approximately 170°).

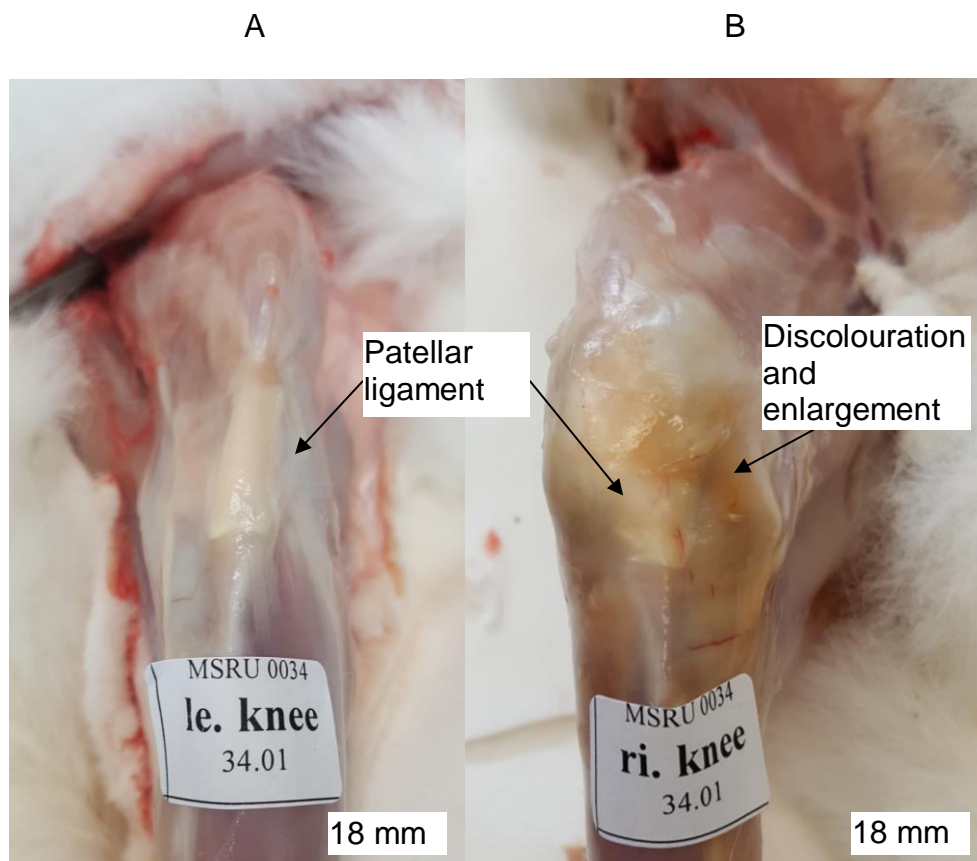
In the coated group, the majority of the surgeries were also successful, though there was another subluxation of the tibial component of the prosthesis caudomedially in rabbit 34.24. Maximum joint flexion at sacrifice for rabbits

34.14, 34.17, 34.22 and 34.24 were 100°, 85°, 135° and 95°, respectively, in the treated joints.

There were no reported cement failures or other abnormalities in any of the rabbits from either group from the University of Zurich.

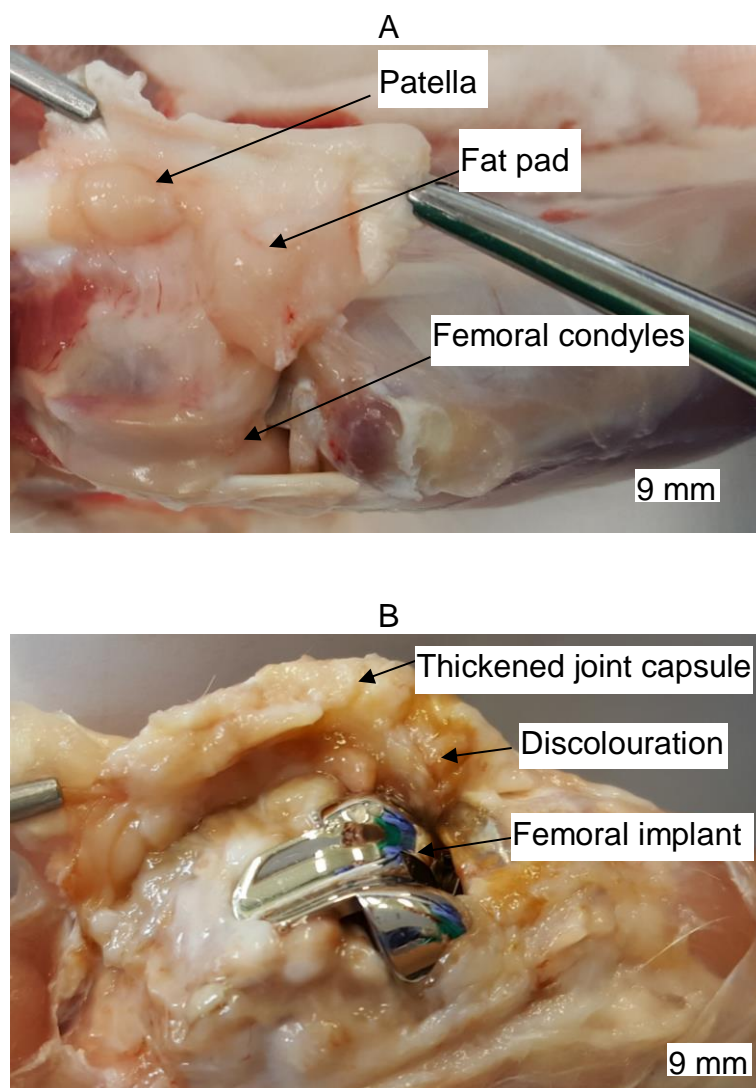
### 5.5.2 Macroscopic observation of stifle joints and periprosthetic tissue

During the dissection of each animal, discolouration and enlargement of each treated stifle joint was observed after removal of the skin and subcutis (Figure 5.8). Enlargement of the joint capsule occurred in all treated joints, particularly in rabbit 34.06 from the uncoated group and rabbits 34.14, 34.17 and 34.24 from the coated group.

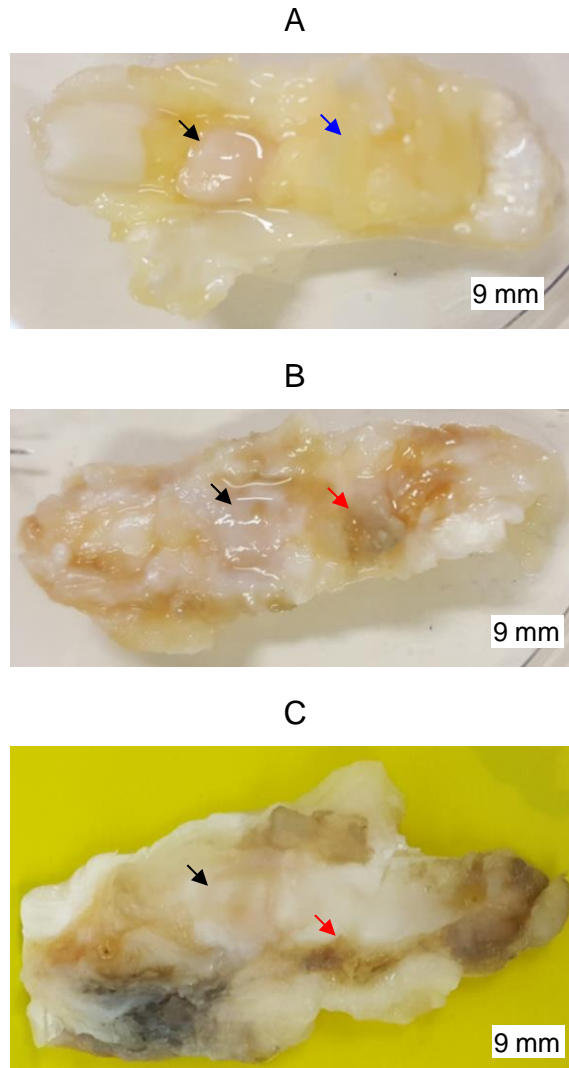


**Figure 5.8. (A) Appearance of an untreated rabbit stifle joint, immediately following sacrifice and removal of the skin and subcutis (rabbit 34.01). (B) Appearance of the contralateral treated rabbit stifle joint.**

The joint capsule tissues including the synovium were thicker and more fibrous and the fat pad was largely replaced by fibrous and uneven tissue on visual inspection of each treated joint (Figure 5.9). There was brown, grey and black discolouration of periprosthetic tissues within the joint capsule of each treated stifle joint, which was not observed in the untreated joints (Figure 5.9 and Figure 5.10). In the uncoated group, discolouration was greatest in rabbit 34.01 and least in 34.07. Tissues were more discoloured in the coated group, with multiple areas surrounding the patella appearing black in each sample of rabbit tissue (Figure 5.10).



**Figure 5.9. Appearance of an untreated rabbit stifle joint (A; 34.01L) and the contralateral treated joint (B; 34.01R; uncoated group) immediately following sacrifice and during dissection.**



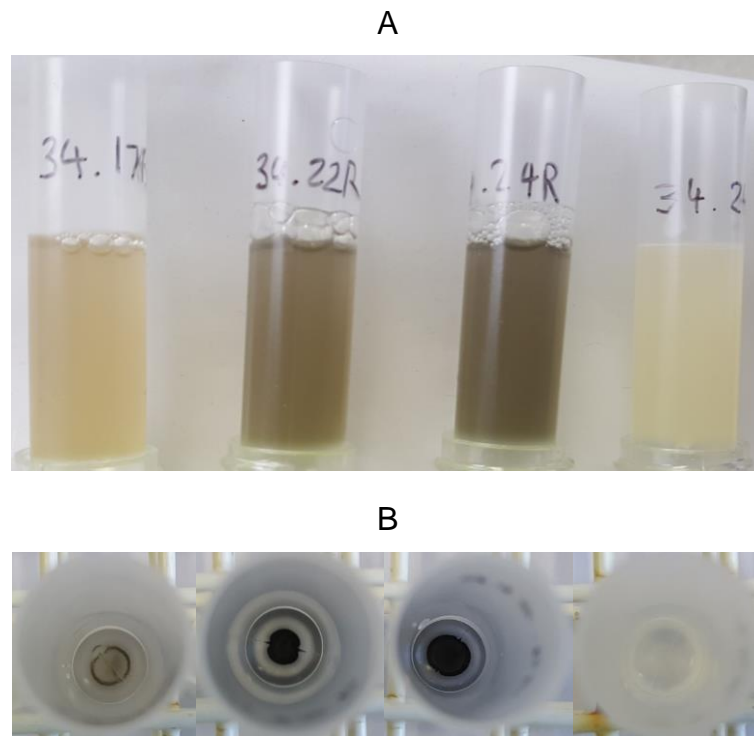
**Figure 5.10. Appearance of the patella, patellar ligament and fat pad from an untreated rabbit stifle joint (A; 34.01L), or from treated joints from the uncoated group (B; 34.01R) and coated group (C; 34.17R). Black arrow heads indicate the patella. Blue arrow heads indicate the fat pad. Red arrow heads indicate infiltration of the fat pad by fibrous tissue.**

### **5.5.3 Particle isolation from periprosthetic tissue samples**

#### **5.5.3.1 Appearance of tissue digests and particle pellets**

Tissues from the fat pad of each of the intact treated joints (34.03, 34.04 and 34.08 in the uncoated group and 34.17, 34.22 and 34.24 in the coated group), in addition to a non-treated contralateral control, were minced and digested enzymatically as part of the particle isolation process described in section 5.4.7. Digested tissues from untreated stifles or from the uncoated group formed a pale, cloudy solution, while tissues from the coated group formed a

grey-coloured solution (Figure 5.11A). Following density gradient ultracentrifugation, particles formed a black pellet at the bottom of each tube (Figure 5.11B), with some particles forming a loose band a few millimetres above the pellet in each tube. Particle pellets were larger in the coated group, and varied in size, with the largest pellet observed in rabbit 34.24 and the smallest pellet observed in 34.17. Pellet sizes corresponded to the colour of the digests, with the darker-coloured digests containing more particles.



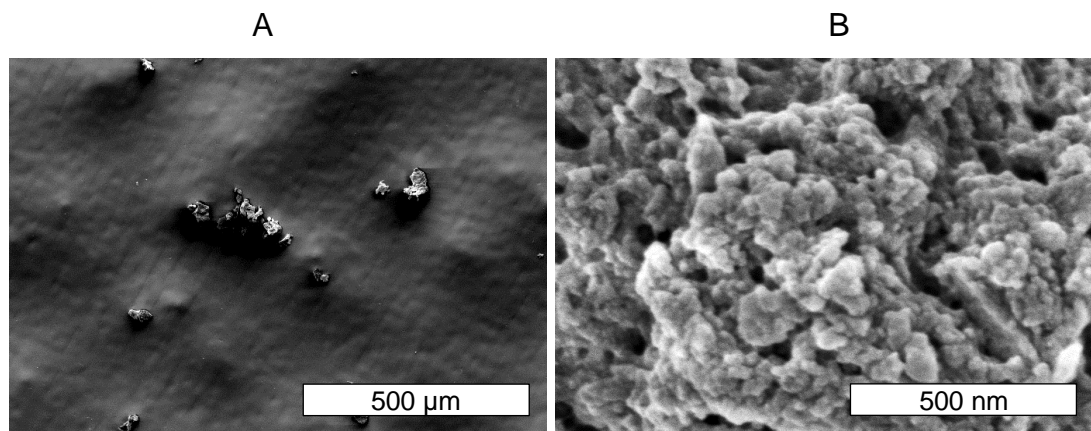
**Figure 5.11. A. Appearance of periprosthetic tissue digests from the SiN-coated group (From left: 34.17R, 34.22R, 34.24R) and a control tissue digest from an untreated stifle joint (34.24L). B. The corresponding particle pellet formed after density gradient ultracentrifugation.**

### **5.5.3.2 Scanning electron micrographs of particles isolated from the uncoated group**

Samples were imaged by scanning electron microscopy, which demonstrated the isolation of particles from each of the three samples of periprosthetic tissue from the uncoated CoCr group (Figure 5.12). Particles were present as dense aggregates of up to approximately 100  $\mu\text{m}$  in size (Figure 5.12A); high magnification views demonstrated that these aggregates were composed of



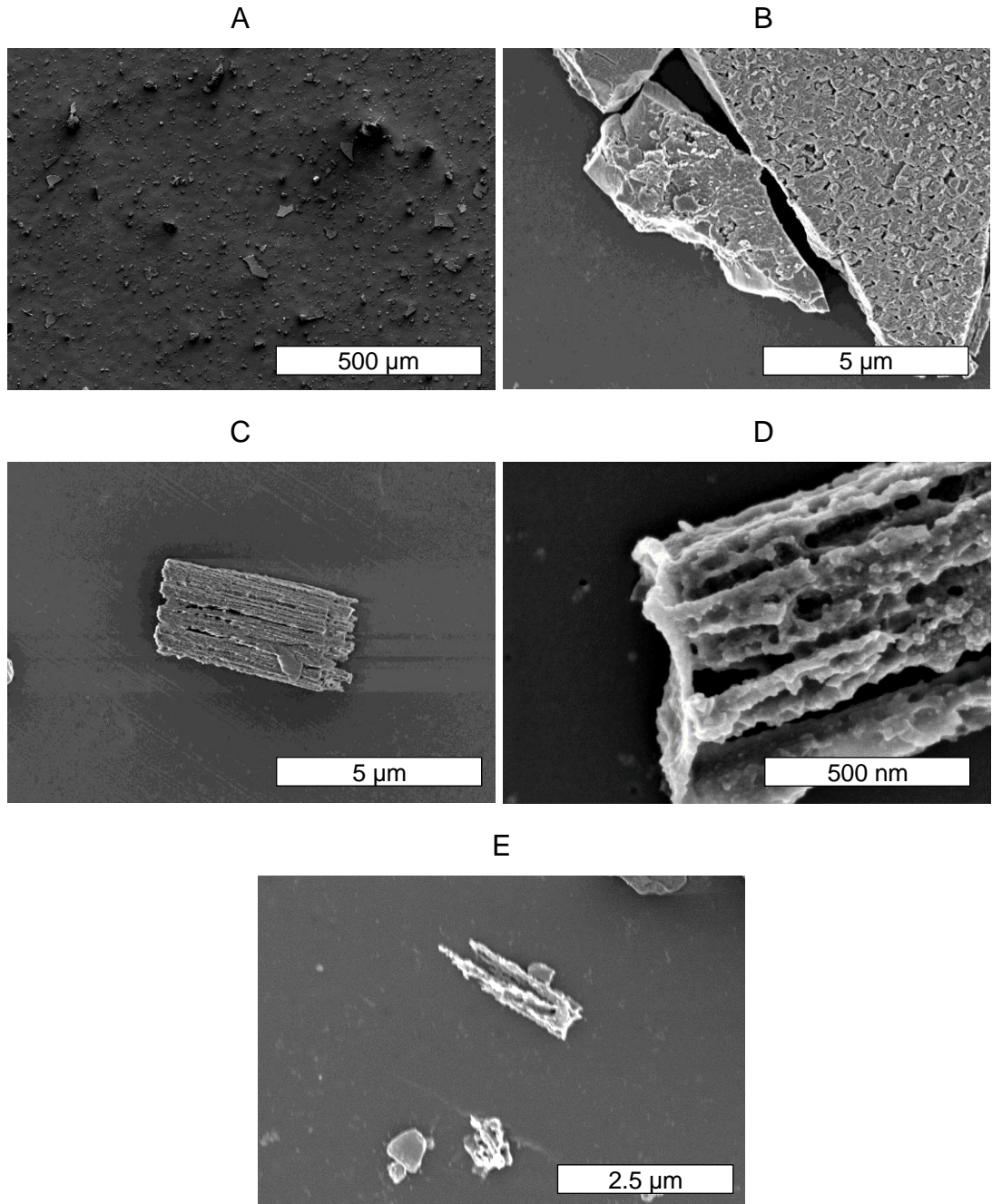
nanoscale oval or spherical particles and were likely CoCr particles (Figure 5.12B).



**Figure 5.12. Scanning electron micrographs of particles isolated from rabbit periprosthetic tissue from rabbit 34.03. A. Low magnification view (100x). B. High magnification view (100,000x).** The particles were resuspended and filtered on 0.015 µm polycarbonate filter membranes; samples were iridium coated.

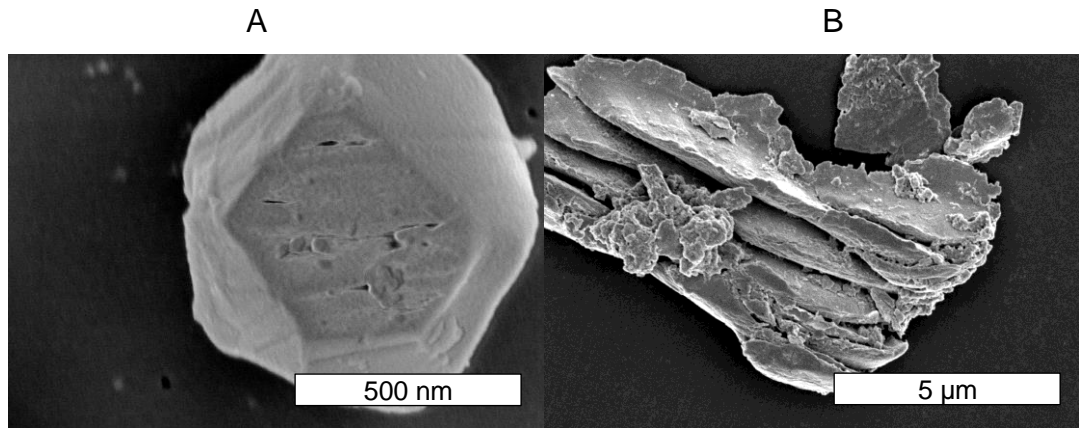
### **5.5.3.3 Scanning electron micrographs of particles isolated from the SiN-coated group**

In the coated group, particles were also successfully isolated from each of the three samples of periprosthetic tissue and were present at greater volumes (Figure 5.13). The same types of dense particle aggregates were present in the coated group, in addition to high volumes of large particles of 1 - 100 µm in size (Figure 5.13A), which were not composed of nanoscale particles and were likely from the coating (Figure 5.13B). Often, the large particles demonstrated a shard-like (Figure 5.12B) or columnar structure (Figure 5.12B-D). The particles often had a minimum diameter of 5 µm in (Figure 5.12C). In addition, many of the columnar particles isolated from rabbit 34.17 had a tapered appearance and a smaller minimum diameter of about 0.5 µm (Figure 5.13E). These types of particles were absent in control tissue from untreated stifle joints in both the coated and uncoated groups.



**Figure 5.13. Particles isolated from periprosthetic tissue from around coated implants from rabbit 34.17.** A. Low (100x) magnification view of particles. B. Shard-like particle and possible coating particles demonstrating columnar deposition from a top-down view. C. Cross-sectional view of a possible coating particle showing columnar structure. D. High (100,000x) magnification view of a possible coating particle showing columnar structure. The particles were resuspended and filtered on 0.015 μm polycarbonate filter membranes; samples were iridium coated.

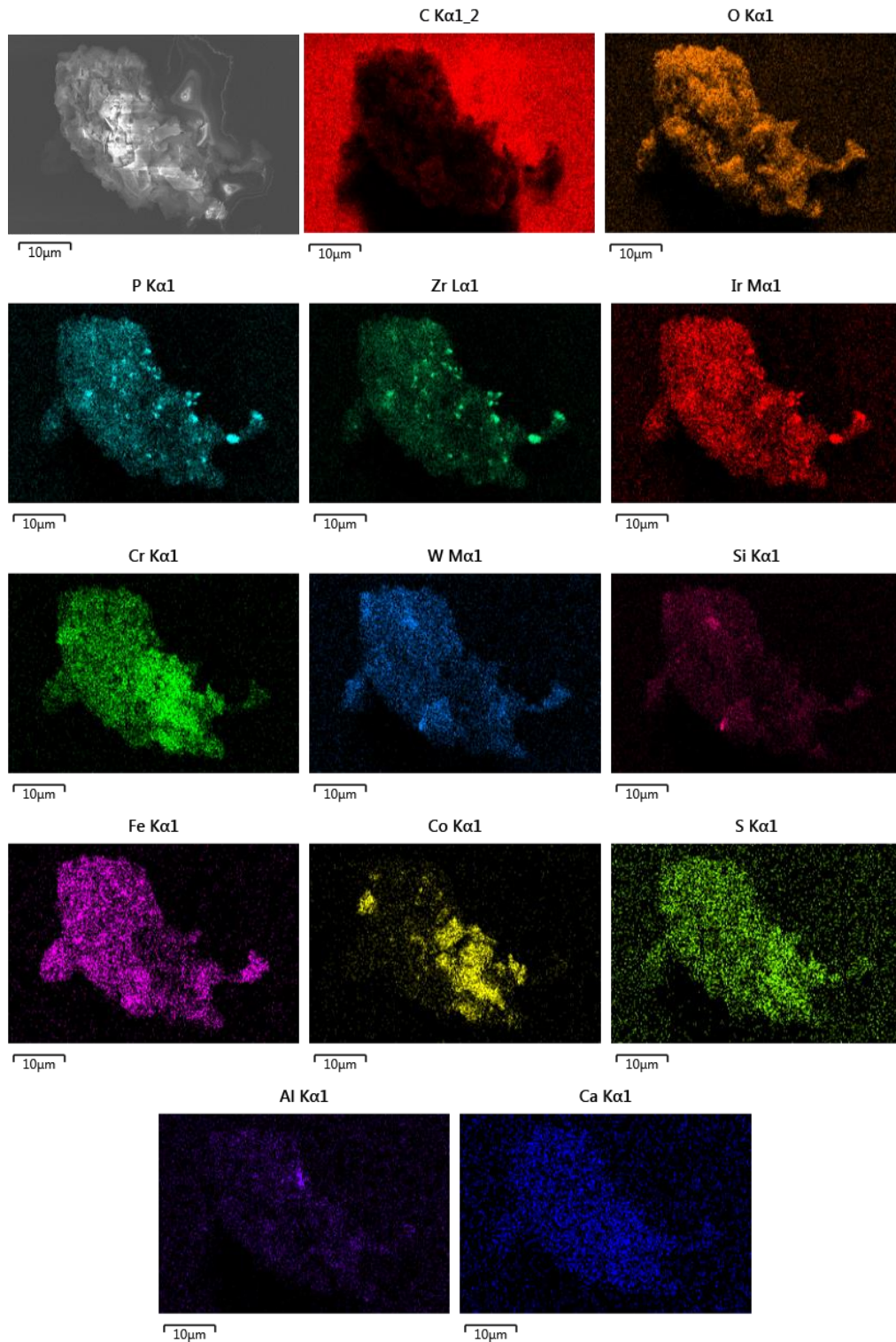
Additionally, large polyhedral particles 0.5-2.0  $\mu\text{m}$  in size were detected in both the uncoated and coated samples, particularly in rabbit 34.17, but not in rabbit 34.24 (Figure 5.14A). Further, large, flake-like particles 2-20  $\mu\text{m}$  in size were detected in rabbits 34.22 and 34.24 of the coated group (Figure 5.14B).



**Figure 5.14. A. High magnification (100,000x) electron micrograph of isolated polyhedral particles (sample from rabbit 34.17). B. View of large, flake-like particles (sample from rabbit 34.24) at 10,000x magnification.**

#### **5.5.3.4 Elemental analysis of particles isolated from the uncoated group**

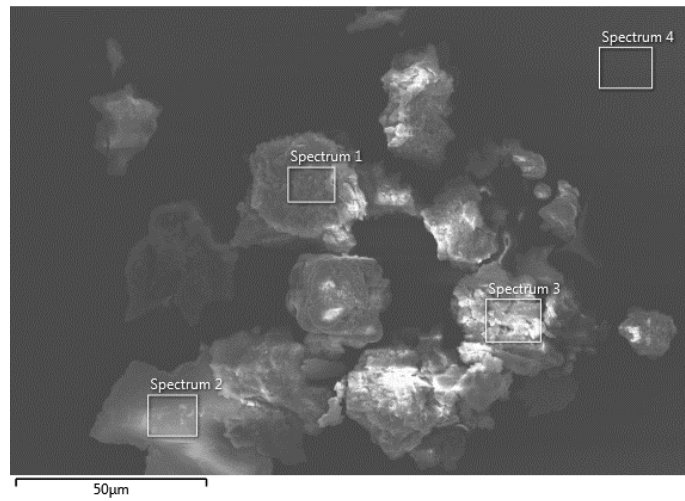
Elemental analysis of the particles was carried out using EDX during scanning electron microscopy on each sample. In the uncoated group, elemental mapping confirmed that the aggregates were composed of CoCr nanoparticles, while the micron-scale polyhedral particles were composed mainly of zirconium and phosphorus (Figure 5.15). However, low levels of a number of contaminants were also identified, including tungsten, silicon, iron, sulphur, aluminium and calcium. These elements, as well as manganese, were also found during spectral analysis of various aggregates, though elemental signals were strongest for cobalt and chromium; molybdenum was also identified (Figure 5.16). The CoCr particles, and also the polyhedral particles, also contained oxygen. The ratio of cobalt and chromium varied within the particles, with some particles containing chromium and little or no cobalt, and some particles containing more cobalt.



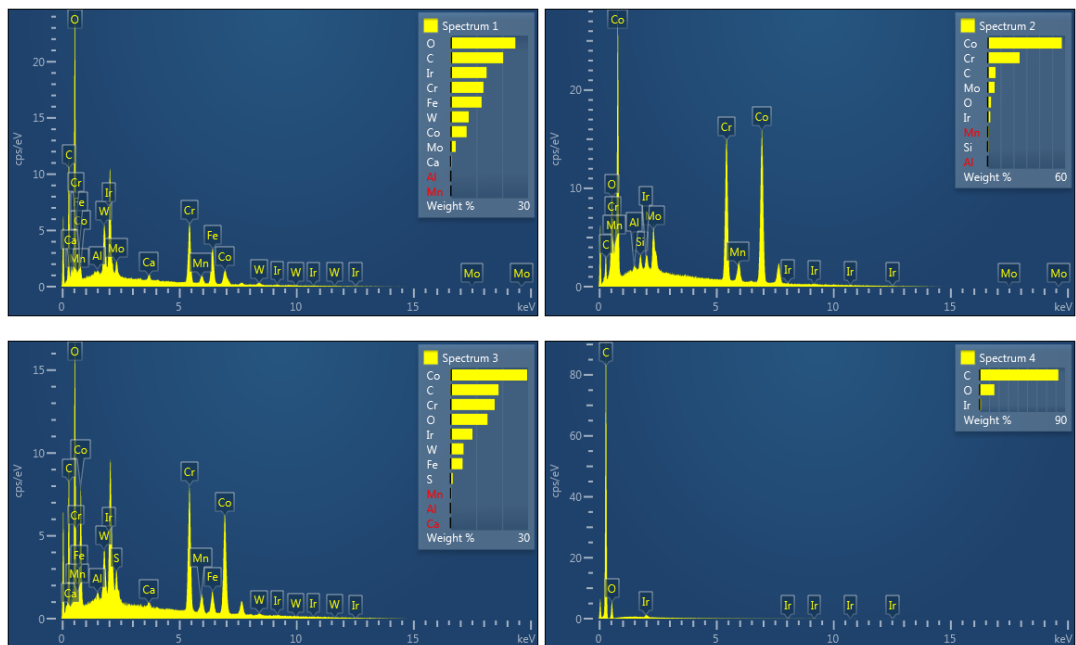
**Figure 5.15. Elemental analysis of particles isolated from rabbit periprosthetic tissue from the uncoated group (34.03).** A scanning electron micrograph showing the area from the which the elemental maps were produced and the corresponding elemental maps, with the chemical symbol of each element given above. The total sample was resuspended and filtered on 0.015 μm polycarbonate filter membranes; samples were iridium coated.



A



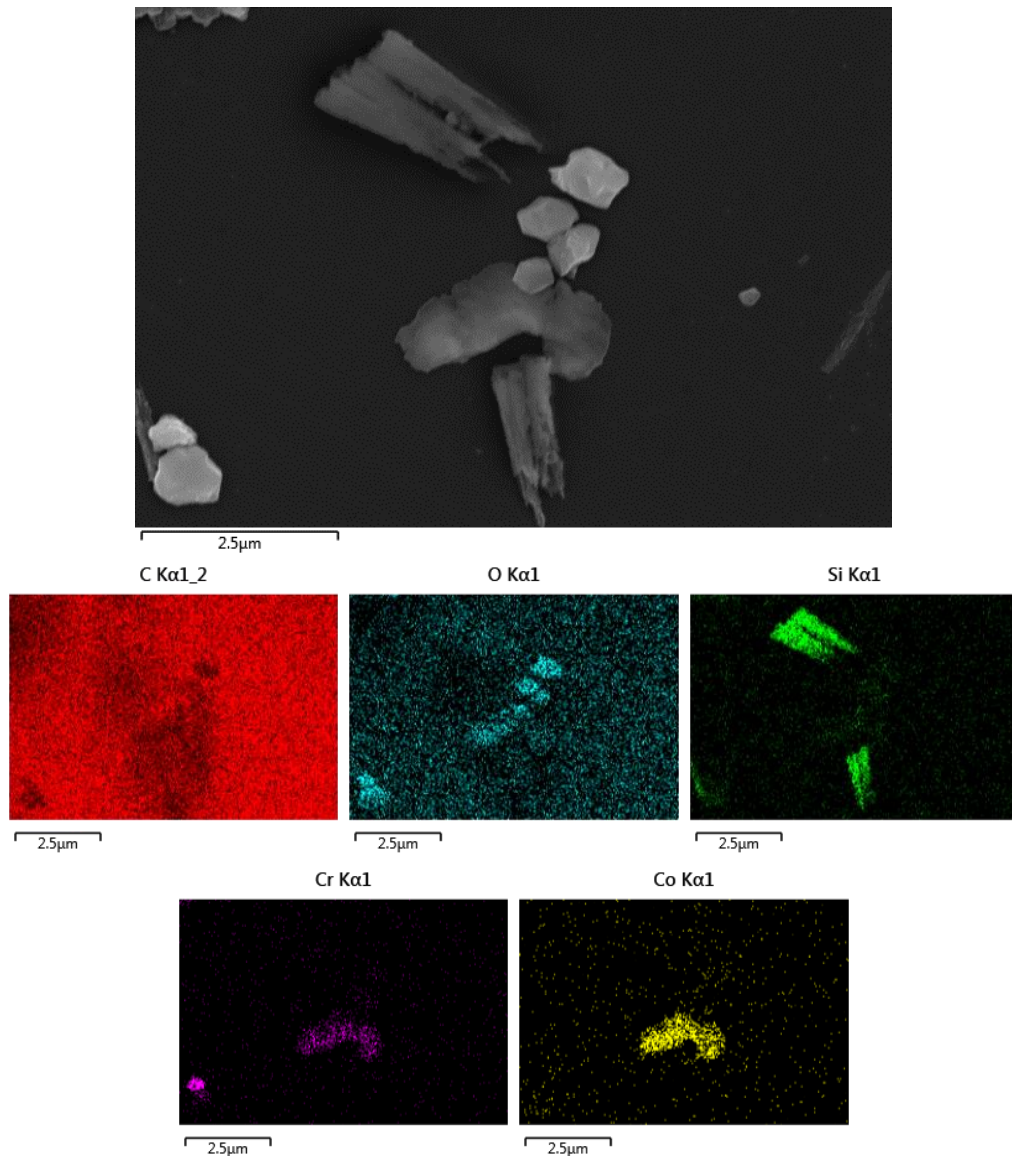
B



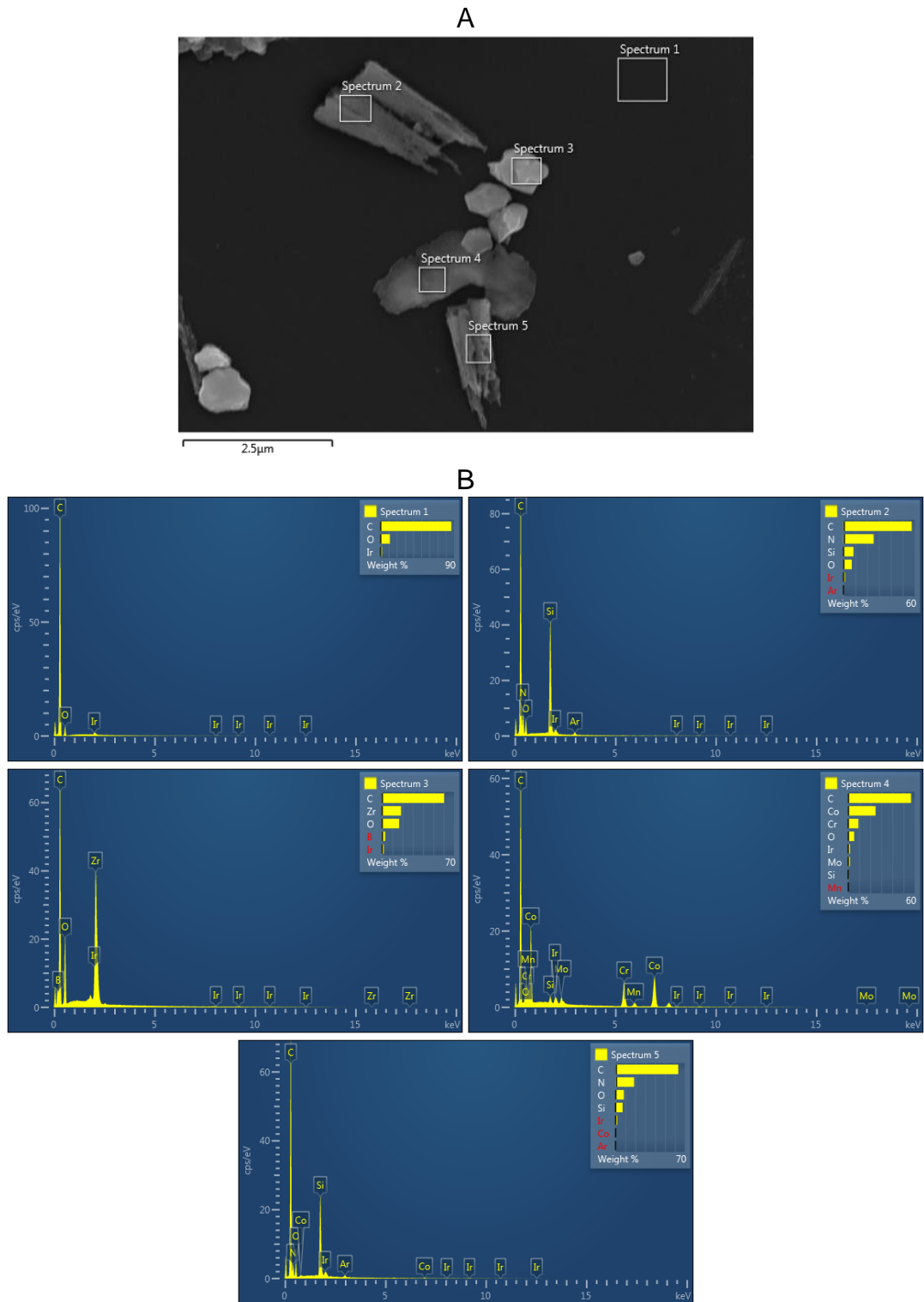
**Figure 5.16. Elemental spectra of CoCr aggregates isolated from rabbit periprosthetic tissue from the uncoated group (34.03).** The total sample was resuspended and filtered on 0.015  $\mu\text{m}$  polycarbonate filter membranes; samples were iridium coated. (A) Scanning electron micrograph showing the area from the which the spectra were produced, (B) the corresponding spectra.

#### **5.5.3.5 Elemental analysis of particles isolated from the SiN-coated group**

Elemental mapping and spectral analysis of particles isolated from the coated group showed that the large particles with a columnar structure were composed of silicon nitride, with traces of argon (Figure 5.17 and Figure 5.18). The silicon nitride particles were not oxidised. Polyhedral particles were mainly zirconium and oxygen, and flake-like particles or aggregates of nanoscale particles were composed of cobalt, chromium and molybdenum. Similarly to the uncoated group, low levels of manganese were also identified, and CoCr particles appeared to be slightly oxidised; once again the ratios of chromium to cobalt varied. Signals from the polycarbonate membrane (carbon and oxygen) and sputter coating (iridium) were also ubiquitous.



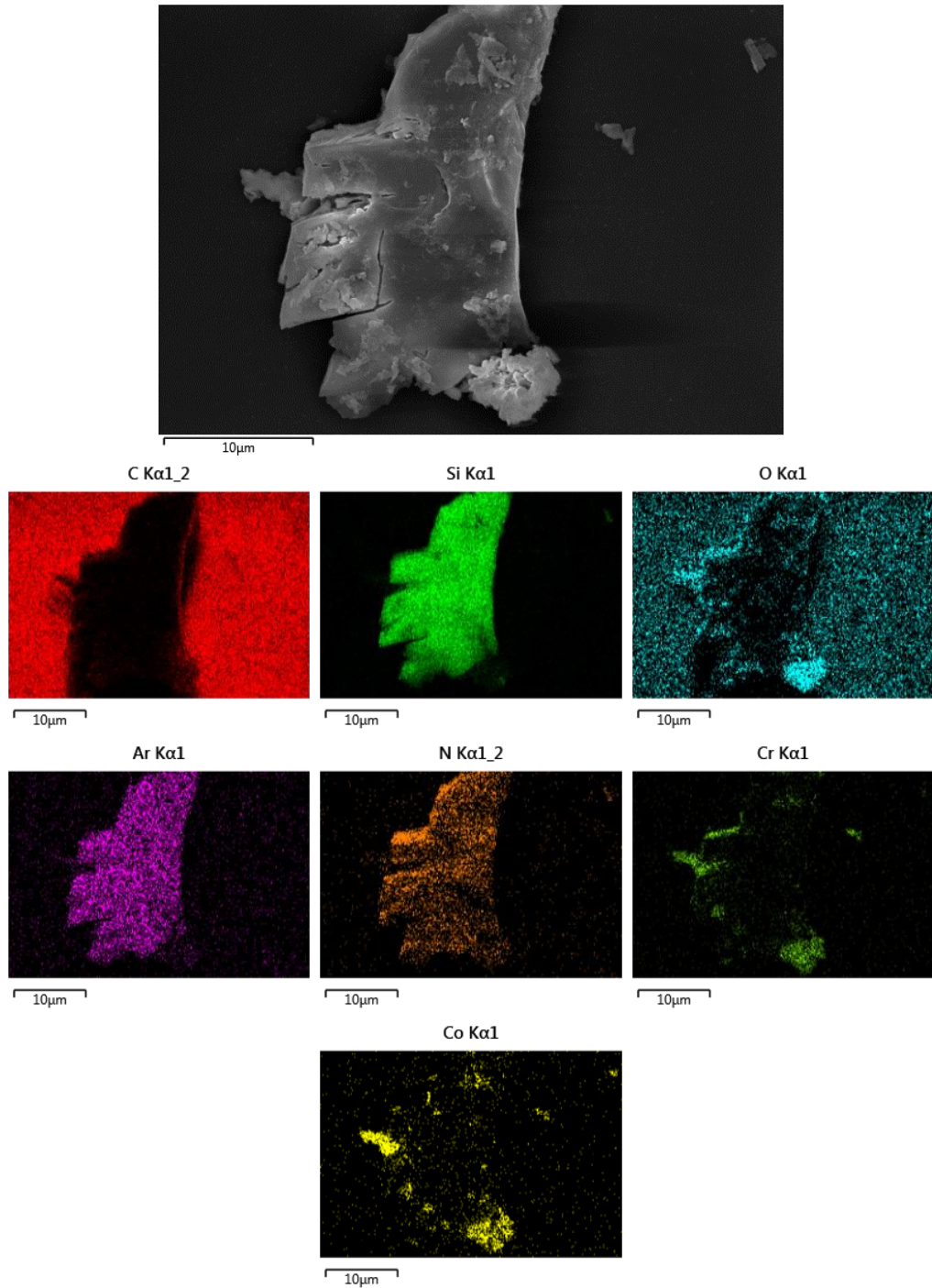
**Figure 5.17. Elemental analysis of particles isolated from rabbit periprosthetic tissue from the coated group (34.17).** A scanning electron micrograph showing the area from the which the elemental maps were produced and the corresponding elemental maps, with the chemical symbol of each element given above. The total sample was resuspended and filtered on 0.015 μm polycarbonate filter membranes; samples were iridium coated.



**Figure 5.18. Elemental spectra of particles isolated from rabbit periprosthetic tissue from the coated group (34.17).** The total sample was resuspended and filtered on 0.015  $\mu\text{m}$  polycarbonate filter membranes; samples were iridium coated. (A) Scanning electron micrograph showing the area from the which the spectra were produced, (B) the corresponding spectra.

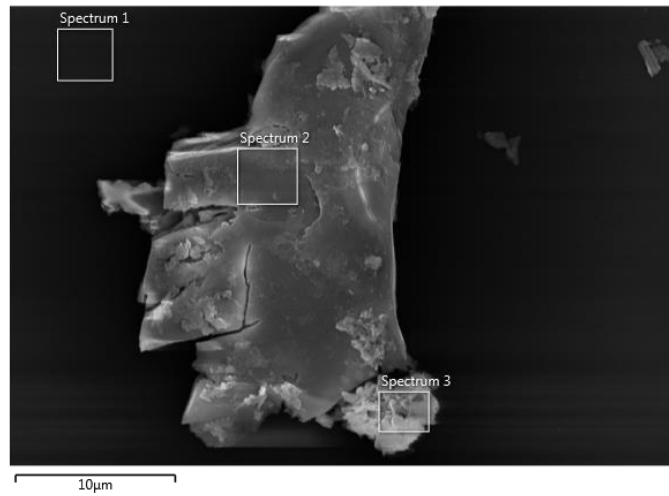


Elemental mapping was also carried out on the large, shard-like particles found in samples from the coated group (Figure 5.19). The shard-like particles were composed of silicon nitride and argon and were not oxidised. CoCr aggregates, which were oxidised, were adhered to the some of the coating particles. The ratio of cobalt to chromium varied. Spectral analysis confirmed that the CoCr aggregates contained the same contaminants as in the uncoated group, including iron, sulphur and manganese (Figure 5.20). Elemental analysis of larger flake-like particles confirmed that these were composed of cobalt, chromium and molybdenum, and were oxidised in certain areas (Figure 5.21).

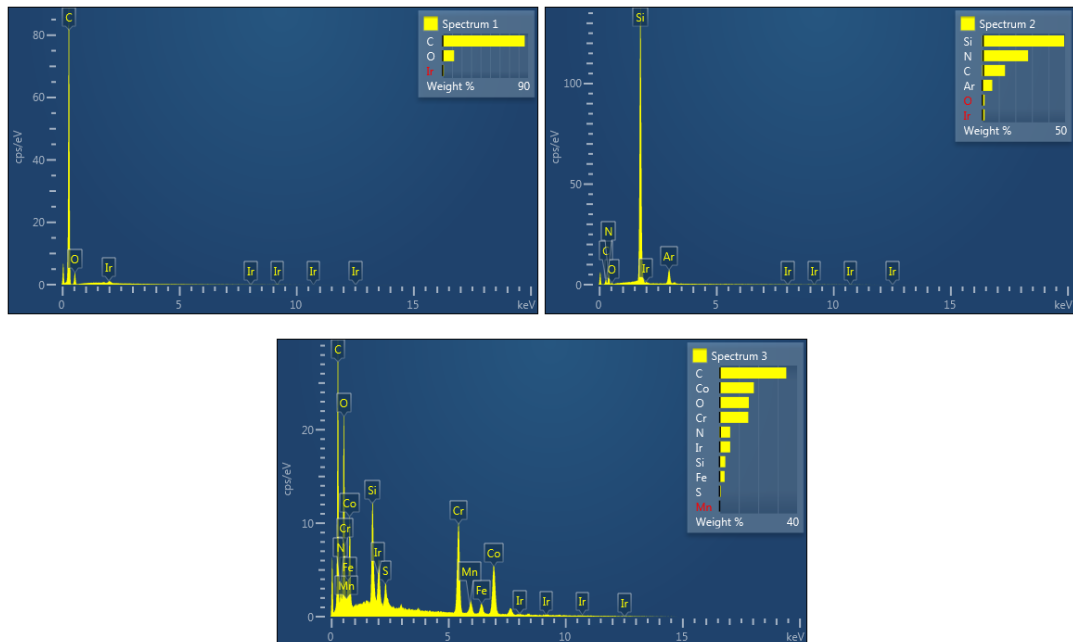


**Figure 5.19. Elemental analysis of particles isolated from rabbit periprosthetic tissue from the coated group (34.24).** A scanning electron micrograph showing the area from the which the elemental maps were produced and the corresponding elemental maps, with the chemical symbol of each element given above. The total sample was resuspended and filtered on 0.015 µm polycarbonate filter membranes; samples were iridium coated.

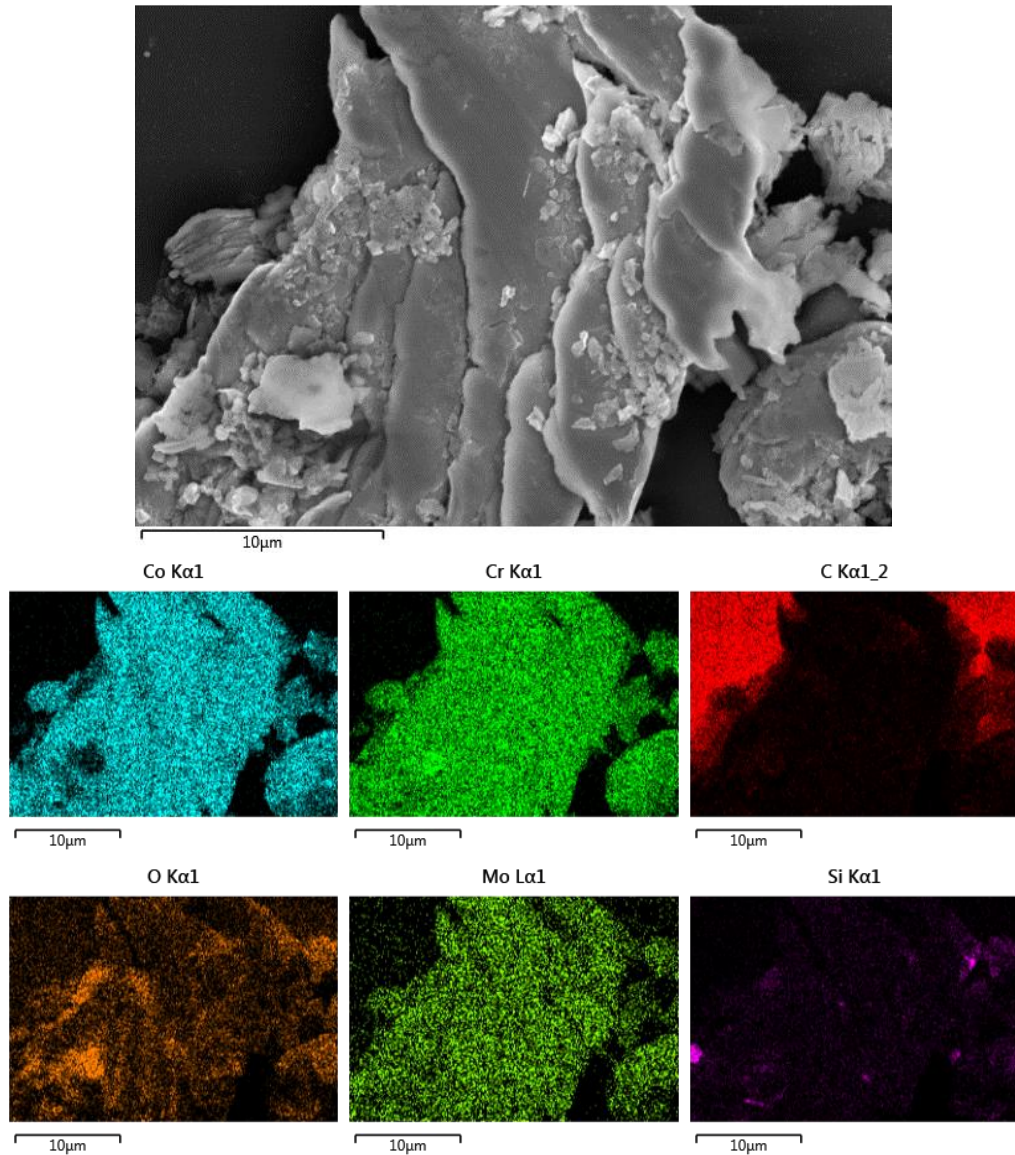
A



B



**Figure 5.20. Elemental spectra of particles isolated from rabbit periprosthetic tissue from the coated group (34.24).** The total sample was resuspended and filtered on 0.015 µm polycarbonate filter membranes; samples were iridium coated. (A) Scanning electron micrograph showing the area from the which the spectra were produced, (B) the corresponding spectra.



**Figure 5.21. Elemental analysis of flake-like CoCr particles isolated from rabbit periprosthetic tissue from the coated group (34.24).** A scanning electron micrograph showing the area from the which the elemental maps were produced and the corresponding elemental maps, with the chemical symbol of each element given above. The total sample was resuspended and filtered on 0.015 μm polycarbonate filter membranes; samples were iridium coated.

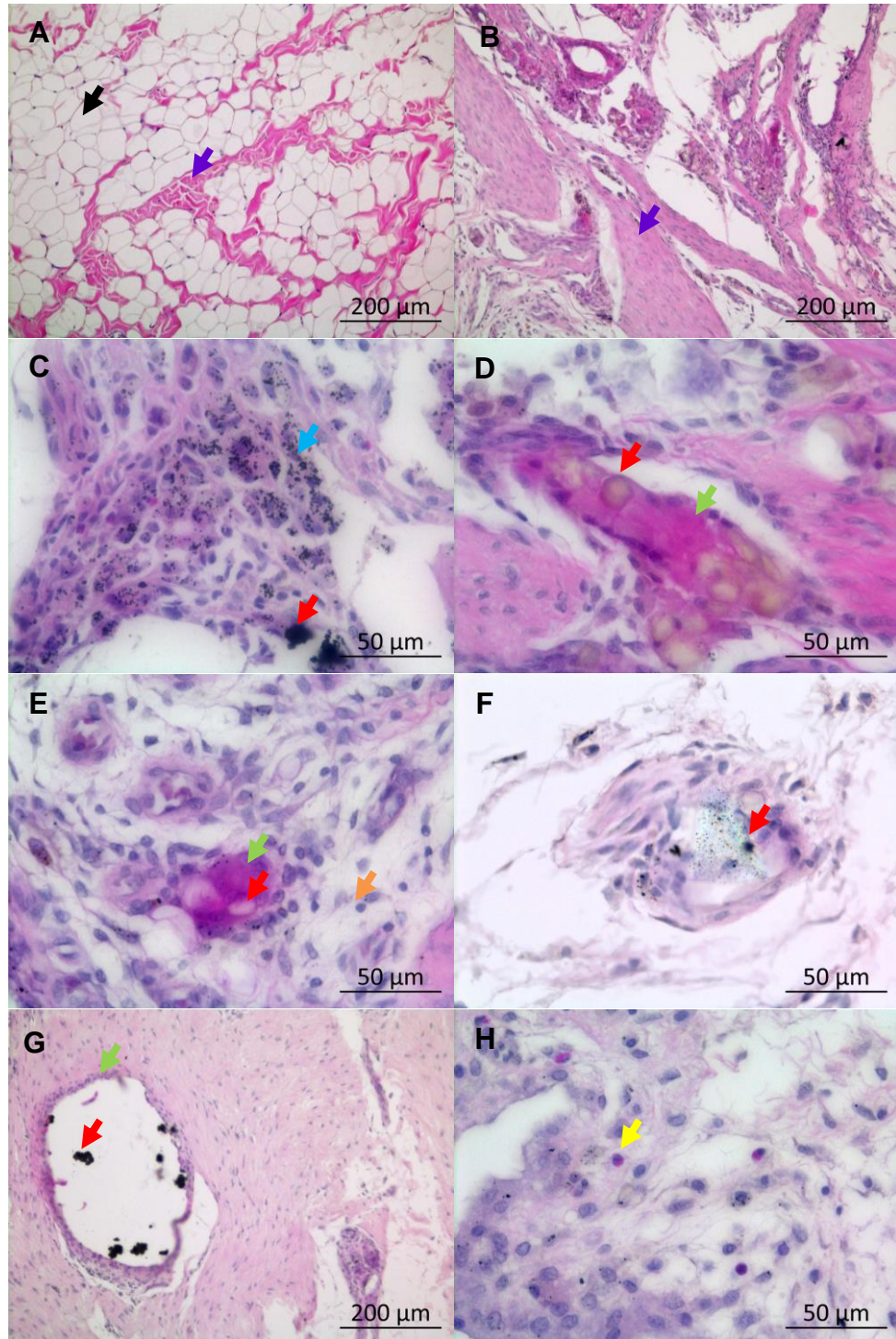
## **5.5.4 Histological analysis of periprosthetic tissue**

### **5.5.4.1 Analysis of treated and untreated tissues from the uncoated group**

The stifle joint tissues from three rabbits (34.01, 34.06 and 34.07) in the uncoated group were analysed by embedding the fat pad in wax, creating serial sections of 5 µm, and staining at least three sections from each rabbit sample with H&E as described in sections 5.4.8.1 and 5.4.8.2. Histological sections were viewed using light microscopy as described in section 5.4.8.3. Any inflammatory cell infiltrates were identified within sections as described in section 2.2.9.6. Untreated joints as well as treated joints were analysed.

In the untreated joints, the fat pad consisted mainly of adipocytes with some fibrous bands containing fibroblasts (Figure 5.22A). No particles or inflammatory cell infiltrates were observed in any of the control joints. In the treated joints of all three of the rabbits from the uncoated group, the fat pad structure was irregular and fibrous, with larger bands of fibroblasts and few adipocytes (Figure 5.22B). Particles were dispersed throughout the fat pad of each treated stifle. Macrophages containing dense particulate matter were present (Figure 5.22C), especially in rabbit 34.06. Round particles approximately 5 - 40 µm in diameter, which were beige in appearance were abundantly present in rabbit 34.01 (Figure 5.22D). The particles were accompanied by a giant cell reaction. Such particles were minimal in the other two rabbits from the uncoated group. Lymphocytes were also present in all samples from the treated joints from the uncoated group (Figure 5.22E). Particles sometimes had a greenish hue, particularly in rabbit 34.06 (Figure 5.22F). In some areas of rabbit 34.07, giant cells surrounding a cavity in the fat pad were observed (Figure 5.22G). The cavities often contained smaller aggregates of wear debris. Eosinophils were present in the fat pad of rabbits 34.01 and 34.07. In rabbits 34.06 and 34.07, other polymorphonuclear cells were also present in lower numbers.





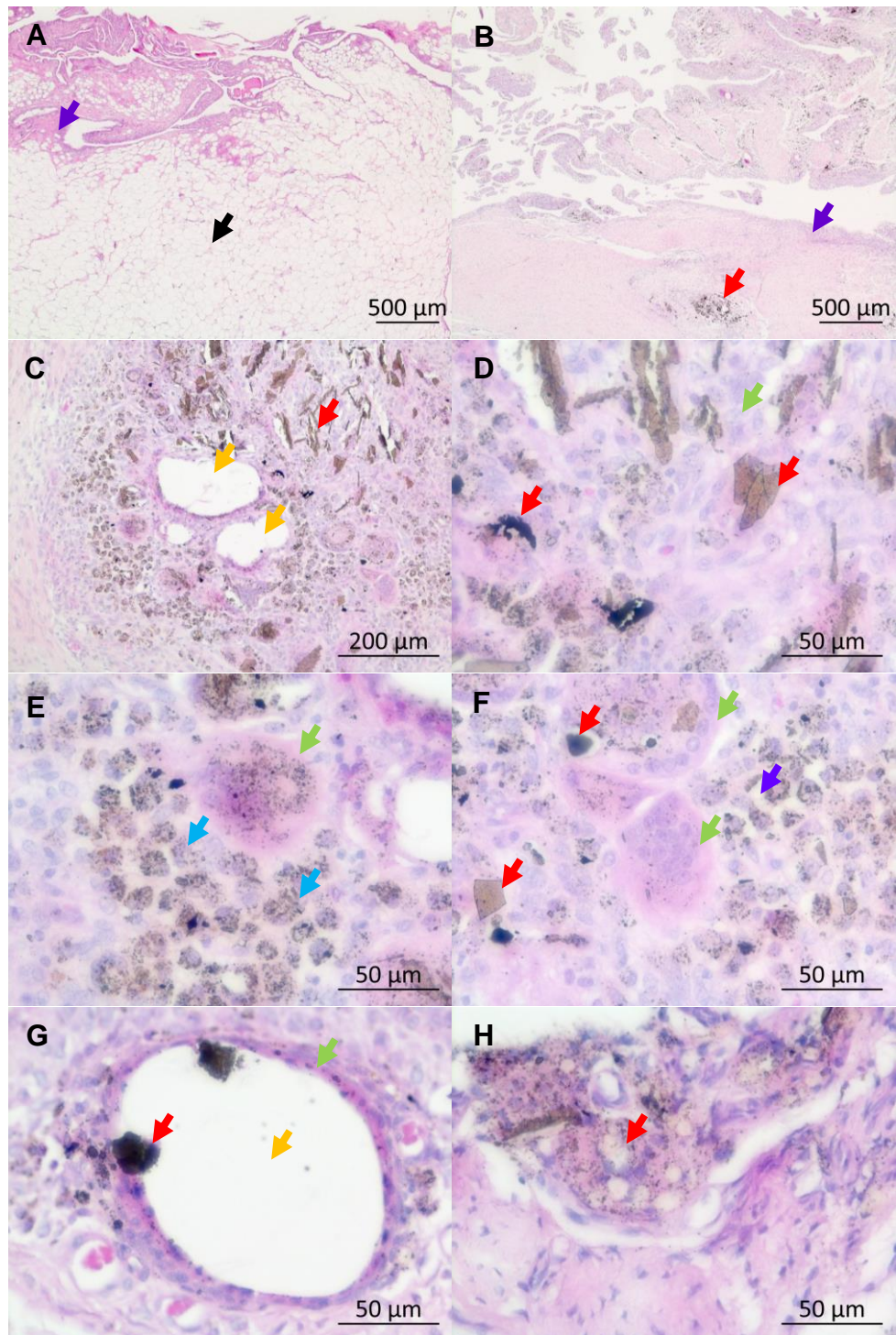
**Figure 5.22. Images of H&E-stained fat pad sections (uncoated group).**

A. Low magnification view of a control section from an untreated rabbit stifle joint (34.01L). B-E. Views of sections from the contralateral treated rabbit stifle joint (34.01R). F-H. Views of sections from additional treated rabbit stifle joints (F: 34.06R; G-H: 34.07R). The images were captured under normal Köhler illumination with a 5x or 40x objective lens. Arrow heads indicate adipocytes (black), fibroblasts (purple), macrophages (blue), particles (red), giant cells (green), lymphocytes (orange) eosinophils (yellow).

#### **5.5.4.2 Analysis of treated and untreated tissues from the SiN-coated group**

The treated and untreated stifle joint tissues from three rabbits (34.14, 34.22 and 34.24) in the SiN-coated group were also analysed histologically in the same way as the uncoated group. As before, the fat pad of each non-treated rabbit stifle joint consisted mainly of adipocytes and lacked any particles or inflammatory cell infiltrates. However, the fat pad of each treated stifle joint was highly irregular and fibrous, with clusters of particles dispersed throughout each joint (Figure 5.23A). The volume of particles observed was similar in the coated group compared with the uncoated group, except in rabbit 34.14, in which it was much greater. In this sample, there was a high volume of large, shard-like particles up to 100  $\mu\text{m}$  in size, which were brown in appearance (Figure 5.23B-D). In addition, similarly to the uncoated group, there were dense particles which were black in appearance; smaller particles or particle aggregates were present mainly within large groups of macrophages (Figure 5.23D and E). The reactions and particle volumes were lower in the other two rabbits, in which there were fewer shard-like particles (34.17), or no shard-like particles (34.24). There were also fewer macrophages and particle aggregates in rabbits 34.17 and 34.24. Giant cell reactions were common in rabbit 34.14 and 34.17 (Figure 5.23F) but were not observed in rabbit 34.24. As with the uncoated group, there were also giant cells surrounding cavities in the fat pad of 34.14R and 34.17R, sometimes with dense particles or particle aggregates (Figure 5.23G). Polymorphonuclear cells, particularly eosinophils, were present in most of the samples. Lymphocytes were present in rabbits 34.14 and 34.24. Round, beige particles of 5-40  $\mu\text{m}$  were also observed in rabbit 34.17 (Figure 5.23H).



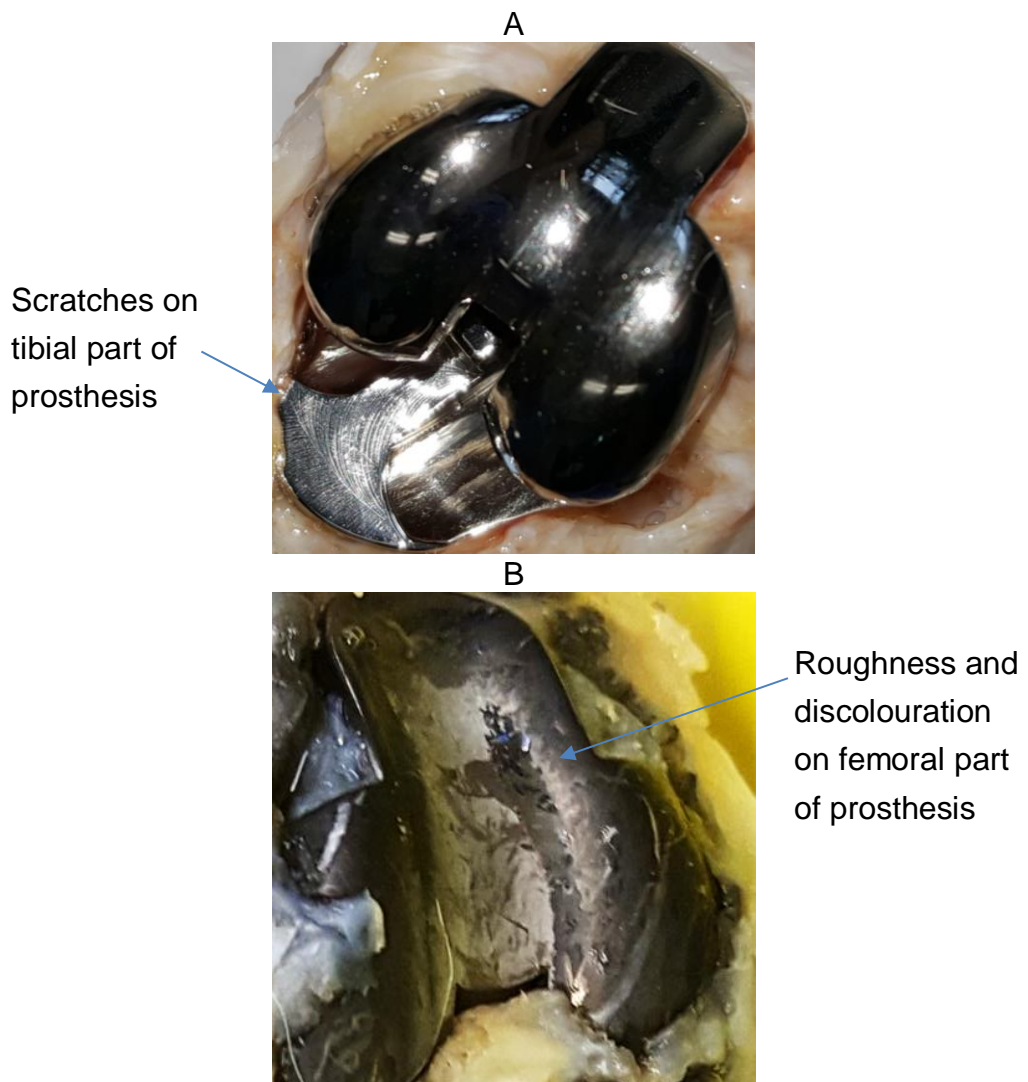


**Figure 5.23. Images of H&E-stained fat pad sections (coated group).** A. Low magnification image of a control rabbit stifle joint (34.14L). B-F. Views of sections from a treated rabbit stifle joint (34.14R). G-H. Views of sections from an additional treated rabbit stifle joint (34.17R). The images were captured under normal Köhler illumination with a 5x or 40x objective lens. Arrow heads indicate adipocytes (black), fibroblasts (purple), macrophages (blue), particles (red), giant cells (green), and cavities in the tissue (orange).



### 5.5.5 Inspection of rabbit prostheses

The prosthesis components were inspected following harvesting of tissue and particle isolation and histological analysis. This revealed that scratches were present on the tibial part of the prosthesis from rabbit 34.01 (uncoated group), even on areas which were not designed to be in contact with the femoral condyles (Figure 5.24A). This indicated luxation of the prosthesis (despite no luxation recorded during fluoroscopic examination of the implant at the University of Zurich). In addition, the coated prosthesis components were rough in appearance, with some areas of light discolouration, indicating *in vivo* alteration and/or delamination of the SiN coating, which was black in appearance prior to implantation (Figure 5.24B).



**Figure 5.24. A. Appearance of retrieved uncoated CoCr prosthesis from rabbit 34.01. B. Appearance of retrieved coated prosthesis from rabbit 34.22.**

### 5.5.6 Summary of results

A summary of the main results of this chapter is shown in Table 5.3 (uncoated group) and Table 5.4 (coated group).

**Table 5.3. Summary of rabbit study results (uncoated group).**

Animal number	In-life observations/ surgical complications	Size of pellet formed during particle isolation	Particle types isolated	Particle types observed within histological sections	Immune cells present
34.01	Slight stiffness in joint	N/A	N/A	Micron-scale spherical particles/cavities; aggregates of dense particles	Giant cells; eosinophils; lymphocytes; macrophages
34.03	Tibial component of the prosthesis subluxated caudomedially after surgery; severe stiffness in joint	small	Nanoscale CoCr; 0.5-2 $\mu\text{m}$ polyhedral zirconium dioxide	N/A	N/A
34.04	Stiffness in joint	small	Nanoscale CoCr; 0.5-2 $\mu\text{m}$ polyhedral zirconium dioxide	N/A	N/A
34.06	Normal joint function	N/A	N/A	Aggregates of dense particles	Abundant macrophages; polymorphonuclear cells; lymphocytes
34.07	Normal joint function	N/A	N/A	Micron-scale spherical particles/cavities; aggregates of dense particles	Giant cells, eosinophils, macrophages, lymphocytes, polymorphonuclear cells
34.08	Severe stiffness in joint	small	Nanoscale CoCr; 0.5-2 $\mu\text{m}$ polyhedral zirconium dioxide	N/A	N/A

Table 5.4. Summary of rabbit study results (coated group).

Animal number	In-life observations/ surgical complications	Size of pellet formed during particle isolation	Particle types isolated	Particle types observed within histological sections	Immune cells present
34.14	Severe stiffness in joint	N/A	N/A	Abundant large, shard-like particles <100 µm and dense particle aggregates; Micron-scale spherical particles/cavities	Giant cells, abundant macrophages, lymphocytes, polymorphonuclear cells
34.17	Severe stiffness in joint	Medium	<100 µm columnar and shard-like SiN; 0.5-2 µm polyhedral zirconium dioxide; nanoscale CoCr;	A few large, shard-like particles <100 µm and dense particle aggregates, micron-scale spherical particles/cavities	Giant cells, macrophages, eosinophils, polymorphonuclear cells
34.22	Stiffness in joint	Large	<100 µm columnar and shard-like SiN; 0.5-2 µm polyhedral zirconium dioxide; nanoscale CoCr; Large flakes of CoCr	N/A	N/A
34.24	Subluxation of the tibial component of the prosthesis caudomedially; severe stiffness in joint	Very large	<100 µm shard-like SiN; nanoscale CoCr; Large flakes of CoCr	Dense particle aggregates	Macrophages, eosinophils, lymphocytes, polymorphonuclear cells

The main results of this chapter were as follows:

- Surgical complications occurred in some of the rabbits, based on communication with the University of Zurich.
- The particle isolation method was successfully applied to six periprosthetic rabbit tissue samples.
- In the uncoated group, nanoscale CoCr particles and micron-scale zirconium particles were retrieved.
- In the coated group, nanoscale and micronscale CoCr particles, micronscale zirconium particles, and micronscale SiN particles were isolated.
- Histological analysis demonstrated abundant macrophages and giant cell reactions in both groups, with generally lower numbers of lymphocytes and polymorphonuclear cells.

## 5.6 Discussion

The results of this study demonstrate successful isolation of particles from rabbit periprosthetic tissues. This was the first time that the particle isolation method developed in Chapter 3 was applied to animal tissue containing wear debris produced by a prosthesis *in vivo*. The results therefore provide further evidence of the effectiveness of the isolation method. Particles were successfully isolated from a total of six different animal samples, despite the use of a small animal model and a relatively short three-month implantation time.

Elemental analysis revealed a degree of chemical contamination of the isolated particles, for which there are several possible sources. The source of argon contamination in the samples from the coated group was likely due to the use of argon as a sputtering gas for coating deposition, and the stainless steel surgical and dissection equipment was likely the source of iron contamination. Moreover, the implant alloy used may contain up to 0.75% iron and 1% manganese, which may explain the detection of these elements (ISO 5832-12). The presence of tungsten on CoCr particles was likely present due to use of sodium polytungstate gradients. Zirconium particles may have been present due to the use of refobacin© bone cement, in which zirconium dioxide was a 15% w/w constituent (Neut *et al.*, 2010). This is further supported by the detection of oxygen signals within the particles. Zirconium dioxide particles in refobacin© bone cement have been described as polyhedral and 1-5  $\mu\text{m}$  in size (Neut *et al.*, 2010), which is highly similar to the zirconium particles isolated in this study. Further, since zirconium dioxide has a density of 5.68  $\text{g}\cdot\text{cm}^{-3}$ , the particles would be expected to pellet at the bottom of tubes during density gradient ultracentrifugation and therefore be isolated with the SiN and CoCr particles. However, the main constituent of the bone cement, PMMA, has a density of 1.18  $\text{g}\cdot\text{cm}^{-3}$  and therefore would not be isolated with the methods used, hence this may be why these particle types were not found in any of the isolated particle samples. The presence of the zirconium dioxide particles indicates a degree of bone cement failure and subsequent release of bone cement particles. It must be noted that the presence of such

contaminants and cement particles may have affected the observed biological responses.

Further evidence for the presence of bone cement particles was obtained during histological analysis, in which round cavities within the tissue and circular beige particles were observed; these were not observed during histological analysis in rabbit 34.24, from which cement particles were also not isolated. The large, round cavities were likely caused by the presence of PMMA, which is known to dissolve in xylene during histological preparation for paraffin embedding of tissues. The multi-nucleated giant cell reaction observed in the histological sections surrounding these particles has been observed in previous studies (Gibon *et al.*, 2017). The circular beige particles were likely another constituent of the bone cement, gentamycin sulphate particles, which have been described as circular particles 5-40  $\mu\text{m}$  in diameter (Neut *et al.*, 2010); these particles are designed to diffuse into the tissue to prevent bacterial contamination. The gentamycin particles appeared to cause a giant cell response.

The large size of the SiN particles isolated most likely indicates coating failure, possibly by delamination from the substrate. It is possible that adhesive failure occurred between the layers of the coating since, based on elemental analysis, the SiN particles that were isolated did not contain the CrN interlayer. In addition, many of the SiN particles were the approximate thickness of the SiN coating (5  $\mu\text{m}$ ). Cohesive failure within the SiN layer likely also occurred in rabbit 34.17, since in this sample a number of smaller SiN particles were observed. Cohesive failure within a coating has also been reported to occur in TiN coatings (Williams *et al.*, 2003). The tapered, shard-like appearance of these particles may have been due to fractures within the SiN layer of the coating. The edges of the SiN coating particles were less defined and were more irregular in appearance compared to SiN coating particles which were analysed by SEM following a pin-on-plate test (Lal, 2017, unpublished data). This is likely the result of particle dissolution over the 12-week *in vivo* period. The presence of large, flake-like CoCr particles in the coated group indicates possible third-body wear of the substrate material. These flake-like particles were common in two of the three periprosthetic tissues from coated implants, suggesting that coating failure may have occurred at a later point or to a lesser

extent in one of the rabbits. This may be the case, as the flake-like particles were found in the rabbit tissues which produced the larger particle pellets following particle isolation, and therefore contained higher volumes of particles. However, elemental analysis did not reveal the presence of CrN particles from the interlayer in any of the samples from the coated group. This may be due to the relative thinness of the CrN interlayer which was applied (0.8  $\mu\text{m}$ ); thus, particle volumes were likely too low for any CrN particles to be identified. The nanoscale CoCr particles isolated from both the uncoated and coated groups were similar to those produced by implant wear under standard simulation (Brown *et al.*, 2006).

In addition, a high dispersion of particles within the fat pad was observed. This suggests that the rabbit model successfully replicated the release of nanoscale particles from a prosthesis and may represent an improvement to models previously used, which employed less clinically relevant devices (Kubo *et al.*, 1999; Goodman *et al.*, 1992; Sacomen *et al.*, 1998; Sundfelt *et al.*, 2002). Green particles were similar to the histological appearance of corrosion products of CoCr described in previous studies (Scharf *et al.*, 2014). Elemental analysis of the particles revealed that the CoCr particles, and not the SiN particles, were oxidised. In addition, some of the CoCr particles were composed mainly of chromium, suggesting the release of cobalt ions and formation of chromium oxides, which have been documented to occur in vivo (Paustenbach *et al.*, 2014). Although several authors suggest that such corrosion results in cell necrosis (Granchi *et al.*, 1998; Gill *et al.*, 2012; Scharf *et al.*, 2014), necrosis and another typical chronic reaction to cobalt chromium, ALVAL, were not apparent in the rabbit samples. A lack of these reactions has also been reported in a study in mice at 40 weeks (Brown *et al.*, 2013). It is likely that such reactions are minimal after relatively short implantation times, as the nanoscale particles are released too gradually for the required concentration of particles to be reached.

Histological analysis of the fat pad from treated joints demonstrated the presence of inflammatory cell infiltrates. This agrees with previous findings that particles are often deposited in the fat pad, causing inflammation (Eymard and Chevalier, 2016). Similarly to results reported by Brown *et al.*, 2013, the histological results suggested that the nanoscale aggregates of CoCr particles

did not cause a giant cell response, as giant cell responses were only present in the tissues from the uncoated group surrounding large circular particles, or in the tissues from the coated group. The CoCr nanoparticles were mainly intracellular due to phagocytosis by macrophages, most likely as part of the innate immune response. This is consistent with previous findings on nanoscale CoCr particles (Athanasou *et al.*, 2016; Man *et al.*, 2017; Brown *et al.*, 2013).

The SiN coated group also contained multi-nucleated giant cells; this response appeared to have been elicited by not only bone cement particles but also SiN coating particles and large CoCr particles produced by third body wear of the implant substrate in rabbit 34.14. Previous findings indicate that multi-nucleated giant cells usually occur in response to large particles from materials including polyethylene and PMMA (Athanasou *et al.*, 2016; Nine *et al.*, 2014), as part of an innate foreign body reaction. Giant cells may also develop in response to large CoCr particles, though such reactions are rare (Xia *et al.*, 2017). To the author's knowledge, giant cells have not been reported in response to SiN particles. However, no large particles or giant cells were observed during histological analysis of tissue from rabbit 34.24, despite the isolation of large SiN particles and large CoCr particles from this tissue sample. This is likely partly due to the difficulty of observing particles using histology, since it is only feasible to observe a selected number of sections which represent a relatively small proportion of the entire sample. In contrast, particle isolation captures almost the entire particle volume contained in a sample (Lal *et al.*, 2016). It is also possible that in this case, large particles were more prevalent in the area of tissue used for particle isolation (fat pad immediately below the patella) and were less prevalent in the area of tissue used for histological analysis (distal end of the fat pad). The dispersion of particles to various anatomical sites has been documented in multiple studies (Urban *et al.*, 2000; Revell, 2008; Brown *et al.*, 2013). Although particle volumes were evidently much greater in the coated group during particle isolation, this did not translate to a higher volume observed in all of the tissue sections, which suggests that particle concentrations varied between the tissue sites. Splitting samples may thus be a sub-optimal approach which could result in certain particle types and reactions being under-observed



during histological analysis. However, it was useful to carry out both particle isolation and histology on certain rabbits to gain additional information about particle types and reactions, since more rabbit samples were not yet available for analysis. This was due to delays in initiation of the rabbit study caused by earlier difficulties in creating a functional coating within the Lifelong Joints Project. With unlimited time, and with sufficient animals from the coated group available, histological analysis would be performed on the entire fat pad, in addition to other tissue sites, including capsular periprosthetic tissue from medial or lateral aspects of the joint, and areas of tissue closer to the bone-cement interface. Further analysis of the retrieved implants would be required to confirm the modes of coating failure and determine whether adhesive failure at the substrate/coating interface may have occurred.

Overall, despite a high volume of SiN particles in the coated group most likely due to SiN coating failure, reactions to SiN particles in the rabbit model did not indicate cytotoxicity and consisted of a primarily macrophage-driven innate immune reaction; however, longer term studies using functional coatings would need to be carried out to test the biocompatibility of SiN coatings for total joint replacement further, as reactions to SiN coating particles must be studied in the absence of other particle types.

## Chapter 6

### Discussion

#### 6.1 General discussion

Adverse reactions to wear debris limit the lifetime of current joint replacements and make them less suitable for younger patients (SHPR; 2010; NJR, 2017). Preclinical testing of implants has traditionally failed to fully evaluate the potential impact of wear debris, leading to the clinical use and subsequent recall of multiple devices (Bosker *et al.*, 2012). There may be several reasons for failure to evaluate wear debris. Firstly, previous guidelines have not mandated isolation and characterisation of wear debris in joint replacements, or the need to test the biocompatibility of joint replacements under adverse conditions involving the production of significant volumes of wear debris (ISO 10993-1, 2009). Preclinical analysis of wear debris generated *in vivo* and associated reactions has been limited by the lack of an animal model which truly replicates clinical observations in humans (Langlois and Hamadouche, 2011) and the lack of a sensitive method to isolate low particle volumes from tissues. As such, most *in vivo* analysis of wear debris and the biological reactions to wear debris has been carried out on explant samples from hip revision surgeries, or from cadavers, long after clinical approval of the device. Novel joint replacement devices employing materials such as SiN, for which there is limited information regarding potential biocompatibility, should be fully tested considering the impact of wear debris prior to clinical use. This PhD project therefore aimed to produce and test a method to retrieve low volumes of SiN particles from tissues, and to evaluate the biocompatibility of SiN particles in an animal model, in comparison to other commonly used orthopaedic materials (CoCr and titanium). To that end, a particle isolation method was developed and applied to two separate animal studies, one of which consisted of a short-term study in rats injected with SiN, CoCr or titanium particles. The other study consisted of rabbits implanted with either SiN-coated or uncoated CoCr prostheses. Biocompatibility of the particles were analysed histologically using the two animal models.

## 6.2 Development and application of a particle isolation method

Methods to isolate particles from tissue samples have been developed (Schmiedberg *et al.*, 1994; Margevicius *et al.*, 1994; Lerouge *et al.*, 1998; Doorn *et al.*; 1998; Schmiedberg *et al.*, 2006; Milosev and Remskar, 2008). However, such methods were not developed with consideration for materials with dissolution properties, were not validated for sensitivity and sometimes yielded poor results due to protein contamination of the particles. Development of an improved method to isolate wear particles from tissue samples was achieved through the experiments detailed in Chapter 3, which demonstrated that low volumes of 0.0025 mm<sup>3</sup> per sample of SiN particles could be retrieved using a method involving enzymatic tissue digestion and density gradient ultracentrifugation using sodium polytungstate gradients. The method was applied to ovine tissue samples doped with SiN, CoCr or titanium particles. Effective removal of proteins and other contaminants from particles was achieved, without introducing extraneous chemical or particulate contamination to samples, demonstrating that the method was effective in retrieving a variety of particle types. Furthermore, particle characterisation demonstrated that the method did not cause significant changes to particle size, aspect ratio or circularity. The same particle isolation methodology was applied to a rat model, in which particles were exposed to *in vivo* conditions for a seven-day time period as detailed in Chapter 4. Histological analysis of tissues from the rat study demonstrated that particles were successfully delivered into the joint space and a significant particle volume was engulfed by cells, indicating that the model was a relevant way to test the particle isolation method and investigate *in vivo* changes to particles. The rat study provided validation that the isolation method developed in Chapter 3 was suitable for application to tissue samples, in which a 7-day time point was used to enable development of a protein corona surrounding particles. Isolation of particles from the rat tissues and subsequent characterisation also demonstrated effective removal of protein and a lack of contamination. Since no statistically significant geometric changes to particles occurred, the rat study also further demonstrated that particles were not affected by the isolation process. The particles were not affected by *in vivo* processes such

as corrosion in phagolysosomes over a short timeframe (seven days). This also demonstrated that significant dissolution of SiN particles did not occur within the seven days *in vivo*; SiN particle sizes were on average 26 nm +/- 1 (SD) before isolation and 27 nm +/- 1 (SD) after isolation. Isolation of particles from periprosthetic tissue as part of a rabbit study, as detailed in Chapter 5, further demonstrated the potential for the technique to be applied to explant samples, as particles were successfully isolated from each rabbit sample following 12 weeks *in vivo*. This demonstrated that particles produced by a prosthesis *in vivo*, and larger SiN particles, as well as zirconium dioxide particles from bone cement, could be retrieved. Proteins were once again effectively removed.

The efficacy of the isolation method in studies involving tissue from multiple animal species and particle types, in which particle sizes ranged from 10 nm to 100  $\mu$ m, as well as a recent collaboration applying the isolation method to human cadaveric samples that has so far shown promising results (unpublished data), gives robust evidence for the suitability of the method to be used in a variety of samples. The isolation method developed as part of this PhD project has been incorporated into a CEN workshop agreement (CWA 17253-1, 2018). The availability of a fully validated, cost effective, quick to perform particle isolation method from tissue which does not require specialist equipment will likely encourage future evaluation of the wear debris associated with orthopaedic implants, especially as recent FDA guidelines have highlighted the need to evaluate wear debris as part of preclinical adverse testing scenarios (FDA, 2016).

Though there was a degree of chemical contamination of the particles isolated from the rabbit tissue samples, detectable levels of iron and manganese may have been present in the alloy to begin with (ISO 5832-12, 2007), and other metal contamination may have occurred during the rabbit surgeries, as stainless-steel surgical equipment was used during implantation. Furthermore, such contamination was consistent in all samples from both the coated and uncoated groups from the rabbit study and was absent in the samples from the cadaveric ovine and rat samples detailed in Chapters 3 and 4. This further indicates that the source of contamination was unlikely to be the isolation process. Similarly, argon was only found in SiN coating particles

of the rabbit study, and it is highly likely that the source was the use of argon in the coating process.

However, traces of tungsten were detected in CoCr particles isolated from doped cadaveric tissues (Chapter 3), the rat stifle joint tissues (Chapter 4), and the rabbit periprosthetic tissue (Chapter 5). Thus, it is highly likely that there is an affinity between tungsten, which is used in the sodium polytungstate density gradients, and CoCr particles. Although it was confirmed that the tungsten did not cause geometric changes to particles in Chapters 3 and 4, the presence of tungsten could affect the biological properties of the particles, and thus limit use of the isolated particles in, for example, *in vitro* cell viability assays. Studies indicate that tungsten is relatively biologically inert (Peuster *et al.*, 2003); nevertheless, future work should aim to improve removal of the tungsten, possibly by addition of further rounds of ultracentrifugation as part of the particle washing protocol. This could be incorporated into the protocol without significant additional time or cost requirements.

### **6.3 Comparison of the animal models**

The use of two separate animal models has highlighted the key advantages and limitations of both (Table 6.1). The rat model had the advantage of allowing a highly controlled dose of particles of a single material to be delivered to the same location within each stifle joint. In addition, the size of rat stifle joints made them amenable to histological analysis of the whole joint, and thus enabled particle dispersion and biological reactions to be analysed in all relevant anatomical locations of each joint. In the rabbit model, whole joint analysis was not feasible due to the time that would be required to decalcify the larger stifle joints. Variations were observed in the size of the particle pellet isolated from each rabbit sample, indicating differences in the amount of wear debris produced, or variation in the amount of wear debris deposited by anatomical site. Further, the presence of multiple particle types in the rabbit samples made it difficult to distinguish which particles were eliciting particular biological reactions. However, a better dispersion of particles within the fat pad was achieved in the rabbit samples compared to the rat samples, in which particles were highly concentrated in certain areas.

This clumping may explain why necrosis was present in the rat samples and not in the rabbit samples. Particle aggregation is also known to affect the biological response to particles (Okuda-Shimazaki *et al.*, 2010). For example, larger aggregates of titanium dioxide lowered cell viability and caused greater increases in the levels of gene expression for biomarkers of stress, inflammation and cytotoxicity, compared to smaller aggregates of the same particles (Okuda-Shimazaki *et al.*, 2010). Since lymphocyte-dominated reactions are known to occur in response to CoCr particles, the lack of these types of reactions in the uncoated group of rabbit samples suggests that there may have been an insufficient volume of nanoscale CoCr particles produced. Thus, a longer time point would be required to generate sufficient particle volumes to study long term biological reactions to the CoCr particles. However, it may be that dissemination of particles in this type of animal model would prevent a high enough concentration of CoCr particles to be reached for reactions such as ALVAL to occur. Since there was significant infiltration of lymphocytes in the rat tissue injected with CoCr particles, directly dosing animal joints with a high dose of particles may be a better approach to rapidly simulate the types of reactions which take years to form in joint replacement patients; however, giant cell reactions may not be replicated using such a method. It has been suggested that *in vivo* models employing prostheses may not produce inflammatory reactions in the same way that direct exposure to particles may elicit, and that direct exposure to particles may better replicate the reactions observed around loose implants (Langlois and Hamadouche, 2011). However, species-specific differences cannot be ruled out as the potential reason for the absence of a significant lymphocytic reaction in the rabbit model. For example, circulating leukocyte populations display marked differences even in animal species that are phylogenetically closely related (Haley, 2003). Human blood may contain 50-70% neutrophils, whereas rat blood and rabbit blood may contain 10-21% and 25-46% neutrophils respectively (Haley, 2003). Further, rat blood has an especially high proportion of lymphocytes (83-100%) compared to the 20-40% of human blood leukocytes which are lymphocytes; mice blood leukocytes are 50-70% lymphocytes (Haley, 2003). These species-specific differences would likely affect the immune response to particles and may explain the lower proportion

of lymphocytes observed in the rabbit tissues compared to the rat tissues. Furthermore, there are species-specific differences with regard to immune cell function. Human alveolar macrophages have been reported to have a greater ability to phagocytose particles compared to rodent alveolar macrophages, possibly due to their greater size (Brain and Mensah, 1983).

**Table 6.1. Advantages and disadvantages of the rat and rabbit model.**

	Rat model	Rabbit model
Advantages	<ul style="list-style-type: none"> <li>• Particle dosage could be controlled</li> <li>• Particles could be analysed before and after <i>in vivo</i> exposure</li> <li>• Positive control (CoCr) particles successfully replicated adverse tissue reactions (lymphocytic infiltrates; necrosis)</li> <li>• Analysis of the whole joint was feasible, enabling the synovium to be analysed</li> </ul>	<ul style="list-style-type: none"> <li>• Particles were generated <i>in vivo</i> by a coating and prosthesis</li> <li>• Chronic reactions to particles could be studied</li> <li>• The timeframe enabled SiN particle dissolution, and a greater level of CoCr particle corrosion, to occur</li> <li>• The longer time point also enabled latent reactions such as giant cell formation to develop</li> <li>• Less particle clumping occurred</li> </ul>
Disadvantages	<ul style="list-style-type: none"> <li>• Particles were not generated <i>in vivo</i>, potentially altering development of a protein corona and aggregation characteristics</li> <li>• Short timeframe and single dosage prevented analysis of chronic reactions to particles</li> <li>• Particle concentration in different sections varied due to clumping</li> </ul>	<ul style="list-style-type: none"> <li>• Particle dosage was not controlled and varied between animals</li> <li>• The positive control (uncoated CoCr prosthesis) failed to replicate adverse tissue reactions to particles</li> <li>• Coating failure led to the production of less relevant coating particles, and the presence of multiple particle types which made it difficult to determine which materials elicited particular reactions</li> <li>• Analysis was performed on the fat pad and not whole joint</li> <li>• Confounding effects of surgery and cement failure</li> </ul>

The two animal studies involved different types of particles generated under different conditions. The size and shape of CoCr and titanium particles generated by pin-on-plate were highly similar between the study from Chapter 3 and the rat study, with only slight differences in the average size of CoCr particles (23 nm compared to 26 nm in the rat study). This may be due to variation between particle generation experiments, possibly caused by human error during set-up of the pin-on-plate machine, or due to minor variation in the surface roughness of the pins and plates used. Nevertheless, the results indicated that generating particles by pin-on-plate is a reliable method to produce particles of a certain size and shape. The effectiveness of using pin-on-plate to produce clinically relevant wear debris is evidenced extensively in the literature (Bohler *et al.*, 2000; Tipper *et al.*, 2001; Firkins *et al.*, 2001; Germain *et al.*, 2003; Brown *et al.*, 2006; Grosse *et al.*, 2015; Lal *et al.*, 2016). Though particles from the rabbit study were generated under more clinically relevant conditions by employing actual coated prostheses rather than model particles, failure of the coating and luxation of certain prostheses limited the production of clinically relevant nanoscale SiN particles in the coated prosthesis group.

In both animal studies, the fat pad was the main anatomical location analysed. Since particles and inflammatory infiltrates were contained mainly within the fat pad of the rat tissues, the fat pad was chosen as the focus for analysis in the rabbit study. The fat pad is known to be infiltrated by inflammatory cells and is a source of proinflammatory cytokines (Eymard and Chevalier, 2016). The current study provides further evidence that the fat pad is a suitable place from which to isolate particles and to study reactions to particles. The fat pad is also thought to contribute to proinflammatory changes in the joint, including changes to the synovial lining (Eymard and Chevalier, 2016). Thus, it is possible that the synovial thickening of the CoCr-injected stifle joints of the rat study was due to proinflammatory signalling by the infiltrates observed within the fat pad.

#### **6.4 Biocompatibility of SiN, CoCr and titanium particles**

Despite the relatively high doses of SiN particles evaluated in the rat and rabbit studies, reactions to SiN particles did not include necrosis. Recruitment



of inflammatory cells was observed, and reactions were primarily macrophage-driven. SiN particles were engulfed by macrophages, as has been reported in *in vitro* studies (Zhang *et al.*, 2011; Lal *et al.*, 2018). Zhang *et al.* (2011) suggested that the morphological differences identified in cells containing SiN particles indicated cellular dysfunction in terms of energy production and protein synthesis. The authors also reported significant TNF- $\alpha$  release from a murine macrophage cell line in response to SiN particles (and zirconia particles) even at low particle doses; however, their results also indicated that SiN particles and other ceramic particles were non-toxic. Importantly, their results differed based on the cell line used, as SiN particles decreased the total intracellular protein content of L929 (mouse fibroblast) cells in a dose-dependent manner but not MG63 (human fibroblast-like) cells. This is further supported by a study by Kue *et al.* (1999), who demonstrated the biocompatibility of SiN based on the response of MG63 cells to SiN discs. An *in vitro* study involving human PBMNCs has shown that neither nanoscale nor micron-scale SiN particles caused cytotoxicity, oxidative stress, genotoxicity or the release of TNF- $\alpha$  (Lal *et al.*, 2018). Similarly, an *in vitro* study investigating the response of L929 cells has shown that SiN in bulk form, as well as titanium and aluminium, had no cytotoxic effects (Neumann *et al.*, 2004). Taken together the data indicates that SiN particles are non-toxic, but their effect on proinflammatory signalling may differ by cell type or species and SiN particles may be more bioactive in murine cells. However, it is also possible that the biological inertness observed in the *in vitro* studies by Lal *et al.* (2018) is due to differences in the way that cultured cells behave compared to cells *in vivo*. Other authors have reported biological inertness of nanoscale alumina and zirconia particles *in vitro* in human cells, yet mild pro-inflammatory responses in rats *in vivo* (Roualdes *et al.*, 2010). The presence of a macrophage-driven response in the rat study and a foreign body response involving giant cells in the rabbit study would suggest that SiN particles are biologically active but non-toxic in these species *in vivo*, though the reactions observed in the rabbit study may have been caused by cement particles and large CoCr substrate particles. Researchers at the University of Zurich have shown that SiN nanoparticles do not cause organ toxicity in rats (Nuss, 2018, unpublished data).

The appearance of SiN coating particles (Figure 5.13) was more irregular and the columnar structure was less defined compared to coating particles isolated from a pin-on-plate wear test (Lal, 2017, unpublished data). This may indicate dissolution of particles within the 12-week period of the rabbit study; thus, the results of both studies indicated that SiN particles begin to dissolve in a detectable way after 1-12 weeks *in vivo*. Our results therefore agree with previous findings that SiN dissolves *in vivo* (Maloney, 2005). Any nanoscale SiN particles, which may have been produced prior to coating failure, may have dissolved entirely, as studies have suggested an *in vivo* dissolution rate of 0.33 - 2 nm per day (Maloney, 2005) and 0.2 – 1.4 nm per day (Pettersson *et al.*, 2016), although the rat study described in this thesis indicated that less dissolution occurred since changes in size were statistically insignificant at the seven-day timepoint.

Our results also agree with previous studies that SiN particles are more biocompatible compared to CoCr particles (Zhang *et al.*, 2011; Lal *et al.*, 2018). CoCr particles may elicit cytotoxicity, oxidative stress, genotoxicity and release of TNF- $\alpha$  in a donor-dependent manner (Lal *et al.*, 2018). The biological responses to the CoCr particles in the rat study agree with previous findings that CoCr particles cause tissue necrosis and lymphocytic infiltrates (Willert *et al.*, 2005; Davies *et al.*, 2005; Donell *et al.*, 2010). Pseudotumours are sometimes also reported in tissues exposed to CoCr particles (Pandit *et al.*, 2008). Furthermore, results from both the rat and rabbit studies provided further evidence of corrosion of CoCr particles *in vivo*, since the ratio of cobalt to chromium was lower in isolated particles in both studies following *in vivo* exposure. Oxidation of CoCr particles was shown to occur *in vivo* in the rat study. Such *in vivo* changes to CoCr particles agree with previous findings (Paustenbach *et al.*, 2014). Giant cells have been shown to develop around large CoCr particles (Xia *et al.*, 2017), which may have occurred in the rabbit tissues, though it was difficult to deduce to which particle type the reaction was directed.

There are species-specific differences in type IV hypersensitivity reactions, which may develop in periprosthetic tissue in response to CoCr particles (Wawrzynski *et al.*, 2017). In humans, the peak of a type IV hypersensitivity response typically occurs after 2-4 days, while in rats and rabbits peak

responses typically occur after 24 h (Turk, 1980). The periprosthetic tissues of THR patients with type IV reactions contain T-cells, macrophages and dendritic cells (Cadosch *et al.*, 2009). Similarly, in inflammatory infiltrates in rats, the peak of a type IV response involved predominantly lymphocytes and monocytes (Haley, 2003), while in rabbits up to 60% of the inflammatory infiltrate may consist of polymorphonuclear cells (Turk, 1980). Further, necrosis is not associated with type IV hypersensitivity reactions in humans and is rare in rats, but is usually present in rabbits (Turk, 1980; Haley 2003). Based on these papers, it is unlikely that hypersensitivity reactions were involved in the rabbit study, but such reactions cannot be ruled out in the rat study.

Titanium particles were only evaluated in terms of biocompatibility in the rat model, in which a minimal reaction involving a low but statistically significant number of lymphocytes occurred. Long term studies in mice have also indicated a favourable biocompatibility profile for titanium particles, and similar to the rat study, no giant cell reactions developed (Rae, 1986). However, other studies have indicated that titanium particles are immunologically active (Shanbhag *et al.*, 1995; Wang *et al.*, 1997; Vermis *et al.*, 2001). Titanium particles below a certain size are known to be phagocytosed by macrophages (Lalor *et al.*, 1991) and are occasionally reported to cause type IV sensitivity reactions (Lalor *et al.*, 1991; Vijayaraghavan *et al.*, 2012). Titanium particles have also been associated with foreign body reactions involving giant cells (La Budde *et al.*, 1994). The minimal reaction to titanium particles observed in the rat study may be due to the fact that the particles were 1 – 100  $\mu\text{m}$  in size and were thus outside the phagocytosable range of 0.1 – 1  $\mu\text{m}$ . Foreign body responses to larger particles may take longer than seven days to fully occur; it has been well documented in the literature that foreign body reactions and the formation of giant cells and granulomatous tissue occurs gradually over time (Higgins *et al.*, 2009). Micronscale titanium particles have also been shown to cause significantly high levels of TNF- $\alpha$  release (Lal *et al.*, 2018). Zhang *et al.* (2011) have shown that a high dose of titanium particles caused significant increases in the expression of TNF- $\alpha$ . However, the increase in TNF- $\alpha$  was less than that observed in cells challenged with SiN and zirconium

dioxide particles. However, it must be noted that differing particle size makes it difficult to draw comparisons.

## **6.5 Limitations of the studies**

In addition to the limitations outlined within the discussion of each chapter, there were general limitations to the animal studies. The clinical contribution of animal studies to medical research in general remains uncertain (Schechter *et al.*, 2002). Besides the usual disadvantages subject to all animal experiments, including anatomical, metabolic and immunological differences to humans and relatively small experimental groups (Pound *et al.*, 2004), it is also difficult to replicate chronic biological reactions to particles whilst controlling for particle dosing. Further, both the rat and rabbit studies involved only one timepoint, which made it difficult to draw conclusions about how particles disseminate and how biological reactions develop over time; it also made it difficult to analyse particle dissolution. There was also only one dose used in the rat study, which made it impossible to determine a dose-dependent relationship between the wear debris and reactions. Furthermore, the limited number of samples meant that in the rabbit study, samples had to be split. Since samples were split, and particle isolation was only carried out on the fat pad, it was not possible to quantify the total volume of particles in the rabbit periprosthetic tissue. These problems are partly due to the lack of a functional SiN coating, which delayed the initiation of the rabbit study and therefore limited the analysis which could be achieved in the given timeframe. The problems encountered regrettably led to substandard SiN coatings being applied to the rabbit prostheses, which prevented the biological evaluation of a functional coating.

Throughout the research described in this PhD, analysis of SiN particles has always been made in comparison to CoCr and titanium particles. This is because CoCr is currently being investigated as a substrate material for a SiN-coated device at the articulating surfaces (Pettersson *et al.*, 2016). CoCr also successfully served as a positive control due to its known toxic and immunological effects (Haddad *et al.*, 2011). Titanium is another possible substrate due to the potential of a SiN coating for application to tapers; corrosion of tapers and subsequent hip replacement failure is a current focus

of research (Morlock *et al.*, 2017). However, it would have been useful to compare SiN to UHMWPE, as this has been a gold standard material for hip replacements (Prever *et al.*, 2009). In addition, SiN should be compared to current generation ceramic materials, including alumina and zirconia particles, for which there is a limited *in vivo* biocompatibility profile (Roualdes *et al.*, 2010).

Finally, an inherent limitation of the particle characterisation used in each results chapter has been the use of manual particle measuring. This prevented very large numbers of particles from being measured and is always subject to a degree of human error. This method was chosen due to the aggregated nature of isolated particles, which prevented accurate automated particle measurements. Similarly, histological analysis by cell counting is also subject to a degree of a human error/subjectivity. In the case of particle characterisation, a method to disaggregate particles would be highly advantageous. Although Billi *et al.* (2012) produced a method to separate and display particles isolated from serum, this method required specialist equipment such as an ultracentrifuge tube cutter, and traps particles within a matrix, thus consuming the particle sample.

## **6.6 Future work**

Future work should aim to evaluate the particles found in H&E stained sections from the rabbit samples by SEM and elemental analysis of unstained, recut sections. This would confirm whether the chemical contaminants were present pre-isolation and also confirm that the oxidation of CoCr particles occurred *in vivo*, as was confirmed as part of the rat study. The analysis would also show whether oxidation of SiN and titanium particles occurred *in vivo*.

Further, the particles isolated from the rabbit tissues should be characterised to provide particle size distributions and data on the aspect ratio and circularity of the particles. An indication of the ratio of the different types of particles could also be calculated by counting particles in elemental maps produce by EDX software. This data could aid the analysis of the biological reactions to particles and future studies of SiN particles by providing data on the types of particles produced under adverse conditions. In addition, cells could be

counted within the fat pad in a similar way to the rat study, to characterise biological responses in the rabbit study and determine whether differences to the controls are significant. This would also aid comparison of the results between animals, between the material groups and between the two animal studies.

Retrieval and subsequent analysis of the rabbit implants, as well as control, non-implanted rabbit prostheses from the coated and uncoated group should be evaluated to further determine how coating failure occurred and to further characterise the wear of the coating and substrate material of the implants. This could be carried out by SEM analysis of implants and by measuring surface roughness with, for example, Talysurf.

Furthermore, analysis of coated implants utilising titanium as a substrate would be useful to characterise the applicability of a SiN coating for the taper junction, though use of a more relevant model for the taper would be better.

Immunohistochemistry could also be used as an alternative method of cell counting, for example by labelling cells with inflammatory cell markers such as CD68, CD3, CD4 and CD8. There are several drawbacks to this method, since it is increasingly recognised that many inflammatory cell markers are expressed in a variety of cells (Beranek, 2005), and since the number of cells counted depends partly on the sensitivity of the staining protocol used. However, such analysis would still provide valuable information, especially as certain markers are directly involved in inflammatory processes. To carry out such labelling, antigen retrieval is often required in formalin-fixed samples. Regrettably, multiple antigen retrieval and macrophage staining protocols were carried out on sections from the rat study, with no positive staining achieved (Appendix D). Although certain studies suggest that decalcification by EDTA leaves most epitopes intact, the present study indicated that prolonged decalcification above room temperature may lead to loss of the CD68 epitope, hence the lack of any specific staining. Significant cross reaction between the rat tissue and antibodies was observed, which may be due to Fc receptors on inflammatory cells binding to anti-mouse secondary antibodies; this phenomenon has been reported elsewhere (Ramos-Vara, 2005). Blocking the tissue with serum did not improve results.

Samples were taken from the synovial fluid of implanted rabbit stifles and stored at  $-80^{\circ}\text{C}$ , although these samples could not be analysed due to time constraints. Synovial fluid extraction was not possible in the rat study, in which the volume of synovial fluid was too low. The rabbit synovial fluid samples could potentially in future be analysed by quantitative PCR. This would involve extraction of the RNA and use of gene-specific primers for generation of cDNA from specific genes of interest. Amplification by PCR would then enable the relative expression of each gene in the different groups to be measured. This would allow expression of inflammatory cytokines known to be involved in the biological reactions to particles, such as TNF- $\alpha$ , IL-1 $\beta$ , IL-6 and IL-8, as well as inflammatory mediators such as COX-2 and iNOS to be quantified in the rabbit samples. This type of analysis is difficult in tissue samples since there is a stochastic element to the dispersion of particles and subsequent locations of inflammatory cell infiltrates. Thus, even multiple tissue samples may not be representative of the joint overall. However, since synovial fluid is homogeneous, these factors would have less of an effect. This type of analysis would be limited by the transient nature of cytokine expression; the expression at sacrifice within the rabbit study could vary due to a multitude of factors, including the relative quantities of wear debris generated by each prosthesis, and thus may not necessarily correlate to greater or lesser biocompatibility of different materials. Since isolated particle pellet sizes visibly differed, and since there was dislocation of the prostheses in certain rabbits, particle amounts were likely to vary between animals. Nevertheless, the presence or absence of significant cytokine expression could help to elucidate the inflammatory pathways elicited by the materials.

Analysis of additional areas of tissue from the rabbit model, for example synovial tissue from medial, lateral and posterior aspects of implants, and even from muscle tissue, which has been known to develop fatty infiltrates in response to wear debris (Kovalak, 2018), could enable further study of particle dissemination and reactions to particles. For example, particle isolation could be carried out from sites further from the joint to determine the extent of dissemination.

However, analysis should be carried out on samples in which functional coatings were employed. In fact, since SiN particles have shown no toxicity

even at high doses, the next logical step for SiN coating testing would be a long-term study in a larger animal, phylogenetically distinct from rats and rabbits. Use of a larger animal could enable biopsies to be taken of periprosthetic tissue from the implant site at several time points; several models have been developed in dogs, pigs and sheep (Langlois and Hamadouche, 2011).

Such future studies could seek to further define the SiN-response pathway. For example, since these studies have shown that SiN particles are phagocytosed by macrophages *in vivo*, future studies could aim to define the mechanism of cellular uptake. It has been shown that particles may be taken up by the clathrin-mediated pathway and/or the caveolae-mediated pathway, with a possible relationship between the mechanism of particle uptake and the cellular response (Liu *et al.*, 2015).

As mentioned in section 6.5, further studies are required to compare SiN to other materials including UHMWPE. These could involve similar methods to those used in the rat study or focus on additional cell studies employing cell types and cell lines not previously studied. However, improvements to the rat model should be made, including the use of a sham injection in the contralateral joint, which could be easily achieved through the injection of PBS or sterile water in the absence of particles. Further, enhancement to the delivery method of the particles could be made. Brown *et al.* (2013) used syngeneic mouse serum and PBS in a 1:1 ratio and four separate injections over a six-week timeframe, which they suggested achieved good particle dispersion. However, no significant reactions to CoCr particles were achieved using their animal model. This may be due to use of a smaller animal and thus administration of a lower dose of particles. Is it important that animal models allow time for any significant reactions to particles to develop to allow screening of unsafe materials, whilst balancing animal welfare. Thus, the rat model may represent a better choice for preclinical testing of materials. There are many drug delivery systems which could be adapted to gradually deliver particles within the joint space as part of an animal model (Tiwari *et al.*, 2012). However, use of these would present challenges in ensuring that particles are well dispersed upon delivery. Also, many systems employ materials such as biodegradable polymers, which could create unintended biological effects.



Development of the rabbit model should focus on use of a different fixation method, such as use of an alternative bone cement, to prevent the release of bone cement particles, since these are known to cause inflammation. It is also possible that a degree of bone cement failure led to loosening of certain implants and thus the luxation identified in certain rabbits. Further development could attempt to produce a cement-less prosthesis design to prevent release of bone cement, whilst avoiding the use of other coatings, such as hydroxyapatite, which can have a positive effect on the osseointegration of an implant (Das and Shukla, 2017).

Development of the particle isolation method could also involve testing on additional materials. There is already evidence that use of the method by Lal *et al.* (2016) for serum samples is suitable for ZTA particles (CWA 17253-1, 2018), and can be combined with other methods to isolate polyethylene particles from the same sample. Future development may include further modification of current methods to facilitate extraction and separation of multiple particle types using a single protocol. This would be especially useful to allow multiple particle types to be easily studied from a single sample. A method to isolate particles from synovial fluid would also be beneficial; this could likely be achieved by incorporation of a hyaluronidase into the method developed in this thesis. Finally, as mentioned in section 6.5, a method to disaggregate particles for characterisation could enable thousands of particles to be analysed in an unbiased way. Alternatively, new software could be developed to enable the recognition of individual particles within aggregates.

## **6.7 Conclusions**

The main aims of this study were to evaluate the biocompatibility of SiN particles. Specific objectives included:

- (A) to develop and validate a sensitive method to isolate SiN wear debris from tissues
- (B) to isolate and analyse wear particles from animal tissues
- (C) to use animal models to evaluate biological responses to particles

- (D) to determination the biocompatibility of silicon nitride coating particles

Regarding (A), this study successfully developed a method for the isolation of wear debris from tissue. The method was shown to have no effect on the size or morphology of SiN or CoCr nanoparticles, or micron-sized titanium particles, and was proven to effectively isolate particle volumes as low as 0.0025 mm<sup>3</sup> per sample.

Regarding (B), the isolation method was applied to a rat model, where the method was shown once again to effectively remove protein; no significant changes to SiN or CoCr particle geometries occurred. Titanium particles were similar in size and morphologies before and after isolation, though particle numbers were insufficient for statistical analysis. *In vivo* changes to the chemical composition of particles were also explored in the rat model. Application of the particle isolation method to a rabbit model also enabled effective isolation of SiN coating particles, CoCr substrate particles, and zirconium dioxide particles from bone cement. The coating particles were 1 – 100 µm in size and were columnar or shard-like in morphology, due to apparent coating failure.

Regarding (C and D), the biocompatibility of SiN particles as well as CoCr and titanium particles were also investigated through the rat and rabbit models. Histological analysis of rat stifle joint tissues injected with high particle doses demonstrated that all three particle types were biologically active, and that the presence of each material caused a degree of inflammation; in the SiN group, numbers of macrophages and not lymphocytes were significantly elevated. However, other morphological changes, including synovial thickness and angiogenesis, were not significant, and no necrosis was detected. In rabbit samples from the coated group, despite apparent coating failure, no necrosis and few lymphocytes were observed, and a moderate macrophage infiltrate was detected. The appearance of SiN particles suggested that a degree of *in vivo* dissolution within the 12-week timeframe had occurred. Overall, SiN particles were relatively biocompatible, particularly in comparison to CoCr particles. However, analysis of a functional SiN coating must be carried out

over a longer timeframe to enable chronic reactions to SiN coating particles to be fully evaluated.

## References

- Abu Amara, S., Leroux, J., & Lechevallier, J. (2014). Surgery for slipped capital femoral epiphysis in adolescents. *Orthop Traumatol Surg Res*, 100(1 Suppl), S157-167.
- Aggarwal, P., Hall, J. B., McLeland, C. B., Dobrovolskaia, M. A., & McNeil, S. E. (2009). Nanoparticle interaction with plasma proteins as it relates to particle biodistribution, biocompatibility and therapeutic efficacy. *Advanced drug delivery reviews*, 61, 428-437.
- Al-Hajjar, M., Leslie, I.J., Tipper, J., Williams, S., Fisher, J. and Jennings, L.M. 2010. Effect of cup inclination angle during microseparation and rim loading on the wear of BIOLOX (R) delta ceramic-on-ceramic total hip replacement. *Journal of Biomedical Materials Research Part B-Applied Biomaterials*, 95B(2), 263-268.
- Al-Hajjar, M., Jennings, L., Begand, S., Oberbach, T., Delfosse, D. and Fisher, J. 2013. Wear of novel ceramic-on-ceramic bearings under adverse and clinically relevant hip simulator conditions. *Journal of Biomedical Materials Research Part B-Applied Biomaterials*. 101(8), 1456-1462.
- Amaral, M., Abreu, C., Oliveira, F., Gomes, J., & Silva, R. (2008). Tribological characterization of NCD in physiological fluids. In (Vol. 17, pp. 848-852): *Diamond and Related Materials*.
- Anderson, J. M., Rodriguez, A., & Chang, D. T. (2008). Foreign body reaction to biomaterials. *Semin Immunol*, 20(2), 86-100.
- Aroukatos, P., Repanti, M., Repantis, T., Bravou, V., & Korovessis, P. (2010). Immunologic adverse reaction associated with low-carbide metal-on-metal bearings in total hip arthroplasty. *Clin Orthop Relat Res*, 468(8), 2135-2142.
- American Society for Testing and Materials (ASTM) (2011). Standard Specification for Wrought Cobalt-28Chromium-6Molybdenum Alloys for Surgical Implants. ASTM F1537. ASTM International, West Conshohocken, PA.
- American Society for Testing and Materials (ASTM) (2013). Standard Guide for Gravimetric Wear Assessment of Prosthetic Hip Designs in Simulator Devices. ASTM F1714-96. ASTM International, West Conshohocken, PA.

- American Society for Testing and Materials (ASTM) (2015). Standard Guide for High Demand Hip Simulator Wear Testing of Hard-on-hard Articulations. ASTM F3047M. ASTM International, West Conshohocken, PA.
- American Society for Testing and Materials (ASTM) (2016). Standard Practice for Characterization of Particles. ASTM F1877. ASTM International, West Conshohocken, PA.
- Baeten, D., Demetter, P., Cuvelier, C., Van Den Bosch, F., Kruithof, E., Van Damme, N., . . . De Keyser, F. (2000). Comparative study of the synovial histology in rheumatoid arthritis, spondyloarthropathy, and osteoarthritis: influence of disease duration and activity. *Ann Rheum Dis*, 59(12), 945-953.
- Bal, B. S., Khandkar, A., Lakshminarayanan, R., Clarke, I., Hoffman, A. A., & Rahaman, M. N. (2008). Testing of silicon nitride ceramic bearings for total hip arthroplasty. *J Biomed Mater Res B Appl Biomater*, 87(2), 447-454.
- Bal, B. S., & Rahaman, M. N. (2012). Orthopedic applications of silicon nitride ceramics. *Acta Biomater*, 8(8), 2889-2898.
- Baumann, B., Rader, C. P., Seufert, J., Nöth, U., Rolf, O., Eulert, J., & Jakob, F. (2004). Effects of polyethylene and TiAlV wear particles on expression of RANK, RANKL and OPG mRNA. *Acta Orthop Scand*, 75(3), 295-302.
- Baxter, R. M., Steinbeck, M. J., Tipper, J. L., Parvizi, J., Marcolongo, M., & Kurtz, S. M. (2009). Comparison of periprosthetic tissue digestion methods for ultra-high molecular weight polyethylene wear debris extraction. *J Biomed Mater Res B Appl Biomater*, 91(1), 409-418.
- Beaulé, P. E., Campbell, P., Mirra, J., Hooper, J. C., & Schmalzried, T. P. (2001). Osteolysis in a cementless, second generation metal-on-metal hip replacement. *Clin Orthop Relat Res*, (386), 159-165.
- Beranek, J. T. (2005). CD68 is not a macrophage-specific antigen. *Ann Rheum Dis*, 64(2), 342-343; author reply 343-344.
- Billi, F., Benya, P., Kavanaugh, A., Adams, J., Ebramzadeh, E., & McKellop, H. (2012). The John Charnley Award: an accurate and sensitive method to separate, display, and characterize wear debris: part 1:

- polyethylene particles. *Clin Orthop Relat Res*, 470(2), 329-338.
- Billi, F., Benya, P., Kavanaugh, A., Adams, J., McKellop, H., & Ebramzadeh, E. (2012). The John Charnley Award: An Accurate and Extremely Sensitive Method to Separate, Display, and Characterize Wear Debris Part 2: Metal and Ceramic Particles. *Clinical orthopaedics and related research*, 470, 339-350.
- Bitar, D., & Parvizi, J. (2015). Biological response to prosthetic debris. *World J Orthop*, 6(2), 172-189.
- Blomfeldt, R., Törnkvist, H., Ponzer, S., Söderqvist, A., & Tidermark, J. (2005). Comparison of internal fixation with total hip replacement for displaced femoral neck fractures. Randomized, controlled trial performed at four years. *J Bone Joint Surg Am*, 87(8), 1680-1688.
- Bohler, M., Mochida, Y., Bauer, T. W., Plenk, H., & Salzer, M. (2000). Wear debris from two different alumina-on-alumina total hip arthroplasties. *Journal of Bone and Joint Surgery-British Volume*, 82B, 901-909.
- Bosker, B. H., Ettema, H. B., Boomsma, M. F., Kollen, B. J., Maas, M., & Verheyen, C. C. P. M. (2012). High incidence of pseudotumour formation after large-diameter metal-on-metal total hip replacement A PROSPECTIVE COHORT STUDY. *Journal of Bone and Joint Surgery-British Volume*, 94B, 755-761.
- Brach Del Prever, E. M., Bistolfi, A., Bracco, P., & Costa, L. (2009). UHMWPE for arthroplasty: past or future? *J Orthop Traumatol*, 10(1), 1-8.
- Brain, J. D., & Mensah, G. A. (1983). Comparative toxicology of the respiratory tract. *Am Rev Respir Dis*, 128(2 Pt 2), 87-90.
- Brockett, C. L., John, G., Williams, S., Jin, Z., Isaac, G. H., & Fisher, J. (2012). Wear of ceramic-on-carbon fiber-reinforced poly-ether ether ketone hip replacements. *J Biomed Mater Res B Appl Biomater*, 100(6), 1459-1465.
- Brown, C., Fisher, J., & Ingham, E. (2006). Biological effects of clinically relevant wear particles from metal-on-metal hip prostheses. *Proc Inst Mech Eng H*, 220(2), 355-369.
- Brown, C., Lacharme-Lora, L., Mukonoweshuro, B., Sood, A., Newson, R. B., Fisher, J., . . . Ingham, E. (2013). Consequences of exposure to peri-articular injections of micro- and nano-particulate cobalt-Chromium

- alloy. *Biomaterials*, 34, 8564-8580.
- Brown, C., Williams, S., Tipper, J. L., Fisher, J., & Ingham, E. (2007). Characterisation of wear particles produced by metal on metal and ceramic on metal hip prostheses under standard and microseparation simulation. *Journal of Materials Science-Materials in Medicine*, 18, 819-827.
- Bylski, D., Wedemeyer, C., Xu, J., Sterner, T., Löer, F., & von Knoch, M. (2009). Alumina ceramic particles, in comparison with titanium particles, hardly affect the expression of RANK-, TNF-alpha-, and OPG-mRNA in the THP-1 human monocytic cell line. *J Biomed Mater Res A*, 89(3), 707-716.
- Cadosch, D., Chan, E., Gautschi, O. P., & Filgueira, L. (2009). Metal is not inert: role of metal ions released by biocorrosion in aseptic loosening – current concepts. *J Biomed Mater Res A*, 91, 1252-1262.
- Campbell, P., Ma, S., Yeom, B., McKellop, H., Schmalzried, T. P., & Amstutz, H. C. (1995). Isolation of Predominantly Submicron-Sized Uhmwpe Wear Particles from Periprosthetic Tissues. *Journal of Biomedical Materials Research*, 29, 127-131.
- Carbone, A., Howie, D. W., McGee, M., Field, J., Pearcy, M., Smith, N., & Jones, E. (2006). Aging performance of a compliant layer bearing acetabular prosthesis in an ovine hip arthroplasty model. *J Arthroplasty*, 21(6), 899-906.
- Casals, E., Pfaller, T., Duschl, A., Oostingh, G. J., & Puentes, V. (2010). Time Evolution of the Nanoparticle Protein Corona. *Acs Nano*, 4, 3623-3632.
- Catelas, I., Bobyn, J. D., Medley, J. J., Zukor, D. J., Petit, A., & Huk, O. L. (2001). Effects of digestion protocols on the isolation and characterization of metal-metal wear particles. II. Analysis of ion release and particle composition. *J Biomed Mater Res*, 55(3), 330-337.
- Catelas, I., Petit, A., Vali, H., Fragiskatos, C., Meilleur, R., Zukor, D. J., . . . Huk, O. L. (2005). Quantitative analysis of macrophage apoptosis vs. necrosis induced by cobalt and chromium ions in vitro. *Biomaterials*, 26(15), 2441-2453.
- Chang, J. D. (2014). Future bearing surfaces in total hip arthroplasty. *Clin Orthop Surg*, 6(1), 110-116.

- Chithrani, B. D., Ghazani, A. A., & Chan, W. C. W. (2006). Determining the size and shape dependence of gold nanoparticle uptake into mammalian cells. *Nano Letters*, 6, 662-668.
- Chu, Z. Q., Zhang, S. L., Zhang, B. K., Zhang, C. Y., Fang, C. Y., Rehor, I., . . . Li, Q. (2014). Unambiguous observation of shape effects on cellular fate of nanoparticles. *Scientific Reports*, 4.
- Cobelli, N., Scharf, B., Crisi, G. M., Hardin, J., & Santambrogio, L. (2011). Mediators of the inflammatory response to joint replacement devices. *Nat Rev Rheumatol*, 7(10), 600-608.
- Crabtree, N., Loveridge, N., Parker, M., Rushton, N., Power, J., Bell, K. L., . . . Reeve, J. (2001). Intracapsular hip fracture and the region-specific loss of cortical bone: analysis by peripheral quantitative computed tomography. *J Bone Miner Res*, 16(7), 1318-1328.
- Crawford, B. J., & Burke, R. D. (2004). TEM and SEM methods. *Methods Cell Biol*, 74, 411-441.
- Cursiefen, C., Maruyama, K., Jackson, D. G., Streilein, J. W., & Kruse, F. E. (2006). Time course of angiogenesis and lymphangiogenesis after brief corneal inflammation. *Cornea*, 25(4), 443-447.
- Darowski. (2007). The care of patients with fragility fracture. In (pp. 8-11): British Orthopaedic Association.
- Das, A., & Shukla, M. (2017). Surface morphology and in vitro bioactivity of biocompatible hydroxyapatite coatings on medical grade S31254 steel by RF magnetron sputtering deposition. *The International Journal of Surface Engineering and Coatings*, 95(5), 267-281.
- Davies, A. P., Willert, H. G., Campbell, P. A., Learmonth, I. D., & Case, C. P. (2005). An unusual lymphocytic perivascular infiltration in tissues around contemporary metal-on-metal joint replacements. *J Bone Joint Surg Am*, 87(1), 18-27.
- Doherty, A. T., Howell, R. T., Ellis, L. A., Bisbinas, I., Learmonth, I. D., Newson, R., & Case, C. P. (2001). Increased chromosome translocations and aneuploidy in peripheral blood lymphocytes of patients having revision arthroplasty of the hip. *J Bone Joint Surg Br*, 83(7), 1075-1081.
- Donell, S. T., Darrah, C., Nolan, J. F., Wimhurst, J., Toms, A., Barker, T. H., .



- . . Group, N. M.-o.-M. S. (2010). Early failure of the Ultima metal-on-metal total hip replacement in the presence of normal plain radiographs. *J Bone Joint Surg Br*, 92(11), 1501-1508.
- Doorn, P. F., Campbell, P. A., Worrall, J., Benya, P. D., McKellop, H. A., & Amstutz, H. C. (1998). Metal wear particle characterization from metal on metal total hip replacements: Transmission electron microscopy study of periprosthetic tissues and isolated particles. *Journal of Biomedical Materials Research*, 42, 103-111.
- Doorn, P. F., Mirra, J. M., Campbell, P. A., & Amstutz, H. C. (1996). Tissue reaction to metal on metal total hip prostheses. *Clin Orthop Relat Res* (329 Suppl), 187-205.
- Dorr, L. D., Bloebaum, R., Emmanuel, J., & Meldrum, R. (1990). Histologic, biochemical, and ion analysis of tissue and fluids retrieved during total hip arthroplasty. *Clin Orthop Relat Res* (261), 82-95.
- Dorr, L. D., Wan, Z., Sirianni, L. E., Boutary, M., & Chandran, S. (2004). Fixation and osteolysis with Metasul metal-on-metal articulation. *J Arthroplasty*, 19(8), 951-955.
- El-Warrak, A. O., Olmstead, M., Schneider, R., Meinel, L., Bettschart-Wolfisberger, R., Akens, M. K., . . . von Rechenberg, B. (2004). An experimental animal model of aseptic loosening of hip prostheses in sheep to study early biochemical changes at the interface membrane. *BMC Musculoskelet Disord*, 5, 7.
- Elsner, J. J., Mezape, Y., Hakshur, K., Shemesh, M., Linder-Ganz, E., Shterling, A., & Eliaz, N. (2010). Wear rate evaluation of a novel polycarbonate-urethane cushion form bearing for artificial hip joints. *Acta Biomater*, 6(12), 4698-4707.
- Esposito, C., Maclean, F., Campbell, P., Walter, W. L., Walter, W. K., & Bonar, S. F. (2013). Periprosthetic tissues from third generation alumina-on-alumina total hip arthroplasties. *Journal of Arthroplasty*, 28, 860-866.
- European Committee for Standardisation (CEN) (2018). Joint implants, Part 1: Novel methods for isolating wear particles from joint replacements and related devices. CEN Workshop Agreement 17253-1. CEN, Brussels, Belgium.
- Eymard, F., & Chevalier, X. (2016). Inflammation of the infrapatellar fat pad.

*Joint Bone Spine*, 83(4), 389-393.

- Food and Drugs Administration (FDA), (2016). Use of International Standard ISO 10993-1, "Biological evaluation of medical devices - Part 1: Evaluation and testing within a risk management process." Guidance for Industry and Food and Drug Administration Staff.
- Firkins, P. J., Tipper, J. L., Saadatzadeh, M. R., Ingham, E., Stone, M. H., Farrar, R., & Fisher, J. (2001). Quantitative analysis of wear and wear debris from metal-on-metal hip prostheses tested in a physiological hip joint simulator. *Bio-Medical Materials and Engineering*, 11, 143-157.
- Garino, J. P. (2000). Modern ceramic-on-ceramic total hip systems in the United States: early results. *Clin Orthop Relat Res* (379), 41-47.
- Gartner, L. P., & Hiatt, J. L. (2001). *Color textbook of histology* (2nd ed.). Philadelphia; London: W.B. Saunders.
- Gelb, H., Schumacher, H. R., Cuckler, J., Ducheyne, P., & Baker, D. G. (1994). In vivo inflammatory response to polymethylmethacrylate particulate debris: effect of size, morphology, and surface area. *J Orthop Res*, 12(1), 83-92.
- Germain, M., Hatton, A., Williams, S., Matthews, J., Stone, M., Fisher, J., & Ingham, E. (2003). Comparison of the cytotoxicity of clinically relevant cobalt–chromium and alumina ceramic wear particles in vitro. *Biomaterials*, 24, 469-479.
- Gibon, E., Córdova, L. A., Lu, L., Lin, T. H., Yao, Z., Hamadouche, M., & Goodman, S. B. (2017). The biological response to orthopedic implants for joint replacement. II: Polyethylene, ceramics, PMMA, and the foreign body reaction. *J Biomed Mater Res B Appl Biomater*, 105(6), 1685-1691.
- Gill, H. S., Grammatopoulos, G., Adshead, S., Tsiologiannis, E., & Tsiridis, E. (2012). Molecular and immune toxicity of CoCr nanoparticles in MoM hip arthroplasty. *Trends Mol Med*, 18(3), 145-155.
- Goodman, S., Trindade, M., Ma, T., Lee, M., Wang, N., Ikenou, T., . . . Smith, R. L. (2003). Modulation of bone ingrowth and tissue differentiation by local infusion of interleukin-10 in the presence of ultra-high molecular weight polyethylene (UHMWPE) wear particles. *J Biomed Mater Res A*, 65(1), 43-50.

- Goodman, S. B. (1994). The effects of micromotion and particulate materials on tissue differentiation. Bone chamber studies in rabbits. *Acta Orthop Scand Suppl*, 258, 1-43.
- Goodman, S. B., Chin, R. C., & Magee, F. P. (1992). Prostaglandin E2 production by the membrane surrounding loose and fixated cemented tibial hemiarthroplasties in the rabbit knee. *Clin Orthop Relat Res*(284), 283-287.
- Granchi, D., Cenni, E., Ciapetti, G., Savarino, L., Stea, S., Gamberini, . . . Pizzoferrato, A. (1998). Cell death induced by metal ions: necrosis or apoptosis? *Journal of materials science: materials in medicine*, 91, 31-37.
- Green, T. R., Fisher, J., Stone, M., Wroblewski, B. M., & Ingham, E. (1998). Polyethylene particles of a 'critical size' are necessary for the induction of cytokines by macrophages in vitro. *Biomaterials*, 19(24), 2297-2302.
- Grosse, S., Haugland, H. K., Lilleng, P., Ellison, P., Hallan, G., & Hol, P. J. (2015). Wear particles and ions from cemented and uncemented titanium-based hip prostheses-A histological and chemical analysis of retrieval material. *Journal of Biomedical Materials Research Part B- Applied Biomaterials*, 103, 709-717.
- Gruener, G., & Camacho, P. (2014). Paget's disease of bone. *Handb Clin Neurol*, 119, 529-540.
- Haddad, F. S., Thakrar, R. R., Hart, A. J., Skinner, J. A., Nargol, A. V., Nolan, J. F., . . . Case, C. P. (2011). Metal-on-metal bearings: the evidence so far. *J Bone Joint Surg Br*, 93(5), 572-579.
- Hafez, H. S., Selim, E. M., Kamel Eid, F. H., Tawfik, W. A., Al-Ashkar, E. A., & Mostafa, Y. A. (2011). Cytotoxicity, genotoxicity, and metal release in patients with fixed orthodontic appliances: a longitudinal in-vivo study. *Am J Orthod Dentofacial Orthop*, 140(3), 298-308.
- Haley, P. J. (2003). Species differences in the structure and function of the immune system. *Toxicology*, 188(1), 49-71.
- Hallab, N. (2001). Metal sensitivity in patients with orthopedic implants. *J Clin Rheumatol*, 7(4), 215-218.
- Hamilton, W. G., McAuley, J. P., Dennis, D. A., Murphy, J. A., Blumenfeld, T. J., & Politi, J. (2010). THA with Delta ceramic on ceramic: results of a

- multicenter investigational device exemption trial. *Clin Orthop Relat Res*, 468(2), 358-366.
- Harman MK, Banks SA, Hodge WA. Wear analysis of a retrieved hip implant with titanium nitride coating (1997). *J Arthroplasty*, 12(8), 938-45.
- Hart, A. J., Quinn, P. D., Sampson, B., Sandison, A., Atkinson, K. D., Skinner, J. A., . . . Mosselmans, J. F. (2010). The chemical form of metallic debris in tissues surrounding metal-on-metal hips with unexplained failure. *Acta Biomater*, 6(11), 4439-4446.
- Hatton, A., Nevelos, J. E., Matthews, J. B., Fisher, J., & Ingham, E. (2003). Effects of clinically relevant alumina ceramic wear particles on TNF-alpha production by human peripheral blood mononuclear phagocytes. *Biomaterials*, 24, 1193-1204.
- Hatton, A., Nevelos, J. E., Nevelos, A. A., Banks, R. E., Fisher, J., & Ingham, E. (2002). Alumina-alumina artificial hip joints. Part I: a histological analysis and characterisation of wear debris by laser capture microdissection of tissues retrieved at revision. *Biomaterials*, 23(16), 3429-3440.
- Haynes, D. R., Crotti, T. N., & Haywood, M. R. (2000). Corrosion of and changes in biological effects of cobalt chrome alloy and 316L stainless steel prosthetic particles with age. *J Biomed Mater Res*, 49(2), 167-175.
- Heide, N., & Schultze, J. (1993). Corrosion stability of TiN prepared by ion implantation and PVD. *Nuclear Instruments and Methods in Physics Research Section B: Beam Interactions with Materials and Atoms*, 80-81, 467-471.
- Hench, L. L. (1991). Bioceramics: from concept to clinic. *Journal of the American Ceramic Society*, 74(7), 1487-1510.
- Higgins, D. M., Basaraba, R. J., Hohnbaum, A. C., Lee, E. J., Grainger, D. W., & Gonzalez-Juarrero, M. (2009). Localized immunosuppressive environment in the foreign body response to implanted biomaterials. *Am J Pathol*, 175(1), 161-170.
- Hofbauer, L. C., Lacey, D. L., Dunstan, C. R., Spelsberg, T. C., Riggs, B. L., & Khosla, S. (1999). Interleukin-1beta and tumor necrosis factor-alpha, but not interleukin-6, stimulate osteoprotegerin ligand gene expression

- in human osteoblastic cells. *Bone*, 25(3), 255-259.
- Holmberg, K., & Mathews, A. (1994). Coatings tribology: a concept, critical aspects and future directions. *Thin Solid Films*, 253(1-2), 173-178.
- Howie, D. W., Vernon-Roberts, B., Oakeshott, R., & Manthey, B. (1988). A rat model of resorption of bone at the cement-bone interface in the presence of polyethylene wear particles. *J Bone Joint Surg Am*, 70(2), 257-263.
- Howlett, C. R., McCartney, E., & Ching, W. (1989). The effect of silicon nitride ceramic on rabbit skeletal cells and tissue. An in vitro and in vivo investigation. *Clin Orthop Relat Res*(244), 293-304.
- Howling, G. I., Barnett, P. I., Tipper, J. L., Stone, M. H., Fisher, J., & Ingham, E. (2001). Quantitative characterization of polyethylene debris isolated from periprosthetic tissue in early failure knee implants and early and late failure Charnley hip implants. *J Biomed Mater Res*, 58(4), 415-420.
- Ingham, E., & Fisher, J. (2000). Biological reactions to wear debris in total joint replacement. *Proc Inst Mech Eng H*, 214(1), 21-37.
- Ingham, E., Fisher, J., & Stone, M. H. (2003). Wear of historical polyethylenes in hip prostheses. Biomechanical success and a biological failure. *Hip International*, 13, S17-S27.
- International Standards Organisation (ISO) (2007). Implants for surgery -- Metallic materials -- Part 12: Wrought cobalt-chromium-molybdenum alloy ISO 5832-12. ISO, Geneva, Switzerland.
- International Standards Organisation (ISO) (2011). Wear of implant materials - Polymer and metal wear particles - Isolation and characterization. ISO 17853. ISO, Geneva, Switzerland.
- International Standards Organisation (ISO) (2011). Implants for surgery -- Partial and total hip joint prostheses -- Part 2: Articulating surfaces made of metallic, ceramic and plastics materials. ISO 7206-2. ISO, Geneva, Switzerland.
- International Standards Organisation (ISO) (2016). Biological evaluation of medical devices -- Part 6: Tests for local effects after implantation. ISO 10993-6. ISO, Geneva, Switzerland.
- Iwanaga, T., Shikichi, M., Kitamura, H., Yanase, H., & Nozawa-Inoue, K. (2000). Morphology and functional roles of synoviocytes in the joint.

*Arch Histol Cytol*, 63(1), 17-31.

- Jaffe, W. L., Strauss, E. J., Cardinale, M., Herrera, L., & Kummer, F. J. (2009). Surface oxidized zirconium total hip arthroplasty head damage due to closed reduction effects on polyethylene wear. *J Arthroplasty*, 24(6), 898-902.
- Keating, J. F., Grant, A., Masson, M., Scott, N. W., & Forbes, J. F. (2006). Randomized comparison of reduction and fixation, bipolar hemiarthroplasty, and total hip arthroplasty. Treatment of displaced intracapsular hip fractures in healthy older patients. *J Bone Joint Surg Am*, 88(2), 249-260.
- Khanna, R, Ong, J., Oral, E., & Narayan, R. (2017). Progress in wear resistant materials for total hip arthroplasty. *Coatings*, 7, 99.
- Khosla, S. (2001). Minireview: the OPG/RANKL/RANK system. *Endocrinology*, 142(12), 5050-5055.
- Kilgus, D. J., Dorey, F. J., Finerman, G. A., & Amstutz, H. C. (1991). Patient activity, sports participation, and impact loading on the durability of cemented total hip replacements. *Clin Orthop Relat Res* (269), 25-31.
- Kim, Y. H. (2004). Titanium and cobalt-chrome cementless femoral stems of identical shape produce equal results. *Clin Orthop Relat Res* (427), 148-156.
- Kinov, P., Leithner, A., Radl, R., Bodo, K., Khoschsorur, G. A., Schauenstein, K., & Windhager, R. (2006). Role of free radicals in aseptic loosening of hip arthroplasty. *J Orthop Res*, 24(1), 55-62.
- Kirkpatrick, C. J., Alves, A., Köhler, H., Kriegsmann, J., Bittinger, F., Otto, M., . . . Eloy, R. (2000). Biomaterial-induced sarcoma: A novel model to study preneoplastic change. *Am J Pathol*, 156(4), 1455-1467.
- Kobayashi, M., & Oka, M. (2004). Characterization of a polyvinyl alcohol-hydrogel artificial articular cartilage prepared by injection molding. *J Biomater Sci Polym Ed*, 15(6), 741-751.
- Kovalak, E., Özdemir, H., Ermutlu, C., & Obut, A. (2018). Assessment of hip abductors by MRI after total hip arthroplasty and effect of fatty atrophy on functional outcome. *Acta Orthop Traumatol Turc*, 52(3), 196-200.
- Kubo, T., Sawada, K., Hirakawa, K., Shimizu, C., Takamatsu, T., & Hirasawa, Y. (1999). Histiocyte reaction in rabbit femurs to UHMWPE, metal, and

- ceramic particles in different sizes. *J Biomed Mater Res*, 45(4), 363-369.
- Kue, R., Sohrabi, A., Nagle, D., Frondoza, C., & Hungerford, D. (1999). Enhanced proliferation and osteocalcin production by human osteoblast-like MG63 cells on silicon nitride ceramic discs. *Biomaterials*, 20(13), 1195-1201.
- Kung, M. S., Markantonis, J., Nelson, S. D., & Campbell, P. (2015). The synovial lining and synovial fluid properties after joint arthroplasty. *Lubricants*, 3(2), 394-412.
- Kurtz, S., Mowat, F., Ong, K., Chan, N., Lau, E., & Halpern, M. (2005). Prevalence of primary and revision total hip and knee arthroplasty in the United States from 1990 through 2002. *J Bone Joint Surg Am*, 87(7), 1487-1497.
- Kurtz, S. M. (2009). *UHMWPE biomaterials handbook: ultra-high molecular weight polyethylene in total joint replacement and medical devices* (2nd ed. ed.). Amsterdam; London: Academic.
- Kyomoto, M., Moro, T., Iwasaki, Y., Miyaji, F., Kawaguchi, H., Takatori, Y., . . . Ishihara, K. (2009). Superlubricious surface mimicking articular cartilage by grafting poly(2-methacryloyloxyethyl phosphorylcholine) on orthopaedic metal bearings. *J Biomed Mater Res A*, 91(3), 730-741.
- La Budde, J. K., Orosz, J. F., Bonfiglio, T. A., & Pellegrini, V. D. (1994). Particulate titanium and cobalt-chrome metallic debris in failed total knee arthroplasty. A quantitative histologic analysis. *J Arthroplasty*, 9(3), 291-304.
- Ladon, D., Doherty, A., Newson, R., Turner, J., Bhamra, M., & Case, C. P. (2004). Changes in metal levels and chromosome aberrations in the peripheral blood of patients after metal-on-metal hip arthroplasty. *J Arthroplasty*, 19(8 Suppl 3), 78-83.
- Lal, S., Caseley, E. A., Hall, R. M., & Tipper, J. L. (2018). Biological Impact of Silicon Nitride for Orthopaedic Applications: Role of Particle Size, Surface Composition and Donor Variation. *Sci Rep*, 8(1), 9109.
- Lal, S., Hall, R. M., & Tipper, J. L. (2016). A novel method for isolation and recovery of ceramic nanoparticles and metal wear debris from serum lubricants at ultra-low wear rates. *Acta Biomaterialia*, 42, 420-428.

- Lalor, P. A., Revell, P. A., Gray, A. B., Wright, S., Railton, G. T., & Freeman, M. A. (1991). Sensitivity to titanium. A cause of implant failure? *J Bone Joint Surg Br*, 73(1), 25-28.
- Langlois, J., & Hamadouche, M. (2011). New animal models of wear-particle osteolysis. *Int Orthop*, 35(2), 245-251.
- Lerouge, S., Huk, O., Yahia, L. H., & Sedel, L. (1996). Characterization of in vivo wear debris from ceramic-ceramic total hip arthroplasties. *Journal of Biomedical Materials Research*, 32, 627-633.
- Leslie, I.J., Williams, S., Isaac, G., Ingham, E., & Fisher, J (2009). High cup angle and microseparation increase the wear of hip surface replacements. *Clin Orthop Relat Res* 467, 2259-2265.
- Li, C. S., Vannabouathong, C., Sprague, S., & Bhandari, M. (2015). The Use of Carbon-Fiber-Reinforced (CFR) PEEK Material in Orthopedic Implants: A Systematic Review. *Clin Med Insights Arthritis Musculoskelet Disord*, 8, 33-45.
- Liu, A., Richards, L., Bladen, C. L., Ingham, E., Fisher, J., & Tipper, J. L. (2015). The biological response to nanometre-sized polymer particles. *Acta Biomater*, 23, 38-51.
- Lu-Yao, G. L., Keller, R. B., Littenberg, B., & Wennberg, J. E. (1994). Outcomes after displaced fractures of the femoral neck. A meta-analysis of one hundred and six published reports. *J Bone Joint Surg Am*, 76(1), 15-25.
- López-Alvarez, M., Solla, E. L., González, P., Serra, J., León, B., Marques, A. P., & Reis, R. L. (2009). Silicon-hydroxyapatite bioactive coatings (Si-HA) from diatomaceous earth and silica. Study of adhesion and proliferation of osteoblast-like cells. *J Mater Sci Mater Med*, 20(5), 1131-1136.
- Ma, L., & Sines, G. (2000). Fatigue behavior of a pyrolytic carbon. *J Biomed Mater Res*, 51(1), 61-68.
- MacDonald, S. J., McCalden, R. W., Chess, D. G., Bourne, R. B., Rorabeck, C. H., Cleland, D., & Leung, F. (2003). Metal-on-metal versus polyethylene in hip arthroplasty: a randomized clinical trial. *Clin Orthop Relat Res* (406), 282-296.
- Mai, K., Verioti, C., Ezzet, K. A., Copp, S. N., Walker, R. H., & Colwell, C. W.



- (2010). Incidence of 'squeaking' after ceramic-on-ceramic total hip arthroplasty. *Clin Orthop Relat Res*, 468(2), 413-417.
- Maloney, W. J., Jasty, M., Rosenberg, A., & Harris, W. H. (1990). Bone lysis in well-fixed cemented femoral components. *J Bone Joint Surg Br*, 72(6), 966-970.
- Maloney, J. M., Lipka, S. A., & Baldwin, S. P. (2005). In Vivo Biostability of CVD Silicon Oxide and Silicon Nitride Films. *Mater Res Soc Symp Proc*, 872.
- Man, K., Jiang, L. H., Foster, R., & Yang, X. B. (2017). Immunological Responses to Total Hip Arthroplasty. *J Funct Biomater*, 8(3).
- Margevicius, K. J., Bauer, T. W., McMahon, J. T., Brown, S. A., & Merritt, K. (1994). Isolation and Characterization of Debris in Membranes around Total Joint Prostheses. *Journal of Bone and Joint Surgery-American Volume*, 76A, 1664-1675.
- Martini, L., Fini, M., Giavaresi, G., & Giardino, R. (2001). Sheep model in orthopedic research: a literature review. *Comp Med*, 51(4), 292-299.
- Matthews, J. B., Green, T. R., Stone, M. H., Wroblewski, B. M., Fisher, J., & Ingham, E. (2000). Comparison of the response of primary human peripheral blood mononuclear phagocytes from different donors to challenge with model polyethylene particles of known size and dose. *Biomaterials*, 21(20), 2033-2044.
- Mazzocchi, M., & Bellosi, A. (2008). On the possibility of silicon nitride as a ceramic for structural orthopaedic implants. Part I: processing, microstructure, mechanical properties, cytotoxicity. *J Mater Sci Mater Med*, 19(8), 2881-2887.
- McEntire, B., & Lakshminarayanan, R. (2012). U.S. Patent Application 13/619,319.
- Menzies, I. B., Mendelson, D. A., Kates, S. L., & Friedman, S. M. (2012). The impact of comorbidity on perioperative outcomes of hip fractures in a geriatric fracture model. *Geriatr Orthop Surg Rehabil*, 3(3), 129-134.
- Millett, P. J., Allen, M. J., & Bostrom, M. P. (2002). Effects of alendronate on particle-induced osteolysis in a rat model. *J Bone Joint Surg Am*, 84-A(2), 236-249.
- Milosev, I., & Remskar, M. (2009). In vivo production of nanosized metal wear

debris formed by tribochemical reaction as confirmed by high-resolution TEM and XPS analyses. *Journal of Biomedical Materials Research Part A*, 91A, 1100-1110.

- Milosev, I., Trebse, R., Kovac, S., Cör, A., & Pisot, V. (2006). Survivorship and retrieval analysis of Sikomet metal-on-metal total hip replacements at a mean of seven years. *J Bone Joint Surg Am*, 88(6), 1173-1182.
- Milošev, L., Antolić, V., Minović, A., Cör, A., Herman, S., Pavlovcic, V., & Campbell, P. (2000). Extensive metallosis and necrosis in failed prostheses with cemented titanium-alloy stems and ceramic heads. *J Bone Joint Surg Br*, 82(3), 352-357.
- Mirsaidi, A., Genelin, K., Vetsch, J. R., Stanger, S., Theiss, F., Lindtner, R. A., . . . Richards, P. J. (2014). Therapeutic potential of adipose-derived stromal cells in age-related osteoporosis. *Biomaterials*, 35(26), 7326-7335.
- Mochida, Y., Boehler, M., Salzer, M., & Bauer, T. W. (2001). Debris from failed ceramic-on-ceramic and ceramic-on-polyethylene hip prostheses. *Clinical orthopaedics and related research*, 113-125.
- Morlock, M., Bünthe, D., Gührs, J., & Bishop, N. (2017). Corrosion of the Head-Stem Taper Junction-Are We on the Verge of an Epidemic?: Review Article. *HSS J*, 13(1), 42-49.
- Moroni, A., Nocco, E., Hoque, M., Diremiglio, E., Buffoli, D., Cantù, F., . . . Apostoli, P. (2012). Cushion bearings versus large diameter head metal-on-metal bearings in total hip arthroplasty: a short-term metal ion study. *Arch Orthop Trauma Surg*, 132(1), 123-129.
- Morrison, C., Macnair, R., MacDonald, C., Wykman, A., Goldie, I., & Grant, M. H. (1995). In vitro biocompatibility testing of polymers for orthopaedic implants using cultured fibroblasts and osteoblasts. *Biomaterials*, 16(13), 987-992.
- Muir, P., Schaefer, S. L., Manley, P. A., Svaren, J. P., Oldenhoff, W. E., & Hao, Z. (2007). Expression of immune response genes in the stifle joint of dogs with oligoarthritis and degenerative cranial cruciate ligament rupture. *Vet Immunol Immunopathol*, 119(3-4), 214-221.
- Murphy, K., Travers, P., Walport, M., & Janeway, C. (2012). *Janeway's immunobiology* (8th ed. ed.). London: Garland Science; London: Taylor

& Francis [distributor].

- National Joint Registry (NJR) (2017). 14th Annual Report. NJR, Hemel Hempstead, United Kingdom.
- Neumann, A., Reske, T., Held, M., Jahnke, K., Ragoss, C., & Maier, H. R. (2004). Comparative investigation of the biocompatibility of various silicon nitride ceramic qualities in vitro. *J Mater Sci Mater Med*, *15*(10), 1135-1140.
- Neut, D., Kluin, O. S., Thompson, J., van der Mei, H. C., & Busscher, H. J. (2010). Gentamicin release from commercially-available gentamicin-loaded PMMA bone cements in a prosthesis-related interfacial gap model and their antibacterial efficacy. *BMC Musculoskelet Disord*, *11*, 258.
- Nevelos, J., Ingham, E., Doyle, C., Streicher, R., Nevelos, A., Walter, W., & Fisher, J. (2000). Microseparation of the centers of alumina-alumina artificial hip joints during simulator testing produces clinically relevant wear rates and patterns. *J Arthroplasty*, *15*(6), 793-795.
- Nevelos, J. E., Ingham, E., Doyle, C., Fisher, J., & Nevelos, A. B. (1999). Analysis of retrieved alumina ceramic components from Mittelmeier total hip prostheses. *Biomaterials*, *20*, 1833-1840.
- Newman, E., Turner, A. S., & Wark, J. D. (1995). The potential of sheep for the study of osteopenia: current status and comparison with other animal models. *Bone*, *16*(4 Suppl), 277S-284S.
- Niedzwiecki, S., Klapperich, C., Short, J., Jani, S., Ries, M., & Pruitt, L. (2001). Comparison of three joint simulator wear debris isolation techniques: acid digestion, base digestion, and enzyme cleavage. *J Biomed Mater Res*, *56*(2), 245-249.
- Nine, M. J., Choudhury, D., Hee, A. C., Mootanah, R., & Osman, N. A. A. (2014). Wear Debris Characterization and Corresponding Biological Response: Artificial Hip and Knee Joints. *Materials (Basel)*, *7*(2), 980-1016.
- Okuda-Shimazaki, J., Takaku, S., Kanehira, K., Sonezaki, S., & Taniguchi, A. (2010). Effects of titanium dioxide nanoparticle aggregate size on gene expression. *Int J Mol Sci*, *11*(6), 2383-2392.
- Olofsson, J., Pettersson, M., Teuscher, N., Heilmann, A., Larsson, K.,

- Grandfield, K., . . . Engqvist, H. (2012). Fabrication and evaluation of SixNy coatings for total joint replacements. *J Mater Sci Mater Med*, 23(8), 1879-1889.
- Onega, T., Baron, J., & MacKenzie, T. (2006). Cancer after total joint arthroplasty: a meta-analysis. *Cancer Epidemiol Biomarkers Prev*, 15(8), 1532-1537.
- Pandit, H., Glyn-Jones, S., McLardy-Smith, P., Gundle, R., Whitwell, D., Gibbons, C. L., . . . Murray, D. W. (2008). Pseudotumours associated with metal-on-metal hip resurfacings. *J Bone Joint Surg Br*, 90(7), 847-851.
- Papageorgiou, I., Yin, Z., Ladon, D., Baird, D., Lewis, A. C., Sood, A., . . . Case, C. P. (2007). Genotoxic effects of particles of surgical cobalt chrome alloy on human cells of different age in vitro. *Mutat Res*, 619(1-2), 45-58.
- Partridge, S., Tipper, J. L., Al-Hajjar, M., Isaac, G. H., Fisher, J., & Williams, S. (2018). Evaluation of a new methodology to simulate damage and wear of polyethylene hip replacements subjected to edge loading in hip simulator testing. *J Biomed Mater Res B Appl Biomater*, 106(4), 1456-1462.
- Paustenbach, D., Galbraith, D., & Finley, B. (2014). Authors' Response to Letters to the Editor Re: Interpreting cobalt blood concentrations in hip implant patients. *Clin Toxicol (Phila)*, 52(5), 569-570.
- Pearce, A. I., Richards, R. G., Milz, S., Schneider, E., & Pearce, S. G. (2007). Animal models for implant biomaterial research in bone: a review. *Eur Cell Mater*, 13, 1-10.
- Pettersson, M., Bryant, M., Schmidt, S., Engqvist, H., Hall, R. M., . . . Persson, C. (2016). Dissolution behaviour of silicon nitride coatings for joint replacements. *Materials Science and Engineering*, 62.
- Peuster, M., Kaese, V., Wuensch, G., von Schnakenburg, C., Niemeyer, M., Fink, C., . . . Hausdorf, G. (2003). Composition and in vitro biocompatibility of corroding tungsten coils. *J Biomed Mater Res B Appl Biomater*, 65(1), 211-216.
- Pound, P., Ebrahim, S., Sandercock, P., Bracken, M. B., Roberts, I., & Group, R. A. T. S. R. (2004). Where is the evidence that animal research

- benefits humans? *BMJ*, 328(7438), 514-517.
- Rae, T. (1986). The biological response to titanium and titanium-aluminium-vanadium alloy particles. II. Long-term animal studies. *Biomaterials*, 7(1), 37-40.
- Raimondi MT, Pietrabissa R. The in-vivo wear performance of prosthetic femoral heads with titanium nitride coating (2000). *Biomaterials*, 21(9), 907-13.
- Rajpura, A., Kendoff, D., & Board, T. N. (2014). The current state of bearing surfaces in total hip replacement. *Bone Joint J*, 96-B(2), 147-156.
- Ramos-Vara, J. A. (2005). Technical aspects of immunohistochemistry. *Vet Pathol*, 42(4), 405-426.
- Ratner, B. D. (2004). *Biomaterials science: an introduction to materials in medicine* (2nd ed. ed.). Amsterdam; London: Elsevier Academic Press.
- Ren, P. G., Lee, S. W., Biswal, S., & Goodman, S. B. (2008). Systemic trafficking of macrophages induced by bone cement particles in nude mice. *Biomaterials*, 29(36), 4760-4765.
- Ren, W., Yang, S. Y., Fang, H. W., Hsu, S., & Wooley, P. H. (2003). Distinct gene expression of receptor activator of nuclear factor-kappaB and rank ligand in the inflammatory response to variant morphologies of UHMWPE particles. *Biomaterials*, 24(26), 4819-4826.
- Revell, P. A. (2008). *Joint replacement technology*. Cambridge: Woodhead.
- Ridzwan, MIZ, Shuib, S, Hassan, A. Y., Shokri, A., & Ibrahim, M. (2007). Problem of stress shielding and improvement to the hip implant designs: A review. In (Vol. 7, pp. 460-467).
- Roualdes, O., Duclos, M. E., Gutknecht, D., Frappart, L., Chevalier, J., & Hartmann, D. J. (2010). In vitro and in vivo evaluation of an alumina-zirconia composite for arthroplasty applications. *Biomaterials*, 31(8), 2043-2054.
- Sacomen, D., Smith, R. L., Song, Y., Fornasier, V., & Goodman, S. B. (1998). Effects of polyethylene particles on tissue surrounding knee arthroplasties in rabbits. *J Biomed Mater Res*, 43(2), 123-130.
- Sadowski, C. M., & Gabay, C. (2006). [Septic arthritis]. *Rev Med Suisse*, 2(57), 702-704, 707-708.
- Savarino, L., Granchi, D., Ciapetti, G., Stea, S., Donati, M. E., Zinghi, G., . . .

- Montanaro, L. (1999). Effects of metal ions on white blood cells of patients with failed total joint arthroplasties. *J Biomed Mater Res*, 47(4), 543-550.
- Savio, J. A., Overcamp, L. M., & Black, J. (1994). Size and shape of biomaterial wear debris. *Clin Mater*, 15(2), 101-147.
- Scharf, B., Clement, C. C., Zolla, V., Perino, G., Yan, B., Elci, S. G., . . . Santambrogio, L. (2014). Molecular analysis of chromium and cobalt-related toxicity. *Sci Rep*, 4, 5729.
- Schechter, A. N., & Rettig, R. A. (2002). Funding priorities for medical research. *JAMA*, 288(7), 832; author reply 832.
- Schmiedberg, S. K., Chang, D. H., Frondoza, C. G., Valdevit, A. D., & Kostuik, J. P. (1994). Isolation and characterization of metallic wear debris from a dynamic intervertebral disc prosthesis. *J Biomed Mater Res*, 28(11), 1277-1288.
- Scholes, S. C., & Unsworth, A. (2000). Comparison of friction and lubrication of different hip prostheses. *Proc Inst Mech Eng H*, 214(1), 49-57.
- Sedrakyan, A. (2012). Metal-on-metal failures--in science, regulation, and policy. *Lancet*, 379(9822), 1174-1176.
- Shanbhag, A. S., Jacobs, J. J., Black, J., Galante, J. O., & Glant, T. T. (1995). Human monocyte response to particulate biomaterials generated in vivo and in vitro. *J Orthop Res*, 13(5), 792-801.
- Shanbhag, A. S., Jacobs, J. J., Glant, T. T., Gilbert, J. L., Black, J., & Galante, J. O. (1994). Composition and Morphology of Wear Debris in Failed Uncemented Total Hip-Replacement. *Journal of Bone and Joint Surgery-British Volume*, 76B, 60-67.
- Shrestha, L. B. (2006). The changing demographic profile of the United States. Library of Congress Washington Dc Congressional Research Service.
- Silva, M., Shepherd, E. F., Jackson, W. O., Dorey, F. J., & Schmalzried, T. P. (2002). Average patient walking activity approaches 2 million cycles per year: pedometers under-record walking activity. *J Arthroplasty*, 17(6), 693-697.
- Skurla, C. P., Pluhar, G. E., Frankel, D. J., Egger, E. L., & James, S. P. (2005). Assessing the dog as a model for human total hip replacement.

- Analysis of 38 canine cemented femoral components retrieved at post-mortem. *J Bone Joint Surg Br*, 87(1), 120-127.
- Sonntag, R., Reinders, J., & Kretzer, J. P. (2012a). What's next? Alternative materials for articulation in total joint replacement. *Acta Biomater*, 8(7), 2434-2441.
- Sonntag, R., Reinders, J., & Kretzer, J. P. (2012b). What's next? Alternative materials for articulation in total joint replacement. *Acta Biomater*, 8(7), 2434-2441.
- Stargardt, T. (2008). Health service costs in Europe: cost and reimbursement of primary hip replacement in nine countries. *Health Econ*, 17(1 Suppl), S9-20.
- Stewart, T., Tipper, J. L., Streicher, R., Ingham, E., & Fisher, J (2001). Long-term wear of HIPed alumina on alumina bearings for THR under microseparation conditions. *J Mater Sci Mater Med*, 12, 1053–1056.
- Stone, D. S., Yoder, K. B., & Sproul, W. D. (1991). Hardness and elastic modulus of TiN based on continuous indentation technique and new correlation. *Journal of Vacuum Science & Technology A: Vacuum, Surfaces, and Films*, 9(4), 2543.
- Sundfeldt, M., Widmark, M., Johansson, C. B., Campbell, P., & Carlsson, L. V. (2002). Effect of submicron polyethylene particles on an osseointegrated implant: an experimental study with a rabbit patello-femoral prosthesis. *Acta Orthop Scand*, 73(4), 416-424.
- Swanson, S. A., Freeman, M. A., & Heath, J. C. (1973). Laboratory tests on total joint replacement prostheses. *J Bone Joint Surg Br*, 55(4), 759-773.
- Swedish Hip Arthroplasty Register (SHAR) (2010). Annual Report. Shar, Gothenburg, Sweden.
- Sze, S. M. (2001). *Semiconductor devices, physics and technology* (2nd ed. ed.). New York; [Chichester]: Wiley.
- Takeichi, T., & Kitamura, O. (2009). Detection of diatom in formalin-fixed tissue by proteinase K digestion. *Forensic Science International*, 190, 19-23.
- Tashjian, A. H., & Levine, L. (1978). Epidermal growth factor stimulates prostaglandin production and bone resorption in cultured mouse

calvaria. *Biochem Biophys Res Commun*, 85(3), 966-975.

- Taylor, R., Bernero, J., Patel, A., Brodke, D., & Khandkar, A. (2010). Silicon nitride: a new material for spinal implants. *Journal of Bone & Joint Surgery*, 92(B),133.
- Theis, J. C., & Ball, C. (2003). Medium-term results of cementless hydroxyapatite-coated primary total hip arthroplasty: a clinical and radiological review. *J Orthop Surg (Hong Kong)*, 11(2), 159-165.
- Tipper, J. L., Firkins, P. J., Besong, A. A., Barbour, P. S. M., Nevelos, J., Stone, M. H., ... & Fisher, J. (2001). Characterisation of wear debris from UHMWPE on zirconia ceramic, metal-on-metal and alumina ceramic-on-ceramic hip prostheses generated in a physiological anatomical hip joint simulator. *Wear*, 250(1-12), 120-128.
- Tiwari, G., Tiwari, R., Sriwastawa, B., Bhati, L., Pandey, S., Pandey, P., & Bannerjee, S. K. (2012). Drug delivery systems: An updated review. *Int J Pharm Investig*, 2(1), 2-11.
- Trindade, M. C., Song, Y., Aspenberg, P., Smith, R. L., & Goodman, S. B. (1999). Proinflammatory mediator release in response to particle challenge: studies using the bone harvest chamber. *J Biomed Mater Res*, 48(4), 434-439.
- Tsaousi, A., Jones, E., & Case, C. P. (2010). The in vitro genotoxicity of orthopaedic ceramic (Al<sub>2</sub>O<sub>3</sub>) and metal (CoCr alloy) particles. *Mutat Res*, 697(1-2), 1-9.
- Turk, J. L. (1980). *Delayed hypersensitivity* (3rd revised ed. ed.). Amsterdam; Oxford: Elsevier/North-Holland Biomedical Press.
- Turner AS, (1993). Static and dynamic histomorphometric data in 9- to 11-year old ewes. *ACVS*, 413.
- United Nations (UN) (2012). World population prospects. The 2012 Revision. UN, New York, United States.
- Unsworth, A., Dowson, D., & Wright, V. (1975). Some new evidence on human joint lubrication. *Ann Rheum Dis*, 34(4), 277-285.
- Urban, R. M., Jacobs, J. J., Tomlinson, M. J., Gavrilovic, J., Black, J., & Peoc'h, M. (2000). Dissemination of wear particles to the liver, spleen, and abdominal lymph nodes of patients with hip or knee replacement. *JBJs*, 82(4), 457-477.



- Ushio, K., Oka, M., Hyon, S. H., Hayami, T., Yura, S., Matsumura, K., . . . Nakamura, T. (2004). Attachment of artificial cartilage to underlying bone. *J Biomed Mater Res B Appl Biomater*, 68(1), 59-68.
- Vermes, C., Chandrasekaran, R., Jacobs, J. J., Galante, J. O., Roebuck, K. A., & Glant, T. T. (2001). The effects of particulate wear debris, cytokines, and growth factors on the functions of MG-63 osteoblasts. *J Bone Joint Surg Am*, 83-A(2), 201-211.
- Vijayaraghavan, V., Sabane, A. V., & Tejas, K. (2012). Hypersensitivity to titanium: a less explored area of research. *J Indian Prosthodont Soc*, 12(4), 201-207.
- Vila, M., Amaral, M., Oliveira, F., Silva, R. F., Fernandes, A., & Soares, M. Residual stress minimum in nanocrystalline diamond films. In (Vol. 89): *Applied Physics Letters*.
- Visentin, M., Stea, S., Squarzoni, S., Antonietti, B., Reggiani, M., & Toni, A. (2004). A new method for isolation of polyethylene wear debris from tissue and synovial fluid. *Biomaterials*, 25(24), 5531-5537.
- Walsh, H., Furman, B., Li, S., (2000). A True, Reproducible Accelerated Aging Protocol To Mimic 5 Year Shelf Aging of UHMWPE. *Orthopaedic Res. Soc*, 542.
- Walsh, N. C., Crotti, T. N., Goldring, S. R., & Gravallesse, E. M. (2005). Rheumatic diseases: the effects of inflammation on bone. *Immunol Rev*, 208, 228-251.
- Wang, A., Stark, C., & Dumbleton, J. H. (1996). Mechanistic and morphological origins of ultra-high molecular weight polyethylene wear debris in total joint replacement prostheses. *Proc Inst Mech Eng H*, 210(3), 141-155.
- Wang, J. Y., Wicklund, B. H., Gustilo, R. B., & Tsukayama, D. T. (1997). Prosthetic metals impair murine immune response and cytokine release in vivo and in vitro. *J Orthop Res*, 15(5), 688-699.
- Wang, W., Ouyang, Y., & Poh, C. K. (2011). Orthopaedic implant technology: biomaterials from past to future. *Ann Acad Med Singapore*, 40(5), 237-244.
- Wang, X., Mabrey, J. D., & Agrawal, C. M. (1998). An interspecies comparison of bone fracture properties. *Biomed Mater Eng*, 8(1), 1-9.

- Wang, X., Shen, X., Li, X., & Agrawal, C. M. (2002). Age-related changes in the collagen network and toughness of bone. *Bone*, 31(1), 1-7.
- Warashina, H., Sakano, S., Kitamura, S., Yamauchi, K. I., Yamaguchi, J., Ishiguro, N., & Hasegawa, Y. (2003). Biological reaction to alumina, zirconia, titanium and polyethylene particles implanted onto murine calvaria. *Biomaterials*, 24(21), 3655-3661.
- Watters, T. S., Cardona, D. M., Menon, K. S., Vinson, E. N., Bolognesi, M. P., & Dodd, L. G. (2010). Aseptic lymphocyte-dominated vasculitis-associated lesion: a clinicopathologic review of an underrecognized cause of prosthetic failure. *Am J Clin Pathol*, 134(6), 886-893.
- Wawrzynski, J., Gil, J. A., Goodman, A. D., & Waryasz, G. R. (2017). Hypersensitivity to Orthopedic Implants: A Review of the Literature. *Rheumatol Ther*, 4(1), 45-56.
- Weinans, H., Huiskes, R., & Grootenboer, H. J. (1992). Effects of material properties of femoral hip components on bone remodeling. *J Orthop Res*, 10(6), 845-853.
- Wienecke, T., & Gøtzsche, P. C. (2004). Paracetamol versus nonsteroidal anti-inflammatory drugs for rheumatoid arthritis. *Cochrane Database Syst Rev* (1), 3789.
- Willert, H. G., Bertram, H., & Buchhorn, G. H. (1990). Osteolysis in alloarthroplasty of the hip. The role of bone cement fragmentation. *Clin Orthop Relat Res* (258), 108-121.
- Willert, H. G., Buchhorn, G. H., Fayyazi, A., Flury, R., Windler, M., Köster, G., & Lohmann, C. H. (2005). Metal-on-metal bearings and hypersensitivity in patients with artificial hip joints. A clinical and histomorphological study. *J Bone Joint Surg Am*, 87(1), 28-36.
- Williams, S., Tipper, J. L., Ingham, E., Stone, M. H., & Fisher, J. (2003). In vitro analysis of the wear, wear debris and biological activity of surface-engineered coatings for use in metal-on-metal total hip replacements. *Proc Inst Mech Eng H*, 217(3), 155-163.
- Willie, B. M., Bloebaum, R. D., Bireley, W. R., Bachus, K. N., & Hofmann, A. A. (2004). Determining relevance of a weight-bearing ovine model for bone ingrowth assessment. *J Biomed Mater Res A*, 69(3), 567-576.
- Wright, T. M. P., & Goodman, S. B. (2001). *Implant wear in total joint*

*replacement: clinical and biologic issues, material and design considerations: symposium, Oakbrook, Illinois, October 2000.* Rosemont, Ill.: American Academy of Orthopaedic Surgeons.

- Xia, Z., Ricciardi, B. F., Liu, Z., von Ruhland, C., Ward, M., Lord, A., . . . Perino, G. (2017). Nano-analyses of wear particles from metal-on-metal and non-metal-on-metal dual modular neck hip arthroplasty. *Nanomedicine*, 13(3), 1205-1217.
- Yang, S. Y., Ren, W. P., Park, Y. S., Sieving, A., Hsu, S., Nasser, S., & Wooley, P. H. (2002). Diverse cellular and apoptotic responses to variant shapes of UHMWPE particles in a murine model of inflammation. *Biomaterials*, 23, 3535-3543.
- Yoon, T. R., Rowe, S. M., Jung, S. T., Seon, K. J., & Maloney, W. J. (1998). Osteolysis in association with a total hip arthroplasty with ceramic bearing surfaces. *J Bone Joint Surg Am*, 80(10), 1459-1468.
- Zhang, Y. F., Zheng, Y. F., & Qin, L. (2011). A comprehensive biological evaluation of ceramic nanoparticles as wear debris. *Nanomedicine*, 7(6), 975-982.
- Zhang, L., Ge, S., & Liu, H. (2015). Experiment investigation on fretting wear and wear debris performance for the stem-cement interface. *Journal of Nanomaterials*, 6.
- Zhao, G. Y., Zhou, M. Y., Zhao, H. L., Chen, X. L., Xie, B. B., Zhang, X. Y., . . . Zhang, Y. Z. (2012). Tenderization effect of cold-adapted collagenolytic protease MCP-01 on beef meat at low temperature and its mechanism. *Food Chem*, 134(4), 1738-1744.
- Ziaee, H., Daniel, J., Datta, A. K., Blunt, S., & McMinn, D. J. (2007). Transplacental transfer of cobalt and chromium in patients with metal-on-metal hip arthroplasty: a controlled study. *J Bone Joint Surg Br*, 89(3), 301-305.
- Zioupou, P., & Currey, J. D. (1998). Changes in the stiffness, strength, and toughness of human cortical bone with age. *Bone*, 22(1), 57-66.
- Zwierzak, I., Baleani, M., & Viceconti, M. (2009). Microindentation on cortical human bone: effects of tissue condition and indentation location on hardness values. *Proc Inst Mech Eng H*, 223(7), 913-918.

## Appendix A

### Lists of all equipment, reagents and consumables

**Table 1. Suppliers and models of equipment used.**

<b>Type of equipment</b>	<b>Supplier and model</b>
Gilson Pipetman	Gilson, UK Various models
Balance	A&D, Jencons Plc, Bedfordshire, UK GR-200
Ultrasonic water bath	VWR International Ltd. Leicestershire, UK USC300T
Incubator	Sanyo Ltd., Japan MIR262
Orbital shaker	Sigma-Aldrich, Irvine, UK KS130
Vortex mixer	Stuart SA8
Six station pin-on-plate reciprocating wear tester including all components	Pye Electric Limited
Microbalance	Mettler XP26
Microbalance	Mettler XP205
Hitachi FEG-SEM	Hitachi SU8230
pH meter	Sigma-Aldrich, Irvine, UK HANNA pH 212
Tissue processor	Leica T2 1020
Sputter coater	Agar Scientific, UK

Filter unit	Millipore, UK XX1002505
EDX system	X-Max EDX system, Oxford, UK
Ultracentrifuge, rotor and buckets	Beckman Optima L-90K
Dissection equipment	Thermo Fisher Scientific Ltd.
Wax oven	Raymond A Lamb E18/31
Wax dispenser	Raymond A Lamb E66
Microtome	Leica RM2125 RTF
Hotplate	Raymond A Lamb E18/1
Histology water bath	Barnstead Electrothermal MH8515

**Table 2. Suppliers and product codes for reagents used.**

<b>Reagent</b>	<b>Supplier</b>	<b>Product code</b>
Bovine serum albumin	Sigma-Aldrich	A7030
Calcium chloride	Sigma-Aldrich, Irvine, UK	10043-52-4
Distel solution	Tristel Solutions Limited	TM309
DPX mountant	Atom Scientific	RRSP29
Eosin Y	Merck Millipore	1.09844.1000
Ethanol absolute, analytical reagent grade	Fisher Scientific, Loughborough, UK	E/0650DF/17
Ethylenediaminetetraacetic acid (EDTA)	Fisher Scientific	11843-0010
Foetal bovine serum	Lonza Biologics, Cambridge, UK	Various
Glycine powder	Sigma-Aldrich, Irvine, UK	G7126
HEPES, acid free, >99.5%	Melford Laboratories LTD, Ipswich, UK	7365-45-9
Hydrochloric acid	H/1150/PB17	Fisher Scientific
Hydrogen peroxide	Sigma-Aldrich	H1009
ImmEdge Hydrophobic Barrier Pen	Vector laboratories	H-4000
Isopropanol	Fisher Scientific, Loughborough, UK	W292907
Mayer's Haematoxylin	Atom Scientific	RRSP60
Methanol	Atom Scientific LTD, Manchester, UK	GPS 1004-G
Neutral Buffered Formalin	Atom Scientific	RRFF4000-G
Buffered papain	Sigma-Aldrich	P3125
Phosphate buffered saline	Oxoid	BR0014G
Proteinase K powder	Fisher Scientific, UK	BP 1700-500

Scott's tap water substitute 10x concentrate	Atom Scientific	RRSP190
Shandon Histoplast paraffin wax	Thermo Fisher Scientific Ltd.	12617956
Silicon Nitride (Si <sub>3</sub> N <sub>4</sub> ) <50 nm powder	Sigma-Aldrich, Irvine, UK	334103
SLS pH buffers	Scientific Laboratories Supplies	PHB1370, PHB1300, PHB1362
Sodium azide 1% solution	G Biosciences	786-299
Sodium chloride	Thermo Fisher Scientific Ltd.	42429-5000
Sodium dodecyl sulphate (SDS), BioReagent, >98.5%	Sigma-Aldrich, Irvine, UK	L3771-500G
Sodium Hydroxide Pellets	Fisher Scientific	BPE359-500
Sodium polytungstate solution (85 % w/v)	Sigma-Aldrich, Irvine, UK	80656-100ML
Sterile filtered water	Baxter, UK	UKF7114
SurfaSil™ Silconizing Fluid	Thermo Scientific, Rockford, USA	42800
Trizma base	Sigma-Aldrich	T-1503
Tween-20	Sigma-Aldrich	P1379
Ultra Vision One detection system, HRP polymer: Ultra V Block Ultravision One HRP Polymer	Thermo Scientific	TL-125-HLJ TA-125-UB TL-125-PHJ
Ultra Vision One Large Volume Detection System, DAB Quanto Chromogen System: DAB Quanto Substrate DAB Quanto Chromogen	Thermo Scientific	TA-125-QHDX
Xylene	Atom Scientific	GPS1001-G

**Table 3. Suppliers and product codes for the consumables used.**

<b>Type of consumable</b>	<b>Supplier</b>	<b>Model</b>
0.015 µm nucleopore polycarbonate filter membrane (25 mm)	Whatman, Maidstone, Kent, UK	110601 (25 mm)
0.02 µm anapore membrane filter	Whatman, Maidstone, Kent, UK	WHA68095502
6 smooth CoCr pins,	School of Mechanical Engineering, University of Leeds	ASTM F1537 HC (>0.2% w/w), curve radius of 100°, Ra 0.01- 0.02µm
6 smooth CoCr plates,	School of Mechanical Engineering, University of Leeds	ASTM F1537 HC (>0.2% w/w), Ra 0.01-0.02µm
Aluminium SEM stubs, carbon adhesives and carbon paint	Agar scientific, Elektron Technology UK Ltd, Essex, UK	Various
Beckman polypropylene centrifuge tubes (14 ml)	Beckman Coulter Ltd., High Wycombe, UK	331374
Beckman polypropylene centrifuge tubes (32 ml)	Beckman Coulter Ltd., High Wycombe, UK	355642
CD68 antibody	AbCam	Ab955
Fine tip stainless steel forceps	Raymond A Lamb	E12
Histology moulds	Raymond A Lamb	E10.8/4161
Microtome blades	Fisher Scientific	SD3050835
Plastic histology cassettes	VWR International	720-0887
Sterile serological pipettes (10ml and 25ml)	Starstedt Ltd., Leicester, UK	86.1254.001 86.1685.001
Superfrost plus microscope slides	SLS	MIC3022



## **Appendix B**

### **Food, housing and environmental parameters of the animal studies**

Data contained in this appendix has been provided by researchers at the University of Zurich.

#### Rat study

Food	A standardized diet (Provimi Kliba, 3436). Community tap water from the city of Zurich was available <i>at libitum</i> .
Housing	Rats were housed in in groups of two to four (depending on weight) in IVC (individually ventilated cage) standard cages (T1500), size 31x41x19 cm.
Environmental	Environmental conditions were continuously monitored using a data logger for temperature and humidity. Temperature range: 19°C - 25°C. Humidity range: 30%- 80%. There was a daylight cycle.

#### Rabbit study

Food	Hay was provided at libitum and rabbit pellets were offered at least once a day. Representative hay and/or straw samples was routinely analyzed for contaminants at UZH. Food and water were not withheld before surgeries. Community tap water from the city of Zurich was available <i>ad libitum</i> .
Housing	Animals were housed 2 to 6 animals per group. The housing space provided at least 8500 cm <sup>2</sup> /animal. Individual cages were used for at least 7 days after surgery. Individual cages provided at least 5600 cm <sup>2</sup> /animal to reduce the animal's movement during recovery. The smaller cage size also facilitated

postoperative monitoring and medication. Animals were separated during feeding periods or at staff discretion to facilitate recording of clinical signs, performance of special investigations and/or to avoid aggressive behavior.

Environmental

Environmental conditions were continuously monitored using a data logger for temperature and humidity (temperature range 5-28°C, relative humidity range 30-80%). There was a daylight cycle.

## Appendix C

### Testing the particle isolation method on particle-injected rat cadavers prior to application to an in vivo study

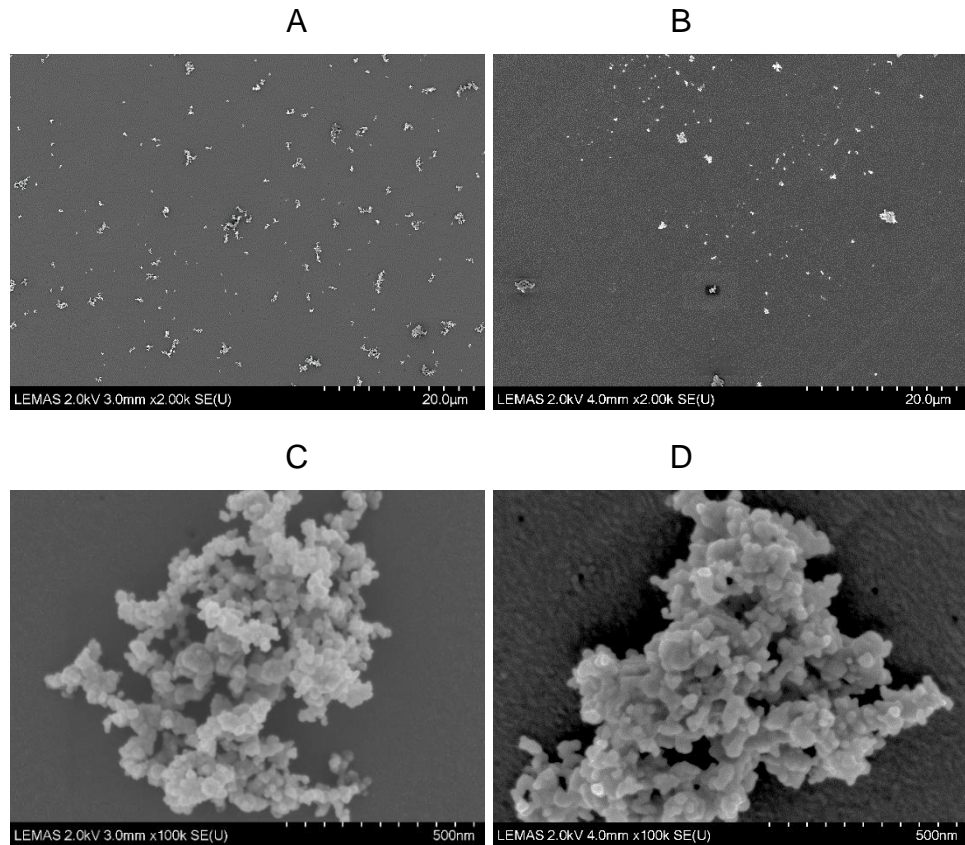
#### Materials and Methods

Materials used for this study are provided in the main materials tables in Appendix A. A  $6.2 \text{ mg.ml}^{-1}$  stock solution of commercial SiN powder was created as described in 2.2.6.2 and diluted  $\frac{1}{2}$  with PBS to create a  $0.9 \text{ mm}^3.\text{ml}^{-1}$  stock. Female Wistar rats were supplied immediately after sacrifice and the hind limbs were skinned and cut midway through the femur and tibia using clippers to enable removal of the stifle joint intact, as described in section 4.4.3. The  $0.9 \text{ mm}^3$  stock was resuspended as described in 2.2.6.2 and used to load a Hamilton syringe (G23). A volume of  $20 \text{ }\mu\text{l}$  of the particle suspension was injected into each rat stifle joint using the method described in 4.4.3. The stifle joints were fixed for 48 h with 10% NBF, after which the NBF was discarded and the pots were filled with 70% ethanol for storage. The stifle joints were washed three times in filtered water by filling each pot and immediately discarding each wash. The intact rat stifle joints were washed three times in filtered water by filling the tube, vortexing the tube, and immediately discarding each wash to remove traces of formalin, ethanol, and exterior contaminants. The patellar ligament, patella, fat pad and synovial tissue continuous with the fat pad was carefully excised as one intact piece using cleaned, sterile dissection equipment in a class II cabinet. The patella was discarded and the soft tissue (approximately 150 mg) was minced to  $1 \text{ mm}^3$ .

The samples were then digested as described in 2.2.8.1 and subjected to density gradient ultracentrifugation and washing as described in 2.2.8.2 and 2.2.8.3. Samples were analysed by scanning electron microscopy as described in 2.2.6.3, 2.2.6.4 and 2.2.6.5.

## Results

Silicon nitride particles isolated from injected rat cadavers appeared to be free from contamination and were very similar to previous SEM images of the SiN particles (Figure 1). Elemental analysis of the particles gave similar results to the non-isolated SiN particles (data not shown); no contaminating elements or pronounced oxidation occurred.



**Figure 1. Scanning electron micrographs of silicon nitride particles (A and C) prior to isolation, and (B and D) following isolation from rat cadavers using the final method, at (A and B) a low magnification and (C and D) a high magnification. Particles were sonicated and filtered onto polycarbonate filter membranes.**

## **Appendix D**

### **Immunohistochemical labelling of macrophages in particle-injected rat stifle joint tissues**

#### **Methods**

Materials for this study are included in the main materials tables (Appendix A). Rat spleen tissues from female Wistar rats were processed, wax embedded and sectioned as described in 4.4.6.1; however, spleen was not decalcified. Sections from the spleen were subjected to antibody labelling for macrophages with an anti-CD68 [clone KP1] antibody, alongside sections from the SiN-injected joint of rat 33.86. The spleen tissue was used as a positive control for macrophages.

#### **Stock solutions for antibody labelling**

##### **Phosphate buffered saline (PBS)**

One DPBS tablet was dissolved in 100 ml distilled water. The pH was adjusted to pH 7.2 -7.4 as described in 2.2.3. The solution was used immediately.

##### **Hydrogen peroxide solution (3 %; v/v)**

A volume of 20 ml hydrogen peroxide (30 %; v/v) was diluted with 180 ml DPBS and used immediately.

##### **Tris buffered saline (TBS), 10x**

A mass of 24g of Trizma base and 88 g of NaCl was dissolved in 700ml of distilled water and the pH was adjusted to 7.6 with 12 M HCl. The solution was made up to 1 litre with distilled water. The solution was autoclaved (121°C, 15psi, 20 minutes) and stored at room temperature for up to one year.

##### **TBS, 1x (final concentration 20 mM Tris, 150 mM NaCl)**

A volume of 100 ml of 10x TBS was diluted in 900 ml of distilled water and used immediately.

##### **TBS containing 0.05 % (v/v) Tween 20 (TBS-T)**

A volume of 500 ml of Tween 20 and 1000 ml of TBS was mixed using a magnetic stirrer and the pH was adjusted to 7.6 by adding 6 M HCl or 6 M NaOH. The solution was stored for up to three months at room temperature.

### **Bovine serum albumin solution (5 % (w/v))**

A mass of 2.5 g of bovine serum albumin was dissolved in 50 ml PBS using a magnetic stirrer and stirrer bar the solution was passed through a 0.2 µm filter into a sterile collection container in a class II cabinet. The solution was aliquoted into smaller volumes into sterile universals and stored frozen for up to six months.

### **Antibody diluent (TBS, 0.1 % (w/v) BSA, 0.1 % (w/v) sodium azide)**

A volume of 6 ml of sodium azide (1% w/v), 300 µl 5 % (w/v) bovine serum albumin and 40 ml TBS was mixed using a magnetic stirrer and the pH was adjusted to 7.6 by adding 6 M HCl or 6 M NaOH. The volume was made up to 60ml with TBS. The solution was stored for three months at 4 °C.

### **10mM Citric acid**

A mass of 2.1 g of citric acid (monohydrate) was dissolved in 900 ml of distilled water, pH was adjusted to pH 6 and the solution was topped up to 1 L with distilled water. The solution was used immediately.

### **Antibody labelling protocol**

Tissue samples were dewaxed and rehydrate as described in 2.2.9.2. Sections were circled using a hydrophobic marker and the slides were transferred to four well plates. Tissue sections were washed for 10 min in TBS on a shaker. Antigen retrieval was carried out by one of the following protocols:

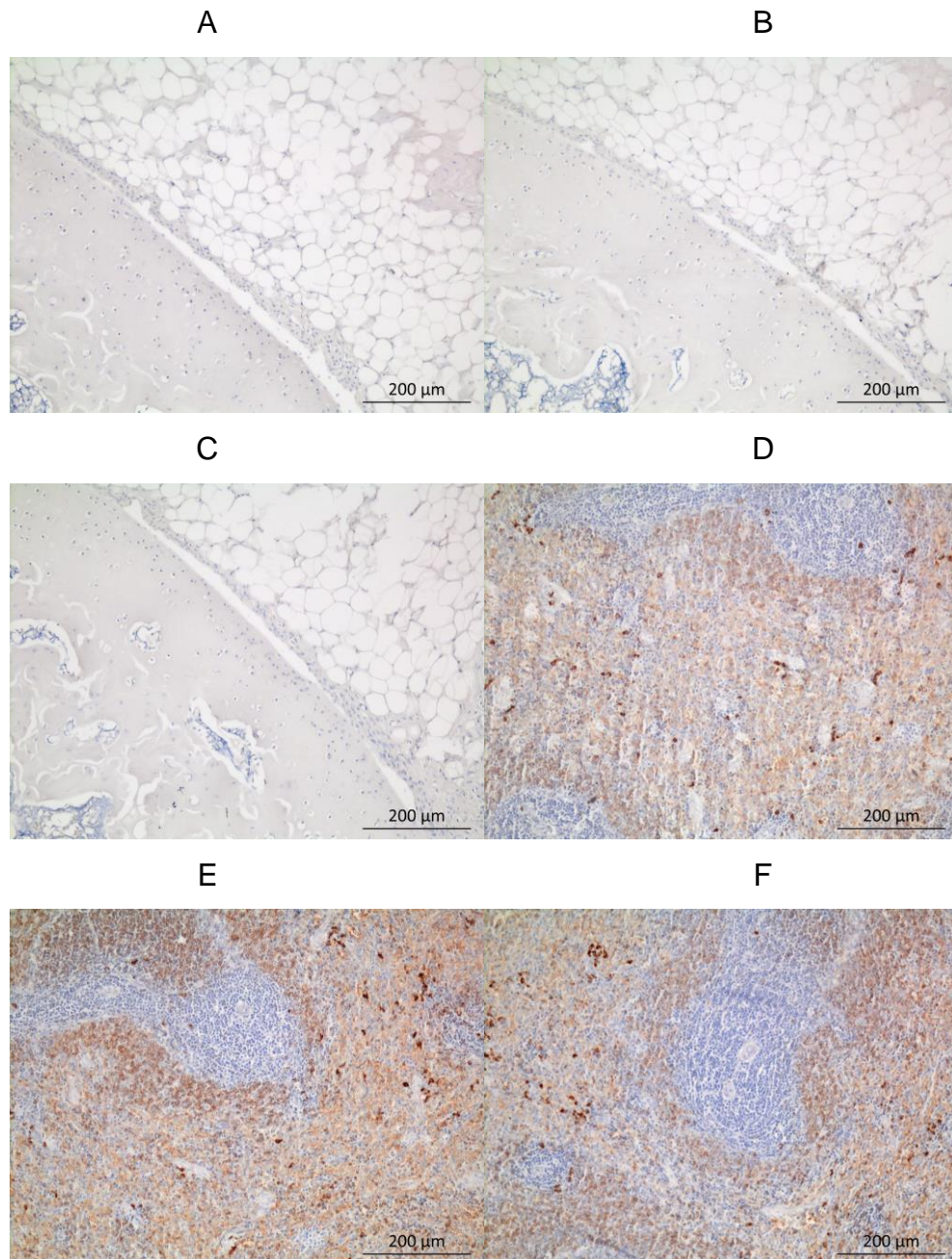
- Proteinase K: drops were added to each section and incubated at room temperature for 20 min, alone or in combination with trypsin-EDTA treatment
- Trypsin-EDTA: drops were added to each section and incubated at room temperature for 5 min
- Water bath treatment in citric acid: A coplin jar was heated to 95°C with citric acid (pH6) in a water bath. When the temperature was reached, slides immersed and incubated for 20 min
- Water bath treatment in antigen unmasking solution: A coplin jar was heated to 95°C with antigen retrieval solution (diluted to working concentration as per manufacturer's instructions) in a water bath.

When the temperature was reached, slides were immersed and incubated for 20 min

Slides were washed in TBS for 10 min. Drops of dual endogenous enzyme block were added to each section until sections were covered and incubated for 10 minutes. Slides were washed in TBS on a shaker for 5 min x3. A monoclonal CD68 antibody was diluted 1/300 with antibody diluent, the same concentration of an isotype control in antibody diluent, or diluent only was applied to cover each section and incubated for 30 mins. Slides were washed in TBS on a shaker for 5 min x3. Drops of polymer-HRP were added to each section and incubated for 30 min. Slides were washed in TBS on a shaker for 5 min x3. Substrate chromagen (20uL liquid DAB chromagen & 1ml substrate buffer) was added to cover each section and incubated for 10 min. Slides were washed four times using distilled water, and subsequently immerse in haematoxylin for 5 seconds. Slides were wash under running tap water until the water ran clear, placed into Scott's tap water for three min and rinsed using tap water for three min. Slides were mounted and viewed as described in sections 2.2.9.4 and 2.2.9.5.

## **Results**

Both positive and negative control tissue sections stained brown in the in the spleen, and no positive staining was achieved for positive or negative control rat stifle sections for any of the antigen retrieval methods used (Figure 1). Results were similar for all antigen retrieval methods.



**Figure 1. Immunohistochemical CD68 labelling of rat tissue sections.** A-C. Rat stifle joint sections from the SiN-injected stifle of rat 33.86; antibody-labelled, isotype control and diluent only control respectively. D-F. Rat spleen sections; antibody-labelled, isotype control and diluent only control respectively. Antigen retrieval was performed by proteinase K; results were similar with other antigen retrieval methods.